

Structural and functional  
characterisation of Uric Acid Permease, a  
fungal nucleobase transporter, with novel  
substrates

Nicole Deacon-Smith

2019 – 2023

Department of Life Sciences, Imperial College London

Submitted in part fulfilment of the requirements for the degree of PhD and the  
Diploma of Imperial College London

## Declaration of Originality

The work presented in this thesis is my own, and all information sources have been appropriately referenced. All experimental work carried out by, or in collaboration with, another party has been appropriately stated in the relevant Materials and Methods section of each chapter.

## Copyright Statement

The copyright of this thesis rests with the author. Unless otherwise indicated, its contents are licensed under a Creative Commons Attribution-Non Commercial 4.0 International Licence (CC BY-NC). Under this licence, you may copy and redistribute the material in any medium or format. You may also create and distribute modified versions of the work. This is on the condition that: you credit the author and do not use it, or any derivative works, for a commercial purpose. When reusing or sharing this work, ensure you make the licence terms clear to others by naming the licence and linking to the licence text. Where a work has been adapted, you should indicate that the work has been changed and describe those changes. Please seek permission from the copyright holder for uses of this work that are not included in this licence or permitted under UK Copyright Law.

## Abstract

The development of novel antifungals capable of eliminating *Aspergillus* fungal infections and improving patient outcomes in Aspergillosis is essential. This work has focussed on Uric Acid Permease, a nucleobase-ascorbate transporter from *Aspergillus nidulans*, as a potential antifungal carrier. The existing crystal structure of UapA-G411V $_{\Delta 1-11}$  in complex with xanthine (PDB 5I6C)<sup>1</sup>, has provided invaluable information about the substrate binding site, and allowed for the structure-guided design of derivatised xanthine analogues. Competitive uptake assays were used to obtain the binding affinity of each of the analogues for UapA in *Aspergillus nidulans*. 3-benzylxanthine (**5**) was identified as a novel ligand of UapA, binding with 35x higher affinity ( $K_i = 0.2 \mu\text{M}$ ) than the native substrates xanthine ( $K_M = 7 \mu\text{M}$ ) and uric acid ( $K_i = 7 \mu\text{M}$ ). This work describes the functional characterisation of 3-benzylxanthine (**5**) using fungal growth assays, and fluorescence microscopy. The effect of this substrate on UapA-WT and the thermostabilised mutants UapA-G411V $_{\Delta 1-11}$  and UapA-Q408E $_{\Delta 1-11}$  was assessed using cellular thermal shift assays (CETSA), fluorescence size-exclusion chromatography (FSEC), CPM-based thermostability assays and nano-differential scanning fluorimetry (nano-DSF). While these approaches had their challenges, they all demonstrated that 3-benzylxanthine (**5**) did not significantly destabilise UapA-WT or the thermostabilised mutants UapA-G411V $_{\Delta 1-11}$  and UapA-Q408E $_{\Delta 1-11}$ . The later part of this work describes attempts to structurally characterize the binding interaction between 3-benzylxanthine (**5**) and UapA using X-ray crystallography, hydrogen-deuterium mass spectrometry (HDX-MS) and cryo-electron microscopy (cryo-EM). While the structure of UapA-WT or its mutants with 3-benzylxanthine (**5**) has not yet been resolved, preliminary results from hydrogen-deuterium mass spectrometry (HDX-MS) suggest that 3-benzylxanthine (**5**) may bind an outward or occluded conformation of UapA-Q408E $_{\Delta 1-11}$ . Structural characterisation of UapA with 3-benzylxanthine (**5**) using cryo-EM is ongoing. Once resolved, this will form the basis of future structure-guided xanthine analogue design initiatives.

## Acknowledgements

Thank you to the Biotechnology and Biological Sciences Research Council (BBSRC) who funded this PhD. I would like to thank my supervisors Prof. Bernadette Byrne and Prof. Matthew Fuchter for their guidance and direction over the past four years. Bernadette, your unwavering support, and kindness has been invaluable.

Thank you to Prof. George Diallinas, who welcomed me to his laboratory at the National and Kapodistrian University of Athens. My time in his lab was so enjoyable, and decisive in the direction of my PhD. Where travel was impossible due to COVID-19, he kindly completed competitive uptake experiments on my behalf. Thank you to George's lab, particularly Dr Sotiris Amillis and George Broutzakis, for useful discussions on UapA structural determination.

Thank you to collaborators Prof. Argyris Politis and Dr Waqas Javed who completed the hydrogen-deuterium exchange mass spectrometry experiments presented in this work. And thank you to Dr Euan Pyle, who completed the founding HDX-MS experiments on UapA, upon which this work is based.

The biggest thank you to Dr Ben Phillips, who volunteered his time to help me with early negative-stain electron microscopy and cryo-electron microscopy experiments. Your advice and support during the last year of my PhD has been so appreciated.

Thank you to my progress review panel, Dr Ernesto Cota and Dr David Mann, whose criticisms and guidance were important to focus my research. Thank you to Prof. Alex Cameron and Dr Maruf Ali for agreeing to be my external and internal examiner respectively.

Thank you to Prof Herb Arst, Dr Marc Morgan, Dr Lisa Haigh, Dr Pete Haycock and Dr Val Pye who provided help and/or advice with *Aspergilli* growth assays, X-ray crystallography, MS, NMR and nano-DSF experiments respectively.

To my colleagues in the Fuchter group, particularly Ollie, Anne, Robert and Raymond, who provided advice during my time at the Molecular Sciences Research Hub, thank you. A big thank you to all the MSc, MRes and BSc students that I had the pleasure of working with, particularly Rinad Alhedaihy. Thank you to my colleagues in the Byrne research group, Dr Cristina Cecchetti, Dr Euan Pyle and Dr Savvas Saouros, who helped me find my feet during my first year in a Biochemistry laboratory. Thank you to James Beattie, Sara Cioccolo, Menby Woubshete and Dr Jack Houghton-Gisby, who made days in the lab so much more enjoyable. Thank you to all those who came and went on the 5<sup>th</sup> floor of SEC, who made this a fun and interesting place to work.

Finally to my friends and family, thank you.

Mum, your unwavering encouragement. Matt, your unwavering criticism.

*Pas problème*

# Table of Contents

<b>Declaration of Originality .....</b>	<b>2</b>
<b>Copyright Statement .....</b>	<b>2</b>
<b>Abstract .....</b>	<b>3</b>
<b>Acknowledgements .....</b>	<b>4</b>
<b>Table of Contents .....</b>	<b>6</b>
<b>Abbreviations.....</b>	<b>11</b>
<b>1. Literature Review .....</b>	<b>14</b>
<b>1.1. Fungal Diseases and Aspergillosis .....</b>	<b>14</b>
1.1.1. Global prevalence of fungal diseases.....	14
1.1.2. Aspergilli and resilience.....	16
1.1.3. The regulated immune response .....	20
1.1.4. Disease progression in immunocompromised individuals.....	21
1.1.5. Existing treatments for Aspergillosis.....	25
1.1.5.1. Azole antifungals .....	25
1.1.5.2. Polyene antifungals .....	27
1.1.5.3. Echinocandin antifungals.....	27
1.1.5.4. Early antifungals .....	28
1.1.6. Efficacy and emergence of resistance.....	30
1.1.7. Emerging antifungals for resistant fungi .....	32
<b>1.2. The cellular membrane .....</b>	<b>33</b>
1.2.1. The lipid bilayer .....	33
1.2.2. Membrane lipids .....	34
1.2.3. Membrane proteins.....	38

1.2.3.1.	Channels.....	41
1.2.3.2.	Transporters .....	41
1.2.3.3.	Mechanisms of transport .....	43
1.2.4.	Challenges in working with membrane proteins .....	46
1.2.4.1.	Detergents .....	47
1.2.4.2.	Alternative membrane-mimetics .....	50
1.2.4.3.	Characterisation of membrane proteins by crystallography .....	52
1.2.4.4.	Characterisation of membrane proteins by cryo-EM .....	54
1.2.4.5.	Characterisation of membrane proteins by alternative methods ..	55
1.2.5.	Membrane proteins as drug targets and biomarkers .....	58
1.2.6.	Membrane proteins as drug carriers.....	60
<b>1.3.</b>	<b>Uric Acid Permease, UapA .....</b>	<b>62</b>
1.3.1.	The NAT transporter family .....	62
1.3.2.	Uric Acid Permease, UapA.....	66
1.3.3.	X-ray crystal structure of UapA.....	68
1.3.4.	Known substrates of UapA .....	71
<b>1.4.</b>	<b>Research Aims .....</b>	<b>76</b>
<b>2.</b>	<b>Design and synthesis of purine analogues.....</b>	<b>78</b>
<b>2.1.</b>	<b>Introduction .....</b>	<b>78</b>
<b>2.2.</b>	<b>Materials and methods .....</b>	<b>80</b>
2.2.1.	Final products .....	80
<b>2.3.</b>	<b>Results .....</b>	<b>84</b>
2.3.1.	Compound design .....	84
2.3.2.	Synthesis .....	88
2.3.2.1.	Derivatisation at position N <sup>9</sup> .....	88
2.3.2.2.	Derivatisation at position O <sup>6</sup> .....	90

2.3.2.3. Derivatisation at position N <sup>3</sup> .....	96
<b>2.4. Discussion .....</b>	<b>98</b>
<b>3. Functional characterisation of nucleotide analogues.....</b>	<b>100</b>
<b>3.1. Introduction .....</b>	<b>100</b>
<b>3.2. Materials and Methods.....</b>	<b>102</b>
3.2.1. <sup>3</sup> H-xanthine competitive uptake assay.....	102
3.2.2. <i>Aspergillus nidulans</i> growth assays.....	104
3.2.3. Fluorescence Microscopy.....	105
3.2.4. Expression of UapA constructs in <i>S. cerevisiae</i> .....	105
3.2.5. Cellular thermal shift assays (CETSA) .....	106
3.2.6. Fluorescence Size Exclusion Chromatography.....	107
3.2.7. Purification of UapA in DDM.....	107
3.2.8. SDS-PAGE Gel Electrophoresis.....	108
3.2.9. Nano-differential scanning fluorimetry (Nano-DSF).....	109
3.2.10. CPM-based stability assays .....	110
<b>3.3. Results .....</b>	<b>111</b>
3.3.1. <sup>3</sup> H-xanthine competitive uptake assay.....	111
3.3.2. <i>Aspergillus nidulans</i> growth assays.....	114
3.3.2.1. Assessing effect of purine analogues on normal fungal growth .	114
3.3.2.2. Novel analogues as nitrogen sources .....	120
3.3.3. Substrate-induced endocytosis of UapA-GFP in <i>A. nidulans</i> .....	122
3.3.4. Thermostability assays of UapA in detergent–solubilised membranes .....	124
3.3.4.1. Cellular thermal shift assays (CETSA) .....	124
3.3.4.2. Fluorescence size-exclusion chromatography (FSEC) .....	128
3.3.5. Thermostability assays of purified UapA in detergent .....	134
3.3.5.1. Fluorescence-based thermostability assays using CPM.....	134
3.3.5.2. Nano-differential scanning fluorimetry (Nano-DSF).....	137



3.4.	<b>Discussion</b>	142
4.	<b>Structural characterisation of UapA with novel substrates</b>	144
4.1.	<b>Introduction</b>	144
4.2.	<b>Materials and methods</b>	146
4.2.1.	Expression and Purification of UapA in DDM	146
4.2.2.	Crystallisation trials	146
4.2.3.	Nanodisc reconstitution for UapA	147
4.2.4.	Nanodisc reconstitution for UapA-GFP	148
4.2.5.	Lipid reconstitution for nanodiscs	149
4.2.6.	MSP1E3D1 expression	149
4.2.7.	MSP1E3D1 purification	150
4.2.8.	Hydrogen-deuterium exchange mass spectrometry	150
4.2.9.	Negative-stain electron microscopy	151
4.2.10.	Cryo-electron microscopy	151
4.3.	<b>Results</b>	153
4.3.1.	Purification of UapA in DDM	153
4.3.2.	Crystallisation trials of UapA	155
4.3.2.1.	Crystallisation of UapA-G411V <sub>Δ1-11</sub> with 3-benzylxanthine (5)	155
4.3.2.2.	Crystallisation of UapA-Q408E <sub>Δ1-11</sub> with 3-benzylxanthine (5)	159
4.3.2.3.	Crystallisation of UapA-WT with 3-benzylxanthine (5)	161
4.3.3.	Reconstitution of UapA into nanodiscs	163
4.3.4.	Reconstitution of UapA-GFP-His into nanodiscs	165
4.3.5.	Electron Microscopy	167
4.3.5.1.	Negative-stain electron microscopy of UapA in DDM	167
4.3.5.2.	Negative-stain electron microscopy of UapA in nanodiscs	168
4.3.5.3.	Cryo-electron microscopy of UapA-Q408E <sub>Δ1-11</sub> in nanodiscs	169
4.3.6.	Hydrogen-deuterium exchange mass spectrometry	172

4.4.	Discussion .....	176
5.	Final Discussion .....	179
6.	Bibliography .....	184
7.	Supplemental Information.....	205
7.1.	Protocols and characterisation data for key intermediates .....	205
7.2.	Nuclear magnetic resonance (NMR) spectra .....	216
7.3.	Mass Spectrometry .....	230

# Abbreviations

[S]	–	Substrate concentration
3D	–	Three-dimensional
5FC	–	5-fluorocytosine
5FU	–	5-fluorouracil
ABC	–	ATP-binding cassette
ABCD	–	Amphotericin B colloidal dispersion
ABL	–	Amphotericin B lipid complex
ABPA	–	Allergic bronchopulmonary aspergillosis
ABTAC	–	Antibody-based PROTACs
ADC	–	Antibody-drug conjugate
AFM	–	Atomic force microscopy
AfUapC	–	Uric Acid Permease C, <i>A. fumigatus</i>
AIDS	–	Acquired immune deficiency syndrome
AMP	–	Antimicrobial peptide
ATP	–	Adenosine triphosphate
A.U.	–	Arbitrary Units
AzgA	–	Hypoxanthine-adenine-guanine transporter, <i>A. nidulans</i>
BSA	–	Bovine Serum Albumin
CDI	–	1,1'-Carbonyldiimidazole
CETSA	–	Cellular thermal shift assay
CHO	–	Chinese hamster ovary (cell)
CI-M6PR	–	Cation-independent mannose 6-phosphate receptor
CntA	–	Concentrative nucleoside transporter A
COPD	–	Chronic obstructive pulmonary disease
COVID-19	–	Coronavirus disease 2019
CPA	–	Chronic pulmonary aspergillosis
CPM	–	7-Diethylamino-3-(4'-Maleimidylphenyl)
cryo-EM	–	Cryo-electron microscopy
CTLA-4	–	Cytotoxic T-lymphocyte-associated antigen 4
D <sub>2</sub> O	–	Deuterated water
DABCO	–	1,4-diazabicyclo[2.2.2]octane
DCM	–	Dichloromethane
DDM	–	n-dodecyl-beta-maltoside
DHA	–	Docosahexaenoic acid
DM	–	n-decyl-beta-maltoside
DMSO	–	Dimethylsulfoxide
DNA	–	Deoxyribonucleic acid
EDTA	–	Ethylenediamine tetraacetic acid
ENT	–	Equilibrative nucleoside transporter
eq	–	Equivalent
ESI	–	Electrospray ionization
FcyB	–	Purine-cytosine permease, <i>A. nidulans</i>
FSEC	–	Fluorescence size exclusion chromatography
FTIR	–	Fourier-transform infrared (spectroscopy)
GDN	–	Glyco-diosgenin
GFP	–	Green fluorescent protein
GNG	–	Glucose-neopentyl glycol
GPCR	–	G-protein coupled receptor

HDX-MS	–	Hydrogen-deuterium mass spectrometry
HEK	–	(Immortalized) human embryonic kidney (cells)
HIV	–	Human immunodeficiency virus
HRMS	–	High Resolution Mass Spectrometry
IC50	–	Half-maximal inhibitory concentration
kDa	–	Kilodalton
keV	–	Kiloelectron volt
$K_i$	–	Inhibition constant
$K_M$	–	Michaelis constant
L-AmpB	–	Liposomal amphotericin B
LB	–	Lysogeny broth
LCP	–	Lipidic cubic phase
LDAO	–	Lauryldimethylamine oxide
LED	–	Light emitting diode
LMNG	–	Lauryl maltose neopentyl glycol
LYTAC	–	Lysosome-targeting chimaeras
MDR	–	Multidrug resistance
MIC	–	Minimum inhibitory concentration
MM	–	Minimal media
MMS	–	Microseed matrix screening
MNG	–	Maltose neopentyl glycol
MRP	–	Multidrug resistance protein
MSP	–	Membrane scaffold protein
MW	–	Molecular weight
MWCO	–	Molecular weight cut off
N-Boc	–	Tert-butyloxycarbonyl protecting group
N/A	–	Not available
NaCl	–	Sodium chloride
NADPH-oxidase	–	Nicotinamide adenine dinucleotide phosphate oxidase
Nano-DSF	–	Nano-differential scanning fluorimetry
$\text{NaNO}_3$	–	Sodium nitrate
NAT	–	Nucleobase Ascorbate Transporter
NBD	–	Nitrobenzoxadiole
NCS2	–	Nucleobase cation symporter-2
NEt3	–	Triethylamine
NG	–	Nonylglucoside
NICE	–	National Institute for Health and Care Excellence
NMR	–	Nuclear magnetic resonance
NSPr	–	Nanodisc scaffold peptide
OAT	–	Organic anion transporter
$\text{OD}_{600}$	–	Optical density at 600 nm
OG	–	Octyl-beta-glucoside
OGNG	–	Octyl glucose neopentyl glycol
PA	–	Phosphatidic acid
PABA	–	Para-amino benzoic acid
PBS	–	Phosphate buffered saline
PC	–	Phosphatidylcholine
PCP	–	Pneumocystis pneumonia
PD-1	–	Programmed cell death protein 1
PDB	–	Protein Data Bank
PE	–	Phosphatidylethanolamine

PEG	–	Polyethylene glycol
PG	–	Phosphatidylglycerol
pH	–	Potential of hydrogen
PI	–	Phosphatidylinositol
PIP2	–	Phosphatidylinositol 4,5-bisphosphate
PROTAC	–	Proteolysis targeting chimera
PS	–	Phosphatidylserine
SAFS	–	Severe asthma with fungal sensitization
SANS	–	Small-angle neutron scattering
SAR	–	Structure-activity relationship
SAXS	–	Small-angle X-ray scattering
SBDD	–	Structure-based drug design
SDS	–	Sodium dodecyl-sulfate
SDS-PAGE	–	Sodium dodecyl-sulfate polyacrylamide gel electrophoresis
SE	–	Standard error of the mean
SLC	–	Solute carrier
SMALPS	–	Styrene maleic acid lipid particle
SNAr	–	Nucleophilic aromatic substitution
sp <sup>2</sup>	–	Mixing of one s and two p atomic orbitals
SVCT	–	Human vitamin C (L-ascorbic acid) transporter
TB	–	Terrific broth
TEV	–	Tobacco etch virus
THF	–	Tetrahydrofuran
TLC	–	Thin layer chromatography
TM	–	Melting Temperature
TMD	–	Transmembrane domain
UapA	–	Uric acid permease A, <i>A. nidulans</i>
UapC	–	Uric acid permease C, <i>A. nidulans</i>
UraA	–	Uracil transporter, <i>A. nidulans</i>
URAT1	–	Human urate transporter 1
UV	–	Ultraviolet
WHO	–	World Health Organisation
WT	–	Wild-type
XChem	–	X-ray structure-accelerated, synthesis-aligned fragment medicinal chemistry
YP	–	Yeast Peptone

# 1. Literature Review

## 1.1. Fungal diseases and Aspergillosis

### 1.1.1. Global prevalence of fungal diseases

Fungal diseases affect over one billion people and contribute to over 1.5 million deaths each year<sup>2</sup>. Despite this, and their detrimental impacts in both veterinary science and agriculture, research into the development of novel antifungals remains hugely neglected. The World Health Organization (WHO), along with the majority of other public health agencies, has historically not monitored fungal infections<sup>2,3</sup>. In October 2022, WHO published its first “fungal priority pathogens list”, which constituted the first global effort to systematically prioritize fungal pathogens<sup>3</sup>. This report identified *Cryptococcus neoformans*, *Candida auris*, *Aspergillus fumigatus* and *Candida albicans* as pathogens in the critical group and most in need of ongoing surveillance and intervention<sup>3</sup>.

The severity of fungal infections ranges from mild and often asymptomatic infections to systemic and potentially life-threatening infections<sup>4</sup>. Severe fungal infections are relatively uncommon, usually only occurring as a consequence of existing health conditions or immunodeficiency. However, increasing incidences of chronic obstructive pulmonary disease (COPD), cancer, asthma, in addition to immunocompromising conditions such as cystic fibrosis and HIV/AIDS, have driven increased numbers of severe fungal infections in both developed and developing countries<sup>4,5</sup>. Fungal infections, particularly those caused by *Aspergillus* fungi, are also common in critical COVID-19 patients. A 2021 study showed that as many as 17.9% of patients with COVID-19, hospitalised in an intensive care unit developed pulmonary *Aspergillus* infection<sup>6</sup>.

Despite the huge variety of fungi on earth, only a fraction are responsible for causing disease, and an even smaller fraction of these are considered serious or life threatening. Of the estimated two million species of fungi on earth, over 600 are known human pathogens<sup>7</sup>. The vast majority of serious or life-threatening fungal infections are caused by organisms from genera *Aspergillus*, which causes aspergillosis, and *Candida*, which causes candidiasis<sup>3</sup>.

The Leading International Fungal Education trust subdivides fungal infections into five groups: invasive fungal infections, chronic lung or deep tissue infections, allergic fungal diseases, mucosal infections, and skin, hair or nail infections<sup>8</sup>. Examples of each have been outlined in Table 1.

Table 1: Examples of each of the five classes of fungal infections, as categorised by the Leading International Fungal Education trust<sup>8</sup>.

Categorisation	Examples
Invasive fungal infections	<ul style="list-style-type: none"> <li>▪ Cryptococcal meningitis</li> <li>▪ Invasive aspergillosis</li> <li>▪ Invasive candidiasis</li> <li>▪ <i>Pneumocystis pneumonia</i> (PCP)</li> </ul>
Chronic or deep tissue infections	<ul style="list-style-type: none"> <li>▪ Chronic pulmonary aspergillosis</li> </ul>
Allergic fungal diseases	<ul style="list-style-type: none"> <li>▪ Allergic bronchopulmonary aspergillosis (ABPA)</li> <li>▪ Severe asthma with fungal sensitisation (SAFS)</li> </ul>
Mucosal infections	<ul style="list-style-type: none"> <li>▪ Oral and oesophageal candidiasis</li> <li>▪ <i>Candida vaginitis</i> (thrush)</li> </ul>
Skin, hair or nail infections	<ul style="list-style-type: none"> <li>▪ Ringworm</li> <li>▪ Athlete's foot</li> </ul>

There are existing treatments available for infections ranging from systemic to superficial, which will be described in Section 1.1.5. Unfortunately, in the more severe examples of fungal infection, high mortality rates persist due to the inability of these treatments to eliminate infections completely<sup>2</sup>.

This work focuses on Aspergillosis, a collection of conditions caused by the filamentous ascomycete *Aspergillus fumigatus*, and to a lesser extent *Aspergillus nidulans*. Of the pathogenic aspergilli, *Aspergillus fumigatus* is the major pathogenic species, followed by *Aspergillus flavus*, *Aspergillus niger* and *Aspergillus terreus*<sup>9</sup>.

### 1.1.2. Aspergilli and resilience

*Aspergilli* are conidial filamentous fungi, first identified under the microscope by Italian priest and biologist Pier Antonio Micheli. The genus was named after the Aspergillum, a holy water sprinkler, due to the characteristic shape of the asexual conidia forming structure, common to all species of the genus<sup>10</sup>. Conidia are released from fruiting bodies called conidiophores, which develop from the network of hyphae via foot cells (Figure 1).

Despite their broad phenotypic similarities, *Aspergilli* differ considerably in their genome sequences, and in their medical and commercial relevance. More than 60 *Aspergillus* species are medically relevant pathogens, with *Aspergillus fumigatus* being the most common cause of serious infections<sup>11</sup>. Other species have roles in commercial microbial fermentations; alcoholic drinks like Japanese sake are made from rice and starchy sources, which need to first be broken down into simpler sugars by *Aspergillus oryzae*<sup>12</sup>. *Aspergillus niger* is the largest source of citric acid worldwide and is used to produce commercially important enzymes including glucose oxidase, pectinase,  $\alpha$ -amylase and glucoamylase<sup>13,14</sup>. Finally, *Aspergillus nidulans* has long



been the model organism of choice for scientific study of the *Aspergilli*, and was one of the first organisms submitted to genome sequencing at the Broad Institute<sup>15</sup>.

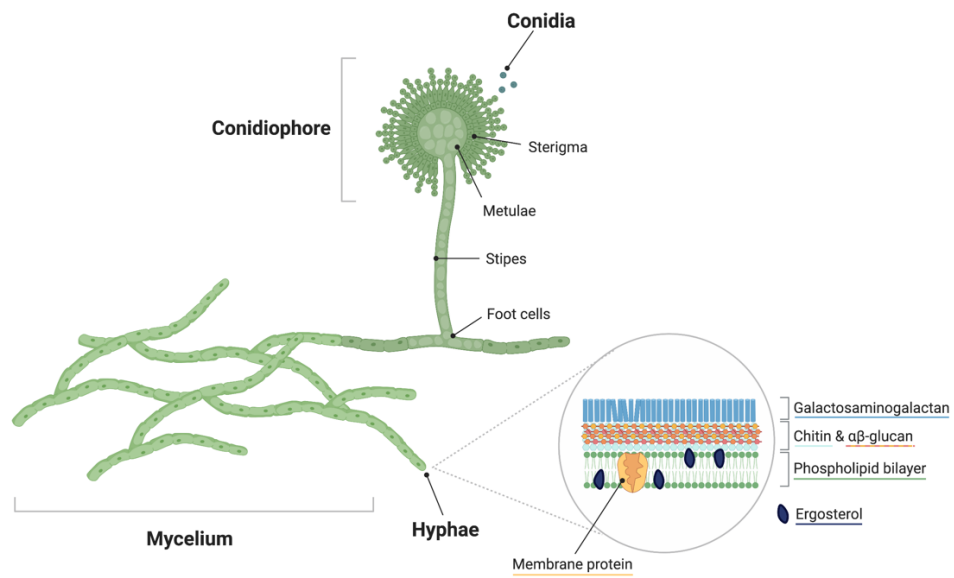


Figure 1: Main physiological structures in *Aspergillus fumigatus*, and organisation of the hyphal and conidial walls and membranes. Conidia are released from fruiting bodies called conidiophores, which develop off the fungal mycelium, or network of hyphae, via foot cells. This figure was created with [www.BioRender.com/](http://www.BioRender.com/) and informed by existing literature<sup>16</sup>.

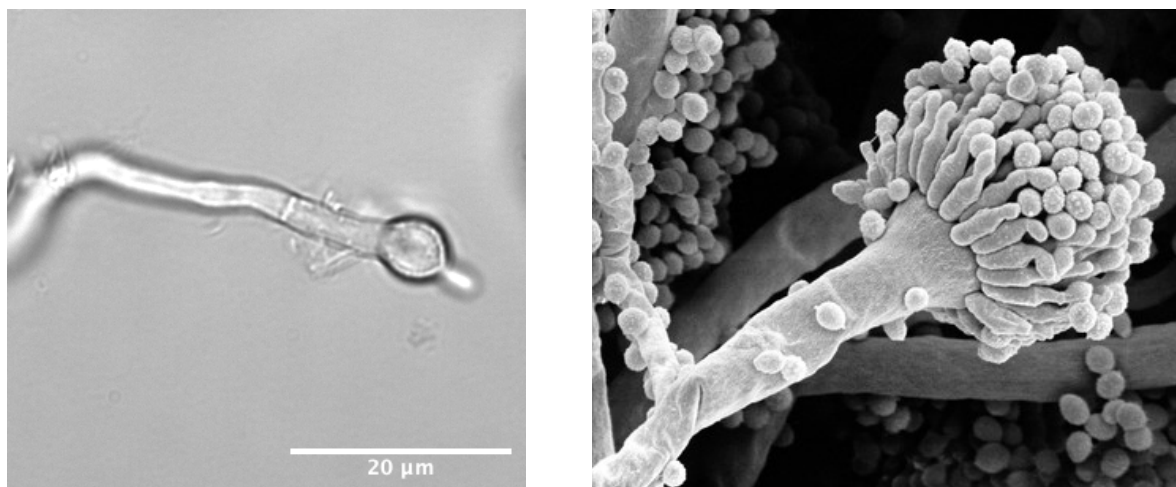


Figure 2: Left, Bright-field microscopy image of a germ tube of wild-type *Aspergillus nidulans* in minimal media agar. Right, Scanning electron micrograph of *Aspergillus fumigatus* culture, showing the conidiophore fruiting body and associated conidia<sup>17</sup>.

*Aspergillus* fungi are aerobic and thrive in oxygen-rich and carbon-rich environments. As with all living organisms, the survival of *Aspergilli* is dependent on acquisition of key nutrients from the external environment, including metals, nitrogen, and macromolecules such as peptides<sup>18</sup>. Interestingly, it has been shown that virulence is strongly correlated with nutrient acquisition, with 78% of nitrogen, iron and zinc metabolism-related genes having direct implication in virulence<sup>19</sup>.

*Aspergilli* are versatile, able to survive on a variety of different nitrogen sources. Examples of nitrogen sources that support *Aspergilli* growth include nitrates (e.g. NaNO<sub>3</sub>), various purines (e.g. L-alanine) and ammonia derivatives (e.g. ammonium salts, NH<sub>4</sub><sup>+</sup>). Iron uptake is essential due to iron's role as an enzyme cofactor and catalyst in the electron transport system. *A. fumigatus* has two distinct mechanisms for the uptake of iron: reductive iron acquisition and siderophore-mediated uptake. These mechanisms appear to work in parallel, with both upregulated in response to iron starvation<sup>20,21</sup>. There are significant redundancies in solute carrier transporters in *Aspergilli*<sup>2</sup>.

*Aspergilli* can survive in challenging environments, including high temperatures, high osmotic pressure and hypoxic microenvironments. They can grow between 12–65 °C, with optimum growth at 37 °C, the average human body temperature<sup>23</sup>. *Aspergillus* hyphae often encounter hypoxic micro-environments at the site of infection, since necrosis and inflammation-induced tissue damage results in local reduction in oxygen supply<sup>24</sup>. The mechanisms by which *Aspergillus fumigatus* adapts in hypoxia is an area of focus for novel drug targets<sup>25</sup>. Key members of these pathways are the sterol-regulatory element binding proteins (SrbA and SrbB). These are known to be essential in the fungal response to hypoxia *in vivo* and key biological processes including iron homeostasis, antifungal azole drug resistance, and virulence<sup>25</sup>.

### 1.1.3. The regulated immune response

*Aspergillus fumigatus* is the most common species to cause disease in individuals with immunodeficiencies<sup>9</sup>. *Aspergilli* are saprotrophs, ubiquitous in the environment and typically found in soil and decaying organic matter, where it has an essential role in carbon and nitrogen recycling<sup>26</sup>. As with all conidial fungi, colonies of this fungus produce thousands of microscopic conidia ( $\varnothing$  2–3  $\mu\text{m}$ , Figure 2), which readily become airborne<sup>9</sup>. Its spores are abundant in the atmosphere, and it is estimated that an individual inhales thousands of these spores each day<sup>9</sup>.

Due to their small size, conidia are able to deposit in alveoli, where they interact with epithelial and innate effector cells<sup>4</sup>. In healthy individuals, most inhaled conidia are cleared by the mucociliary action of the respiratory epithelium<sup>27</sup>. Respiratory epithelial cells are able to internalize any remaining conidia and traffic them to the lysosome<sup>28</sup>. It has been shown *in vitro* that these phagocytosed conidia no longer germinate. In addition, spores have been shown to be internalised and destroyed by alveolar macrophages<sup>29,30</sup>. First line immune cells, on recognition of specific fungal motifs, recruit neutrophils and other inflammatory cells through release of cytokines and chemokines (Figure 3)<sup>44</sup>.

Neutrophils are capable of sequestering both conidia and hyphae through distinct, non-phagocytic mechanisms<sup>31</sup>. Unlike conidia, hyphae are too large for cell-mediated internalization. Consequently, neutrophil-mediated NADPH-oxidase induced damage is the dominant host defence against these larger forms<sup>31</sup>. In addition to these cell-mediated mechanisms of elimination, antimicrobial peptides (AMPs) secreted by the airway epithelium contribute to host defence by destabilizing fungal cell membranes<sup>4</sup> (Figure 3). AMPs are key components of the innate immune system. AMPs disrupt the highly organised lipid bilayer by providing alternate

surfaces for lipid hydrocarbon and headgroups interaction and can interact with one another to form pore-like transmembrane channels<sup>27</sup>.

The majority of host defence against Aspergillosis is cell-mediated and often neutrophil-dependent<sup>4</sup>. Consequently, when neutrophil levels are low, characteristic of the immunocompromised and immunosuppressed, individuals are left vulnerable to prolonged *Aspergillus* infection.

#### 1.1.4. Disease progression in immunocompromised individuals

Aspergillosis can manifest as invasive, chronic and allergic fungal diseases (Figure 3), and it is a major cause of disease and death in individuals with prior lung conditions (e.g. tuberculosis, asthma, cystic fibrosis and chronic obstructive pulmonary disease (COPD)), and in those who are immunodeficient, as a result of HIV/AIDS, organ transplantation or chemotherapy.

As described in Section 1.1.3, *Aspergillus* species produce airborne spores (conidia), which generally enter the body via the respiratory tract. In immunocompetent individuals, infection is transient, with spores eliminated by the innate immune system. In individuals with compromised immune systems, spore germination can lead to growth of a fungal mycelium body, or Aspergilloma, in cavities caused by prior lung conditions<sup>32</sup>.

In Aspergilloma, the fungus grows within lung cavities formed during prior lung diseases, such as tuberculosis or sarcoidosis<sup>32</sup>. Any lung disease, which causes cavities, can leave an individual vulnerable to developing an Aspergilloma. The spores penetrate the lung cavity and germinate, forming a fungal mycelium body. The fungus secretes allergens and toxic metabolites, which may result in the illness becoming symptomatic. Treatment ranges from surgical removal of the aspergilloma,

if possible, to the application of anti-fungal agents (e.g. itraconazole, voriconazole, amphotericin B, posaconazole)<sup>32</sup>. The latter are discussed in Section 1.1.5. While oral itraconazole helps symptoms in many patients, it rarely resolves the disease, since it often fails to eliminate the fungus in the cavity. Consequentially, chronic pulmonary aspergillosis (CPA) may require long-term, and potentially lifelong, antifungal treatment<sup>32</sup>.

Generally, *Aspergillus* infection can be asymptomatic, however symptoms often result from the host's allergic immune response to spores, as observed in allergic bronchopulmonary aspergillosis (ABPA)<sup>32,33</sup>. This is more frequent in asthmatics and cystic fibrosis patients, and can result in permanent lung damage, fibrosis and bronchiectasis. Some patients with severe asthma are sensitised to *Aspergillus* species, but do not have ABPA, instead suffering with severe asthma with fungal sensitisation (SAFS)<sup>32</sup>. Both ABPA and SAFS are routinely treated with steroidal-based therapies and oral itraconazole<sup>32</sup>.

*Aspergillus* bronchitis and sinusitis are infections of the airway and sinuses respectively. Individuals with bronchiectasis are particularly vulnerable to airway infection with *Aspergillus*. This disease appears to be highly represented in cystic fibrosis patients and individuals with reduced lung function. Both conditions can take the form of allergic sinusitis, growth of a fungal body or invasive aspergillosis<sup>34</sup>.

Ultimately invasive aspergillosis, where the fungus penetrates the blood stream, can be fatal. The fungus can transfer from the lung, through the blood stream, to the brain or to other organs, which include the eye, the heart, the kidneys and the skin. Current treatment for invasive Aspergillosis involves the application of a variety of antifungal agents intravenously<sup>32</sup>. However, patients with invasive aspergillosis, even following aggressive treatments with existing antifungals, have high fatality rates<sup>34</sup>.

Treatment of Aspergillosis is also challenging due to the ability of spores to remain dormant for prolonged periods of time before germinating. Germination is where spores make a morphological switch to hyphal growth. Germination can occur extracellularly, in the warm, moist, nutrient rich environment of the pulmonary alveoli or alternatively in type II pneumocyte endosomes following their endocytosis<sup>4,35</sup>.

Filamentous fungal growth and immune system dysregulation has numerous down-stream consequences, including mechanical damage to the pulmonary alveoli by epithelial penetration and invasion of the vascular epithelium<sup>4,35</sup> (Figure 3).

Pathogenic *Aspergilli* produce and secrete proteases and elastases, enzymes which breakdown macromolecular polymers collagen and elastin. Collagen and elastin are crucial components in the human lung, enabling tissue flexibility. Their breakdown serves both to weaken lung tissue ready for invasion and to release carbon-sources for uptake into the fungus<sup>36</sup>. Angioinvasion leads to invasive aspergillosis, the most advanced form of the disease (Figure 3). Invasive aspergillosis is uncommon; Infection usually remains localised, with fungal dissemination via the blood stream extremely uncommon, and only observed in severely immunocompromised individuals<sup>4</sup>.

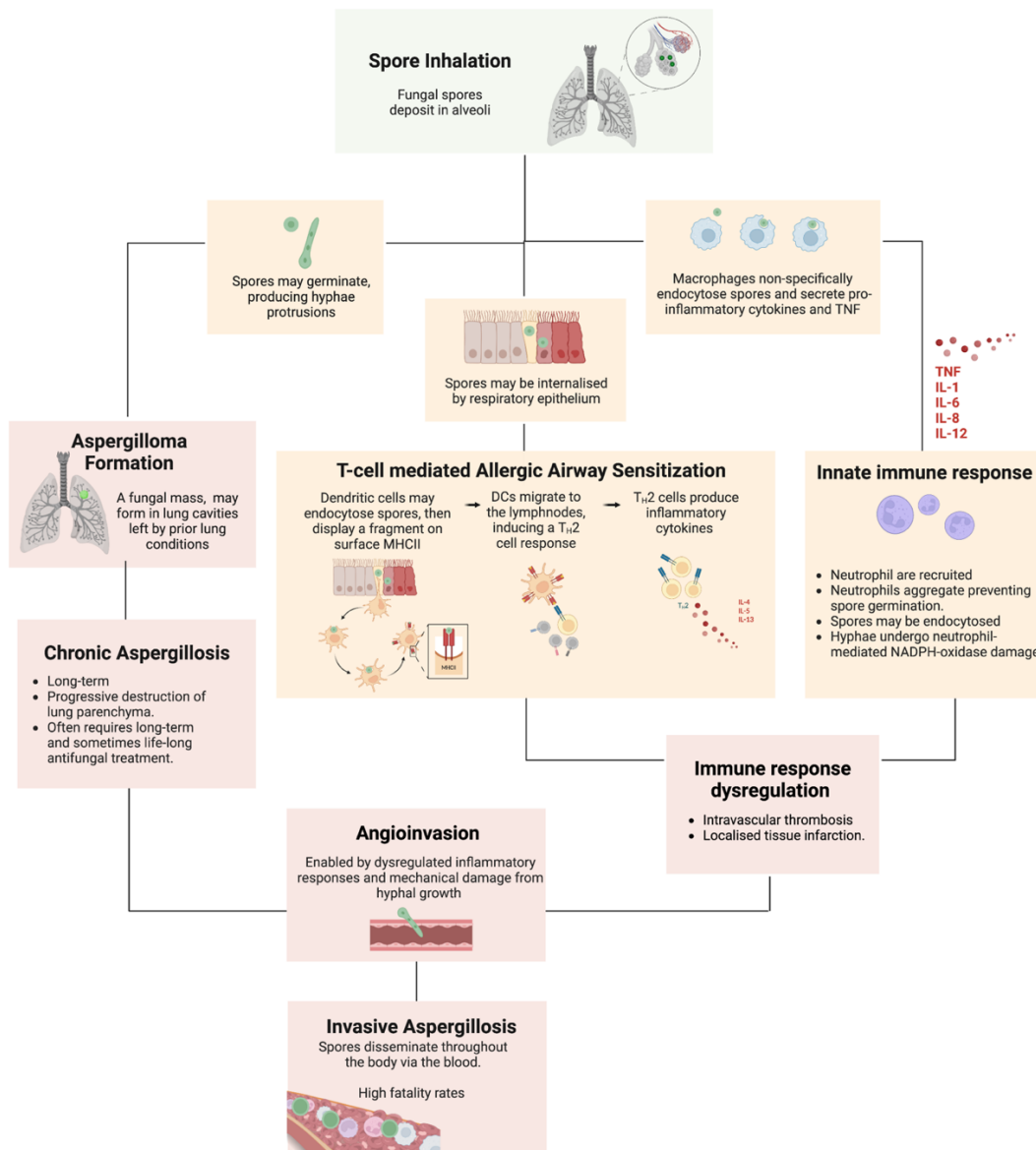


Figure 3: Potential consequences of *Aspergillus* infection. Spore inhalation can lead to germination and formation of a fungal mass, or Aspergilloma. Non-clearance of the fungal mass can result in chronic aspergillosis, which often requires long-term and life-long treatment. Immune response dysregulation may occur through dendritic cell and T-cell mediated allergic airway sensitisation. Spores may also be non-specifically endocytosed by macrophages, inducing an inflammatory innate immune response through the recruitment of neutrophils and secretion of pro-inflammatory cytokines. Ultimately both mechanical damage from fungal growth and immune response dysregulation can result in damage to the vascular system, angioinvasion and ultimately invasive aspergillosis. Invasive aspergillosis involves spore dissemination through the blood and is the most advanced form of the disease. This figure was created with [www.BioRender.com/](http://www.BioRender.com/) and informed by literature<sup>28-31</sup>.



### 1.1.5. Existing treatments for Aspergillosis

Aspergillosis treatment varies depending on the form of the disease. Surgical removal of the fungus is only attempted when infection is localised, as in Aspergilloma, and where the mass is causing life-affecting symptoms, such as shortness of breath or difficulty breathing<sup>32,37</sup>. The most common course of treatment for all forms of aspergillosis, is the use of antifungal agents. The different classes of antifungals available for the treatment of aspergillosis have been summarised in Figure 4. Available antifungals for the treatment of aspergillosis and other fungal diseases have been summarised in Table 2.

#### 1.1.5.1. Azole antifungals

Antifungals in the azole subclass, named after their characteristic azole ring, inhibit the growth of a wide range of fungi species<sup>38</sup>. They are classified into two groups: the imidazoles and the triazoles. Imidazoles contain two nitrogen atoms in the azole ring; examples include clotrimazole (Figure 4), econazole, ketoconazole, miconazole, and tioconazole. Triazoles differ by containing three nitrogens in the azole ring; examples include itraconazole (Figure 4), fluconazole, posaconazole, and voriconazole. Azole antifungals share the same mechanism of action: they inhibit the cytochrome P450 dependent enzyme lanosterol 14 $\alpha$ -demethylase, which converts lanosterol to ergosterol, the main sterol present in the fungal cell membrane. Depletion of ergosterol damages the cell membrane resulting in fungal cell death<sup>38</sup>. The triazoles, particularly itraconazole and voriconazole, are used more frequently in the treatment of Aspergillosis, due to their favourable safety profile and efficacy relative to their imidazole predecessors<sup>38</sup>.

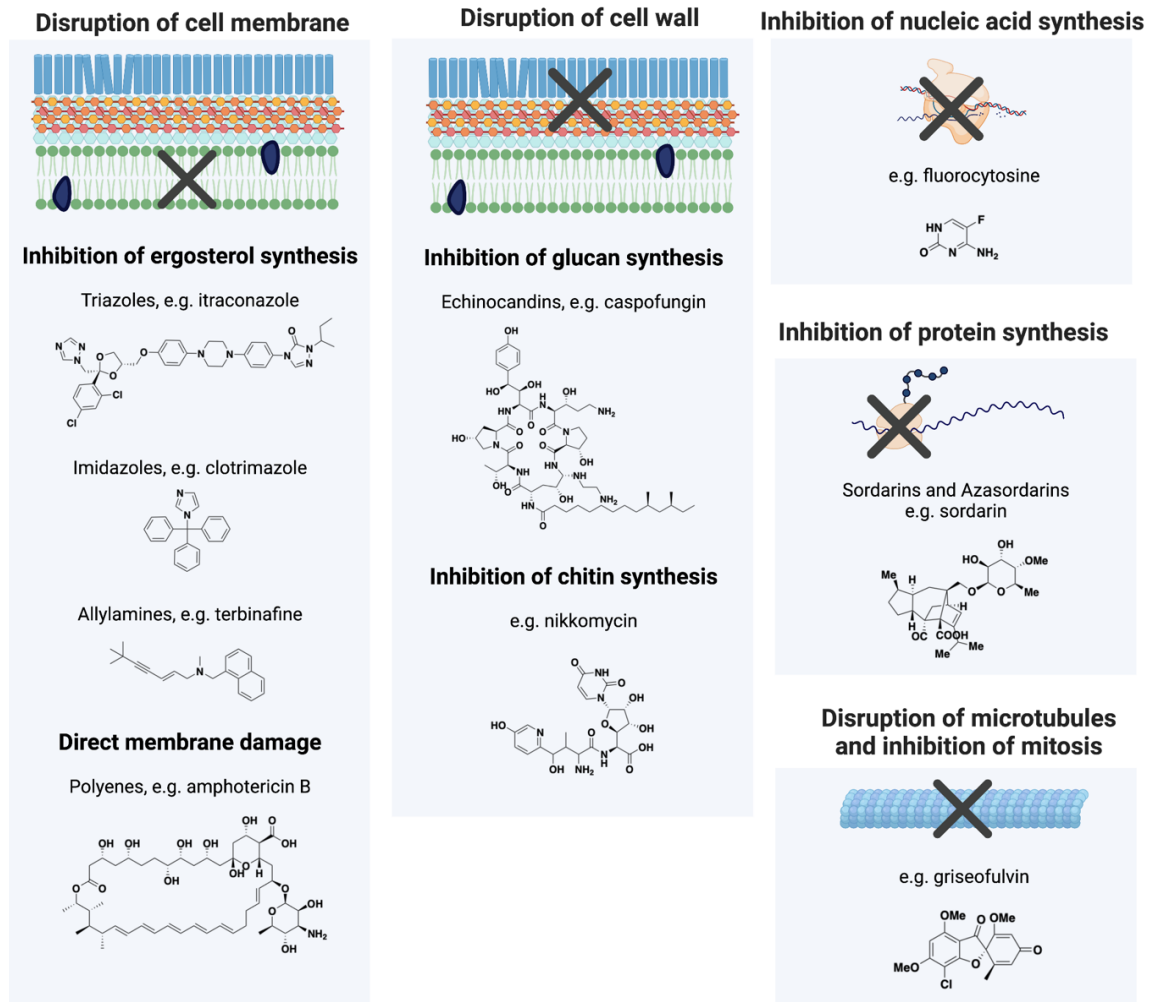


Figure 4: Different mechanisms of action of existing antifungals for Aspergillosis, including cell membrane and cell wall disruption, inhibition of nucleic acid and protein synthesis and microtubule formation. Examples of each class of antifungal are given, with the respective chemical structure. This figure was created with [www.BioRender.com/](http://www.BioRender.com/) and ChemDraw 19.0.

#### 1.1.5.2. Polyene antifungals

Polyene antifungals are ionophores, which bind ergosterol, a component of fungal cell membranes, inducing formation of pores, rapid leakage of monovalent ions ( $K^+$ ,  $Na^+$ ,  $H^+$  and  $Cl^-$ ), which causes fungal cell death<sup>39</sup>. Polyenes used in the treatment of fungal infections include nystatin, natamycin, and amphotericin B. However, neither nystatin and natamycin have been used in the treatment of Aspergillosis. Nystatin and natamycin are used in the treatment of dermal, oesophageal and vaginal candidiasis, and fungal eye infections respectively. Amphotericin B is the only polyene that has been routinely used to treat Aspergillosis, however its use has been associated with severe nephrotoxicity. There have been attempts to combat reported symptoms, by making Amphotericin B available in multiple forms: liposomal (L-AmpB), lipid complex (ABLC) and colloidal dispersion (ABCD) therapies. These formulations of Amphotericin B are routinely used in the treatment of invasive Aspergillosis<sup>40,41</sup>. While nephrotoxicity may be reduced with the lipid formulations of this polyene, it can still occur, especially with higher doses or prolonged administration<sup>42</sup>.

#### 1.1.5.3. Echinocandin antifungals

Three echinocandin antifungal agents are currently approved for clinical use in the United States: caspofungin, micafungin, and anidulafungin<sup>43</sup>. The echinocandins have a unique mechanism of action where they inhibit  $\beta$ -(1,3)-D-glucan synthase, an enzyme crucial for the synthesis of  $\beta$ -(1,3)-D-glucan, an essential component of the cell wall of several fungi species<sup>44</sup>. The echinocandins exhibit fungistatic activity against most *Aspergillus* and *Candida* species, including strains that are fluconazole-resistant. Caspofungin (Figure 4) has demonstrated particular efficacy as a last-resort treatment for invasive aspergillosis<sup>44</sup>.

#### 1.1.5.4. Early antifungals

Prior to the introduction of the azole antifungals in the 1960s, there were few antifungals clinically available: nystatin, amphotericin B, 5-fluorocytosine (5FC) and griseofulvin. While nystatin and amphotericin B are both polyenes and follow the same mechanism of action, griseofulvin and 5FC are mechanistically distinct from other antifungals<sup>45</sup> (Figure 4).

Griseofulvin was the first antifungal isolated but was not made clinically available until 1958. Griseofulvin binds alpha and beta tubulin, interfering with the function of spindle and cytoplasmic microtubules fungal cell mitosis<sup>46</sup>.

5FC is a purine analogue and exerts its antifungal effects by interfering with DNA and protein synthesis. 5FC is transported into susceptible fungi by cytosine permease then deaminated to 5-fluorouracil (5FU) by cytosine deaminase<sup>47</sup>. 5FU impairs protein synthesis, with downstream metabolic products interfering with RNA biosynthesis and fungal DNA synthesis. The absence of cytosine deaminase in mammalian cells allows for selective effects on fungal cells. Since its approval in 1957, 5FC has been used in the treatment of *Candida* and *Cryptococcus* infections. However, its use has been restricted in the treatment of aspergillosis due to minimal *in vitro* activity<sup>48</sup>.

Table 2: The different classes of antifungals available for the treatment of aspergillosis and other mycoses, informed by the National Institute for Health and Care Excellence (NICE).<sup>59</sup> Further references indicated in last column.

Year	Drug	Class	Mechanism	Susceptible fungi	Localisation	Formulation	Efficacy against <i>Aspergilli</i>	Toxicity	Ref
1949	Nystatin	Polyene	Induces pore formation	<i>Candida</i>	Oral, perioral	Tablet, capsule, oral suspension, cream.	Not effective	None reported	60
1956	Amphotericin B	Polyene	Induces pore formation	<i>Aspergillus, blastomyces, candida, coccidioides, and</i>	Systemic	Intravenous infusion	Yes, resistance present	Severe nephrotoxicity	61
1957	5-fluorocytosine	N/A	Inhibition of nucleic acid synthesis	<i>Candida, cryptococcus, other long-standing infections</i>	Systemic	Oral, intravenous infusion	Not effective	Bone marrow suppression and nephrotoxicity	62
1958	Griseofulvin	N/A	Disruption of microtubules and inhibition of mitosis	<i>Dermatophytes</i>	Oral, vaginal, dermal	Oral, topical	Not effective	Skin damage, neutropenia and nephrotoxicity	46
1969	Clotrimazole	Azole	Inhibition of ergosterol synthesis	<i>Aspergillus, candida, dermatophytes</i>	Vaginal, dermal	Cream, spray, topical solution	Yes, resistance present	Gastro-intestinal disturbances, neurological	63
1979	Miconazole	Azole	Inhibition of ergosterol synthesis	<i>Candida, dermatophytes</i>	Oral, vaginal, dermal, nail	Oral, cream	Not effective	None reported	64
1980	Ketoconazole	Azole	Inhibition of ergosterol synthesis	<i>Candida, dermatophytes</i>	Oral, dermal	Oral, cream	Not effective	Severe nephrotoxicity	65
1990	Fluconazole	Azole	Inhibition of ergosterol synthesis	<i>Aspergillus, candida, cryptococcus, dermatophytes</i>	Oral, dermal, vaginal	Oral, intravenous infusion	Yes, resistance present	Nephrotoxicity	66
1992	Itraconazole	Azole	Inhibition of ergosterol synthesis	<i>Aspergillus, candida, cryptococcus, dermatophytes,</i>	Oral, dermal, vaginal, systemic	Oral, intravenous infusion	Yes, resistance present	Nephrotoxicity	67

Table 2 continued

Year	Drug	Class	Mechanism	Susceptible fungi	Localisation	Formulation	Efficacy against <i>Aspergilli</i>	Toxicity	Ref
1995	Amphotericin B Lipid Complex	Polyene	Induces pore formation	As for Amphotericin B	Systemic	Intravenous infusion	Yes, resistance present	Severe nephrotoxicity	61
1996	Amphotericin B Colloidal Dispersion	Polyene	Induces pore formation	As for Amphotericin B	Systemic	Intravenous infusion	Yes, resistance present	Severe nephrotoxicity	61
1997	Liposomal Amphotericin B	Polyene	Induces pore formation	As for Amphotericin B	Systemic	Intravenous infusion	Yes, resistance present	Severe nephrotoxicity	61,68
2001	Caspofungin	Echinocandin	Inhibition of glucan synthesis	<i>Aspergillus, candida</i>	Systemic	Intravenous infusion	Yes, resistance present	Nephrotoxicity, hypokalemia	69
2002	Voriconazole	Azole	Inhibition of ergosterol synthesis	<i>Aspergillus, candida, scedosporium, fusarium,</i>	Systemic	Oral, intravenous infusion	Yes, resistance present	Nephrotoxicity	70
2005	Micafungin	Echinocandin	Inhibition of glucan synthesis	<i>Candida</i>	Systemic	Intravenous injection	Not effective	Nephrotoxicity, hypokalemia	71
2006	Anidulafungin	Echinocandin	Inhibition of glucan synthesis	<i>Candida</i>	Systemic	Intravenous injection	Not effective	Nephrotoxicity, hypokalemia	72
2006	Posaconazole	Azole	Inhibition of ergosterol synthesis	<i>Aspergillus, candida fusarium, chromoblastomycosis,</i>	Systemic	Oral, intravenous infusion	Yes, resistance present	Nephrotoxicity	73
2007	Terbafine	N/A	Inhibition of ergosterol synthesis	<i>Dermatophytes</i>	Dermal, nails	Oral, cream	Not effective	Hepatotoxicity	74
2019	Ibrexafungerp	N/A	Inhibition of glucan synthesis	<i>Candida</i>	Vaginal	Oral	Not effective	None reported	75

As antifungal usage spread, incidences of antifungal resistance emerged. The clinical impact of this is severe due to the limited number of available therapies for fungal infections<sup>44</sup>. Major contributors to antifungal resistance include their clinical and agricultural overuse<sup>49</sup>. Susceptibility to azole antifungals varies geographically due to both fungal strain variation, varying prescription tendencies and agricultural practices<sup>50</sup>. Pathogen resistance mechanisms include upregulation of efflux pumps, and mutations in the drug target.

Efflux pumps, such as AfMDR4 have been shown to contribute to azole, namely voriconazole, resistance<sup>50,51</sup>. Other mechanisms known to increase resistance to azole antifungals include point mutations within the gene, CYP51A. CYP51A encodes the target protein lanosterol 14 $\alpha$ -demethylase, a component of the ergosterol synthesis pathway<sup>50</sup>. Orthologous mutations in ERG11, the gene responsible for production of the related enzyme in *Candida* species, have also been identified, resulting in *Candida* strains resistant to azoles. Mutations in CYP51A and ERG11 both result in increased transcription of the gene, leading to increased synthesis of the enzyme<sup>52</sup>.

To overcome azole resistance, the echinocandins have been recommended for treatment of invasive candidiasis and aspergillosis in immunocompromised patients and in those who have had prior azole exposure<sup>50</sup>. The mechanism of action is different from that of the azoles, and as a result these molecules have been shown to maintain potent *in vitro* activity against many *Candida* isolates that have developed resistance to fluconazole and the other triazoles. However, resistance to the echinocandins has been shown to develop due to exposure-induced mutations within highly conserved regions of the FKS1 and FKS2 genes, which encode subunits of the glucan synthase enzyme<sup>53</sup>. As with azole resistance, analogous pathways have

been observed in *Candida* species, and it is often advised a patient's exposure history should be considered alongside routine clinical *in vitro* susceptibility assays<sup>50</sup>.

#### 1.1.7. Emerging antifungals for resistant fungi

Ultimately, a variety of antifungals with distinct mechanisms of action will be required to overcome the emergence of resistant strains. It is clear that while existing antifungals often relieve symptoms, they rarely eliminate the fungus entirely, and are accompanied by undesirable side effects<sup>32</sup>.

To meet this need, there are several antifungals under preclinical and clinical evaluation. These include agents that are mechanistically similar to existing azole and echinocandin antifungal classes, but with improved pharmacokinetic and pharmacodynamic properties<sup>54</sup>. The concern is that these agents will fall prey to similar mechanisms of resistance. There are also compounds with novel mechanisms of action in clinical trials, which may overcome current mechanisms of resistance, in addition to the adverse effects of the clinically available antifungals<sup>50</sup>. Novel mechanisms of action include inhibition of fungal pyrimidine biosynthesis<sup>55</sup>, inhibition of fungal glycosylphosphatidylinositol biosynthesis<sup>56</sup> and collapse of fungal mitochondrial membranes<sup>57</sup>. In addition, aluminium chelators have been shown to cause rapid antifungal effects following their transport into fungal cells via siderophore iron transporter 1, a transporter absent in mammalian cells<sup>58</sup>.

The development of novel antifungals capable of eliminating *Aspergillus* infections and improving patient outcomes is essential. While these latest advancements are promising, it is important to continue developing compounds with novel mechanisms of actions, in order to outrun emerging fungal resistance.



## 1.2. The cellular membrane

### 1.2.1. The lipid bilayer

The cellular membrane physically separates the intracellular and extracellular environments. The cellular membrane has key roles that include ensuring the cell's structural integrity, enabling selective cell permeability and the maintenance of membrane potentials. Compartmentalisation allows for the establishment of distinct physiological conditions either side of the cellular membrane.

The cellular membrane itself is composed of a continuous bilayer of phospholipids with embedded proteins, cholesterol, and glycolipids<sup>76</sup> (Figure 5). The hydrophilic head groups of the lipids face outwards, interacting with one another and the aqueous environment on either side of the membrane. The hydrocarbon tails self-associate to form a hydrophobic core<sup>76</sup> (Figure 5). Lipids assemble spontaneously into bilayers; this arrangement is driven by the entropically-favourable interactions between lipids and the aqueous environment<sup>77</sup>.

The membrane's hydrophobic core is responsible for selective cell permeability; it restricts the passage of molecules into and out of cells. While small, non-polar molecules such as oxygen (O<sub>2</sub>) and carbon dioxide (CO<sub>2</sub>) can diffuse passively across the cell membrane, larger, charged and/or polar molecules cannot. Movement of these large and polar species require a range of specialised integral membrane transporters<sup>77</sup>.

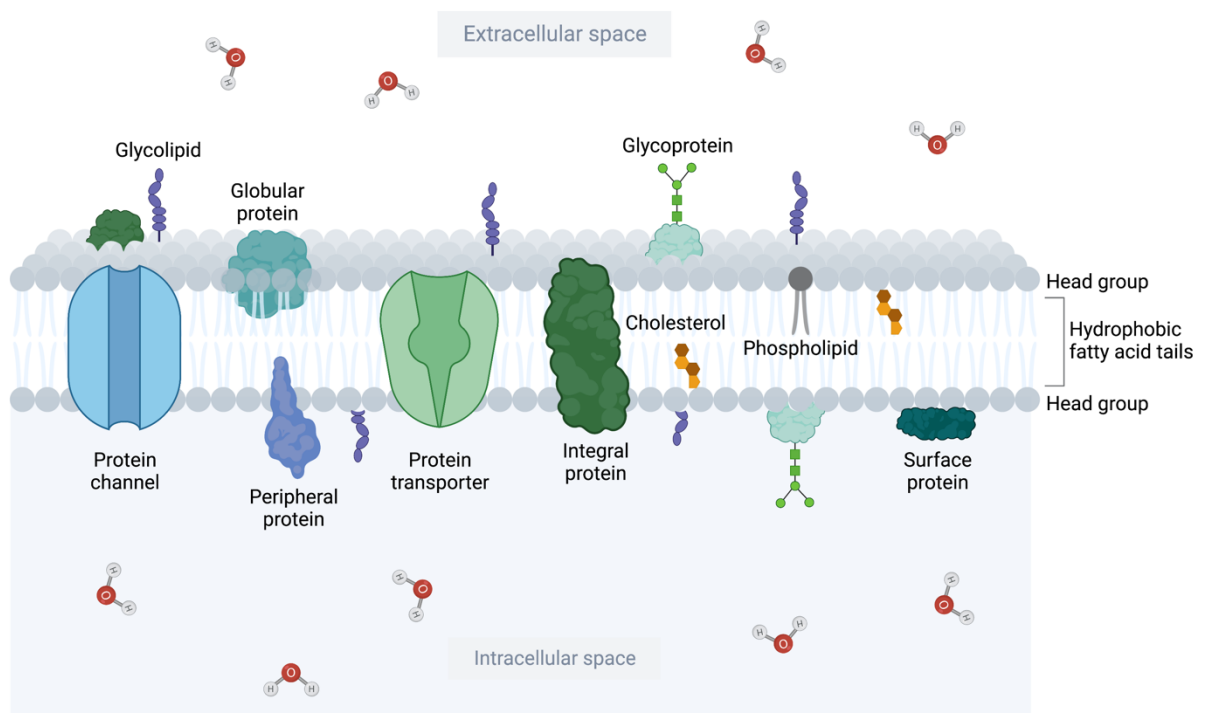


Figure 5: Structure of the phospholipid bilayer. Embedded proteins can be integral or peripheral, and modified by carbohydrates to produce glycoproteins. Most of the membrane lipids are phospholipids, with some modified by carbohydrates to produce glycolipids. Cholesterol is found embedded in both leaflets of the phospholipid bilayer. This figure was created with [www.BioRender.com/](http://www.BioRender.com/) and adapted from the template “Phospholipid Bilayer Membrane”.

### 1.2.2. Membrane lipids

At 4–5 nm thick, the lipid bilayer consists of approximately  $5 \times 10^6$  lipid molecules/ $\mu\text{m}^2$ <sup>76</sup>. Lipid composition greatly differs between membrane type and between organisms, which reflects their varied roles in cellular recognition and cell signalling. There are three major classes of membrane lipid molecules – phospholipids, sterols, and glycolipids<sup>76</sup> (Table 3). Of these, the most abundant type of membrane lipid is the glycerophospholipid<sup>76</sup>. Glycerophospholipids comprise a glycerol-phosphate moiety, hydrophobic fatty acid chains and a hydrophilic head group.

Phospholipids fall into two classes, distinguished by the overall charge of the head group: zwitterionic phospholipids (e.g. phosphatidylethanolamine and phosphatidylcholine) and anionic phospholipids (e.g. phosphatidylinositol and phosphatidylglycerol). Each class contains a range of species, where the fatty acid chains vary in length and saturation<sup>76</sup>.

Glycolipids are lipids that have been glycosylated by the covalent addition of a carbohydrate. Their roles include maintaining the stability of the cell membrane and facilitating cellular recognition, crucial to the immune response and intercellular connections<sup>76</sup>. Sphingolipids have key roles in cellular recognition and adhesion. They are composed of a backbone of sphingoid bases, a fatty acid tail and a polar head group attached at the primary hydroxyl. Sphingolipids are universal in eukaryotes, but rare in bacteria and archaea<sup>78</sup>.

Sterols, such as cholesterol and ergosterol, have distinct structures to the phospholipids and glycolipids. Cholesterol and ergosterol consists of a hydroxyl head group, a fused four-ring steroid structure, and a short hydrocarbon side chain (Figure 6). Sterols are species-specific: mammalian membranes contain cholesterol, while fungal and protozoa membranes contain ergosterol<sup>79</sup>.

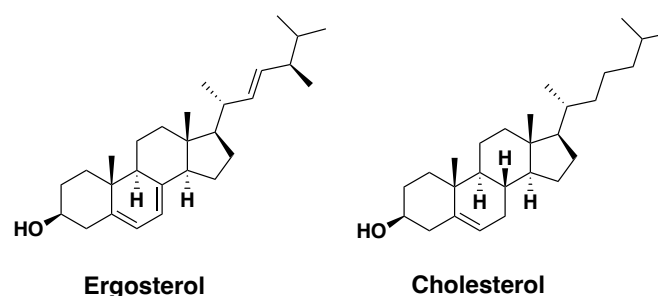


Figure 6: Chemical structures of cholesterol and ergosterol.

As described in Section 1.2.1, membrane lipids associate with one another within the membrane, forming non-covalent and primarily transient interactions with

each other and embedded membrane proteins. Lipids can be divided into three classes according to their role in structure and function: specific, annular and bulk lipids<sup>80</sup>.

Lipid interactions with membrane proteins can be highly specific, with roles in modulating protein structure and function<sup>80</sup>. Examples of lipid interactions that are known to be crucial for membrane protein function are summarised in Table 3, as described by Renard *et al*<sup>80</sup>. Specific lipids can remain bound even under strongly delipidating conditions. Annular lipids are those that are directly in contact with the protein's transmembrane regions, forming a shell of motion-restricted lipids. Interactions with lipids in the annular belt are more transient, and thus more prone to exchange for detergent molecules than specific or structural lipids<sup>81</sup>. Annular lipids still have crucial roles in structure and function (e.g. facilitating conformational changes and stabilising intermediate conformational states of transporters)<sup>81</sup>. The rest of the lipid environment are generalised as bulk lipids, which show even lower binding affinity for the protein. The role of bulk lipids in membrane protein structure and function has not been determined, beyond an essential role in providing lateral pressure<sup>82</sup>.

Table 3: Summary of protein-lipid interactions identified for secondary active transporters, ATP-dependent pumps/transporters, channels and GPCRs. Modified from Renard *et al*<sup>80</sup>.

	2° Active Transporters	ATP-Dependent Transporters	Channels	GPCRs
Cholesterol	Activity regulation	Activity and changes in conformation; Modulation of substrate binding affinity	Channel inhibition	Activation; Allosteric regulation; Oligomerisation; Signalling; Stability; Lower affinity ligand binding
PA			Activity	Stabilisation
PE	Dimer formation and function; Conformer stability		Conformer stabilisation; Channel desensitisation	Agonist and antagonist binding affinities; Increase G protein coupling
PC				Dimerisation; $\beta$ -arrestin interaction and function; Increase G protein coupling
PG	Oligomerisation and function		Conformer stabilisation; Channel desensitisation	Increase or decrease G protein coupling; Active conformer stability; $\beta$ -arrestin interaction and function
PS	Dimer formation			Stabilisation; Dimerisation; Decrease G protein coupling
PI	Dimer formation and function; Possible stabilisation			
PIP2	Possible dimer stabilisation		Activation; Inactive conformer stability	Active conformer stability; $\beta$ -arrestin interaction; Complex stability; G protein recruitment
Glycolipids Sphingolipids				Ligand binding; Signalling; Allostery
Cardiolipin	Oligomerisation; Allosteric regulation			
DHA and unsaturated tails				Active conformer stability; Increase G protein coupling; Partitioning to lipid rafts; Oligomerisation

### 1.2.3. Membrane proteins

Membrane proteins constitute anywhere between 25–75% of most plasma membranes by mass<sup>83</sup>. They are of major biological and therapeutic interest, due to their diverse roles in many fundamental cellular processes, including cell signalling, molecular transport, and enzymatic reactions such as photosynthesis and respiration<sup>83</sup>.

Membrane proteins can be either integral or peripheral. Integral membrane proteins are embedded in both lipid monolayers, and span the whole membrane, while peripheral proteins are only associated with one side of the membrane<sup>79</sup> (Figure 5). Examples of integral membrane proteins are membrane channels (Section 1.2.3.1) and transporters (Section 1.2.3.2). Channels and transporters are responsible for movement of substrates, which due to their size, charge, polarity or lack of a favourable concentration gradient, are unable to diffuse across the cell membrane<sup>76</sup>.

Membrane proteins are composed of largely hydrophobic transmembrane domains, which form stabilising interactions with the hydrophobic environment of the membrane. These transmembrane domains are connected by exposed hydrophilic regions, or loop domains. In many membrane transporters, these regions are largely disordered, composed of hydrophilic residues, and are stabilised by interactions with the aqueous environment<sup>76</sup>.

Transmembrane domains are composed of either  $\alpha$ -helices or  $\beta$ -sheets, secondary structures that are stabilised by H-bonding. In  $\alpha$ -helices, every backbone N–H group forms a hydrogen bond with the backbone C=O group of the amino acid located four residues earlier along the protein sequence, using every available H-bond donor and acceptor within the polypeptide backbone. The helix is curved

allowing each amino acid side chain to point outwards, shielding the hydrophilic backbone from the hydrophobic core of the membrane (Figure 7). In  $\beta$ -sheet transmembrane domains, the  $\beta$ -strands are connected laterally by H-bonds, forming a curved barrel-like structure. Hydrophilic side chains are buried in the protein, while hydrophobic side chains point outward forming interactions with the hydrophobic core of the membrane (Figure 7).

Alpha-helical membrane proteins are more common. It has been estimated that 27% of all human proteins are  $\alpha$ -helical membrane proteins<sup>84</sup>. Beta-barrel proteins are predominantly found in the outer membranes of gram-negative bacteria, cell walls of gram-positive bacteria, and outer membranes of mitochondria and chloroplasts<sup>85</sup>. An example of an  $\alpha$ -helical membrane protein is the eukaryotic purine/H<sup>+</sup> symporter, UapA from *Aspergillus nidulans* (Figure 7), the topic of this thesis. An example of a  $\beta$ -sheet based membrane protein is the sucrose-specific porin ScrY from *Salmonella typhimurium*<sup>86</sup> (Figure 7).

Membrane transporter oligomerisation, where protein monomer subunits assemble to form larger more complex structures, is known to have essential roles in their trafficking and function<sup>87</sup>. Dimerisation is essential for correct trafficking, as well as function, of the nucleobase-ascorbate transporter, UapA (Figure 7) to the cell membrane<sup>1</sup>. In addition, membrane proteins are often glycosylated by the covalent attachment of an oligosaccharide. Oligosaccharides in outer cell membranes are oriented toward the extracellular environment, with key roles in cell recognition, adhesion, intercellular signalling and cell-pathogen interactions<sup>88</sup>.

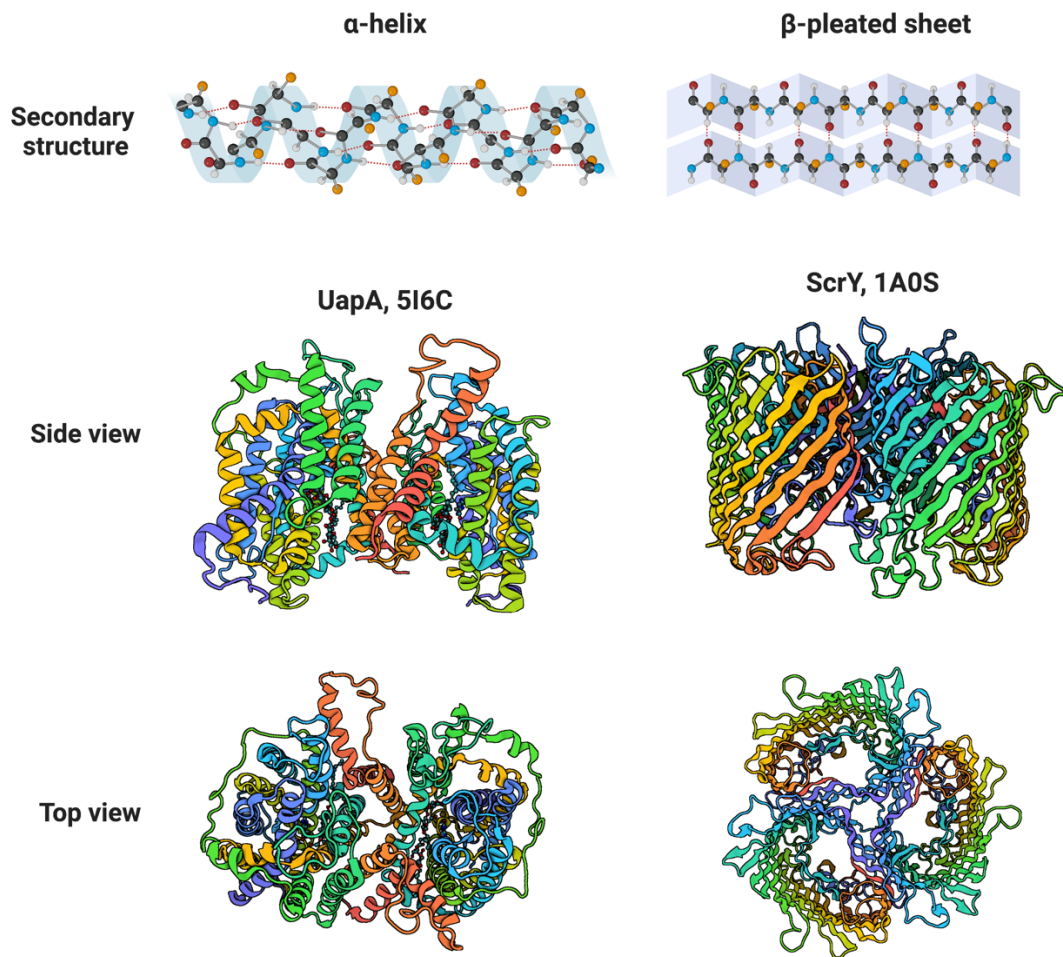


Figure 7:  $\alpha$ -helices and  $\beta$ -sheets are secondary structures common to all proteins. Membrane proteins can be formed of predominantly alpha-helical transmembrane domains, such as the eukaryotic nucleobase-ascorbate transporter, UapA from *Aspergillus nidulans* (PDB 5I6C)<sup>1</sup>. Membrane proteins can also possess predominantly beta-sheet transmembrane domains, such as in the sucrose-specific porin ScrY from *Salmonella typhimurium* (PDB 1A0S)<sup>96</sup>. This figure was created with [www.BioRender.com/](http://www.BioRender.com/) with structures imported directly from the Protein Data Bank (PDB).



### 1.2.3.1. Channels

Integral membrane transporters can be classified as channels or transporters. Channels form pores in the membrane, which selectively allow molecules to translocate the cellular membrane by facilitated diffusion, down their electrochemical gradient. The translocation pore contains filters, which select based upon properties such as substrate size, polarity and charge. Channel activity is also mediated by gating mechanisms; the gating mechanism varies between channels, but is often sensitive to pH, membrane potential, mechanical stress or ligand binding<sup>89</sup>. The interactions between the substrate and the translocation pore are transient, enabling fast substrate translocation relative to transporters<sup>90</sup> (Section 1.2.3.2). The first atomic-level structure of an ion channel was the prokaryotic potassium channel from *Streptomyces lividans*, KcsA<sup>91</sup>, published in 1998.

### 1.2.3.2. Transporters

Unlike membrane carriers, transporters can facilitate the movement of molecules across the membrane against their concentration gradient. Generally, transporters possess a relatively high affinity binding site open to one side of the membrane. Substrate binding induces a conformational rearrangement of the protein, allowing the substrate to translocate the membrane<sup>77</sup>. This is known as the alternating access mechanism, and was first described in 1966<sup>92</sup>. Transport of substrates is much slower than through channel proteins (Section 1.2.3.1) since, unlike channels, each transport event requires marked conformational rearrangements of the protein. In addition, transporters are only able to transport one molecule at a time<sup>90</sup>.

There are two main classes of transporter: primary or secondary active transporters. Primary active transporters utilise adenosine triphosphate (ATP) hydrolysis to drive transport of a substrate against its concentration gradient.

Meanwhile, secondary active transporters couple substrate transport to the thermodynamically favourable transport of an ion (e.g.  $\text{Na}^+$  or  $\text{H}^+$ ) down its concentration gradient. Transport of the coupled ion can either be in the same direction as the transport of the substrate (symport) or in the opposite direction (antiport). Examples of three classes of symporter, and two classes of antiporters can be found in Figure 8. An example of a secondary active symporter is the xanthine or uric acid/ $\text{H}^+$  transporter UapA<sup>93</sup> (Figure 7) from *Aspergillus nidulans*, the topic of this thesis.

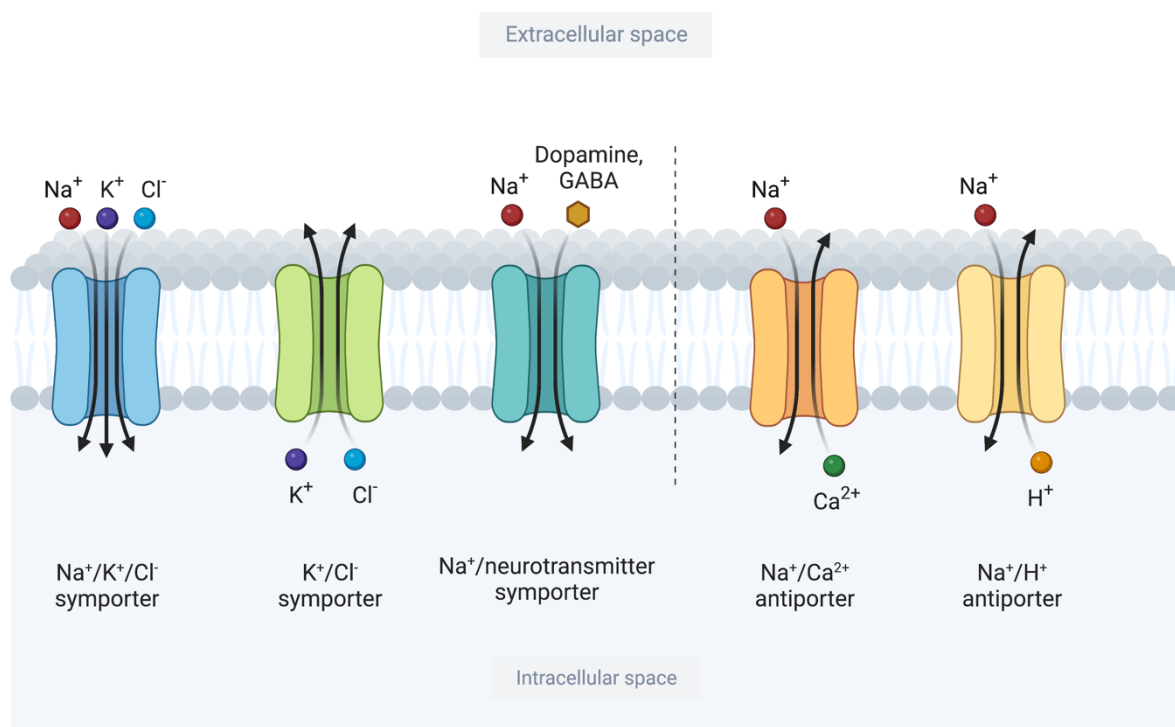


Figure 8: Examples of three classes of symporter, and two classes of antiporters. Transporters are often coupled to  $\text{Na}^+$  (red) or  $\text{H}^+$  (orange) ions. This figure was created with [www.BioRender.com/](http://www.BioRender.com/), and adapted from the template “Examples of Secondary Active Transporters”.

### 1.2.3.3. Mechanisms of transport

For secondary active transporters there are three reported models for mechanisms of transport: the rocker-switch, the rocker-bundle and the elevator model. These models are depicted in Figure 9, and describe different protein conformation changes that drive movement of substrate across the membrane.

In the rocker-switch model (Figure 9), the substrate binding site is located roughly halfway across the membrane between two protein domains. The substrate binding site is exposed to one side of the membrane, and on binding of the substrate, the two domains rotate around the binding site, exposing the substrate binding site to the opposite side of the membrane<sup>94</sup>. An example of a transporter thought to function via a rocker-switch mechanism is the glycerol-3-phosphate transporter (GlpT) found in the inner membrane of *Escherichia coli*<sup>95</sup>.

In the rocker-bundle model (Figure 9), the substrate binding site is again located at the interface between the two protein domains, halfway across the membrane. The main difference is that in the rocker-bundle model, one of these protein domains remains static in the membrane, while the other moves in order to expose the binding site to the other side of the membrane. An example of a protein which transports its substrate via the rocker-bundle mechanism is the bacterial amino acid transporter LeuT<sup>96</sup>.

The elevator model (Figure 9) differs from the other two mechanisms in that both the substrate and substrate binding domain move through the membrane. The transporter is made up from an oligomerisation domain and transport domain. The substrate binding site is located within the transport domain, and, upon binding, it undergoes a large rigid-body movement against the oligomerisation domain, transporting the substrate to the other side of the membrane. The elevator model was

first reported for the transport of glutamate across bacterial membranes and was based on a comparison between the outward and inward facing crystal structures of GltPh<sup>97</sup>. The transport mechanism and its kinetics have also been explored using high-speed atomic force microscopy (AFM) in a lipidic bilayer<sup>98</sup>.

Secondary active transporters follow Michaelis-Menten kinetics. Transporters bind a single substrate molecule in each transport cycle. This means that the substrate affinity, dissociation constants and transport capacities or rates can be directly measured, as for soluble enzymes<sup>94</sup>.

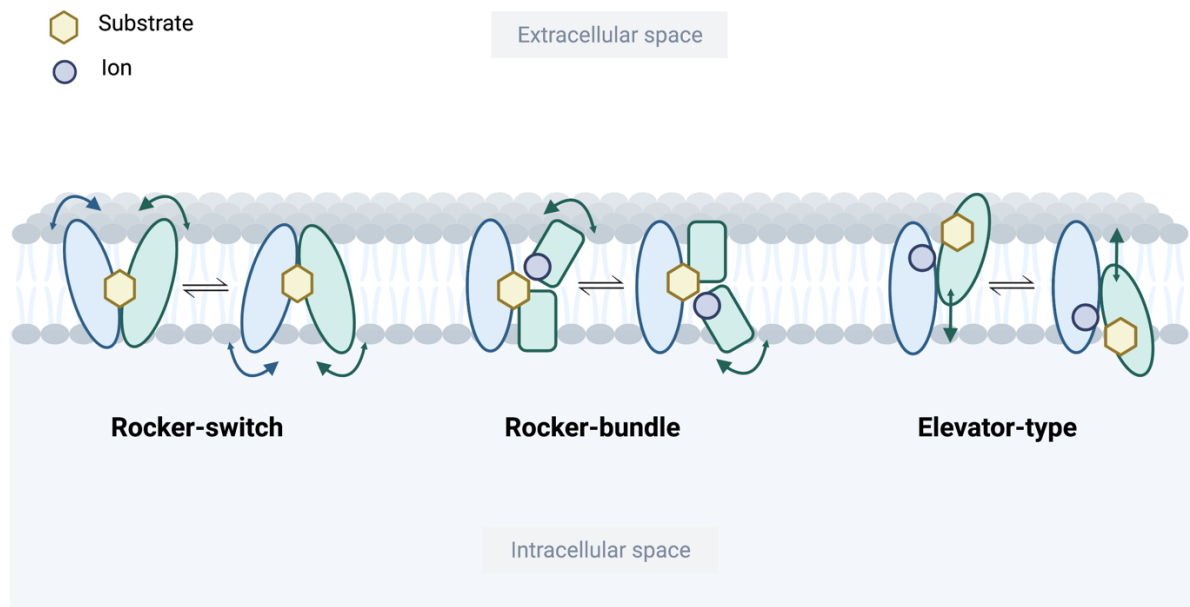


Figure 9: In the rocker-switch and rocker-bundle mechanisms, the substrate binding site (yellow) is located approximately halfway across the lipid bilayer. On binding of the substrate, one (rocker-bundle) or both (rocker-switch) domains rotate around the binding site, exposing the substrate binding site to the opposite side of the membrane. In the elevator mechanism, the substrate and substrate binding site move together through the membrane. The substrate binding site (yellow) is located within the core domain (green), and, upon binding, it undergoes a large rigid-body movement against the gate (pale blue), transporting the substrate to the other side of the membrane. This figure was created with [www.BioRender.com/](http://www.BioRender.com/).

#### 1.2.4. Challenges in working with membrane proteins

There has been significant investment into membrane protein research due to their importance both biologically and as drug targets<sup>99,100</sup>. The relatively low number of membrane protein structures is a direct consequence of the characteristics of membrane proteins; membrane proteins have hydrophobic surfaces, are highly flexible, and lack stability in detergent<sup>101</sup>. These characteristics are problematic in the expression, purification, and structural characterisation of membrane proteins.

Expression of membrane proteins usually requires recombinant approaches to produce sufficient quantities of protein for downstream analysis<sup>102</sup>. The major recombinant expression systems for eukaryotic membrane proteins are *E. coli* (e.g. BL21, C43 and C41 strains), yeasts (e.g. *Pichia Pastoris* and *Saccharomyces cerevisiae*), insect cells (e.g. *Spodoptera frugiperda*, *Trichoplusia ni*), and mammalian cells (e.g. human embryo kidney (HEK) and Chinese hamster ovary (CHO) cells)<sup>102</sup>. However, recombinant expression in heterologous systems has disadvantages, since the protein may no longer be expressed in its native environment, and mechanisms for post-translational modifications and chaperones for correct folding may be lacking. In addition, native protein-lipid interactions may not be retained, resulting in reduced protein stability and/or function<sup>102</sup>.

During their purification, membrane proteins are extracted from their native or non-native membrane environments with detergents. Membrane proteins have a tendency to aggregate or denature outside of the biological membranes, and are highly unstable in aqueous solution<sup>103</sup>. Detergents displace membrane lipids by interfering with protein-lipid interactions. Since they share the amphipathic properties of membrane proteins and lipids, they can crudely mimic the lipid environment, shielding the hydrophobic protein regions from solvent, allowing the maintenance of the protein in aqueous solution<sup>104</sup>.

#### 1.2.4.1. Detergents

The extraction efficiency of membrane proteins from biological membranes varies considerably with different detergents. In addition, conditions that provide optimal extraction may be incompatible with long term stability and structure determination<sup>104</sup>. Generally, detergents with longer acyl chains are more efficient at solubilization and stabilization, while shorter chain detergents allow for the formation of smaller detergent micelles. Smaller micelles allow for tighter crystal lattice packing and in turn, often better diffraction<sup>105,106</sup>.

Common detergent families used in the purification and crystallisation of membrane proteins are the maltosides, glucosides, amine oxides and polyoxyethylene glycols<sup>107</sup>. A significant number of crystal structures are associated with the use of classical detergents<sup>104,108</sup> such as n-dodecyl  $\beta$ -D-maltoside (DDM), n-decyl- $\beta$ -D-maltopyranoside (DM), octyl-beta-glucoside (OG) and lauryldimethylamine-N-oxide (LDAO) (Figure 10).

?

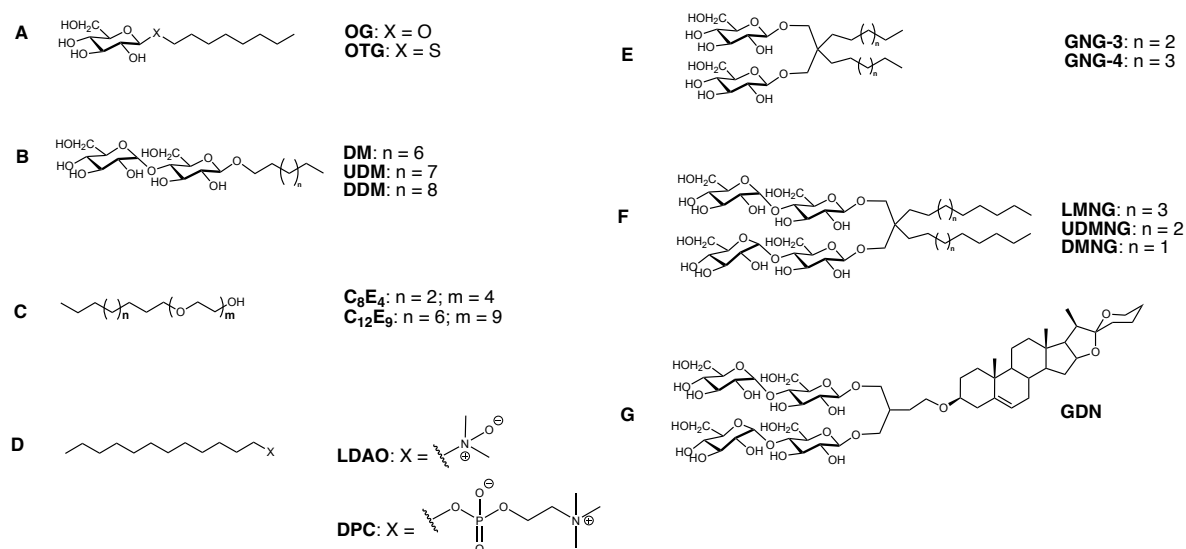


Figure 10: Representative chemical structures of some classical (A – D) and second-generation detergents (E – G). A, octyl-beta-glucoside (OG) and octyl-thio-glucoside (OTG). B, n-decyl-β-D-maltoside (DM), undecyl-β-D-maltoside (UDM) and n-dodecyl-β-D-maltoside (DDM). C, polyoxyethylenes (C<sub>8</sub>E<sub>4</sub> and C<sub>12</sub>E<sub>9</sub>). D, lauryldimethylamine-N-oxide (LDAO) and dodecyl phosphocholine (DPC). E, glucose neopentyl glycols (GNGs). F, maltose neopentyl glycols (MNGs). G, glycodiosgenin (GDN). This figure was created with ChemDraw 19.0, and has been informed by Lee *et al*<sup>104</sup>.



There has been significant investment into the development of novel detergents, which have been comprehensively reviewed by Lee *et al*<sup>104</sup>. The GNGs and MNGs (Figure 10) are examples of second-generation detergents, which have revolutionised membrane protein solubilization, purification and structural determination<sup>104</sup>. The GNGs and MNGs have a dimeric structure compared with the classical detergents; OGNG and LMNG are dimers of OG and DDM (Figure 10) respectively, and form larger micelles than their monomeric counterparts<sup>104</sup>. LMNG, in particular, has demonstrated high efficacy for the stabilisation of diverse membrane proteins, including GPCRs and transporters<sup>104</sup>. Glycodiosgenin (GDN, Figure 10) is structurally similar to LMNG, retaining the branched dimaltoside as the hydrophilic group. However, the hydrophobic group in GDN has been replaced by a steroid group, diosgenin. GDN has been shown to have high homogeneity, good water solubility, and low toxicity<sup>104</sup>.

The emergence of novel detergents has allowed for the extraction, purification and structural characterisation of otherwise challenging membrane protein targets<sup>104</sup>. There has been extensive research into detergent optimisation and high-throughput stability screening<sup>108</sup>. Unfortunately, it remains challenging to find the optimal detergent for a particular target or function. Additionally, membrane proteins are still relatively unstable in detergent, with the protein more liable to aggregation and unfolding than in the biological membrane<sup>109</sup>. In addition, detergents are known to strip away lipids, which may be important for structure and/or function<sup>110</sup>. Consequently, there have been significant efforts in developing alternative systems that better mimic the lipid bilayer.

#### 1.2.4.2. Alternative membrane-mimetics

Nanodiscs (Figure 11) are disk-shaped lipid bilayers, stabilized by two amphipathic helical proteins, membrane scaffold proteins (MSP)<sup>111</sup>. The MSP forms a 'belt', protecting the hydrophobic centre of the lipid bilayer from the aqueous environment. The size of the resulting complexes is dependent upon the length of the membrane scaffold protein and the stoichiometry of the lipids used during the self-assembly process<sup>112</sup>. The lipid composition of the nanodiscs can also be varied, enabling studies on protein-lipid interactions<sup>113,114</sup>. Membrane proteins reconstituted into nanodiscs have been studied using a variety of structural techniques, including nuclear magnetic resonance (NMR), cryo-electron microscopy (cryo-EM), small-angle X-ray scattering (SAXS) and neutron scattering.

Peptidiscs (Figure 11) are comprised of multiple copies of an amphipathic bi-helical peptide, termed nanodisc scaffold peptide (NSPr)<sup>115</sup>. NSPr domains wrap around the target membrane protein, protecting the hydrophobic transmembrane domains. Unlike with nanodiscs, additional lipids are not required for successful reconstitution, except the specific and annular lipids that co-purify with the protein<sup>115</sup>.

These membrane mimetic systems offer a more physiologically relevant membrane environment than traditional detergents. However, prior to reconstitution into nanodiscs or peptidiscs, the protein must be prepared in detergent first. This means that key lipids may already have been removed, resulting in the loss of information regarding important protein-lipid interactions.

Styrene maleic-acid lipid particles (SMALPs) offer an alternative detergent-free method for the extraction of membrane proteins from the bilayer, while retaining key annular lipids. However, the heterogeneity of the resulting sample, due to limited control over size remains a significant issue<sup>116</sup>.

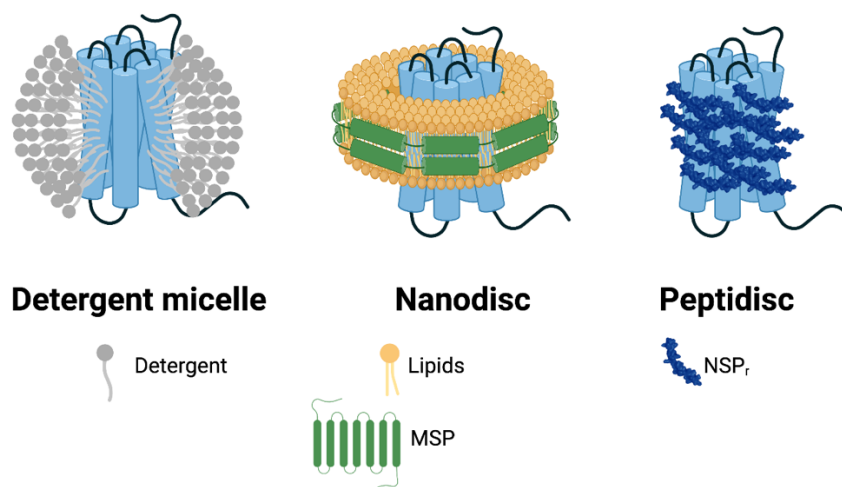


Figure 11: Structure of the detergent micelle, nanodiscs and peptidiscs. Detergents (grey), lipids (yellow) and membrane scaffold proteins (MSP, green), and peptides (navy) are used to shield the hydrophobic transmembrane domains of membrane proteins (blue) in each structure respectively. Specific and annular lipids have not been shown. This figure was created with [www.BioRender.com/](http://www.BioRender.com/).

#### 1.2.4.3. Characterisation of membrane proteins by crystallography

Since the first crystal structure of a membrane protein was published in 1985<sup>117</sup>, structural characterisation of membrane proteins has been dominated by crystallisation of detergent-solubilised protein. Crystallisation can be achieved by vapour diffusion or lipidic cubic phase. Recent technologies such as liquid handling robots and the development of commercial crystallisation screens, have aided crystallography efforts<sup>118,119</sup>.

Sitting drop crystallisation is the most common vapour diffusion crystallisation method. A drop composed of a mixture of protein sample and reagent is left in vapour equilibration with a larger reagent reservoir. To achieve equilibrium, water vapour leaves the drop, diffusing into the reservoir. Consequently, the sample and reagent in the drop increase in concentration until the reagent concentration in the drop reaches that of the reservoir. Alternatives to sitting drop crystallisation include hanging drop crystallisation, where the drop is inverted, and microbatch crystallisation performed under oil.

Lipidic cubic phase (LCP) crystallisation is an alternative to vapour diffusion and utilises a membrane-mimetic matrix, which allows for stabilization and crystallization of membrane proteins in a lipidic environment<sup>120</sup>. The detergent-solubilised protein is added to the cubic phase and the protein exchanges into the matrix, where crystals may form.

Once crystals have been obtained, either by LCP or traditional vapour diffusion, multiple approaches can be used to improve crystals and their diffraction. Examples of variables for optimisation include temperature, pH range, precipitants and concentration range of the buffer<sup>121</sup>. In addition, methods such as additive screening or seeding can be utilised<sup>122,123</sup>. Seeding or micro matrix seeding (MMS)

involves creating protein 'seeds' by the mechanical disruption of existing crystals, which are then used to supplement the drops of new crystallisation screens<sup>123</sup>. Seeds act as nucleation points for crystal growth, and often improve the quality and reproducibility of existing protein crystals<sup>123</sup>.

There are two main strategies for the determination of protein-ligand complexes: co-crystallisation and soaking<sup>124</sup>. Co-crystallisation involves allowing the protein to crystallise in the presence of the ligand, while soaking involves the addition of the ligand once crystals have formed. Soaking existing protein crystals with ligands is the most efficient method to yield protein structures for structure-based drug discovery, but in some cases soaking results in damage to the crystals, interfering with packing and resulting in poor diffraction<sup>124</sup>. In addition to crystallising compounds of interest, new technologies have allowed crystallography to be re-developed as a hit identification method. Fragment screening using crystallography, such as XChem at the Diamond Light Source, Oxfordshire, has become a powerful tool in early-stage drug discovery<sup>125</sup>.

Data collection processes have also undergone technological advances; microfocus beamlines can be set up for *in situ* crystallography, where crystals can be screened without harvesting<sup>126</sup>. Membrane proteins crystals are often extremely fragile and liable to radiation damage. Improved cryo-cooling systems and ability to use line or grid scan methodologies for initial crystal screening have also reduced damage to the crystal prior to a full data collection<sup>127</sup>.

Despite numerous advances in membrane protein crystallisation and data collection, structural determination of membrane proteins using X-ray crystallography remains challenging, and requires finding conditions which enable the target to crystallise<sup>101</sup>. There are numerous alternative methods that allow for structural characterisation of membrane proteins: negative-stain electron microscopy,

cryogenic electron microscopy (cryo-EM), nuclear magnetic resonance, hydrogen-deuterium exchange mass spectrometry (HDX-MS), small-angle X-ray scattering (SAXS) and Fourier transform infrared (FTIR) spectroscopy.

#### 1.2.4.4. Characterisation of membrane proteins by cryo-EM

Cryo-EM has revolutionised the structural characterisation of membrane proteins, enabling atomic-level structural characterisation of proteins in more physiologically representative membrane-mimetic environments<sup>128</sup>. Samples are adsorbed onto metal grids, blotted to form a thin aqueous layer, and vitrified by plunge freezing in liquid ethane. Cryo-EM data collection involves the collection of many electron micrographs, which sample the membrane protein complex in different conformations and orientations. In short, particles are 'picked', aligned and combined to generate three-dimensional (3D) reconstructions of the protein<sup>128</sup>.

Cryo-EM was first developed in the 1970s, with the vitrification of catalase crystals, bacteriophages, membranes and DNA fragments<sup>129</sup>. Since its introduction, cryo-EM has enabled structural characterisation of large proteins and complexes. Since cryo-EM imaging is built upon phase contrast, visualizing smaller proteins is challenging; the resulting particles generally have low signal to noise ratios, making downstream data processing, particularly particle alignment, challenging<sup>130</sup>.

More advanced microscopes and electron sources, direct electron detectors with more powerful acceleration voltages (200 keV or 300 keV), automated data collection, and user-friendly data processing software have significantly advanced the field of membrane protein structural biology and yielded many spectacular membrane protein structures<sup>131</sup>.

In addition to technological advancements, there have also been improvements in sample preparation, with the development of novel detergents that reduce detergent background<sup>104</sup>. LMNG and GDN have been discussed in Section 1.2.4.1, but both have shown great applicability to the stabilisation of membrane complexes, including GPCRs and transporters, ready for cryo-EM<sup>104</sup>. In some cases, sample homogeneity may be improved by using glycerol gradient centrifugation (GraDeR) to remove free detergent monomers and micelles from LMNG detergent stabilized membrane complexes<sup>132</sup>. Novel membrane mimetic systems such as peptidiscs, nanodiscs, proteoliposomes, SMALPs, some of which were discussed in Section 1.2.4.2, generally improve protein stability, whilst maintaining a more native environment<sup>133</sup>.

Despite some successes, studying smaller membrane proteins (<150 kDa) remains challenging. One strategy has been to increase the size of the membrane protein complex under study. Antigen binding fragments (Fabs), antibodies and megabodies, have proved valuable in better stabilising small membrane protein complexes for cryo-EM, aiding particle picking and alignment<sup>134-136</sup>.

#### 1.2.4.5. Characterisation of membrane proteins by alternative methods

Other characterisation methods include solution or solid state nuclear magnetic resonance (solution or solid-state NMR) spectroscopy, hydrogen-deuterium exchange mass spectrometry (HDX-MS), small-angle X-ray scattering (SAXS), small-angle neutron scattering (SANS) and Fourier transform infrared (FTIR) spectroscopy.

Solution NMR requires complexes that have fast rotational diffusion. This restricts the applicability of this method to proteins in lipid micelles or small bicelles and nanodiscs<sup>137</sup>. Solid-state NMR does not have the same limitations, since it can

be applied to static samples or samples that are mechanically rotated at high speed<sup>138,139</sup>. As a consequence, it can be used to study systems with restricted mobility, including high molecular weight proteins, supramolecular assemblies, and membrane proteins in their native phospholipid environment<sup>140</sup>. Using solid-state NMR, membrane proteins can be studied in lipid bilayers. As discussed in Section 1.2.2, this is important, since protein structure, function and dynamics is dependent upon the structure and composition of the lipid bilayer<sup>138</sup>. As an example, solid state NMR has been used to study membrane proteins such as RV1861, a membrane protein from *Mycobacterium tuberculosis*, reconstituted into liposomes<sup>141</sup>.

Hydrogen-deuterium exchange mass spectrometry (HDX-MS) has proven to be an invaluable method to understand membrane protein structure and function<sup>142</sup>. HDX-MS involves exposing folded proteins to deuterated water (D<sub>2</sub>O). This allows for rapid H/D exchange of the amide backbone in disordered solvent-exposed regions. Protons in tightly folded regions are protected from exchange, resulting in lower to no deuterium uptake. Mass spectrometry-based peptide mapping allows for measurement of mass shifts of peptide fragments<sup>142</sup>. While this method does not provide atomic resolution structures, it can sample protein in different orientations and conformational states, and can be used to study large structural changes in a protein between two different conditions (e.g. mutagenesis, ligand-binding, inhibitor-binding or other conformational changes).

Small-angle X-ray scattering (SAXS) and small-angle neutron scattering (SANS) can also be used to investigate the low-resolution structure and conformational changes of membrane proteins. While the resolution from SAXS is typically lower than with X-ray diffraction, the major benefit is that there is no requirement for protein crystallisation<sup>143</sup>. An example of the successful application of SAXS analysis to a membrane protein is that of aquaporin-0 (AQP0), solubilized in DDM<sup>144</sup>. SANS utilises neutron radiation rather than X-ray radiation. Neutrons are less



energetic than X-rays with the same wavelength, in turn reducing radiation damage<sup>145</sup>. This is important for samples that are more sensitive to radiation damage, such as membrane proteins<sup>146</sup>. Crucially, neutron scattering is also compatible with isotopic labelling; X-rays interact with hydrogen and deuterium identically but scatter differently<sup>145</sup>. By differential isotopic-labelling of subunits (contrast variation), SANS becomes a powerful tool for studying multisubunit complexes. This technique can be applied to the examination of protein-protein, protein-DNA, protein-lipid and protein-detergent interactions.

Similar to SAXS and SANS, Fourier transform infrared (FTIR) spectroscopy does not provide atomic-resolution molecular structure. However, it does allow for examination of conformation changes occurring in proteins upon functional transitions or intermolecular interactions<sup>147</sup>. Similarly to SANS, isotopic labelling can be employed to protein-protein interactions and interactions of proteins with lipids, the membrane and other biomolecules<sup>147</sup>.

Membrane proteins are challenging to study, due to their intrinsic characteristics: partially hydrophobic surfaces, flexibility and lack of stability. Advancements in membrane protein extraction, stabilisation in membrane mimetic systems and technologies for their structural determination have made the structural characterisation of these proteins more accessible.

### 1.2.5. Membrane proteins as drug targets and biomarkers

As discussed in Section 1.2.3, membrane proteins have broad and diverse roles across the proteome. This is reflected in their versatility as drug targets across a range of therapeutic areas<sup>148</sup>. Membrane proteins are also attractive drug targets due to their accessibility on the surface of cells, which reduces concerns of low lipid-bilayer permeability of drugs<sup>149</sup>. In addition, disease is often associated with changes in membrane protein expression or their modification, making plasma membrane proteins a useful source of disease biomarkers<sup>150</sup>.

Examples of classes of membrane protein drug targets include GPCRs, cytokine receptors, ion channels and transporters<sup>99,100</sup>. As of 2018, it was estimated that approximately 700 approved drugs target GPCRs, constituting 35% of all approved drugs<sup>151</sup>. Transporters such as solute carriers (SLC) are also notable drug targets; SLC transporters are targets for several approved drugs, including diuretics, neuropsychiatric drugs, and antidiabetic therapeutics<sup>152</sup>. Most of these function by inhibiting transporter activity<sup>152</sup>. In addition, SLC transporters have essential roles in the absorption, distribution and elimination of drugs, as discussed in Section 1.2.6.

Since membrane proteins are cell-surface, SLC transporters also represent possible targets for antibody-based therapies such as monoclonal antibodies<sup>152</sup>. Monoclonal antibodies are a targeted drug therapy; they bind specifically to antigens, such as membrane proteins or polysaccharides, on the surface of their target. They have multiple mechanisms of action, including antibody-dependent cell-mediated cytotoxicity and modulation of the immune system through inhibition of immune checkpoint inhibitors such as CTLA-4 and PD-1<sup>153</sup>. While many antibody-based therapies have been reported against GPCRs or receptors, few targeting transporters have been reported<sup>154</sup>. So far, monoclonal antibodies have been generated against the inward- and outward-facing states of the glucose transporter GLUT4, which have

potential therapeutic applications in diabetes<sup>155</sup>. There have also been monoclonal antibodies reported as inhibitors of the iron transporter ferroponin and multi-drug resistant protein 4 (MRP4)<sup>156,157</sup>.

The joint role of membrane proteins as biomarkers and drug targets, makes them candidates for monoclonal antibodies and bifunctional molecules, such as antibody-drug conjugates (ADCs), LYTACs and AbTACs. ADCs also take advantage of antibody specificity, but instead of modulating the immune response, they direct non-specific cytotoxic agents towards the antigen-presenting target. ADCs are composed of two major components: a monoclonal antibody (mAb) and a cytotoxic component, often made from a chemotherapy agent, which are connected via a chemical linker. ADCs have found particular relevance in the field of cancer-therapy, since they take advantage of target antigens which are only expressed on cancer cell surfaces<sup>158</sup>.

Lysosome-based chimeras (LYTACs) and antibody-based chimeras (AbTACs) also take advantage of the specificity of antibodies<sup>159</sup>. LYTACs are antibodies conjugated to a ligand specific for cation-independent mannose 6-phosphate receptor (CI-M6PR). The CI-M6PR binding ligand targets the protein for the lysosome degradation pathway<sup>160</sup>. AbTACs are antibodies conjugated to a ligand specific for membrane-bound E3 ligases. This system that has been used to target the cell-surface immune checkpoint protein PD-L1 for E3 ligase-mediated degradation<sup>161</sup>. LYTACs and AbTACs are related to proteolysis targeting chimeras (PROTACs). PROTACs are similarly composed of two active domains and a linker<sup>162</sup>. However the antibody is replaced by a small molecule that selectively binds the target protein, while the second half recruits cytoplasmic E3 ubiquitin ligase. This directs the target protein for degradation by the ubiquitin-proteasome system. However, since PROTACs rely on recruitment of cytosolic E3 ubiquitin ligase, they are not suitable for the targeting of membrane proteins<sup>162</sup>.

### 1.2.6. Membrane proteins as drug carriers

As well as potential drug targets, membrane proteins are drug carriers, mediating cellular uptake of antimicrobials, anticancer agents, antivirals and antifungals<sup>163</sup>. For example, 5-fluorocytosine is a known antifungal, whose activity against *Aspergillus nidulans* is dependent on expression of FcyB, a purine-cytosine permease (Section 1.1.5.4)<sup>164</sup>. Another example includes rat and rabbit ileal bile acid transporter, which is a sodium-dependent transporter of bile acid, and bile acid-drug conjugates. The drugs are coupled to the hydroxyl group on the bile acid ring system, enabling their transport through the membrane via this transporter<sup>165,166</sup>.

Drug interactions with membrane transporters are not limited to uptake; transporters have important roles spanning the absorption, distribution and ultimately elimination of structurally and functionally diverse drugs<sup>148</sup>. In particular, there has been significant investment in understanding transporters expressed in the endothelium of the blood–brain barrier and in the epithelial cells of the intestine, liver and kidney<sup>148</sup>.

Their role in absorption, distribution, and elimination, make membrane proteins key determinants of the pharmacokinetic, safety and efficacy profiles of drugs<sup>148</sup>. Transporters are also known to mediate drug–drug interactions that are responsible for drug toxicities<sup>148</sup>. Examples of transporter-mediated drug–drug interactions have been comprehensively reviewed by Giacomini *et al*<sup>148</sup>.

Transporters are also major determinants of resistance. Where drug function is responsible for its uptake via transporters, downregulation of the transporter can result in decreased intracellular concentration of the drug, and thus reduced efficacy. This is a major resistance mechanism for *Aspergillus fumigatus* in response to 5-fluorocytosine<sup>164</sup>. In addition, transporters are also actively involved in drug efflux<sup>148</sup>.

Efflux pumps reduce the intracellular concentration of the drug and ability to act on their intracellular target, as reported for azole antifungals in *Aspergillus*<sup>161</sup> and discussed in Section 1.1.6.

There are two main classes of drug transporter<sup>148</sup>, those belonging to the ATP-binding cassette family (ABC), and the SLC family. The fundamental difference between ABC and SLC transporters is that ABC transporters are primary active transporters, while SLC transporters use either secondary active transport or facilitative diffusion. There is significant interest in transporters from both classes, but particularly those with broad substrate specificities. Examples of key transporters include multidrug resistance protein 1 (MDR1/ABCB1) and the organic anion transporter 1 (OAT1/SLC22A6)<sup>148,167</sup>.

### 1.3. Uric Acid Permease, UapA

#### 1.3.1. The NAT transporter family

Nucleobase-Ascorbate Transporters (NAT) are secondary active transporters, and members of the wider solute-carrier (SLC) family. NAT transporters, also known as nucleobase/cation symporter 2 (NCS2) proteins, span all biological kingdoms, including *Animalia*, *Plantae*, *Fungi*, *Protista* and *Monera* (Figure 12). NAT transporters share some structural homology with one another but can be divided into three distinct classes with respect to substrate specificity<sup>168</sup> (Table 4).

Table 4: Three distinct classes of NAT transporter, distinguished by their substrate specificity.

Class	Present in	Substrate specificity	Example
I	Bacteria, fungi, plants	Xanthine and/or uric acid	UapA, a uric acid/xanthine/H <sup>+</sup> symporter from <i>Aspergillus nidulans</i> <sup>1</sup>
II	Bacteria	Uracil	UraA, the uracil/H <sup>+</sup> symporter from <i>Escherichia coli</i> <sup>169</sup>
III	Vertebrates	L-ascorbic acid	SVCT1, an ascorbate/Na <sup>+</sup> symporter in humans <sup>170</sup>

NAT transporters share a highly conserved signature motif ([Q/E/P]<sup>408</sup>-N-X-G-X-X-X-X-T-[R/K/G]<sup>417</sup>). This motif is located in transmembrane domain 10 of both uric acid permease (UapA)<sup>93</sup> and the uracil symporter UraA<sup>169</sup> (Figure 13). Systematic mutagenesis of residues within this motif in Uric Acid Permease (UapA) showed that these residues are important for function and substrate translocation<sup>171</sup>. For example, conservative mutagenesis of residues Q408, N409 and G411 modified the kinetics and specificity of UapA, without affecting targeting of the transporter to the plasma membrane<sup>171</sup> (Section 1.3.2).

This motif is conserved within SVCT1 and SVCT2, the human high-affinity sodium-vitamin C transporters (Figure 13). These proteins are responsible for maintaining cellular L-ascorbic acid levels, with roles in protecting cells from oxidative

stress<sup>172,173</sup>. SVCT1 is expressed primarily in epithelial tissues, while SVCT2 is more broadly distributed throughout the body<sup>172</sup>. SVCT1 and SVCT2 share 64% sequence identity. The third SVCT, SVCT3, is poorly understood. SVCT3 shares much lower sequence similarity with SVCT1 (29%) and SVCT2 (30%), and varies in the otherwise widely conserved NAT signature motif (Figure 13).

Phylogenetic analysis (Figure 12) of the purine/pyrimidine NAT transporters and the SVCTs indicates a relationship between them, but also an evolutionary distance. There is high sequence identity in some key regions, such as the NAT motif, suggesting these proteins share a common ancestor, despite the distinct substrate specificities<sup>172</sup>. While UapA can recognize *L*-ascorbate with extremely low affinity, no mutation has been identified to date that can change the specificity of the fungal NAT transporters from nucleobases to *L*-ascorbic acid<sup>174</sup>. Together, this suggests that slow progressive evolution was required to obtain ascorbate-specific NATs.

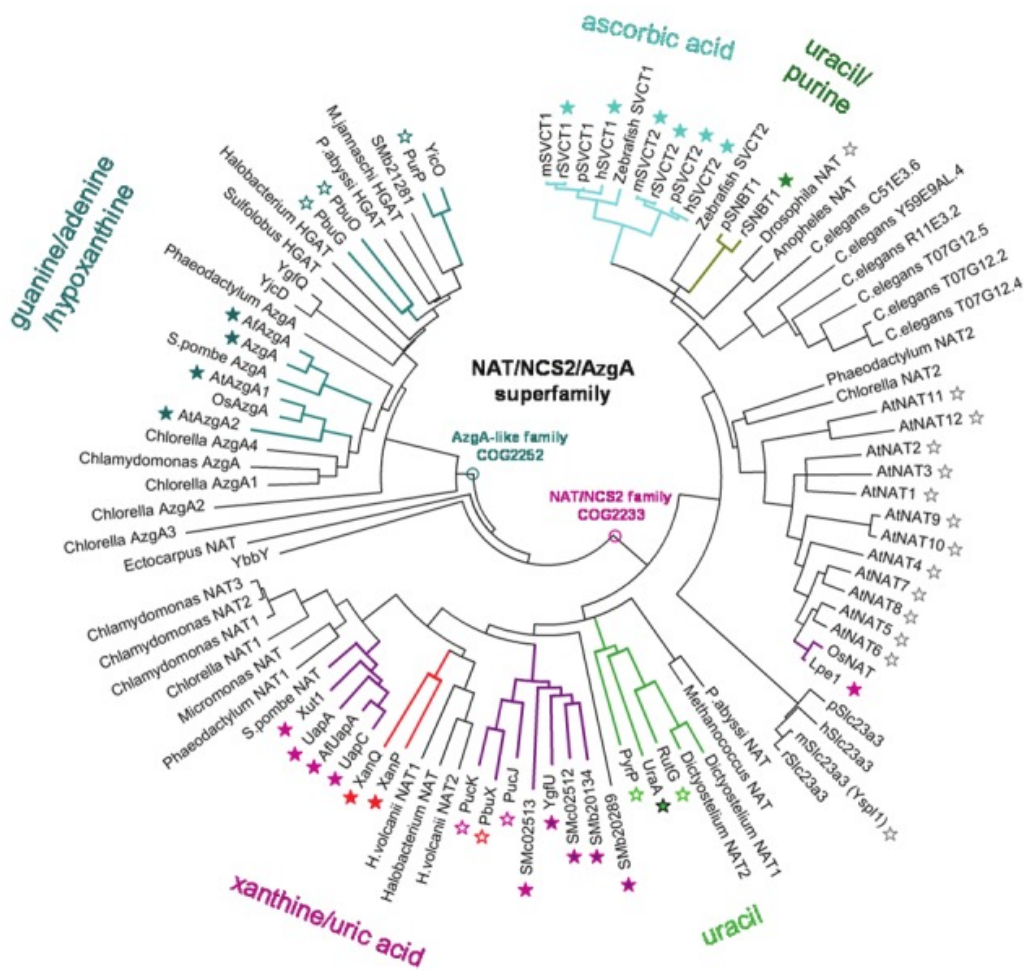


Figure 12: Phylogenetic tree from literature<sup>175</sup> of known members of the nucleobase-ascorbate transporter or nucleobase-cation symporter-2 (NAT/NCS2) family.



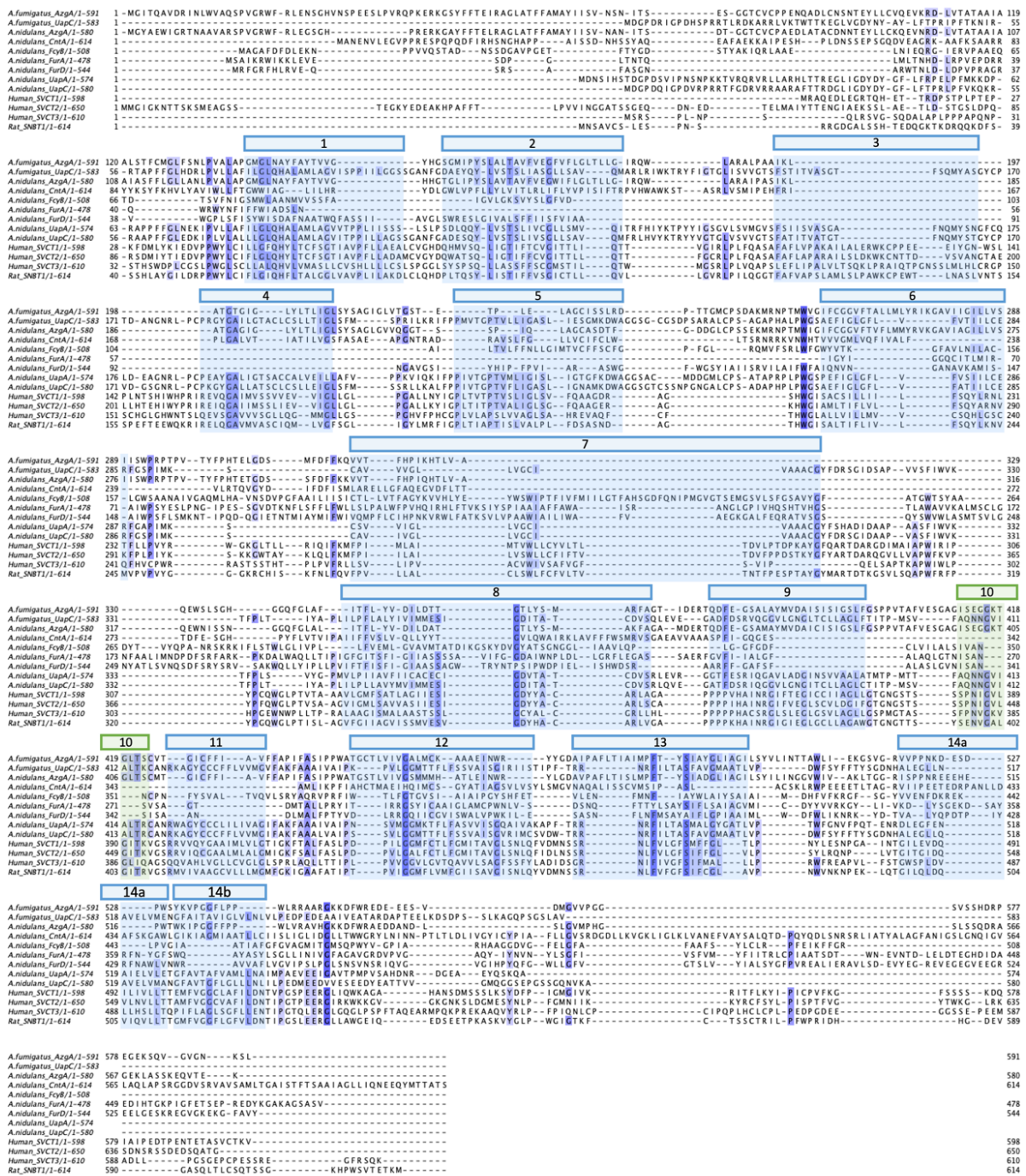


Figure 13: Sequence alignment for key members of the NAT and ENT transporter family, central to this thesis. This includes 7 key nucleobase transporters from the pathogenic *Aspergillus fumigatus* (AfUapC and AfAzgA), 3 human L-ascorbic acid transporters (SVCT1, SVCT2, SVCT3) and rat SNBT1. Transmembrane helices 1-14b of UapA are indicated. Transmembrane domain 10, which contains the NAT motif is highlighted in green. Sequence alignment generated in Jalview 2.11.2.2 with ClustalO.

### 1.3.2. Uric Acid Permease, UapA

UapA is a high affinity, high-capacity proton-coupled symporter of xanthine and uric acid (Figure 14) from *Aspergillus nidulans*. UapA's homologue in the pathogenic fungus *Aspergillus fumigatus*, AfUapC, is responsible for transporting the same oxidised purines<sup>22,176</sup>.

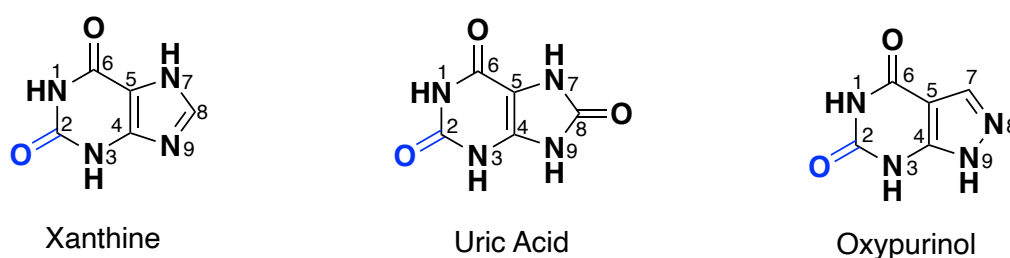


Figure 14: Chemical structures of xanthine and uric acid, oxidised purines. Atom numbers are shown, following numbering conventions. Xanthine and uric acid are oxidised purines, due to the carbonyl present at position 2 (blue). This figure was created with ChemDraw 19.0.

UapA is one of seven key purine and nucleotide transporters present in *A. nidulans*, each with a different purine specificity profile<sup>177</sup>. Of these, UapA shows the greatest sequence identity with UapC (60%, Figure 13), the general purine permease from *A. nidulans*. UapA and UapC have similar affinities for xanthine and oxypurinol (Figure 14), but UapC has an approximately 20-fold lower affinity for uric acid and binds other purines with low affinity (1–2 mM)<sup>178</sup>.

UapA and UapC share high sequence homology (61-63%, Figure 13) with the high-affinity, high-capacity purine symporter AfUapC from *A. fumigatus*<sup>22</sup>. AfUapC demonstrates overlapping substrate specificity to UapA and UapC, transporting xanthine and uric acid<sup>22</sup>. The binding site is highly conserved between these proteins, indicating that a substrate of UapA, is also likely to be a substrate of AfUapC; The NAT region is highly conserved between UapA, UapC and AfUapC, with AfUapC consistent except for the final residue (Q-N-N-G-V-I-A-L-T-[K/R]) (Figure 13).

Crucially, UapA shares low sequence identity with human NATs, SVCT1 and SVCT2 (20% and 18%, Figure 13), which are specific for *L*-ascorbic acid. The NAT region in SVCT1 and SVCT2 (P-**N**-I-**G**-V-L-G-I-**I**-K) differs from UapA in all but four residues (bold). Three of these residues (underlined) are highly conserved across all NAT transporters. In humans, ENT1, 2 and 3 are the main purine transporters, and demonstrate varying selectivity for adenine, guanine, hypoxanthine and cytosine<sup>179</sup>. These transporters belong to the equilibrative nucleoside transporter (ENT) family, which use cation coupling for substrate interaction, and are functionally different to UapA and other NAT transporters<sup>179</sup>. Crucially, they demonstrate no selectivity for the oxidised purines xanthine and uric acid<sup>179</sup>. Oxidised purine transporters in humans are limited to uric acid transporters, notably human urate transporter 1 (URAT1). URAT1 is a member of the organic anion transporter (OAT) family and is located in the membrane of renal proximal tubule cells, where it mediates uric acid reabsorption and elimination<sup>180</sup>. Together, this reduces concerns that an antifungal based upon xanthine, targeting *Aspergillus* via UapA will also be a substrate of host transporters.

### 1.3.3. X-ray crystal structure of UapA

Prior structural studies on UapA yielded an X-ray crystal structure of the thermostabilised mutant, UapA-G411V<sub>Δ1-11</sub>, as a homodimer in the inward-facing conformation, in complex with xanthine<sup>1,93,176</sup> (Figure 15, 5I6C, 3.7Å). This crystal<sup>1,93,176</sup> structure provides an opportunity for structure-based drug design (SBDD) of purine analogues, which may be tolerated by the substrate binding site, and thus allow for transport across the fungal membrane.

Genetic stabilisation of UapA involved truncation of 11 amino acids at the N-terminus and a point mutation at residue Gly411. Gly411 is found in TMD10, within the NAT domain. The G411V mutant shows loss of transport function, reduced conformational flexibility and increased stability<sup>93</sup>.

This crystal structure revealed that UapA function is contingent on homodimerisation, and that native substrates appear to traverse the membrane via an elevator mechanism (See Section 1.2.3.3). Upon substrate binding to the binding site, the transport domain moves through the membrane, sliding against the relatively immobile dimerisation domain, carrying the substrate through the membrane<sup>1,114</sup> (Figure 15).

This crystal structure also confirmed the binding site of xanthine, which is represented in Figure 16 as both the PyMOL structure and simplified interaction diagram. This binding mode suggests that xanthine forms  $\pi$ -interactions with the aromatic rings of Phe155 and Phe406 (Figure 16). The carbonyl at position 6, and nitrogen at position 7 seem to form a bidentate hydrogen bonding interaction with the side chain of Glu356. Meanwhile a second bidentate hydrogen bonding interaction is proposed between the nitrogen at position 1, carbonyl at position 2 and the side chain of Gln408 (Figure 16). This is consistent with previous mutational and functional

analyses, which revealed that Gln408 is essential for specificity, substrate binding and transport<sup>1,181</sup>.

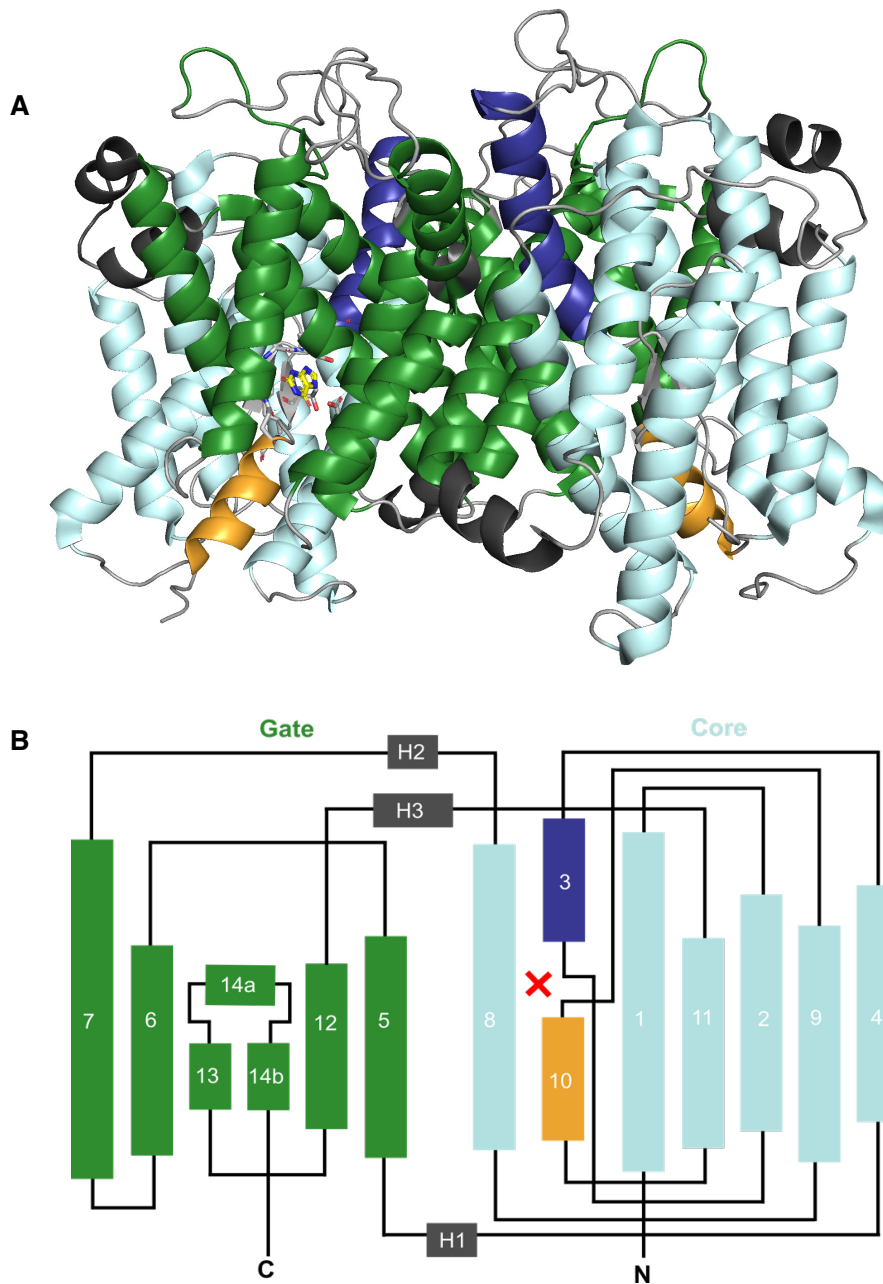


Figure 15: Top, UapA-G411V $\Delta$ <sub>1-11</sub> homodimer<sup>1</sup> coloured according to three key domains: the gate/dimerization domain (green), core/substrate binding domain (blue). The substrate binding includes key residues on TMD8 (blue) and TMD10 (orange). Bottom, Corresponding graphical representation of the transmembrane helices which make up the core and gate domains.

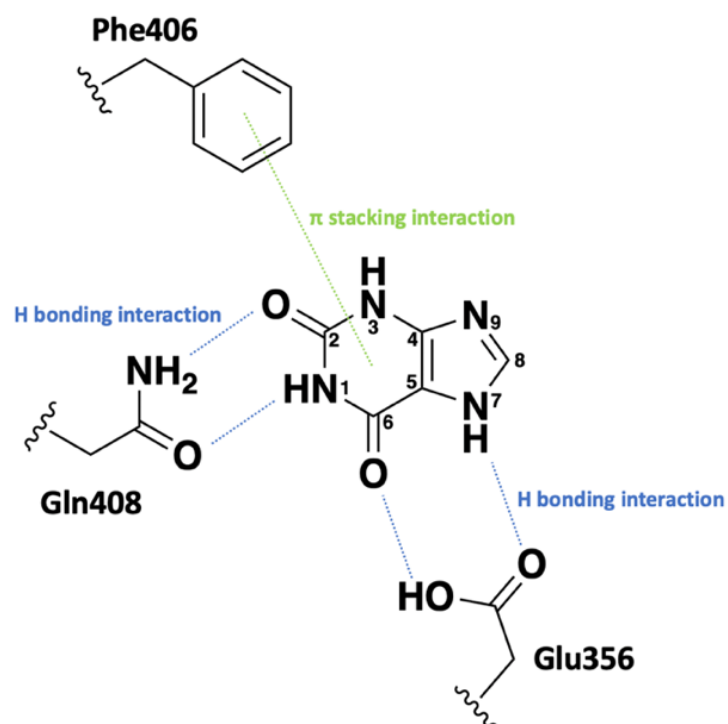
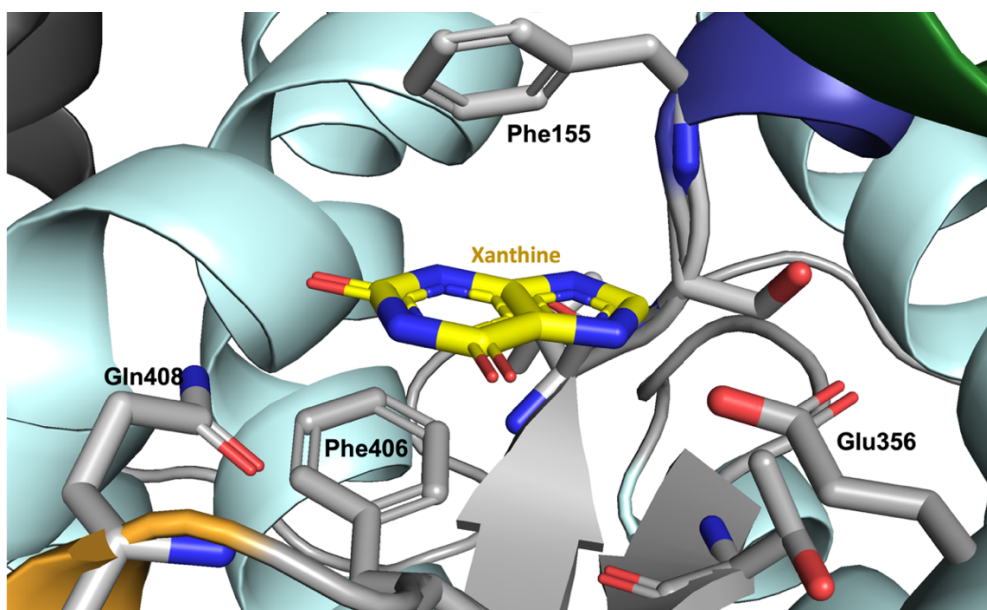


Figure 16: Top, X-ray crystal structure of UapA-G411V $\Delta$ <sub>1-11</sub> in complex with xanthine (yellow) PDB, 5I6C<sup>1</sup>. Key residues Phe155, Glu356 and Gln408 have been highlighted. Bottom, Diagram showing proposed interactions between xanthine and three key residues found in the UapA substrate binding site.

#### 1.3.4. Known substrates of UapA

Previous studies by Diallinas *et al*, have reported the substrate specificity of UapA and a range of other nucleobase transporters present in *Aspergillus nidulans*. UapA shows strong substrate specificity for xanthine and uric acid, but also binds 3-methylxanthine, 2-thioxanthine, oxypurinol, 8-methylxanthine, 9-methylxanthine, 8-azaxanthine, 1-methylxanthine and 6-thioxanthine with decreasing affinity in the range 28–346  $\mu\text{M}$ <sup>182,183</sup> (Table 5). Binding affinities were calculated either by measuring the uptake of labelled substrate ( $K_M$ ) in germinating *Aspergillus nidulans* conidiophores, or in competition with labelled substrate ( $K_I$ ).

UapA shows no significant affinity ( $> 1 \text{ mM}$ ) for purines hypoxanthine, adenine, guanine, 7-methylxanthine and 7-deazaxanthine (Table 5). The complete lack of affinity for hypoxanthine, which differs from xanthine only by replacement of the oxygen donating group at position 2 for a hydrogen, demonstrates the selectivity of UapA for oxidised purines. This is consistent with the crystal structure and interaction profile given in Figure 16, where this carbonyl is important for forming a hydrogen bonding interaction with Gln408. Guanine, like hypoxanthine, lacks a carbonyl capable of forming a hydrogen bonding interaction at position 2. Instead, guanine has a nitrogen group ( $\text{NH}_2$ ) which is a hydrogen bond donor rather than acceptor, disrupting this key interaction.

It is unsurprising that adenine, which like hypoxanthine lacks the carbonyl at position 2 shows no affinity for UapA. Adenine also differs in lacking the carbonyl at position 6, instead having an  $\text{NH}_2$  group. This disrupts the proposed hydrogen bonding interaction this group has with Glu356 in UapA (Figure 16). UapA also shows no affinity for 7-methylxanthine and 7-deazaxanthine. Clearly, removal of this nitrogen (7-deazaxanthine) or modification (7-methylxanthine) removes the ability for this nitrogen to form a hydrogen bonding interaction with Glu356. Interestingly, oxypurinol which lacks the nitrogen at this position, instead having it at position 8, retains binding



affinity for UapA. It may be that oxypurinol is binding with a slightly different conformation than the other substrates, but this is not yet fully understood.

Finally, UapA shows no affinity for the pyrimidines cytosine, thymine and uracil, which all lack the 6,5 ring system common to purines. For example, cytosine, despite being structurally similar to the 6-membered ring of xanthine, lacks the 5-membered ring which has been shown in the crystal structure to form a key hydrogen bonding interaction with Glu356 (Figure 16).

This binding data highlights the importance of a carbonyl or hydrogen bond acceptor group (e.g. S, 2-thioxanthine) at position 2. It has also highlighted the importance of a carbonyl or hydrogen bond acceptor group at position 6. Finally, an unmodified nitrogen at position 7 is crucial, to retain a hydrogen bond interaction with Glu356. There is no binding data to interrogate the importance of the nitrogen at position 1, however the crystal structure suggests that this is forming a key hydrogen bonding interaction with Gln408.

Interestingly, allopurinol, which is known to be transported by UapA, does not possess the nitrogen at position 7, nor the carbonyl at position 2. These are groups that have been suggested to be crucial for UapA binding. However, earlier studies have indicated that allopurinol is transported into fungal cells via an alternative translocation mechanism to xanthine, which may explain why it is not subject to the same substrate specificity constraints<sup>184</sup>.

In order to retain binding affinity of any synthesized purines for UapA, and transport by the main transport mechanism, these structure-activity relationships suggest that positions 1, 2, 6 and 7 should be left unmodified, or modified in a way that retains these key hydrogen bonding interactions.

Table 5: The structures of purine and pyrimidine analogues, and their relative affinities for UapA and mutant UapA-Q408E, where they are available in the literature.

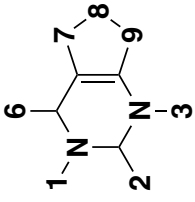
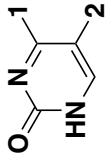
												UapA WT, $K_{M/I}$ / $\mu$ M	UapA Q408E $\Delta$ 1-11, $K_{M/I}$ / $\mu$ M	Transported by UapA?	Elicits UapA turnover?	Ref
	1	2	3	6	7	8	9	1	2							
Xanthine	H	O	H	O	NH	CH	N:				7	16	✓	182		
Uric Acid	H	O	H	O	NH	CO	N:				7	21	✓	182		
3-methylxanthine	H	O	Me	O	NH	CH	N:				28	-	X	183,185		
2-thioxanthine	H	S	H	O	NH	CH	N:				63	-	✓	183,185		
Oxypurinol	H	O	H	O	CH	NH	NH				100	>1000	✓	182		
8-methylxanthine	H	O	H	O	NH	CMe	N:				100	-	-	183		
9-methylxanthine	H	O	H	O	N:	CH	NMe				200	-	-	183		
8-azaxanthine	H	O	H	O	N:	NH	N:				247	-	-	183		
1-methylxanthine	Me	O	H	O	NH	CH	N:				280	-	-	183		
6-thioxanthine	H	O	H	S	NH	CH	N:				346	-	✓	183,185		

Table 5 continued

Allopurinol	:	H	:	H	:	O	CH	NH	NH			*	*	✓	X	184,185
Hypoxanthine	H	H	:	O	N:	O	CH	NH	NH			>1000	71	X	X	182,185
Adenine	:	H	:	NH <sub>2</sub>	N:	NH <sub>2</sub>	CH	NH	NH			>1000	>1000	X	X	182
Guanine	H	NH <sub>2</sub>	:	O	N:	O	CH	NH	NH			>1000	-	X	X	183,185
7-methylxanthine	H	O	H	O	NMe	O	CH	N:	CH			>1000	-	-	-	183
7-deazaxanthine	H	O	H	O	CH	O	CH	NH	NH			>1000	-	-	-	183
Uracil										O	H	>1000	-	X	X	183,185
Thymine										O	Me	>1000	-	X	X	183,185
Cytosine										NH <sub>2</sub>	H	>1000	-	X	X	183,185
Allantoin										Not structurally related to purines or pyrimidines.		>1000	-	X	X	185

#### 1.4. Research Aims

Unlike existing antifungals (see Section 1.1.5), this work proposes to harness integral membrane transporters to specifically transport cytotoxic small molecules into fungal cells, to act on intracellular targets. As discussed in Section 1.2.6, membrane proteins have previously been utilised to mediate cellular uptake of antimicrobials, anti-cancer agents and anti-virals<sup>186</sup>.

The research described in this thesis focuses on Uric Acid Permease (UapA) as a potential drug carrier (Section 1.3.2). This work will use the native substrate of UapA, xanthine, as a scaffold for rational structure-based drug design. This is with the aim of designing xanthine-cytotoxic drug conjugates that can translocate the fungal cellular membrane specifically via the UapA transporter. This approach is similar to that of the bifunctional biologics and molecules described in Section 1.2.5, with xanthine as the specificity element, enabling transport, conjugated to a cytotoxic element. The lack of membrane transporters specific for oxidised purines in human cells, reduces concerns of cross-reactivity of these xanthine-cytotoxic drug conjugates in humans, with cellular uptake specific to fungal cells,

Fortunately, some structure-activity relationship data is already available for the chemical space around xanthine, as summarised in Section 1.3.4. This information, along with the X-ray crystal structure of UapA in complex with xanthine will be used to inform initial small molecule design. Initially, small changes such as the introduction of a benzyl group at different positions on the xanthine scaffold will be made, to assess if bulky groups will be tolerated by UapA's substrate binding site.

Following their synthesis, the toxicity of these analogues will be assessed on *A. nidulans* using *in vitro* fungal growth assays. This work will also aim to functionally and structurally characterise any binding interactions between these novel analogues

and UapA. If these novel analogues bind UapA, it will be important to establish if they are being transported by UapA, or if they act as non-transportable inhibitors, which will be probed using fluorescence microscopy.

Novel analogues that cause *Aspergillus* toxicity and/or bind UapA with high affinity may then be prioritised for structural studies. Better understanding the binding interaction between these novel analogues and UapA will be important in guiding the next round of compound synthesis.

## 2. Design and synthesis of purine analogues

### 2.1. Introduction

As discussed in Section 1.4, this work proposes to harness UapA to either specifically transport small molecules into fungal cells to act on an intracellular target or use UapA as a biomarker, allowing for the direction of cytotoxic elements toward fungal cells. Due to the existence of an X-ray crystal structure of a genetically stabilised mutant of UapA in complex with xanthine, this work has used xanthine as a scaffold for rational structure-informed design. There are multiple strategies that could be taken to achieve either of these objectives, such as a traditional structure-activity relationship (SAR) approach, involving slight structural changes to known ligands (e.g. xanthine) or the construction of drug conjugates.

The construction of drug conjugates is a compelling strategy, and may be likened to other heterobifunctional approaches like antibody drug conjugates (ADCs), drug-hybrids, proteolysis targeting chimeras (PROTACs) or lysosome targeting chimeras (LYTACs)<sup>162</sup>. These bifunctional molecules have been discussed in Section 1.2.5. With the exception of drug-hybrids, all of these therapeutic classes are composed of two major components: a specificity element and an active component. Drug-hybrids, are where two known drugs are combined or hybridised in a single molecule. Drug-hybrids can have key benefits over the non-hybridised, including delayed resistance, reduced toxicity, ease of treatment of co-infection and lower cost of preclinical evaluation<sup>187</sup>.

Whilst none of the above strategies have been utilised for the design of antifungal agents previously, bifunctional approaches may take advantage of the unique landscape that is the fungal cell membrane, using native membrane proteins such as UapA, as biomarkers or drug carriers.

This work proposes to advance knowledge of the fungal transporter UapA, exploring the chemical space around its native substrate xanthine, and moving toward a bifunctional small molecule, composed of a specificity domain with high affinity for UapA, and an active domain, a non-specific cytotoxic component. This may allow for preferential direction of the cytotoxic element toward fungal cells, resulting in an increased local concentration of the cytotoxic compound in proximity of the fungus. This is similar to the principle of ADCs, but in this case, the antibody is replaced by a small molecule which is known to bind with high affinity to a transmembrane protein<sup>1</sup>.

UapA could be harnessed to specifically transport a drug conjugate into fungal cells to act on an intracellular target or be used as a tether, with the drug-conjugate remaining extracellular. It is important to note that membrane proteins have previously been utilised to mediate cellular uptake of antimicrobials, anticancer agents and antivirals<sup>186</sup>. 5FC (see Section 1.1.5.4) is an example of a toxic purine known to be transported by an integral membrane transporter in *Aspergillus*<sup>62</sup>.

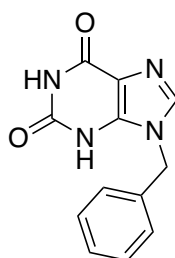
## 2.2. Materials and methods

Compounds **7**, **11** and **18** were commercially available. Unless otherwise stated, all chemicals used were purchased from Sigma Company Ltd (Dorset, UK), Fluorochem Ltd (Derbyshire, UK) and Tokyo Chemical Industry UK Ltd (Oxfordshire UK). Consumables were used as purchased from VWR International Ltd (Leicestershire, UK), Integra Biosciences Ltd (Nottingham, UK) and Sigma-Aldrich Company Ltd (Dorset, UK). Thin Layer Chromatography (TLC) was carried out using silica TLC plates (Si<sub>60</sub>, F254) and visualized with UV light (254 nm, 365 nm). Nuclear magnetic resonance (NMR) spectroscopy collection was carried out using a 400/500 MHz Bruker spectrometer. NMR data analysis was carried out using MestReNova 11.0 (2016). High-resolution mass spectrometry (HRMS) was performed by the Mass Spectrometry Service Centre, Imperial College London.

Protocols and characterisation data for final compounds follow. Relevant spectra can be found in Supplementary Information. Further protocols and characterisation data for intermediates can be found in Supplementary Information.

### 2.2.1. Final products

#### 1: 9-benzyl-3,9-dihydro-1*H*-purine-2,6-dione



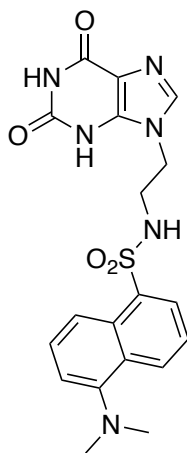
5-amino-1-benzyl-1*H*-imidazole-4-carboxamide (**9**, 0.50 g, 2.3 mmol, 1.0 eq) and 1,1'-carbonyldiimidazole (0.45 g, 2.8 mmol, 1.2 eq) were suspended in THF (10 mL), and the mixture refluxed (70 °C, 17 hours). Crushed ice was added to the



reaction mixture, and the title compound precipitated as a white crystalline powder, which was collected by filtration (27.0 mg, 0.11 mmol, 5%), and washed with ether.

$^1\text{H}$  NMR (400 MHz, DMSO)  $\delta$  12.04 (s, 1H), 10.54 (s, 1H), 7.74 (s, 1H), 7.43 – 7.23 (m, 5H), 5.26 (s, 2H).  $^{13}\text{C}$  NMR (101 MHz, DMSO)  $\delta$  158.7, 137.2, 129.3, 128.3, 127.7, 47.0. HRMS (ESI<sup>+</sup>): calculated for  $\text{C}_{12}\text{H}_{11}\text{N}_4\text{O}_2^+$  243.0882, found 243.0885.

**2**: 5-(dimethylamino)-*N*-(2-(2,6-dioxo-1,2,3,6-tetrahydro-9*H*-purin-9-yl)ethyl)naphthalene-1-sulfonamide

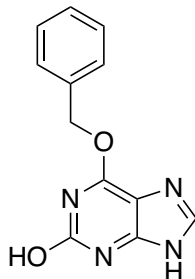


**2** was synthesized via the intermolecular cyclisation of intermediate **10** (50 mg, 0.12 mmol, 1 eq). This followed the protocol reported for the synthesis of compound **1** from intermediate **9**. Compound **2** was obtained as a pale yellow crystalline product (5.32 mg, 0.012 mmol, 10%).

$^1\text{H}$  NMR (400 MHz,  $\text{D}_2\text{O}$ )  $\delta$  8.18 (dd,  $J$  = 8.7, 3.0 Hz, 2H), 8.06 (d,  $J$  = 7.3 Hz, 1H), 7.73 (d,  $J$  = 7.7 Hz, 1H), 7.56 (td,  $J$  = 8.2, 4.0 Hz, 2H), 7.04 (s, 1H), 3.85 (dd,  $J$  = 6.8, 3.8 Hz, 2H), 3.46 (dd,  $J$  = 6.8, 3.8 Hz, 2H), 3.25 (s, 6H).  $^{13}\text{C}$  NMR (101 MHz,  $\text{D}_2\text{O}$ )  $\delta$  140.7, 133.9, 130.4, 127.8, 127.7, 126.7, 126.0, 125.9, 124.4, 118.8, 115.0, 46.5, 43.6, 41.3. (some  $^{13}\text{C}$  environments are not resolved). LCMS (ESI<sup>-</sup>): 5-98%

gradient AcCN/H<sub>2</sub>O, RT 8.30, mass calculated for C<sub>19</sub>H<sub>19</sub>N<sub>6</sub>O<sub>4</sub>S<sup>-</sup> 427.1189, found 427.1227.

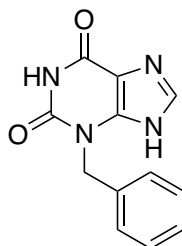
**3:** 6-(benzyloxy)-9*H*-purin-2-ol



Compound **13**, 6-(benzyloxy)-9*H*-purin-2-amine (0.3 g, 1.2 mmol, 1 eq) in acetone (6 mL) was poured into a solution of sodium nitrite (2.5 g) in water (6 mL). Acetic acid (3 mL) was added to the suspension with stirring. Minimum acetone was added to dissolve suspended solid. The pale yellow/green solution was stirred (3 hours, room temperature). The mixture was neutralised with addition of sodium hydroxide (pH 6-8). The aqueous solution was filtered, concentrated in vacuo, and the title compound was obtained following washes with water (0.282 g, 1.2 mmol, 97%).

<sup>1</sup>H NMR (400 MHz, DMSO) δ 13.33 (s, 1H), 11.81 (s, 1H), 8.04 (s, 1H), 7.52 (m, 2H), 7.42 (m, 2H), 7.37 (m, 1H), 5.49 (s, 2H). <sup>13</sup>C NMR (101 MHz, DMSO) δ 159.6, 157.1, 153.4, 141.8, 136.5, 128.9, 128.9, 128.7, 68.0. HRMS (ESI<sup>+</sup>): calculated for C<sub>12</sub>H<sub>11</sub>N<sub>4</sub>O<sub>2</sub><sup>+</sup> 243.0882, found 243.0875

5: 3-benzyl-3,9-dihydro-1*H*-purine-2,6-dione



5,6-diamino-1-benzylpyrimidine-2,4(1*H*,3*H*)-dione (**26**, 50 mg, 0.22 mmol, 1 eq) in formic acid (1 mL) was heated to reflux (1 hour). Formic acid was evaporated in vacuo. The residue was dissolved in aqueous sodium hydroxide (10%, 1 mL) and ethanol (0.3 mL). The mixture was heated to reflux (1 hour), cooled to 0 °C. On acidification of the mixture by addition of hydrochloric acid, a white solid precipitated. The title compound was collected by filtration, washed with water and dried in vacuo (28.1 mg, 0.12 mmol, 55%).

<sup>1</sup>H NMR (400 MHz, DMSO) δ 13.52 (s, 1H), 11.20 (s, 1H), 8.01 (s, 1H), 7.37 – 7.27 (m, 4H), 7.30 – 7.20 (m, 1H), 5.12 (s, 2H). <sup>13</sup>C NMR (101 MHz, DMSO) δ 155.2, 151.5, 149.7, 141.2, 137.6, 128.9, 128.0, 127.8, 107.6, 45.5. HRMS (ESI): calculated for C<sub>12</sub>H<sub>9</sub>N<sub>4</sub>O<sub>2</sub><sup>-</sup>, 241.0720 found 241.0728.

Compounds **4** and **6** were not synthesized in this work.

## 2.3. Results

### 2.3.1. Compound design

The X-ray crystal structure of UapA-G411V $\Delta_{1-11}$  in complex with xanthine (see Section 1.3.3) provides important information regarding the binding mode of xanthine<sup>1</sup>. Xanthine forms  $\pi$ - $\pi$  interactions with the aromatic system of Phe406, and hydrogen-bonding interactions with Glu356 and Gln408 (Figure 17).

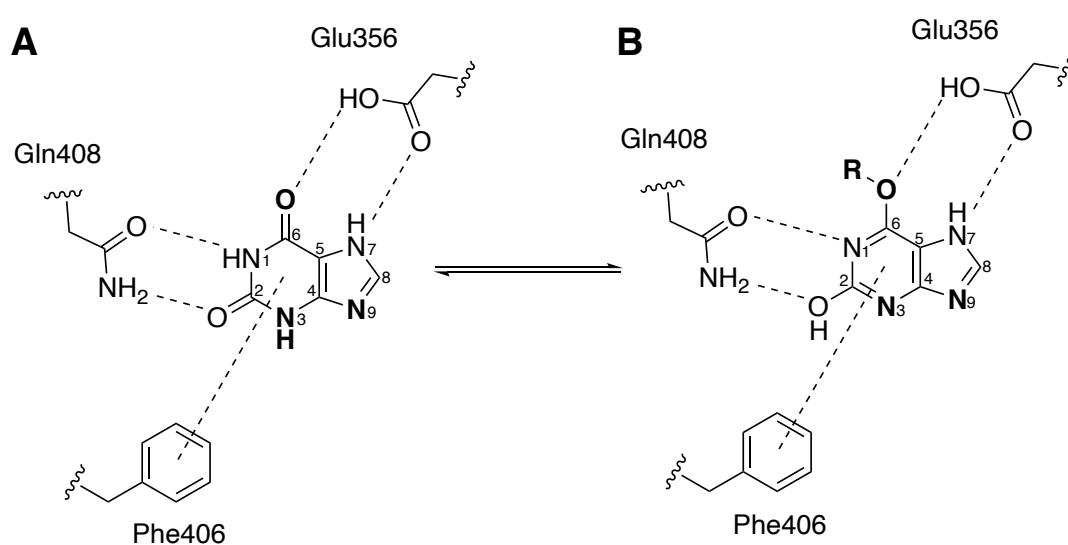


Figure 17: Ligand-protein interaction diagram showing proposed interactions between xanthine and three key residues found in the substrate binding site of UapA, Glu356, Phe406 and Gln408. The purine is planar, due to  $sp^2$  hybridisation. Delocalisation allows for different resonance forms A and B. Potential positions for derivatisation,  $N^3$ ,  $N^9$  and  $O^6$ , are indicated in bold.

As discussed in Section 1.3.3, the carbonyl at position 6, and nitrogen at position 7 seem to form a bidentate hydrogen bonding interaction with the side chain of Glu356. A second bidentate hydrogen bonding interaction is proposed between the nitrogen at position 1, carbonyl at position 2 and the side chain of Gln408 (Figure 17). Crucially, the nitrogen atoms at positions 3 and 9 do not appear to form key interactions with the UapA binding site, and have vectors pointing into the cleft between the substrate-binding site and TMD8. Together with existing binding data

that showed that 3-methylxanthine and 9-methylxanthine retain some specificity for UapA (28  $\mu\text{M}$  and 200  $\mu\text{M}$  respectively), positions 3 and 9 have been proposed as suitable positions on the heterocycle for derivatisation<sup>183,185</sup> (Figure 18).

Position 6 is another proposed position on the heterocycle for derivatisation. A carbonyl or sulfur at position 6 is shared by all strong substrates of UapA (< 1 mM). The carbonyl is known to be essential for forming a key hydrogen bonding interaction with Glu356 (Figure 17). However due to the delocalised  $\pi$ -system of these purine analogues, it is possible to derivatise at this position through an ether linkage, whilst not interrupting this key hydrogen bonding interaction (Figure 18).

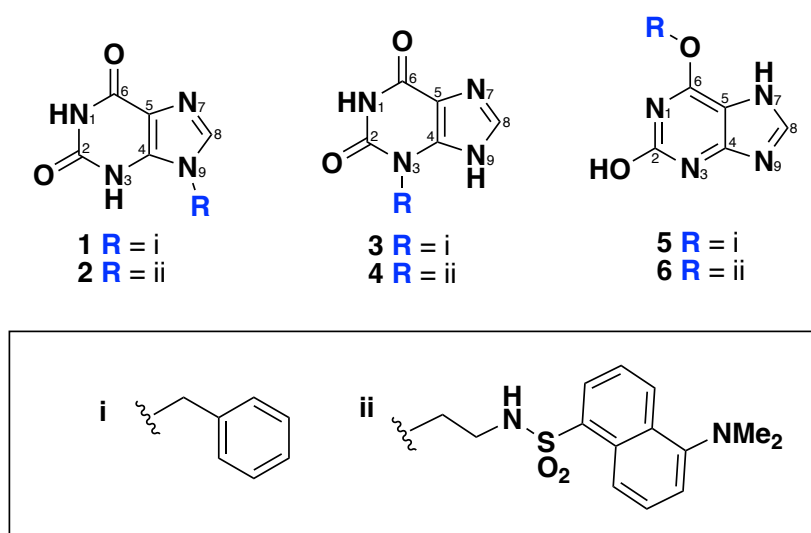


Figure 18: Structures of proposed xanthine analogues. Compounds **1** and **2** are derivatised at position N<sup>9</sup>. Compounds **3** and **4** are derivatised at position O<sup>6</sup>, and Compounds **5** and **6** are derivatised at position N<sup>3</sup>. Compounds **1**, **3** and **5** have a benzyl group (i) introduced, while **2**, **4** and **6** have a dansyl fluorophore joined via an ethyl linker (ii).

Initially, it was pertinent to establish whether large functional groups can be tolerated at these three positions (N<sup>9</sup> O<sup>6</sup> and N<sup>3</sup>). This would determine the strategy taken – whether to form larger drug conjugates, or make smaller SAR type changes to the xanthine scaffold. To this end, 6 target molecules were identified: Compounds **1**, **3** and **5** have a benzyl moiety at positions N<sup>9</sup> O<sup>6</sup> and N<sup>3</sup> respectively (Figure 18).

Compounds **2**, **4** and **6**, have a proposed dansyl fluorophore attached at the same positions via an ethylenediamine linker (Figure 18). A xanthine-fluorophore conjugate may enable direct visualisation of the cellular localisation of these molecules using fluorescence. If these compounds bind and/or are still transported by UapA, this could allow for the establishment of fluorescence-based competitive transport assays, a more accessible and safer alternative to existing radioactivity-based competitive transport assays<sup>178</sup>, described in Chapter 3. In addition, uptake of these molecules may be visible using fluorescence confocal microscopy.

The dansyl group ( $\lambda_{\text{exc}}/\lambda_{\text{em}} \approx 360/450$  nm) was the fluorophore of choice, due to its demonstrated versatility and propensity for live-cell imaging<sup>188,189</sup>. The dansyl group (fused 6, 5) is, amongst coumarin (fused 6, 6) and nitrobenzoxadiazole (NBD, fused 6, 5), one of the smaller fluorophores available (Figure 19). This is preferable due to the compact nature of the substrate binding site in UapA. An ethylenediamine linker was preferred over a more rigid conjugated system, since this would allow the compound more 3-dimensional flexibility, offering it a better chance of being accommodated in the UapA binding site. Future work may involve varying the linker, but also varying the choice of fluorophore. While dansyl fluorophores typically have excitation and emission wavelengths of 360 nm and 450 nm respectively, the NBD fluorophore fluoresces toward the infrared, at higher wavelengths ( $\lambda_{\text{exc}}/\lambda_{\text{em}} \approx 467/539$  nm). This would be an interesting choice, allowing for co-visualisation with GFP.

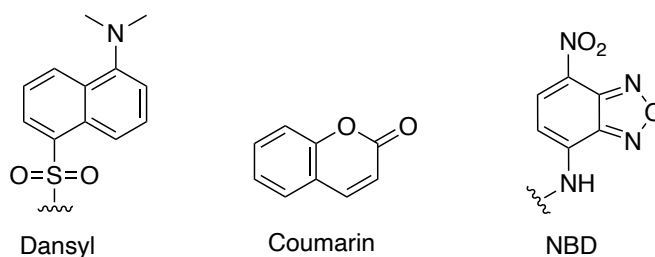


Figure 19: Chemical structures of the dansyl (fused 6,6 ring system; 360/450 nm), coumarin (fused 6,6 ring system) and NBD (fused 6,5 ring system; 467/539 nm) fluorophores (approximate  $\lambda_{\text{exc}}/\lambda_{\text{em}}$ ).

Initial work involved establishing synthetic routes for the planned xanthine analogues, focussing on derivatisation at positions N<sup>9</sup> (Compound **1** and **2**), O<sup>6</sup> (**3** and **4**), and N<sup>3</sup> (**5** and **6**). The structures of the intended compounds are given in Figure 18. The synthetic routes and their optimisation are outlined in Section 2.3.2.

## 2.3.2. Synthesis

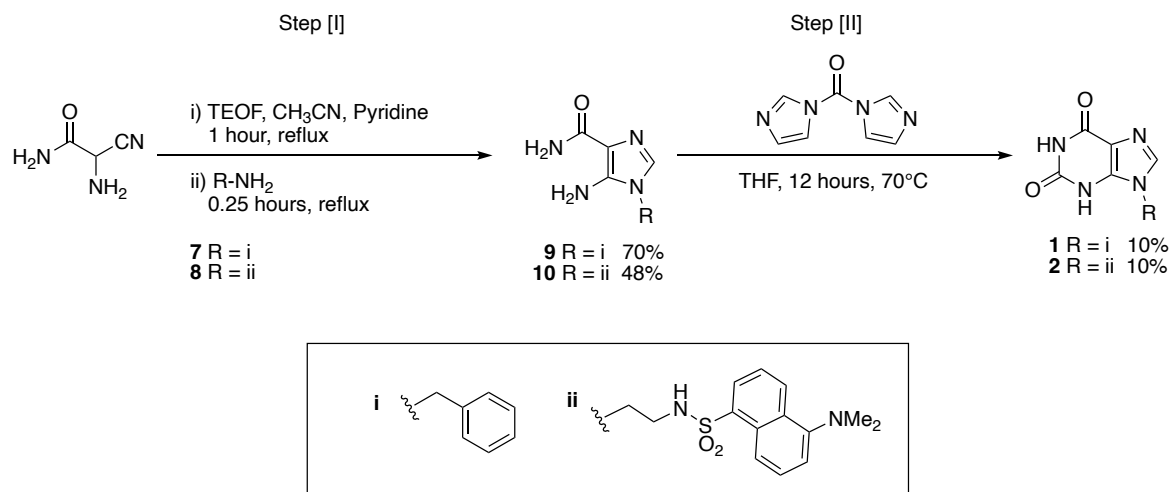
### 2.3.2.1. Derivatisation at position N<sup>9</sup>

The general route proposed for derivatisation at position N<sup>9</sup> involved the formation of the key 5-amino-1-substituted-imidazole-4-carboxamide intermediates using various amines (**7** or **8**), 2-amino-2-cyanoacetamide, and triethyl orthoformate as raw materials, as reported in the literature<sup>190</sup>, and generalised in Scheme 1. Initially, 2-amino-2-cyanoacetamide was refluxed with triethyl orthoformate in acetonitrile, with pyridine as a catalyst, followed by the later addition of the respective amine (**7** or **8**). This work gave the 5-amino-1-substituted-imidazole-4-carboxamide predecessors (**9** and **10**) to Compounds **1** and **2** in 70% and 48% yield respectively.

While the initial amine for **1**, benzyl alcohol (**7**), was commercially available, the starting amine **8** was formed in a nucleophilic substitution reaction of ethylenediamine with dansyl chloride in dichloromethane (DCM) with triethylamine as base (Scheme 2) in 75% yield.

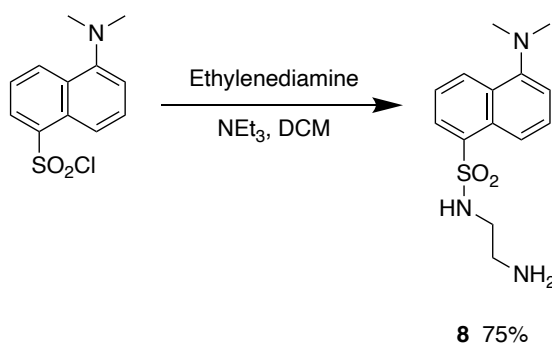
In the literature, following their formation, these 5-amino-1-substituted-imidazole-4-carboxamide intermediates were cyclised under reflux with sodium methoxide, to form the hypoxanthine scaffold<sup>190</sup>. However, hypoxanthine lacks the carbonyl at position C<sup>2</sup> known to be crucial for hydrogen bonding with Gln408 (Figure 17). Instead, the 5-amino-1-substituted-imidazole-4-carboxamide intermediates (**9** and **10**) used 1,1'-carbonyldiimidazole (CDI) in tetrahydrofuran (THF) at 70 °C to form the asymmetrical urea scaffold present in compounds **1** and **2** (Scheme 1). While these conditions have not been reported for cyclisation of this 5,6-fused ring scaffold before, they have been reported for the formation of related 6,6-fused ring systems<sup>191,192</sup>. Fast hydrolysis of CDI was countered by addition of further equivalents, until the reaction appeared completed by thin layer chromatography (TLC). Despite this, the cyclisation was poorly yielding (10%) for synthesis of compound **1** and **2**.





Scheme 1: Synthetic route for Compound **1** (R = i, benzyl) and **2** (R = ii, 5-(dimethylamino)-N-ethylnaphthalene-1-sulfonyl). Step [I] involves the formation of 5-amino-1-substituted-imidazole-4-carboxamide intermediates (**9**, **10**) using various amines (**7**, **8**), 2-amino-2-cyanoacetamide, and triethyl orthoformate as raw materials, in a protocol adapted from literature<sup>190</sup>. Step [II] involved intermolecular cyclisation of intermediates (**9**, **10**) with 1,1'-carbonyldiimidazole (CDI) in tetrahydrofuran (THF) at 70 °C to yield final purine analogues **1** and **2**.

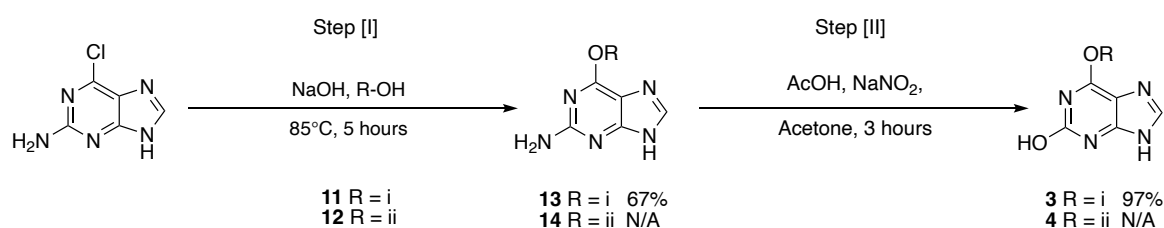
If functional (Chapter 3) and structural (Chapter 4) characterisation of **1** and **2** indicate that that position N<sup>9</sup> is a valuable point of derivatisation, further work would be invested in optimisation of this step. This may involve simply changing solvents and reaction temperatures, but may also involve the use of more harsh ring closing reagents, such as urea or triphosgene<sup>193,194</sup>. Urea in particular has been well reported for these cyclisations, but was avoided in this work due to the harsh conditions (200 °C) often required for reaction completion<sup>193</sup>. Phosgene and triphosgene were also avoided in favour of CDI, due to their significantly higher toxicity<sup>195</sup>.



Scheme 2: Synthesis of the starting amine **8** involved a nucleophilic substitution reaction of ethylenediamine with dansyl chloride in dichloromethane (DCM) with triethylamine as base.

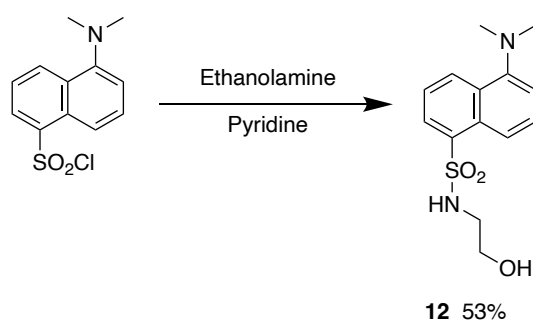
### 2.3.2.2. Derivatisation at position O<sup>6</sup>

For derivatisation at position 6 (Compounds **3** and **4**), an initial synthetic route was designed (Scheme 3) where the substituted alcohol (**11** or **12**) is used to displace the chloride ion of 6-chloroguanine in a nucleophilic aromatic substitution reaction (S<sub>N</sub>Ar). Similar S<sub>N</sub>Ar reactions have been reported in literature for simple alkoxides using sodium hydroxide<sup>196</sup>. The S<sub>N</sub>Ar reaction was followed by an oxidation using sodium nitrite and acetic acid in acetone, which oxidised position C<sup>2</sup>, to convert from the guanine-like scaffold (**13**) to the xanthine-like scaffold (**3**), as previously reported<sup>197</sup>. The S<sub>N</sub>Ar reaction and subsequent oxidation was successful for the synthesis of **3**, with yields of 67% and 97% for each step.



Scheme 3: Proposed synthetic route for **3** (R = i, benzyl) and **4** (R = ii, 5-(dimethylamino)-N-ethylnaphthalene-1-sulfonamide). Step [I] involves displacement of the chloride ion of 6-chloroguanine in a nucleophilic aromatic substitution (S<sub>N</sub>Ar) by derivatised alkoxides (**11** or **12**), in a protocol adapted from literature<sup>196</sup>. Step [II] involves oxidation of the guanine-like scaffolds **13** and **14** at position 2 using sodium nitrite and acetic acid in acetone<sup>197</sup>.

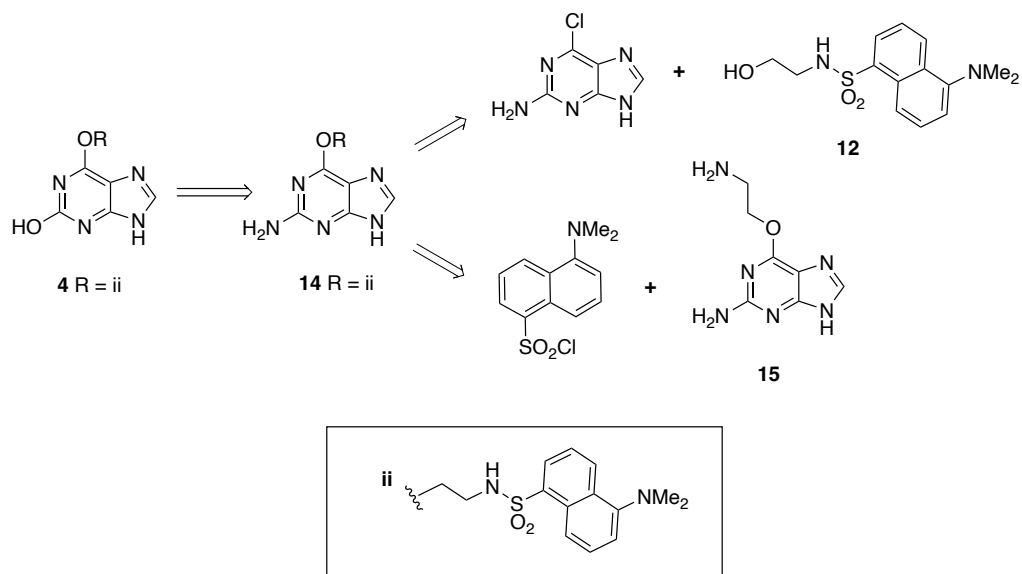
While the substituted alcohol **11** was commercially available, **12** was not. Instead, it was formed in a nucleophilic substitution reaction of ethanolamine with dansyl chloride in pyridine at 53% yield (Scheme 4).



Scheme 4: Synthetic route for compound **12** involved the addition of the ethanolamine linker to the dansyl fluorophore involved a nucleophilic substitution reaction between dansyl chloride and ethanolamine in pyridine (53% yield).

Unfortunately, in the subsequent  $S_NAr$  reaction between **12** and 6-chloroguanine to produce **14** (Scheme 3), there was no consumption of the starting material 6-chloroguanine. It was hypothesized that this was due to poor nucleophilicity of the amine **12**. To combat this, a stronger base and solvent combination was used: sodium hydride (NaH) in dimethylformamide (DMF). However, there was still no evidence of substitution by nuclear magnetic resonance (NMR).

To counter this, the order of these two steps was changed; adding the ethanolamine linker to the purine scaffold first to produce **15** and following it with the addition of the fluorophore (Scheme 5).



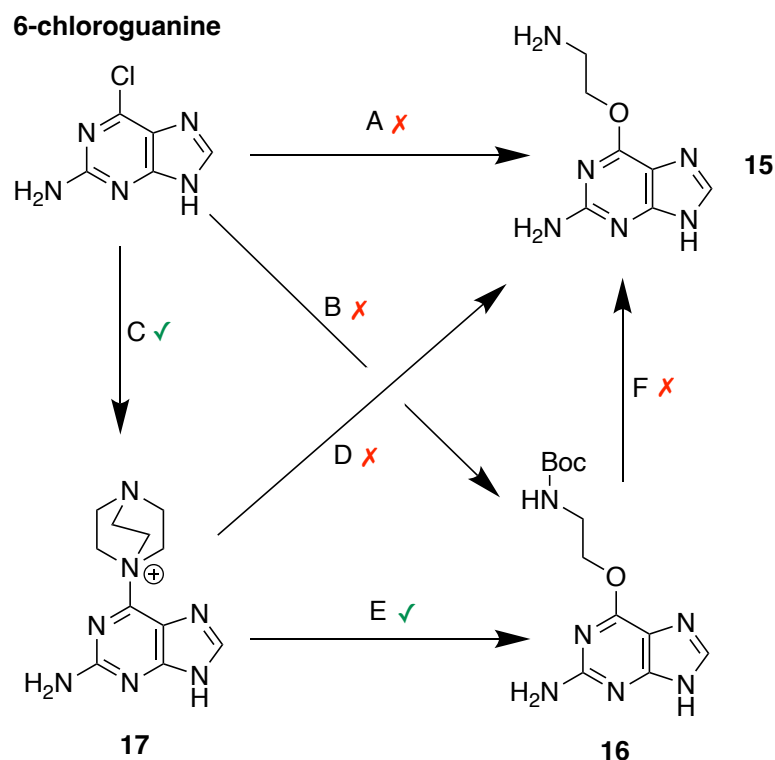
Scheme 5: Partial retrosynthetic analysis for the synthesis of **4**, from key intermediate **12**, or **15**. The original synthetic route outlined in Scheme 3 involved addition of the ethanolamine linker to the dansyl group first, producing intermediate **12**. The new synthetic route instead involves addition of the ethanolamine linker to the purine scaffold first, to produce the new intermediate **15**.

To this end, the nucleophile was exchanged for ethanolamine, keeping sodium hydride as base, and 1,4-dioxane as solvent, but no consumption of 6-chloroguanine was observed (Reaction A, Scheme 6). Ethanolamine was exchanged for *N*-Boc ethanolamine, keeping sodium hydride as base, and 1,4-dioxane as solvent, to produce the Boc-protected analogue of **15**, **16** (Reaction B, Scheme 6). Again, no consumption of 6-chloroguanine was observed. In these reactions, it became clear that solubility of 6-chloroguanine in 1,4-dioxane may be a contributing factor. However, following changing the base and solvent combination, compound **16** was still not successfully isolated. TLC indicated that there had been no consumption of 6-chloroguanine using sodium hydride in dimethylformamide, despite the addition of excess *N*-Boc ethanolamine.

An alternative approach used was to improve the leaving group of the S<sub>N</sub>Ar reaction. Following a protocol reported in literature, a DABCO-purine **17** was formed, which has been shown to undergo facile displacement reactions with alkoxides to

form the desired 6-oxy-substituted purines<sup>198</sup> (Reaction C, Scheme 6). This was performed as reported in literature, in DMSO, with the product filtered off as a precipitate with 98% yield. The subsequent displacements with various alkoxides (ethanolamine or N-Boc ethanolamine) were performed in DMSO with NaH as a base, at room temperature (Reaction D or E, Scheme 6). Using these conditions there was still no displacement of the DABCO leaving group. Upon slowly raising the temperature to 100 °C, there was finally displacement of the DABCO group by N-Boc ethanolamine yielding the intermediate **16** at a 12% yield (Reaction F, Scheme 6). The rounds of optimisation for this S<sub>N</sub>Ar reaction can be found summarised in Table 6.

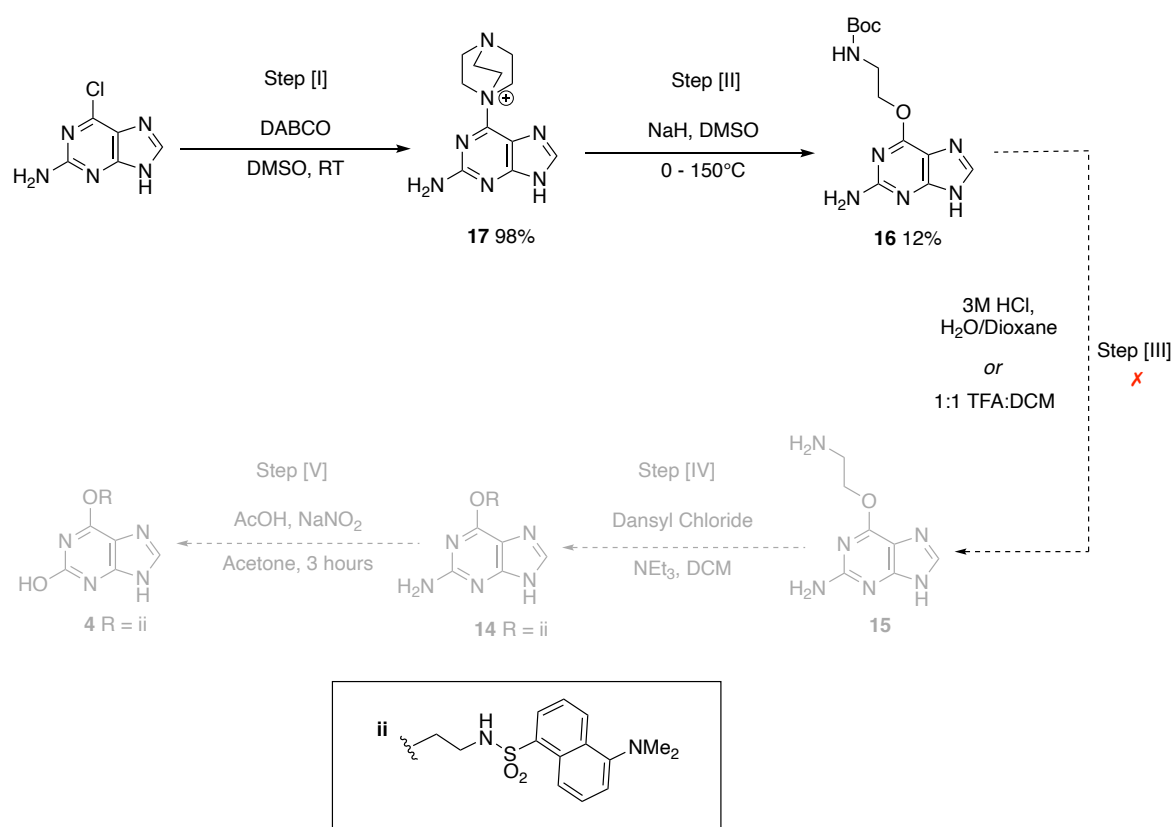
However, the subsequent deprotection to produce key intermediate **15** proved challenging, with apparent degradation of **16** following treatment with 3M hydrochloric acid in dioxane or water (Reaction F, Scheme 6). The alternative deprotection condition of 5 eq trifluoroacetic acid in dichloromethane, also appeared to result in degradation of the starting material. Further exploration around milder deprotection conditions, perhaps potassium carbonate (K<sub>2</sub>CO<sub>3</sub>), is required. A proposed synthetic route for future optimisation is presented in Scheme 7. Ultimately, if simple alkoxide linkers are not synthetically tractable, then alternative linkage types could also be explored at this position. Unfortunately, this optimisation could not be completed within this funding period.



Scheme 6: A and B, The desired route for the addition of the ethanolamine or N-Boc ethanolamine linker to 6-chloroguanine to produce **15** or **16** respectively was unsuccessful. C, The displacement of the chlorine for a DABCO group to produce key intermediate **17** was successful. D, The subsequent displacement of the DABCO group of **17** by the ethanolamine linker to produce **15** was unsuccessful. E, There was ultimately successful displacement of the DABCO group of **17** by N-Boc ethanolamine to produce **16**. F, The subsequent deprotection of **16** to produce **15** was unsuccessful. The reactants and condition combinations used for S<sub>N</sub>Ar replacements (A, B, D and E) are summarised in Table 6.

Table 6: Reactants and condition combinations used for S<sub>N</sub>Ar replacement of leaving group chloride ion or DABCO ion, to form O<sup>6</sup>-linked moieties.

	Electrophile	Nucleophile	Base	Solvent	T/ °C	Observation
N/A	6-chloroguanine	<b>12</b> , 1.2 eq R-OH	NaOH	AcCN	90	No consumption of 6-chloroguanine
N/A	6-chloroguanine	<b>12</b> , 1.2 eq R-OH	NaH	DMF	100	No consumption of 6-chloroguanine
A	6-chloroguanine	5.0 eq ethanolamine	NaH	Dioxane	90	No consumption of 6-chloroguanine
B	6-chloroguanine	Ex. N-Boc ethanolamine	NaH	Dioxane	90	No consumption of 6-chloroguanine
B	6-chloroguanine	Ex. N-Boc ethanolamine	NaH	DMF	100	No consumption of 6-chloroguanine
D	<b>17</b> . 6-DABCO guanine	Ex.ethanolamine	NaH	DMSO	0-100	No consumption of 6-DABCO guanine
N/A	<b>17</b> . 6-DABCO guanine	<b>12</b> , 1.2 eq R-OH	NaH	DMSO	0-100	Trace intermediate <b>14</b> found by LCMS
E	<b>17</b> . 6-DABCO guanine	Ex. N-Boc ethanolamine	NaH	DMSO	0-100	12% yield of desired intermediate <b>16</b>



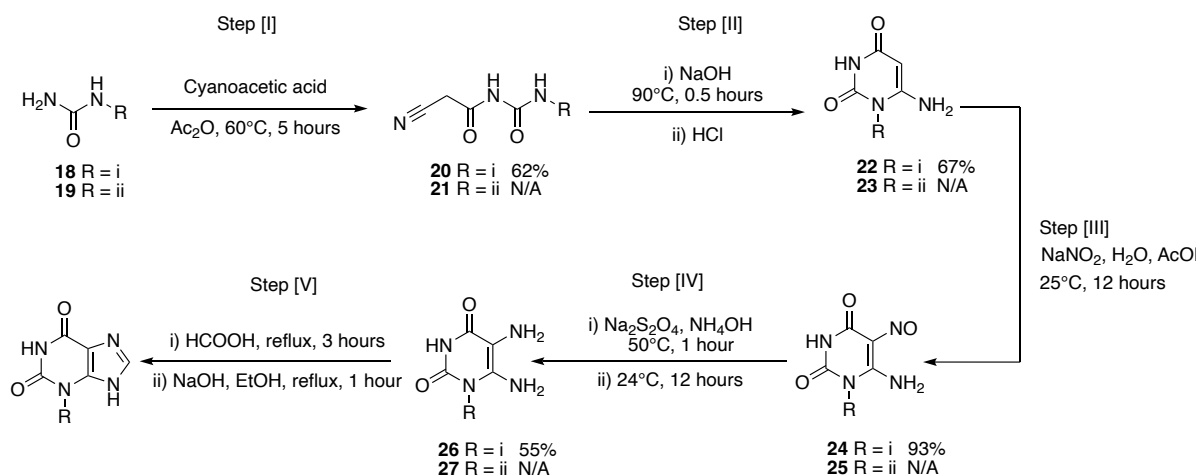
Scheme 7: Progress of synthetic route optimisation for Compound **4** (R = ii, 5-(dimethylamino)-N-ethylnaphthalene-1-sulfonamide). Step [I] involved displacement of chloride of 6-chloroguanine by DABCO to produce the DABCO-purine **17** in 98% yield. The DABCO group was subsequently displaced in Step [II] by a Boc-protected ethanolamine in a nucleophilic aromatic substitution (S<sub>N</sub>Ar) to produce the key intermediate **16** in 12% yield. The proposed subsequent steps [III], [IV] and [V] were not successfully completed due to apparent degradation of intermediate **16** in Step [III].

### 2.3.2.3. Derivatisation at position N<sup>3</sup>

Finally, derivatisation of xanthine at position N<sup>3</sup> to synthesise compound **5** followed an established synthetic route<sup>199</sup>, which detailed formation of derivatised xanthines (Scheme 8) from asymmetrical in four steps.

The formation of the initial asymmetrical urea **20** had not yet been reported for primary amides like 2-cyanoacetamide but was achieved in 62% yield using reported asymmetrical urea formation conditions<sup>200</sup>. The asymmetrical urea **20** was cyclised with sodium hydroxide to afford the desired 1-alkyl-5,6-diaminouracil **22** in 67% yield<sup>199</sup> (Scheme 8, Step II). This was followed by nitrosation at position C<sub>5</sub> of the pyrimidine ring of **22** with sodium nitrite in acetic acid to give **24** in 93% yield (Scheme 8, Step III). The nitroso group of **24** was subsequently reduced with sodium dithionite to the respective 6-aminouracil **26** in 55% yield (Scheme 8, Step IV). The intermediate **26** was then refluxed with formic acid to give an amide intermediate, followed by cyclization in sodium hydroxide, to afford the desired xanthines **5** in 55% yield<sup>199</sup> (Scheme 8, Step V).





Scheme 8: Progress of synthetic route optimisation for Compound **5** (R = i, benzyl) and proposed synthetic route for **6** (R = ii, 5-(dimethylamino)-N-ethylnaphthalene-1-sulfonamide). Step [I] involved formation of a substituted asymmetrical urea (**20**), which underwent an intramolecular cyclisation in Step [II] to produce **22**. Subsequent steps [III] [IV] involve insertion of a nitroso group (**24**), and subsequent reduction to the amines (**26**). In step [V], **26** underwent intermolecular cyclisation with formic acid to give **5**<sup>199</sup>. The analogous synthesis of Compound **6** not completed in this work due to time constraints.

Unfortunately, due to COVID-19, and limited time available, the analogous synthesis of Compound **6** was not completed. Rather than focussing on synthesis, the functional, binding and structural characterisation of synthesized analogues was prioritised.

## 2.4. Discussion

The X-ray crystal structure of UapA-G411V $_{\Delta 1-11}$  in complex with xanthine has provided invaluable information regarding the binding mode of xanthine.<sup>1</sup> This has enabled the structure guided design of analogues of the native substrate xanthine. Based upon the available crystal structure and existing binding data for methylated xanthine molecules<sup>183,185</sup>, positions N<sup>3</sup>, O<sup>6</sup> and N<sup>9</sup> were considered potential vectors on the xanthine heterocycle for derivatisation.

The benzylated xanthine series (Compound **1**, **3** and **5**) were synthesized successfully following the adaption of protocols existing in literature and their subsequent optimisation.

Compound **1** was synthesized in 2 steps, with an overall yield of 7%. Compound **2** was synthesized in 3 steps with an overall yield of 3%. Despite the low overall yields, derivatisation at position N<sup>9</sup> of xanthine appears to be synthetically tractable. The low yields of compounds **1** and **2** were primarily caused by poor yields in the final step: the intermolecular cyclisation with CDI (10%, Step [II], Scheme 1). As discussed in Section 2.3.2.1, improving the yield of this step may involve simply changing solvents and reaction temperatures, but may also involve the use of more harsh ring closing reagents, such as urea or triphosgene<sup>193,194</sup>.

Compound **3** was synthesized in 2 steps with an overall yield of 65%, following an established protocol<sup>198</sup>. The synthesis of compound **4** proved more challenging. Extensive optimisation around reaction conditions and different nucleophile–electrophile combinations produced the key intermediate **16**. Further exploration around milder deprotection conditions, perhaps potassium carbonate (K<sub>2</sub>CO<sub>3</sub>), is required.

A proposed synthetic route for future optimisation is presented in Scheme 7. Ultimately, if simple alkoxide linkers continue to prove synthetically challenging, then alternative linkage types could also be explored at this position.

Compound **5** was synthesized in 5 steps as described in literature<sup>199</sup>, with an overall yield of 12%. Yields for each step varied between 55–93%. Synthesis of compounds with an attached dansyl fluorophore (Compound **2**, **4** and **6**) proved more challenging. Compound **6** was not synthesized in this work.

Future work may involve continued optimisation of the synthetic routes for these two remaining compounds. This work prioritised the functional, binding, and structural characterisation of compounds **1**, **2**, **3** and **5**, and **13**.

## 3. Functional characterisation of nucleotide analogues

### 3.1. Introduction

As described in Chapter 2, the benzylated xanthine compounds (**1**, **3** and **5**) were synthesized successfully, following the adaption of protocols existing in literature and their subsequent optimisation, Compound **2**, which has a dansyl fluorophore conjugated at position N<sub>9</sub> and the synthetic precursor to Compound **3**, compound **13**, were all successfully synthesized. Structures of the synthesized analogues (Figure 20) were confirmed using nuclear magnetic resonance (NMR) and high resolution mass spectrometry (HRMS).

This chapter describes the functional characterisation of these analogues; it is important to understand how these new analogues interact with UapA, if at all. Initially, competitive uptake assays using <sup>3</sup>H-xanthine were used to determine if these compounds inhibit xanthine uptake, through either competitive, non-competitive or uncompetitive inhibition (Section 3.3.1). Fungal growth assays were used to determine if any of the synthetic analogues were toxic to strains of *Aspergillus nidulans*, and if this toxicity is dependent on UapA or other nucleobase transporter (UapC, AzgA, FurD, FurA, FcyB, CntA) expression (Section 3.3.2). It was then important to understand if these analogues are being transported by UapA, which was probed using fluorescence microscopy (Section 3.3.3).

Finally, if these analogues are found to bind to UapA, it was important to know if they stabilise or destabilise the protein. A number of thermostability techniques including cellular thermal shift assays (CETSA), fluorescence size exclusion chromatography (FSEC), nano-differential scanning fluorimetry (nano-DSF) and thermal denaturation analysis using CPM, a thiol-reactive fluorescent probe, have been used in this work to determine the stability of UapA and thermostabilised mutants in different environments (Section 3.3.4 and 3.3.5).

Where appropriate, commercially available purine analogues (Figure 20) have been included for comparison: xanthine, hypoxanthine, uric acid, 1-methylxanthine, 3-methylxanthine, 7-methylxanthine, 2-thioxanthine, 6-chloroguanine, allopurinol, oxypurinol, 5-fluorocytosine, and 5-fluorouracil.

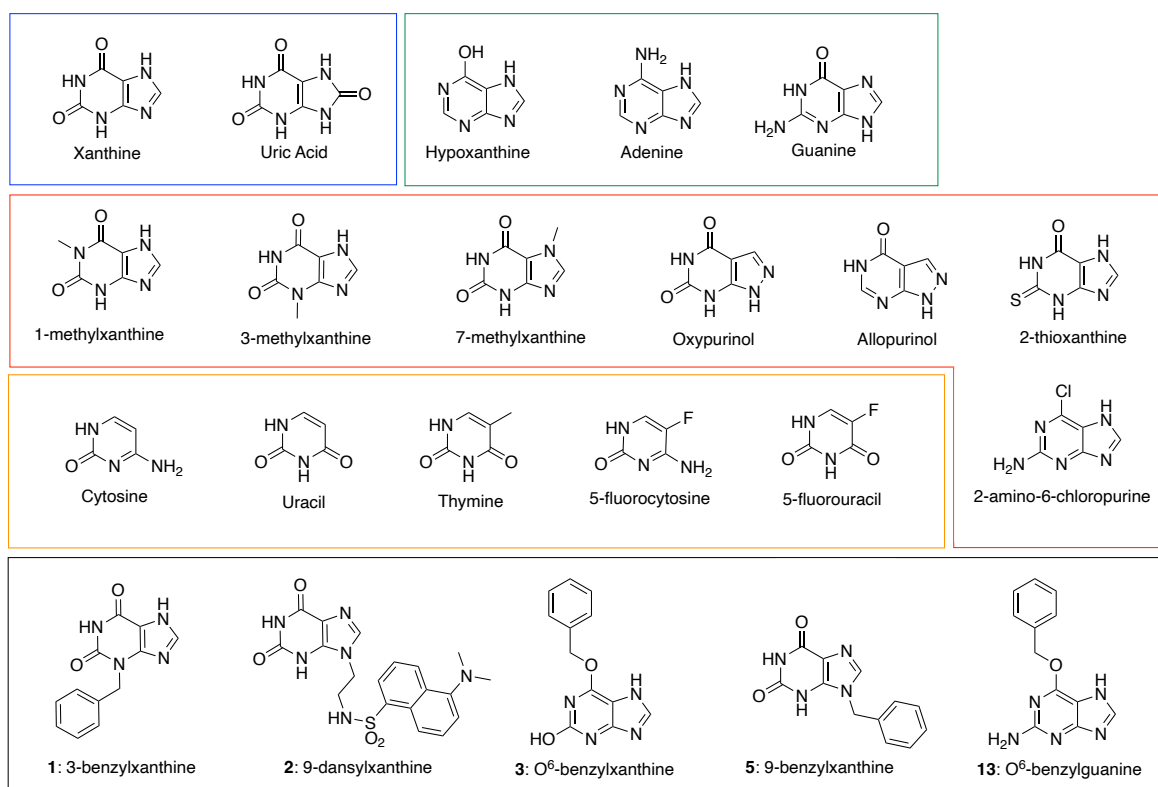


Figure 20: Chemical structures of native UapA substrates (blue), commercially available purine (red) and pyridine (orange) analogues, and newly synthesized purine analogues (black), which are under discussion in this chapter.

## 3.2. Materials and Methods

### 3.2.1. <sup>3</sup>H-xanthine competitive uptake assay

Unfortunately, the following experiment could not be completed by myself at Imperial College London. Due to COVID-19, I was unable to travel to our collaborator's lab, where they have an appropriate set up for working with radiolabelled substrates. Consequentially, the following work was kindly completed by our collaborator Professor George Diallinas in the Department of Biology at the National and Kapodistrian University of Athens. This followed an established protocol for Transport Assays in *Aspergillus nidulans*<sup>201</sup>, detailed below for completion.

The strain used in this work was  $\Delta$ ACZ pAN510-GFP, which contains loss-of-function mutations in the three major purine transporters AzgA, UapC and UapA, in addition to a genetically non-identified mutation *fur<sup>R</sup>* that results in 5-fluorouracil resistance and lack of uracil uptake capacity<sup>171</sup>. A UapA-GFP fusion was then reintegrated at the genomic *uapA*- locus by homologous recombination<sup>202</sup>.

Minimal media (MM) glucose petri dishes were inoculated with the *A. nidulans* strain of interest, and incubated for 96 hours at 37 °C. A quarter of the full colony was resuspended in 0.01% v/v Tween<sup>®</sup> 80 in water (2 mL). The sample was vortexed to separate the conidiospores, filtered through a nylon net filter (60  $\mu$ M), and used to inoculate a 100 mL secondary MM culture (1% glucose, 10 mM NaNO<sub>3</sub>). Additional supplements and concentrations for *A. nidulans* strains follow those published by the Fungal Genetics Stock Centre. This culture was incubated for 3–5 hours (37 °C, 140 RPM) to allow the germinating conidiospores to reach germ tube emergence.

Conidiospores were collected by centrifugation (5 minutes. 3000 g, room temperature). The supernatant was discarded, and the pellet resuspended in 5 mL

MM. The spore suspension was aliquoted (75  $\mu$ L) and incubated for 5 minutes at 37  $^{\circ}$ C prior to the addition of the radiolabelled substrate  $^3$ H-xanthine (25  $\mu$ L in water).

A mixture of  $^3$ H-xanthine and unlabelled substrate of interest was added, and the experiment incubated at 37  $^{\circ}$ C for 60 seconds. The transport reaction was stopped by adding an equal volume (100  $\mu$ L) of unlabelled xanthine at 100–1000 $\times$  excess concentration relative to the radiolabelled substrate, and transferred to ice. The samples were centrifuged (11000 g, 3 minutes, 4  $^{\circ}$ C), the supernatant removed by aspiration under vacuum, and the pellet was washed with ice cold MM (1 mL), centrifuged (11000 g, 3 minutes, 4  $^{\circ}$ C). Again, the supernatant was removed, and the pellet resuspended in scintillation fluid (1 mL). The eppendorfs were transferred to scintillation vials, and a scintillation counter used to measure substrate accumulation in the cells.

To determine  $K_i$  values, different substrate concentrations were used with a fixed incubation time of 60 seconds. The stock solutions were prepared containing a fixed concentration of  $^3$ H-xanthine and increasing concentrations of non-radiolabelled substrates. Each measurement at each concentration was performed in triplicate. To calculate initial uptake rates, radioactive counts were converted to substrate concentration/minute/conidiospores. Initial uptake rates were plotted against concentration. Competitive inhibition was expected;  $K_i$  measurements were determined by estimating IC50 values (inhibitor concentration for obtaining 50% inhibition).  $K_i = IC50 / (1 + [S]/K_M)$ , where [S] is the fixed concentration of radiolabelled substrate used and  $K_M$  is the Michaelis-Menten constant.  $K_i$  values were approximated as IC50 values since the [S] is low, at least 10-fold lower than the  $K_M$ .

### 3.2.2. *Aspergillus nidulans* growth assays

Strains of *Aspergillus nidulans* used in this work were obtained from Professor George Diallinas' laboratory at National & Kapodistrian University of Athens. These include the *WT*,  $\Delta 7$ ,  $\Delta ACZ$  and  $\Delta ACZ$  pAN510GFP strains, whose transporter expression ( $\checkmark$ ) and knockout ( $X$ ) patterns are summarised in Table 7.  $\Delta ACZ$  and  $\Delta ACZ$  pAN510-GFP (see Section 3.2.1) strains contain loss-of-function mutations in the three major purine transporters AzgA, UapC and UapA, in addition to a genetically non-identified mutation *fur<sup>R</sup>* that results in 5-fluorouracil resistance and lack of uracil uptake capacity<sup>171</sup>.

Table 7: Summary of transporter presence ( $\checkmark$ ) and absence ( $X$ ) in the four *Aspergillus nidulans* strains. \*This strain has a loss-of-function mutation in UapA, with a functional UapA-GFP fusion construct reintegrated at the genomic *uapA*- locus by homologous recombination.

		Transporter						
		UapA	UapC	AzgA	FurD	FurA	FcyB	CntA
Strain of <i>Aspergillus nidulans</i>	WT	$\checkmark$	$\checkmark$	$\checkmark$	$\checkmark$	$\checkmark$	$\checkmark$	$\checkmark$
	$\Delta 7$	$X$	$X$	$X$	$X$	$X$	$X$	$X$
	$\Delta ACZ$	$X$	$X$	$X$	$\checkmark$	$\checkmark$	$\checkmark$	$\checkmark$
	$\Delta ACZ$ pAN510-GFP	$\checkmark^*$	$X$	$X$	$\checkmark$	$\checkmark$	$\checkmark$	$\checkmark$

Depending on the experiment, MM agar with 1% glucose (pH 6.8) was supplemented with a nitrogen source (either 2.5 mM *L*-alanine, 10 mM NaNO<sub>3</sub> or 1 mM purine analogue) and 2 mg/L para-aminobenzoic acid (PABA).

In experiments where toxicity of purine analogues was being assessed, the given purine analogue was added at 100  $\mu$ M, in addition to the primary nitrogen source (2.5 mM *L*-alanine, 10 mM NaNO<sub>3</sub>). Plates were inoculated with spores from the *A. nidulans* strain under investigation and incubated at 25 or 37 °C for 48 or 96 hours respectively.



### 3.2.3. Fluorescence Microscopy

The strain of *Aspergillus nidulans* used for microscopy ( $\Delta$ ACZ pAN510-GFP) was described in Section 3.2.1, and was obtained from Professor George Djalinas' laboratory at National & Kapodistrian University of Athens.

Samples for fluorescence microscopy were prepared using a protocol established in literature<sup>185</sup>. The samples were prepared in untreated 35 mm  $\mu$ -dishes suitable for fluorescence microscopy. Minimal media agar with 1% glucose (pH 6.8) was supplemented with 10 mM NaNO<sub>3</sub> and 2 mg/L PABA. Spores of  $\Delta$ ACZ pAN510-GFP were used to inoculate the cultures, and the cultures incubated for 16 hours at 25 °C. Substrates were added to the now germinating conidiospores, to a final concentration of 100  $\mu$ M. The samples were visualised after 2-4 hours using an Inverted Widefield Microscope with LED illumination Zeiss Axio Observer inverted microscope. Images were acquired with a Hamamatsu Flash 4.0 fast camera using the Zen acquisition software. Images were processed in Fiji ImageJ.

### 3.2.4. Expression of UapA constructs in *S. cerevisiae*

In a protocol previously described, UapA constructs were individually inserted into an SmaI-linearised vector pDDGFP2, and the resultant expression plasmids transformed into a protease-deficient strain of *S. cerevisiae* (FGY217-pep4 $\Delta$ )<sup>1,93,176</sup>. FGY217 cells were grown to OD<sub>600</sub> = 0.6 in YP (50 mL, 2% glucose; 30 °C, 300 RPM), harvested (3724 g, 5 minutes, 4 °C), washed with H<sub>2</sub>O (25 mL) and LiAc (1 mL, 100 mM), and resuspended in LiAc (400  $\mu$ L, 100 mM). The cell suspension (50  $\mu$ L) was added to 50% PEG-3350 (240  $\mu$ L). Carrier DNA (50  $\mu$ g) and the pDDGFP2 vector containing UapA (0.75  $\mu$ g) in water (50  $\mu$ L) was added, the mixture incubated (30 minutes, 30 °C) and heat shocked (25 minutes, 42 °C). Cells were pelleted (8000 g, 15 seconds), resuspended in H<sub>2</sub>O (100  $\mu$ L) and positive transformants selected on -URA. Transformants were grown to OD<sub>600</sub> = 0.6 in -URA drop out media (2% glucose;

30 °C, 300 RPM), and diluted in -URA (0.1% glucose,  $OD_{600}=0.12$ ). Cultures were incubated (30 °C, 300 RPM) until  $OD_{600}=0.6$  and expression induced by addition of 2% galactose. The culture was incubated (30 °C, 300 RPM, 22+ hours), cells pelleted (4 °C, 3724 g, 10 minutes), resuspended in buffer A (50 mM Tris HCl pH 7.5, 1 mM EDTA, 0.6 M sorbitol), and stored (-80 °C).

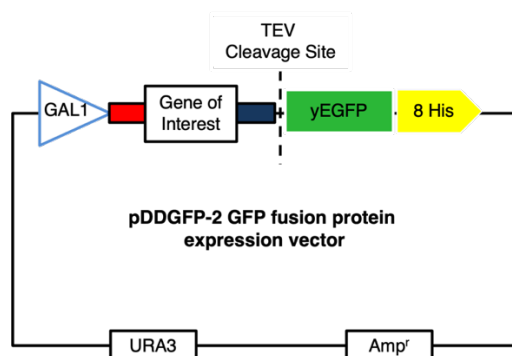


Figure 21: UapA constructs were inserted as gene of interest into pDDGFP2. The expression of UapA, TEV cleavage site, yEGFP and 8-HisTag was under control of inducible promoter GAL1. Amp<sup>r</sup> and URA3 were used as selection markers for cloning in bacteria and yeast respectively.

### 3.2.5. Cellular thermal shift assays (CETSA)

*S. cerevisiae* cells expressing GFP-tagged UapA were thawed, protease inhibitor (cOmplete, EDTA-free) added, and cells disrupted under pressure (25, 30, 33, 36 KPSI, Constant Systems Ltd CF1 Cell Disruptor). Unbroken cells were pelleted (4 °C, 10000 g, 10 minutes) and discarded. The membranes were pelleted (4 °C, 195400 g, 2 hours) and homogenized in buffer B (20 mM Tris HCl pH 7.5, 0.3 M sucrose). Following incubation with 1% DDM (4 °C, 2 hours), unsolubilised material was pelleted (4 °C, 22000 g, 1 hour), and the solubilised membranes ( $[protein]_{final}=0.1$  mg/mL) incubated with a range of purine substrates ( $[substrate]_{final}=1$  or 20 mM, 4 °C, 1 hour). The mixtures were aliquoted (20  $\mu$ L, 50  $\mu$ L or 80  $\mu$ L) and incubated at given temperature (30–75 °C, 6 minutes), followed by room temperature (3 minutes). Aggregated material was pelleted (4 °C, 14000 g, 10 minutes), and the supernatant (10  $\mu$ L) combined with SDS loading buffer and separated on a Novex 12% Tris-Gly Gel (90 minutes, 125V, 23 mA) alongside a BenchMark™ Fluorescent

Protein Standard. Bands were visualised using a CAS-3000 imaging system (460 nm).

### 3.2.6. Fluorescence Size Exclusion Chromatography

*S. cerevisiae* cells expressing GFP-tagged UapA were thawed, protease inhibitor (cOmplete, EDTA-free) added, and cells disrupted under pressure (25, 30, 33, 36 KPSI, Constant Systems Ltd CF1 Cell Disruptor). Unbroken cells were pelleted (4 °C, 10000 g, 10 minutes) and discarded. The membranes were pelleted (4 °C, 195400 g, 2 hours) and homogenized in buffer C ( $V_{\text{tot}}=200$  mL; PBS pH 7.4, 100 mM NaCl, 10% glycerol, 1% DDM). Unsolubilised material was discarded following centrifugation (4°C, 195400 g, 45 minutes). The solubilised material was incubated with the given substrate (1 mM) for 1 hour. Aggregated material was discarded following centrifugation (4°C, 195400 g, 10 minutes), and injected onto a pre-equilibrated Superose 6 Increase 10/300 GL column (20 mM TRIS pH 7.5, 150 mM NaCl, 0.03% DDM), at a flow rate of 0.25 mL/min.

Fractions (200  $\mu$ L) were collected in Greiner 96 well Black/Clear Bottom Plates, and fluorescence measured using a SpectraMax M2e (Molecular Devices), with an excitation wavelength of 488 nm and emission wavelength of 512 nm.

### 3.2.7. Purification of UapA in DDM

Cells were thawed, protease inhibitor (cOmplete, EDTA-free) added, and cells disrupted under pressure (25, 30, 33, 36 KPSI). Unbroken cells were pelleted (4 °C, 10000 g, 10 minutes) and discarded. The membranes were pelleted (4 °C, 195400 g, 2 hours) and homogenized in buffer B (20 mM Tris HCl pH 7.5, 0.3 M sucrose). The GFP-His-tagged protein was purified, according to a protocol outlined in literature<sup>176</sup> and summarised below.

Protease inhibitor (cOmplete, EDTA-free) was added, and the protein solubilised (4°C, 270 RPM, 1 hour) in buffer C ( $V_{\text{tot}}=200$  mL; PBS pH 7.4, 100 mM NaCl, 10% glycerol, 1% DDM). Unsolubilised material was discarded following centrifugation (4°C, 195400 g, 45 minutes). The supernatant was combined with imidazole (10 mM) and incubated with Ni<sup>2+</sup>-NTA resin suspended in buffer D (100 mL; PBS pH 7.4, 100 mM NaCl, 10 mM imidazole, 10% glycerol, 0.03% DDM) at 4°C for 2 hours. The resin was added to a gravity column and allowed to settle, before being washed with buffer D and buffer E (300 mL; PBS pH 7.4, 100 mM NaCl, 30 mM imidazole, 10% glycerol, 0.03% DDM). The protein was eluted with buffer F (50 mL; PBS pH 7.4, 150 mM NaCl, 10% glycerol, 310 mM imidazole, 0.03% DDM)

TEV protease was added (1:1 TEV:UapA) and the mixture dialysed (12 kDa MWCO) with buffer G (1500 mL; 20 mM TRIS pH 7.5, 150 mM NaCl, 5% glycerol, 0.03% DDM) for 16 hours. Aggregated protein was pelleted (5 minutes, 2095 g, 4°C), the supernatant filtered (0.2 µm), 10 mM imidazole added and the sample loaded onto a pre-equilibrated His-Trap (5 mL). Flow through was concentrated (100 kDa MWCO) and then injected into a pre-equilibrated Superdex 200 Increase 10/300 GL SEC column (20 mM TRIS pH 7.5, 150 mM NaCl, 0.03% DDM).

### 3.2.8. SDS-PAGE Gel Electrophoresis

Protein fractions (5 µL) were combined with SDS loading buffer (5 µL) and separated on a NuPage™ 4-12% Bis-Tris SDS-PAGE Gel (35 minutes, 200V, 120 mA), alongside a Novex pre-stained ladder. Gels were rinsed, Coomassie-stained and visualised in a BioRad Gel Imaging System.

### 3.2.9. Nano-differential scanning fluorimetry (Nano-DSF)

UapA (WT, Q408E<sub>Δ1-11</sub> or G411V<sub>Δ1-11</sub>) was purified according to Section 3.2.7. Purified UapA was then concentrated or diluted to 1.0 mg/mL in buffer H (20 mM TRIS pH 7.5, 150 mM NaCl, 0.03% DDM) containing the given substrate in a 30 μL aliquot, to a final substrate concentration of 1 mM. The samples were incubated for 16 hours, aggregated protein pelleted by centrifugation (4°C, 25500 g, 10 minutes). The sample was loaded into NanoTemper Prometheus NT.48 Standard Capillaries ready for measurement with a NanoTemper Prometheus NT.48 nano-DSF, accompanied by PR.ThermControl (version 2.1.2) software.

The excitation power of the device was set to reach a fluorescence emission signal (330 nm) between 10,000-20,000 RFU. The melting temperature experiment ran between 15–95 °C, with a temperature ramp rate of 1 °C per minute. The melting curve was followed by monitoring the 350/330nm ratio. Samples were analysed in quadruplicate alongside a control of the protein without any substrate. The 350/330 nm ratio signal was plotted against temperature ( °C) in GraphPad Prism 7.0. The apparent melting temperature ( $T_m$ ) was interpolated from a standard sigmoidal curve fitting.

### 3.2.10. CPM-based stability assays

Purified UapA (WT, Q408E<sub>Δ1-11</sub> or G411V<sub>Δ1-11</sub>) was concentrated to 10.0 mg/mL in buffer H (20 mM TRIS pH 7.5, 150 mM NaCl, 0.03% DDM). The assay solution was prepared in Greiner 96 well Black/Clear Bottom Plates with 1 μL of UapA (10 mg/mL), 0.9 μL of substrate (100 mM in 300 mM NaOH) in a total volume of 147 μL (20 mM TRIS pH 7.5, 150 mM NaCl). The 7-Diethylamino-3-(4'-Maleimidylphenyl)-4-Methylcoumarin (CPM) dye was prepared by dissolving in DMSO (4 mg/mL), followed by 100× dilution in 20 mM Tris-HCl pH 7.5, 150 mM NaCl, 0.03% w/v DDM.

Following incubation of the protein with the substrate for 1 hour, A 3 μl aliquot of the CPM preparation was added to each well in the dark. The fluorescence ( $\lambda_{exc} = 387$  nm,  $\lambda_{em} = 463$  nm) was measured every 5 minutes, for 120 minutes, at 40 °C, using a SpectraMax M2 fluorimeter (Molecular Devices). The raw fluorescence readings were normalised to the fluorescence reading for the most unfolded protein. This enabled calculation of the estimated percentage of unfolded protein for each condition against time. The experiments were repeated (n=3), and the data fitted to a single exponential decay curve using GraphPad Prism 9.

### 3.3. Results

#### 3.3.1. <sup>3</sup>H-xanthine competitive uptake assay

Unfortunately, the following experiment could not be completed by myself at Imperial College London. Due to COVID-19, I was unable to travel to our collaborator's lab, where they have an appropriate set up for working with radiolabelled substrates. Consequentially, the following work was kindly completed by our collaborator Professor George Diallinas in the Department of Biology at the National and Kapodistrian University of Athens.

As described in literature<sup>201</sup>, <sup>3</sup>H-xanthine uptake in minimal media can be assayed in germinating conidiospores of *A. nidulans*. Germinating conidiospores were solubilised and incubated with a mixture of radiolabelled substrate (usually <sup>3</sup>H-xanthine) and unlabelled inhibitor of interest. Uptake was quenched on ice with excess unlabelled substrate. Conidiospores were pelleted, washed, and solubilised in scintillation solution, with radioactive counts per minute measured. By varying the identity of the unlabelled substrate, and by varying the proportion of unlabelled and radiolabelled substrate, it was possible to identify inhibition constants ( $K_i$ ). A smaller  $K_i$  indicates the unlabelled substrate is a better inhibitor of <sup>3</sup>H-xanthine uptake. This may be through blocking radiolabelled substrate uptake or competing for the same binding site. However, without changing the identity of the radiolabelled substrate, which is challenging due to the need for obtaining novel <sup>3</sup>H-labelled substrates, it is not possible to differentiate between non-transportable and transportable competitive inhibitors in this assay format.

Kinetic analysis was conducted on *A. nidulans* strain  $\Delta$ ACZ pAN510-GFP, which contains loss-of-function mutations in the three major purine transporters AzgA, UapC and UapA, following and reintroduction of GFP-tagged UapA at the *uapA*-locus<sup>171</sup>. This is an ideal model since it removes activity of the closely related AzgA

and UapC transporters, allowing for a clean background. This work found that compounds **1**, **2**, **3**, **5** And **13** all inhibited  $^3\text{H}$ -xanthine uptake when provided in 1000x excess (Figure 22).

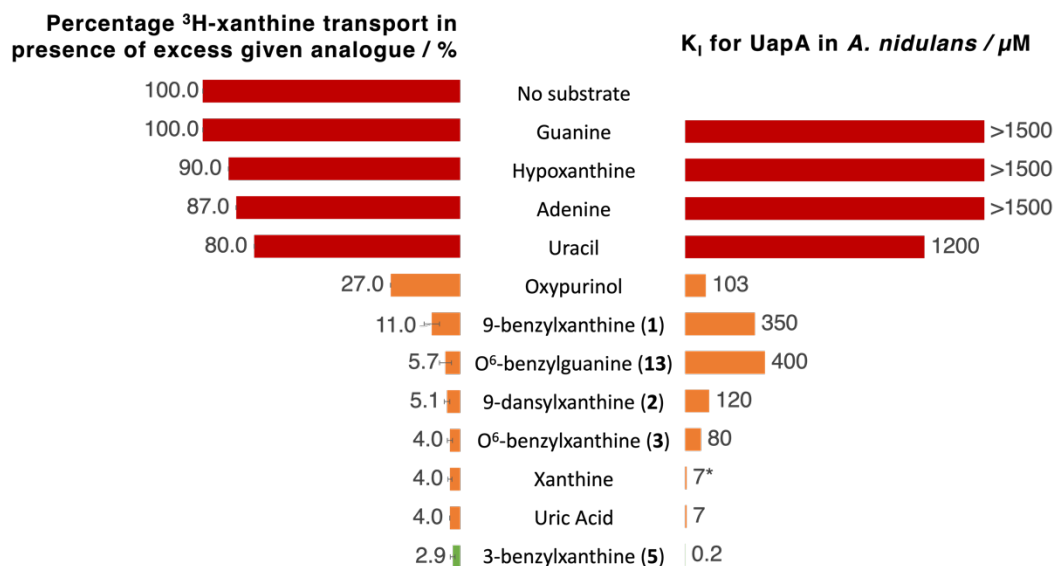


Figure 22: Left, Percentage radiolabelled xanthine uptake activity remaining in germinating *A. nidulans*  $\Delta\text{ACZ}$  pAN510-GFP conidiospores on addition of 1000x excess unlabelled purine analogue ( $n=3$ ). Standard deviations included for novel compounds **1**, **2**, **3**, **5** and **13**. Data not available for other purine analogues in existing literature<sup>177,181,203</sup>. Right, Binding affinity of existing and novel substrates for UapA in  $\Delta\text{ACZ}$  pAN510-GFP ( $K_i$  /  $\mu\text{M}$ ). \*Value indicated for xanthine is  $K_M$  ( $\mu\text{M}$ ), rather than  $K_i$ .

Interestingly, it appears derivatisation at position N<sup>3</sup> is well tolerated. This is in agreement with previous work<sup>181</sup> that found 3-methylxanthine binds UapA with high affinity, with a  $K_i$  of 28  $\mu\text{M}$ . Compound **5**, which has a benzyl group at the same position, binds UapA has an inhibition constant 35x greater ( $K_i = 0.2 \mu\text{M}$ ) than xanthine and uric acid. It is unclear whether this is due to specific binding interactions between the benzyl group and nearby aromatic residues, or if this is a result of non-specific hydrophobic interactions. It is also unknown whether 3-methylxanthine or compound **5** are transported by UapA, or if they act as a non-transportable inhibitors of UapA activity.



Compounds **1** and **2**, which have benzyl and dansyl moieties at position N<sup>9</sup> respectively, also significantly inhibit radiolabelled xanthine uptake with only 5-11% uptake activity remaining, when the given compound is in 1000× excess. This is much more comparable to native substrates xanthine and uric acid (4%) than to substrates such as guanine, hypoxanthine, adenine and uracil (80–100%)<sup>181</sup>, which are known not to be transported by UapA, but are instead transported by other nucleobase transporters present in *A. nidulans*. Interestingly, the inhibition constant is approximately 3-fold smaller for compound **2** ( $K_i = 120 \mu\text{M}$ ) than Compound **1** ( $K_i = 350 \mu\text{M}$ ), which may suggest that the larger bulkier dansyl-based side chain in **2** is accommodated by the substrate binding site.

Finally, compounds **3** and **13** have a benzyl group at position O<sup>6</sup>. The inhibition constant for compound **3** ( $K_i = 80 \mu\text{M}$ ) was approximately 11× greater than the Michaelis constant for the native substrate xanthine ( $K_M = 7 \mu\text{M}$ ). Of the synthesized xanthine analogues in this work, **3** has the second lowest  $K_i$ . Compound **13**, which shares the benzyl moiety at position O<sup>6</sup>, but has an amine rather than carbonyl at position 2 (guanine-like scaffold), has a 5× higher inhibition constant, which supports the hypothesis that the carbonyl at position 2 is important for UapA recognition. Section 2.3.1 describes how this carbonyl appears to be important for forming a key hydrogen bonding interaction with Gln408 in the substrate binding site. Of the newly synthesized substrates, compound **13** has the lowest binding affinity for UapA. Interestingly though, the percentage inhibition of radiolabelled xanthine transport is much higher for compound **13** relative to guanine, demonstrating that the addition of the benzyl group at position O<sup>6</sup> of guanine improves binding affinity to UapA. However, it is unclear whether this is a specific binding interaction with nearby aromatic residues, or if this is a result of non-specific hydrophobic interactions.

### 3.3.2. *Aspergillus nidulans* growth assays

#### 3.3.2.1. Assessing effect of purine analogues on normal fungal growth

The novel substrates Compound **1**, **2**, **3**, **5** and **13** appear to be binding UapA, with affinities varying between 0.2–400  $\mu\text{M}$ . It was next important to establish if these compounds are toxic to *Aspergillus* and if so, if this toxicity is dependent upon UapA transporter expression (i.e. they show specificity for UapA). Furthermore, if these compounds are toxic, and this toxicity is dependent on transporter expression, or if they act as nitrogen sources, this provides evidence that these compounds are not just binding UapA and inhibiting xanthine uptake, but are also being transported.

Early investigations into these purine analogues involved assessing their toxicity against strains of *Aspergillus nidulans*. Four strains were surveyed including the wild type (WT) strain, which expresses all of the key nucleobase transporters, and the  $\Delta 7$  strain which lacks the 7 key nucleobase transporters (FurD, FurA, FcyB, UapA, UapC, AzgA, CntA)<sup>178</sup>. The substrate selectivity of these 7 key transporters is summarised in Table 8, and is broad but overlapping, providing redundancy in substrate uptake<sup>178</sup>.  $\Delta\text{ACZ}$  contains loss-of-function mutations in the three major purine transporters AzgA, UapC and UapA. Finally,  $\Delta\text{ACZ}$  pAN510-GFP, in addition to carrying the same triple knockout also expresses GFP-tagged UapA<sup>202</sup>. The UapA allele is integrated by homologous recombination in tandem at the genomic uapA-locus<sup>202</sup>. It has been shown that this construct still functions and has the same selectivity filter as UapA-WT<sup>202</sup>. This final strain, when compared with  $\Delta\text{ACZ}$ , allows for direct assessment of the effect of UapA with a clear background. In addition, the GFP tag enables visualisation of the protein localising to the membrane using fluorescence confocal microscopy<sup>185</sup> (Section 3.3.3).

Growth tests were carried out at pH 6.8, at 37 °C and 25 °C for 48 and 96 hours respectively. 37 °C was included as it is the physiologically relevant temperature for

*Aspergillus* infection in humans. 25 °C was included, since at lower temperatures *Aspergilli* demonstrate stress responses, generally resulting in slower growth, reduced spore generation and differential expression of key membrane transporters (H. Arst, personal communication, 3<sup>rd</sup> February 2021). These factors may impact upon a strain's sensitivity to the novel purine analogues. *L*-alanine was used as the sole nitrogen source since its uptake is independent of the 7 key nucleobase transporters. Other independent nitrogen sources that have been used include ammonium or nitrates (NaNO<sub>3</sub>). *L*-alanine was preferred as it is more derepressing than ammonium or nitrate nitrogen sources, and does not result in alkylation of the growth media (H. Arst, personal communication, 3<sup>rd</sup> February 2021).

Table 8: Substrate selectivity of 7 key nucleobase transporters in *Aspergillus nidulans*<sup>177</sup>.

Transporter	Main Substrate(s)	Also Transports
FurD	Uracil	Allantoin, Uric Acid
FurA	Allantoin	Uracil, Uric Acid
FcyB	Cytosine, General Purine	5-fluorocytosine
UapA	Uric Acid, Xanthine	Allopurinol
UapC	Uric Acid, Xanthine	Oxypurinol
AzgA	Hypoxanthine, Adenine, Guanine	
CntA	General nucleotide	

As expected, normal growth is observed on 2.5 mM *L*-alanine with no additional substrate (Figure 23). The fungus forms a mycelium, a translucent network of hyphae. The green pigment comes from the production of spores during a stress response. On an agar plate, the fungi can only grow in two dimensions, across the surface of the agar. However, the fungus tries to grow in the third dimension resulting in crowding of hyphae, competition for nutrient sources and spore production.

In all cases 2.5 mM *L*-alanine was included as the primary nitrogen source. With the addition of xanthine (100 µM) or hypoxanthine (100 µM) increased growth is observed by strains which possess the transporters UapA (WT, ΔACZ pAN510-GFP) and AzgA (WT) respectively. Both xanthine and hypoxanthine can be used as

nitrogen sources, resulting in increased growth relative to when 2.5 mM *L*-alanine was used as the sole nitrogen source. It did not appear that addition of 100  $\mu$ M 1-methylxanthine, 3-methylxanthine, 7-methylxanthine or 6-chloroguanine had any significant effect on fungal growth at this concentration, at either 25 °C or 37 °C (Figure 23).

It is known that 3-methylxanthine binds UapA ( $K_M = 28 \mu$ M), but it is thought not to be transported, since it does not induce endocytosis of the GFP-tagged transporter<sup>185</sup> (Section 3.3.3). Native substrates of UapA have been shown to induce a conformational change in the transporter, allowing for binding of arrestin, and formation of the endocytosis complex<sup>185</sup>. Distinguishing between compounds that bind UapA and are not toxic, and those that are transported is challenging. In order to prove that the substrate is being transported, isotopic labelling or liquid chromatography mass spectrometry methods would be required to allow for direct measurement of substrate uptake. Likewise, 2-thioxanthine does not appear to significantly affect growth of any *A. nidulans* strain. This is expected, since earlier studies demonstrated that 2-thioxanthine is transported by UapA, has no observed toxicity, but is metabolised to 2-thiouric acid, which interferes with conidiation<sup>204</sup>.

As expected, 5-fluorouracil (5FU), a cytotoxic compound, exhibited toxicity against all strains of *A. nidulans*<sup>205</sup>. As discussed in Section 1.1.5.4, 5-fluorocytosine usually only demonstrates toxicity against strains that possess the FcyB transporter (WT,  $\Delta$ ACZ and  $\Delta$ ACZ pAN510-GFP)<sup>164</sup>. It would be expected to exhibit normal growth of  $\Delta$ 7 on media containing 5-fluorocytosine (5FC), since it should not be transported into the cell. However limited growth of  $\Delta$ 7 is observed: a mycelium forms, but spore production seems to be suppressed (Figure 23). Similar phenotypes were observed at 25 °C (Figure 23). This may be a consequence of non-specific toxicity at higher concentrations, or alternatively this may result from *L*-alanine uptake resulting in overexpression of alternative transporters or catabolite repression.

A subsequent study on the effect of 5FU and 5FC on *A. nidulans* strains with NaNO<sub>3</sub> rather than *L*-alanine as the primary nitrogen source was more consistent with the latter hypothesis; it was shown that  $\Delta 7$  grew comparably on media in the presence and absence of 5FC (Figure 24). In addition,  $\Delta 7$  grew better on media containing 5FU with NaNO<sub>3</sub> as the primary nitrogen source, rather than *L*-alanine. This suggests that *L*-alanine increases fungal sensitivity to these known antifungals, which may be due to catabolite repression or differential transporter expression.

Repeating growth assays for novel analogues **1**, **2**, **3**, **5** and **13** with NaNO<sub>3</sub> as the primary nitrogen source (Figure 24) showed that these compounds still did not have any significant effect on growth of any of the four strains of *A. nidulans*. This reduced concerns that *L*-alanine induced-catabolite repression or differential transporter expression may affect the toxicity of these novel analogues.

It did not appear that any of the novel analogues **1**, **2**, **3**, **5** and **13** had any significant effect on growth of any of the four strains of *A. nidulans*, when either *L*-alanine (Figure 23) or NaNO<sub>3</sub> (Figure 24) were used as the primary nitrogen source at 37 °C or 25 °C. This is not surprising, since we are more interested in whether these compounds bind UapA and are transported, in order to identify potential branch points for derivatisation.

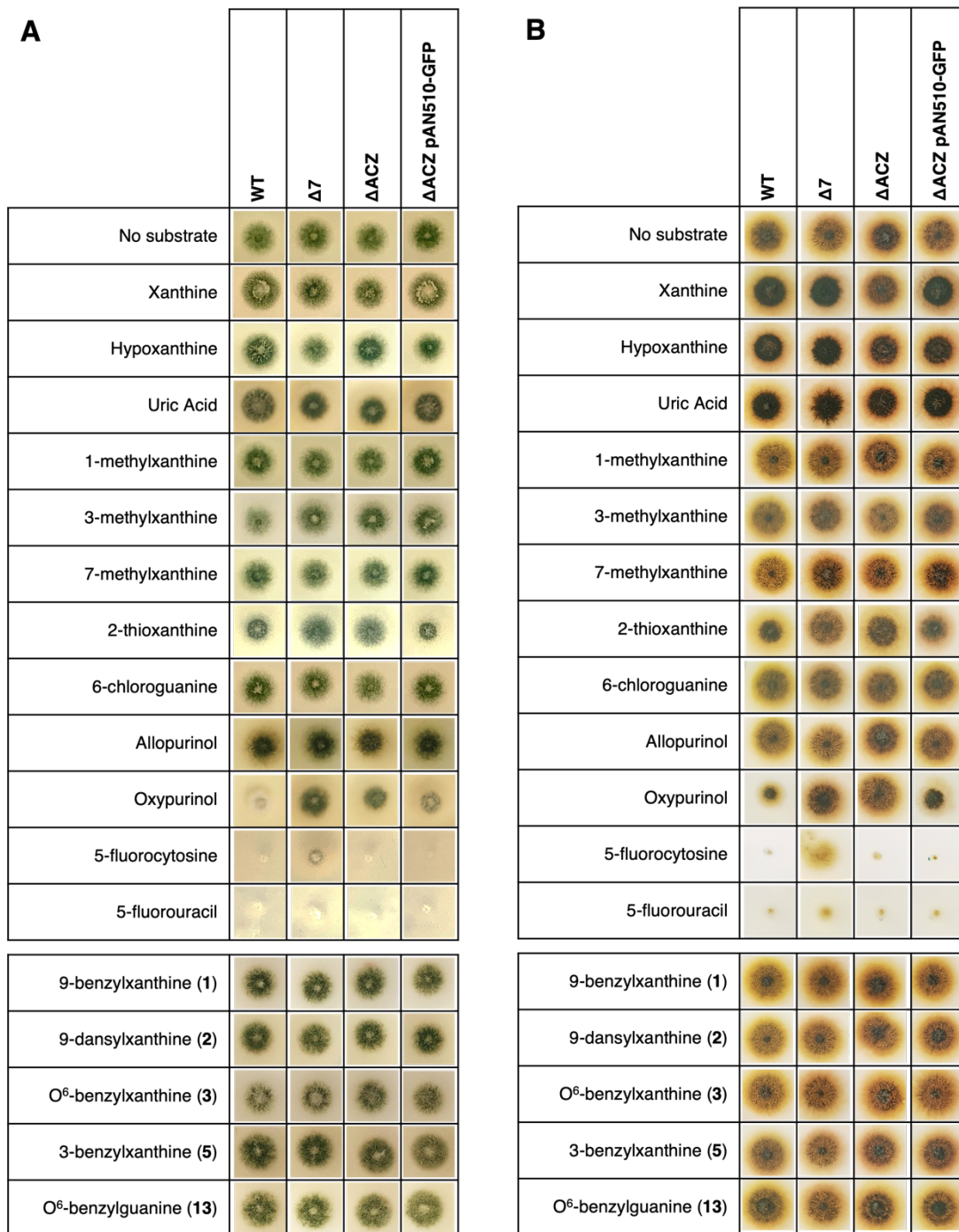


Figure 23: A, Growth assays of four strains of *A. nidulans* (WT,  $\Delta 7$ ,  $\Delta ACZ$ ,  $\Delta ACZ$  pAN510-GFP) on minimal media supplemented with 1% glucose and PABA (2 mg/L), with *L*-alanine (2.5 mM) as the major nitrogen source and addition of named purine analogue (100  $\mu$ M). Plates were inoculated and incubated at 37 °C for 48 hours. Images presented are representative of n=2. B, Analogous growth assays where plates were incubated at 25 °C for 96 hours.


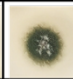
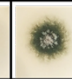
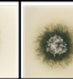
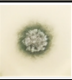
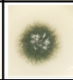
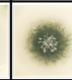
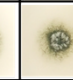

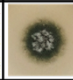
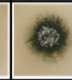
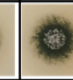

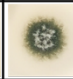
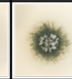
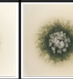
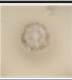
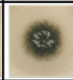
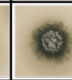
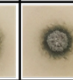

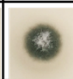



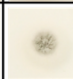




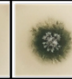
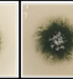

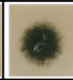
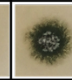
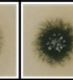

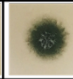
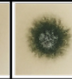
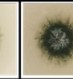

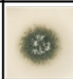
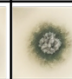
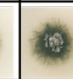
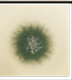
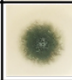

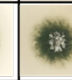
	WT	$\Delta 7$	$\Delta ACZ$	$\Delta ACZ$ pAN510-GFP
No substrate				
2-thioxanthine				
6-chloroguanine				
Allopurinol				
Oxypurinol				
5-fluorocytosine				
5-fluorouracil				
9-benzylxanthine (1)				
9-dansylxanthine (2)				
O <sup>6</sup> -benzylxanthine (3)				
3-benzylxanthine (5)				
O <sup>6</sup> -benzylguanine (13)				

Figure 24: Growth assays of four strains of *A. nidulans* (WT,  $\Delta 7$ ,  $\Delta ACZ$ ,  $\Delta ACZ$  pAN510-GFP) on minimal media supplemented with 1% glucose and PABA (2 mg/L), with NaNO<sub>3</sub> (10 mM) as the major nitrogen source and addition of named purine analogue (100  $\mu$ M). Plates were inoculated, and incubated at 37 °C for 48 hours. Images presented are representative of n=2.

### 3.3.2.2. Novel analogues as nitrogen sources

While the growth experiments demonstrated that compounds **1**, **2**, **3**, **5** and **13** are not toxic to *A. nidulans* strains at 100  $\mu$ M, they were not able to determine if these compounds bind and are transported by UapA, or if they can act as nitrogen sources for fungal growth. If these compounds can act as nitrogen sources, this would indicate that these compounds can be carried by purine transporters present in *A. nidulans*.

To answer this key scientific question, minimal media agar was supplemented with 1% glucose, 2 mg/L pabaA and 1 mM of the respective purine analogue. Plates were inoculated with WT *A. nidulans* and incubated for 48 hours at 37 °C (Figure 25). Plates using *L*-alanine (2.5 mM) and sodium nitrate (10 mM) as the sole nitrogen sources were included as positive controls, while media containing no nitrogen source, or toxic analogues 5FC (1 mM) and 5FU (1 mM) were included as negative controls. This work demonstrates that allopurinol, oxypurinol, 1-methylxanthine, 3-methylxanthine, 7-methylxanthine, 2-thioxanthine, and compounds **1**, **3**, **5** and **13** are not effective sole nitrogen sources at this concentration. As expected, xanthine, hypoxanthine and uric acid are suitable sole nitrogen sources at this concentration. This work also found that 6-chloroguanine is another nitrogen source capable of supporting growth of WT *A. nidulans* at this concentration. Due to its similarity to the structure of guanine, it is likely that 6-chloroguanine is transported by AzgA. This could be confirmed by comparing growth profiles of strains possessing and lacking the AzgA transporter on media containing 6-chloroguanine as the sole nitrogen source.

This experiment found that **1**, **3**, **5** and **13** are not effective sole nitrogen sources at 1 mM. However, this does not mean that these compounds are not being



transported by UapA. Compound **2** was excluded from this experiment due to insufficient material.


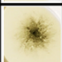


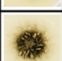
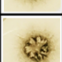
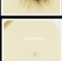












	WT
No substrate	
L-Alanine (2.5 mM)	
NaNO <sub>3</sub> (10 mM)	
Xanthine	
Hypoxanthine	
Uric Acid	
1-methylxanthine	
3-methylxanthine	
7-methylxanthine	
2-thioxanthine	
6-chloroguanine	
Allopurinol	
Oxypurinol	
5-fluorocytosine	
5-fluorouracil	
9-benzylxanthine (1)	
O <sup>6</sup> -benzylxanthine (3)	
3-benzylxanthine (5)	
O <sup>6</sup> -benzylguanine (13)	

Figure 25: Growth assays of WT *A. nidulans* on minimal media supplemented with 1% glucose and para-aminobenzoic acid (PABA, 2 mg/mL), with the indicated compound as the major nitrogen source. Unless otherwise indicated, the concentration of the given compound was fixed at 1 mM. Compound **2** was excluded due to insufficient material. Plates were inoculated and incubated at 37 °C for 48 hours. Images presented are representative of n=2

### 3.3.3. Substrate-induced endocytosis of UapA-GFP in *A. nidulans*

Compounds **1**, **3**, **5** and **13** have demonstrated no toxicity towards *A. nidulans* at 100  $\mu$ M, and are not effective sole nitrogen sources at 1 mM. However, this does not mean that these compounds are not being transported by UapA.

Previous work has identified a downregulation mechanism of the uric acid/xanthine transporter UapA. GFP-tagged UapA is endocytosed in the presence of substrates, and sorted into the multivesicular body pathway, ready for degradation<sup>185</sup>. Substrate-induced endocytosis has been shown to be dependent on UapA activity. As shown in Figure 26, native substrates xanthine and uric acid induce endocytosis of UapA. Generally, it has been shown that substrates transported by UapA induce its turnover<sup>185</sup>. However, known substrates oxypurinol and allopurinol do not. The latter may be due to allopurinol using an alternative translocation mechanism to the native substrates<sup>184</sup>.

The addition of Compound **1**, **2**, **3**, **5** and **13** to germinating conidia of  $\Delta$ ACZ pAN510-GFP did not result in observable substrate-induced endocytosis (Figure 26). This may indicate that these substrates, despite binding UapA (see Section 3.3.1) are not transported. However, this is not conclusive, since oxypurinol and allopurinol are both transported by UapA but do not induce endocytosis<sup>184</sup><sup>184</sup>. Further investigations are required into the behaviour of these small molecules with UapA.

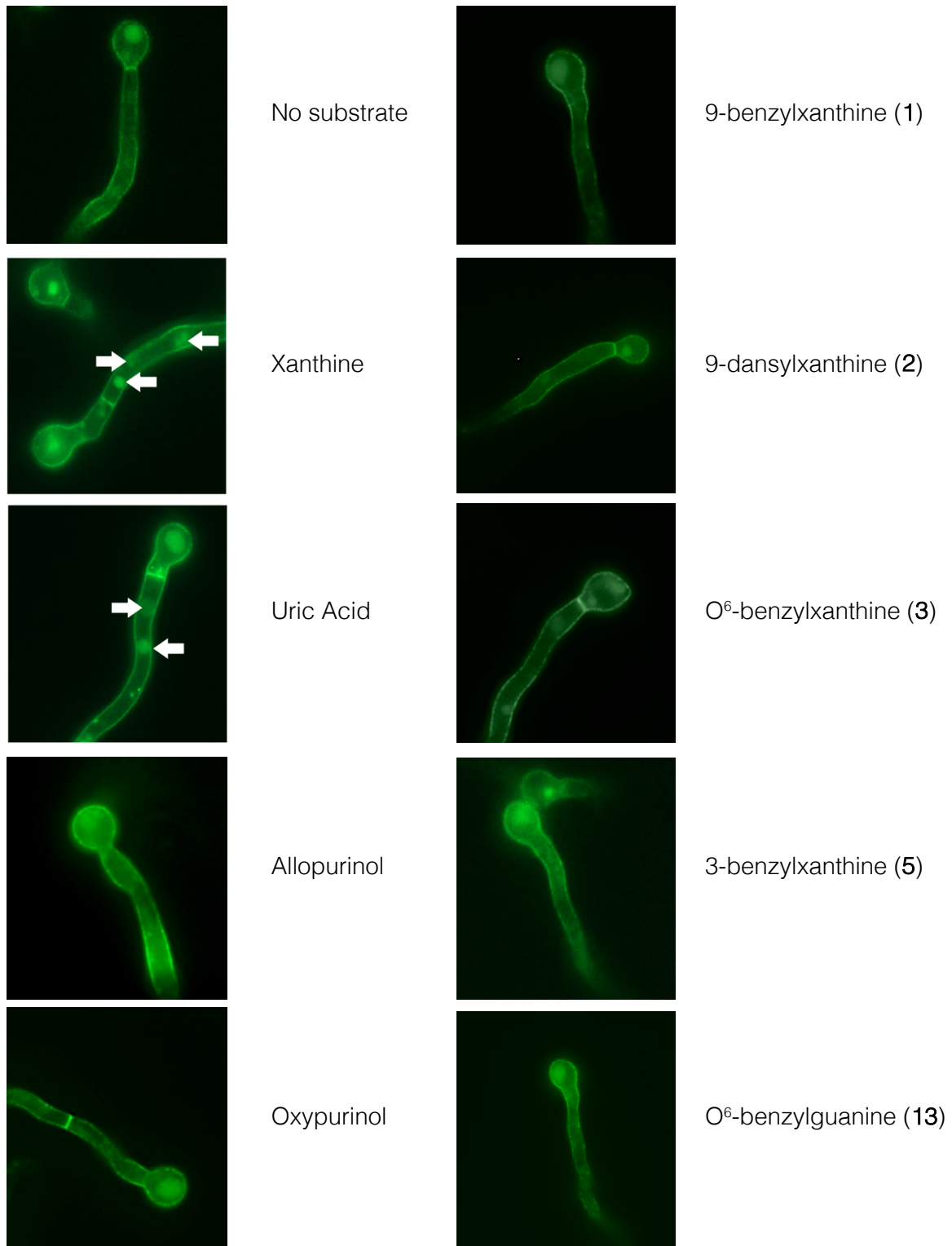


Figure 26: Fluorescence microscopy showing the effect of purine analogues (100 mM, 4 hours) on UapA-GFP localization in the plasma membrane of germinating conidiospores of *A. nidulans*  $\Delta$ ACZ  $\rho$ AN510-GFP. Addition of xanthine and uric acid alone resulted in endocytosis of UapA-GFP, resulting in GFP-labelled vacuoles and endosomes (examples are indicated by white arrows).

### 3.3.4. Thermostability assays of UapA in detergent–solubilised membranes

Thermal denaturation experiments are useful tools in determining the comparative stability of proteins across a variety of conditions, including protein sequence mutation, small molecule concentration, buffer pH or ionic strength, redox potential, additive or detergent concentration<sup>206</sup>. Protein stability can be quantified using a variety of approaches, including cellular thermal shift assays (Section 3.3.4.1), fluorescence size exclusion chromatography (Section 3.3.4.2), dye-based differential scanning fluorimetry (Section 3.3.5.1) and nano differential scanning fluorimetry (Section 3.3.5.2). Cellular thermal shift assays and fluorescence size exclusion chromatography can utilise whole-cell, cell-lysate or solubilised membrane samples<sup>207,208</sup>. These offer a significant advantage over differential scanning fluorimetry, which requires purified protein samples.

#### 3.3.4.1. Cellular thermal shift assays (CETSA)

Cellular thermal shift assays (CETSA) are used routinely for identifying chemical engagement with soluble proteins in crude whole cell samples. More recently, they have been reported as a strategy for identifying small molecule engagement with solute carriers<sup>209</sup>, such as SLC16A1 (MCT1) and SLC1A2 (EAAT2). CETSA relies on the principle that as the temperature increases, protein shifts from a folded stable state to an unfolded or denatured state. On substrate or ligand binding, a protein target can be stabilised or destabilised, causing a shift in thermal denaturation temperature (Figure 27).

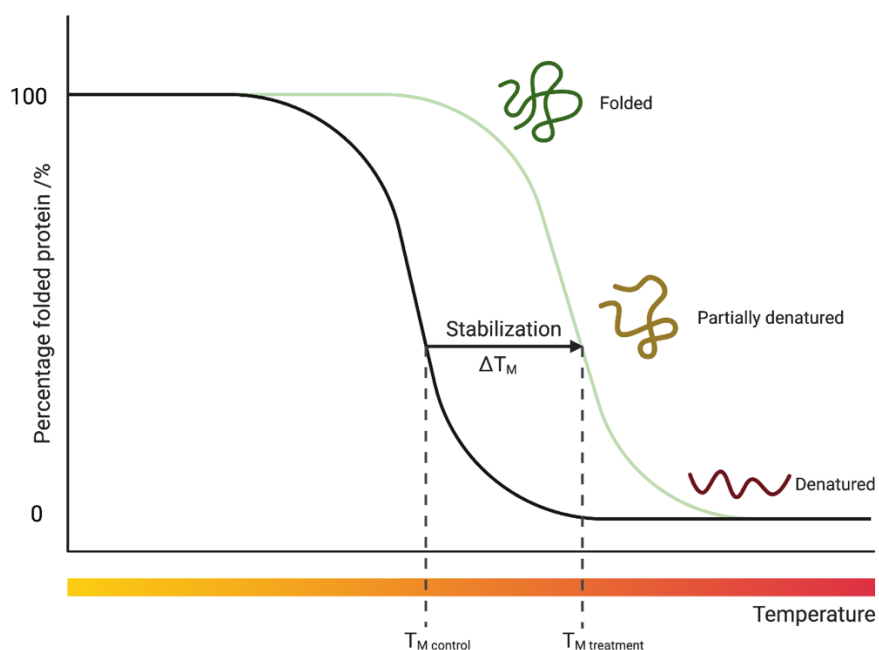


Figure 27: Principles of thermal shift assays. Where a particular treatment causes stabilisation of a protein, this will become apparent with a shift in melting curve (black) to the RHS (green). The melting temperature,  $T_m$ , refers to the temperature at which 50% of the protein is denatured. With stabilised proteins, this will be at a higher temperature. This figure was created with [www.BioRender.com/](http://www.BioRender.com/), and adapted from the template “Thermal Shift Assay Principle”.

Target engagement of existing substrates of UapA and novel analogues with UapA may be assessed using a variant of the assay described in literature<sup>209</sup>. Here the quantity of soluble GFP-tagged UapA-WT was assessed using in-gel fluorescence, rather than by Western blot analysis.

UapA-WT was expressed in *S. cerevisiae*, cells were disrupted, the membranes isolated by centrifugation. Membranes were solubilised with DDM and insolubilised material discarded. The solubilised membranes (0.1 mg/mL UapA-WT), were incubated ( $\pm$  1 mM xanthine) for 1 hour at 4 °C, before being incubated at a given temperature (ice, 35-70 °C) for 6 minutes, and then cooled at room temperature for 3 minutes. Denatured and unfolded protein was removed by centrifugation, and the remaining soluble GFP-tagged protein was separated on an 12% Tris-Glycine SDS-PAGE gel. The GFP-tagged protein was visualised using in-

gel fluorescence. Initial results appeared to suggest that there was observable stabilisation, with significantly more protein present in solution at 40, 45 and 50 °C, when xanthine is present compared to protein prepared in the absence of xanthine. (Figure 28)

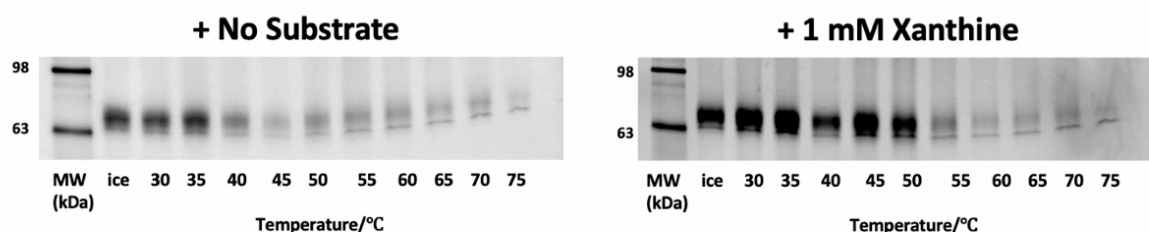


Figure 28: 1% DDM solubilised membranes expressing UapA-WT were incubated with and without 1mM xanthine for 1 hour, before being incubated at the given temperature (ice - 75 °C) for 6 minutes, and left to rest at room temperature for 3 minutes. Aggregated protein was pelleted by centrifugation and the soluble fraction separated on a 12% Tris-Glycine SDS-Page gel (125 V, 23 mA, 90 minutes), with the GFP-tagged protein visualised using in-gel fluorescence (460 nm). Samples were run alongside a BenchMark™ Fluorescent Protein Standard. Images representative of n=2.

This initial experiment suggested that 40-50 °C may be a useful temperature window for discriminating between strong and weak binders of UapA-WT. This result is consistent with published data<sup>93</sup> that found the apparent melting temperature of UapA-WT to be around 43 °C.

Subsequently, solubilised membranes from *S. cerevisiae* (0.15 mg/mL UapA-WT), were incubated with a variety of purine analogues (1 mM) for 1 hour, before being incubated at temperatures between 40-60 °C for 6 minutes. Aggregated protein was pelleted, the soluble fraction separated on a Tris-Glycine SDS-PAGE gel, and the GFP-tagged protein visualised using in-gel fluorescence (Figure 29). However, the same trends in stability of UapA-WT were not observed. UapA-WT should have been significantly destabilised at these temperatures in the absence of substrate, but significant protein was still present following incubation at 60 °C. Repetition (n=3) of these experiments produced inconsistent results.

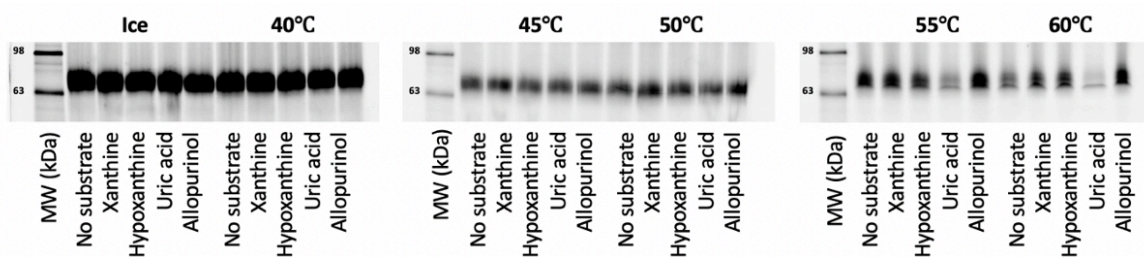


Figure 29: Solubilised membranes were incubated with 1 mM purine analogue for 1 hour, before being incubated on ice or at 40-60 °C for 6 minutes, followed by room temperature for 3 minutes. Aggregated protein was pelleted and the soluble fraction was separated on a 12% Tris-Glycine SDS-PAGE gel (125 V, 23 mA, 90 minutes). The GFP-tagged protein visualised using in-gel fluorescence (460 nm). Samples were run alongside a BenchMark™ Fluorescent Protein Standard.

Initial optimisation around aliquot size, protein concentration and substrate concentration (1-20 mM) had no benefit. The next step would be to change the duration of heat shock. It may be that with larger aliquot sizes, the entire volume may not be reaching the temperature of the heat block. In addition, it may be possible that the substrate has been added at too high a concentration. Previous work has shown that adding substrate in too high concentrations can result in destabilising of the protein, as shown for the binding of sulfonate derivatives to BSA<sup>210</sup>. Further optimisation of this assay would be required before it is possible to extract quantitative information regarding chemical engagement with UapA.

#### 3.3.4.2. Fluorescence size-exclusion chromatography (FSEC)

Fluorescence size exclusion chromatography (FSEC) takes advantage of the same C-terminal GFP-His<sup>9</sup> tag utilised in the prior cellular thermal shift assay (Section 3.3.4.1) to conduct thermostability assays in crude membranes. FSEC, unlike the cellular thermal shift assay allows you to determine monodispersity of detergent-solubilised samples. This technique can also be applied to construct, detergent, lipid and substrate screening<sup>93</sup>. FSEC requires significantly less material than traditional methods, such as differential scanning fluorimetry and circular dichroism, and allows for high-throughput screening of membrane proteins in detergent.

Heated protein samples can be treated with a panel of substrates and analysed by FSEC. This approach has been used previously to screen ligands, ions, and lipids, including newly designed cholesterol derivatives for the *Danio rerio* P2X4 receptor and *Caenorhabditis elegans* GluCl<sup>207</sup>. More recently it has been applied to UapA, where it was shown that addition of 1 mM xanthine significantly stabilised 1% NG-solubilised UapA-WT and UapA-G411V, but not UapA-Q408E<sup>93</sup> (Figure 30).



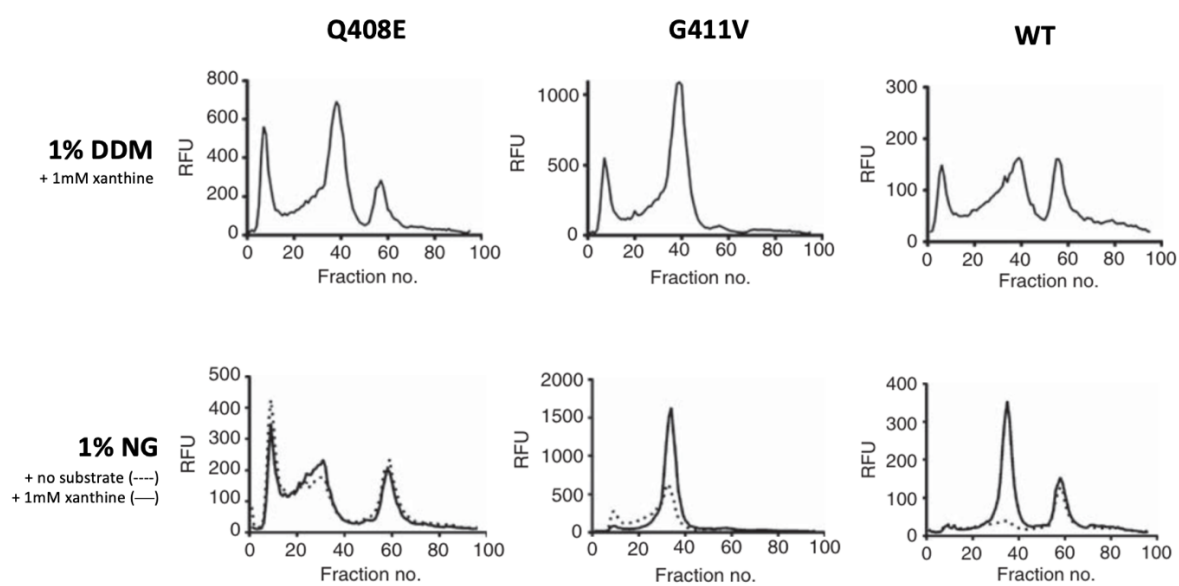


Figure 30: Published un-heated fluorescence size exclusion chromatographs for UapA-Q408E, UapA-G411V and UapA-WT in the presence of different detergents (1% DDM or NG). For 1% NG, the effect of adding 1 mM xanthine (solid line), compared to no substrate (dotted line) was demonstrated. Figure adapted from literature<sup>93</sup>.

This work sought to use fluorescence size exclusion chromatography to assess whether we could see significant stabilisation or destabilisation of two different UapA thermostabilised constructs in the presence of different substrates.

UapA-G411V $\Delta_{1-11}$  is a thermostabilised construct, which is locked in the inward-facing conformation. By comparing the relative fluorescent units (RFU) for UapA-G411V $\Delta_{1-11}$  mutant with different substrates, it does not appear that 3-benzylxanthine (5) stabilises the UapA-G411V $\Delta_{1-11}$  mutant relative to no substrate. On heating the sample to 45 °C, there is still no significant difference in stabilisation of UapA-G411V $\Delta_{1-11}$  with no substrate, xanthine or 3-benzylxanthine (5) (Figure 31).

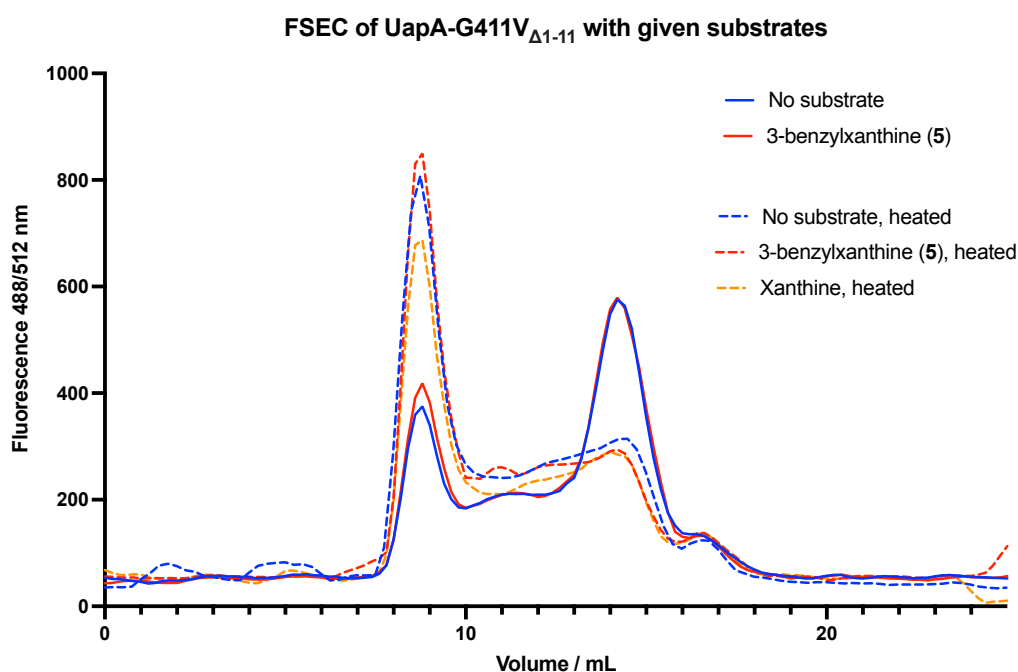


Figure 31: Fluorescence size exclusion chromatographs for heated (dashed) and unheated (solid) UapA-G411V $\Delta_{1-11}$  in the presence of different substrates (n=1): no substrate (blue), 3-benzylxanthine (5, red), hypoxanthine (green) and xanthine (orange). Figures were generated in GraphPad Prism 9.

Repetition of the same experiment for UapA-Q408E $\Delta_{1-11}$  found that there was also no significant stabilisation of UapA-Q408E $\Delta_{1-11}$  with different substrates (Figure 32). Unlike UapA-G411V $\Delta_{1-11}$ , which is locked in the inward facing conformation, UapA-Q408E $\Delta_{1-11}$  is not conformationally locked, but has markedly reduced activity and higher affinity for hypoxanthine compared to WT<sup>93</sup>. Again, on heating the sample to 45 °C, there was still no significant difference in stabilisation of UapA-Q408E $\Delta_{1-11}$  with the different substrates xanthine, hypoxanthine or 3-benzylxanthine (**5**) (Figure 32).

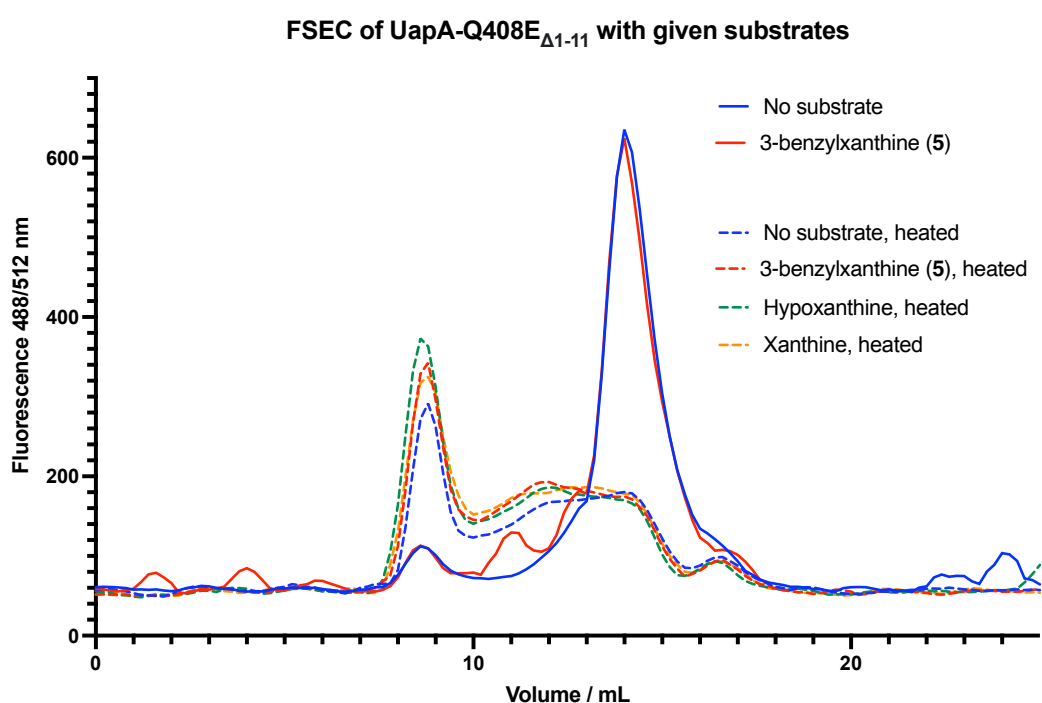


Figure 32: Fluorescence size exclusion chromatographs for heated (dashed) and unheated (solid) UapA-Q408E $\Delta_{1-11}$  in the presence of different substrates (n=1): no substrate (blue), 3-benzylxanthine (**5**, red), hypoxanthine (green) and xanthine (orange). Figures were generated in GraphPad Prism 9.

Finally, as for UapA-G411V $\Delta_{1-11}$  and UapA-G411V $\Delta_{1-11}$ , UapA-WT showed no observable stabilisation in the presence of different substrates, with or without heating to 45 °C (Figure 33).

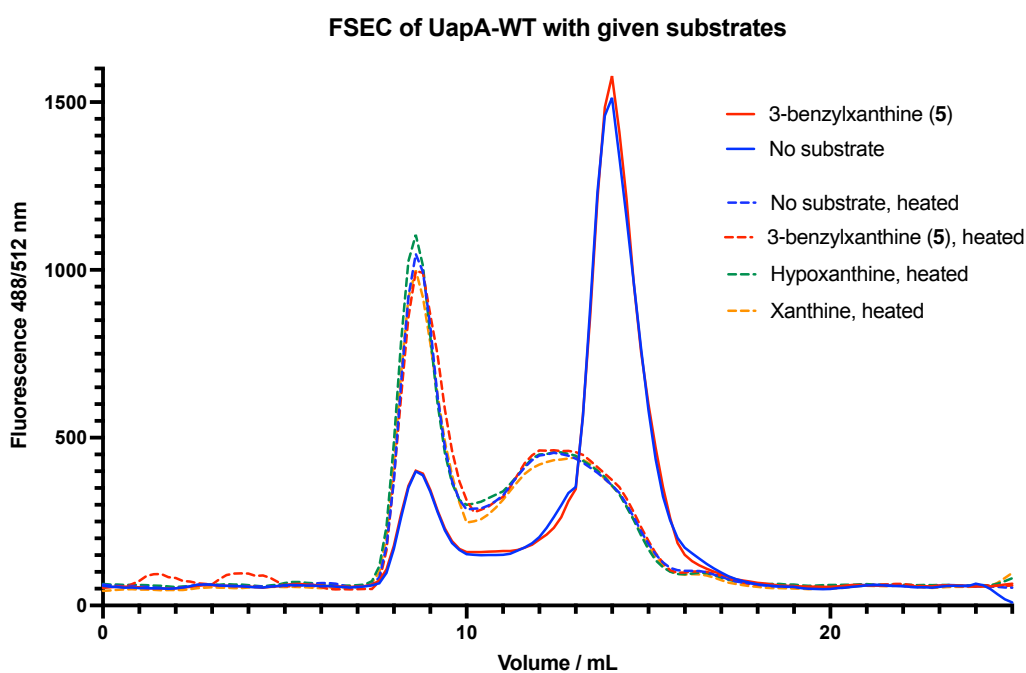


Figure 33: Fluorescence size exclusion chromatographs for heated (dashed) and unheated (solid) UapA-WT in the presence of different substrates (n=1): no substrate (blue), 3-benzylxanthine (5, red), hypoxanthine (green) and xanthine (orange). Figures were generated in GraphPad Prism 9.

Ultimately, there was not a significant difference in protein stability on the addition of different substrates. This is a crude solubilised membrane sample, where indirect effects, such as the heterogeneous lipidic environment, are difficult to exclude. As with the previous cellular thermal shift assay, it is possible the substrate has been added at too high a concentration, resulting in non-specific interactions.

Future work could involve repeating this experiment using NG rather than DDM as the solubilisation detergent. NG does not stabilise UapA as well as DDM<sup>93</sup>. However, as described earlier, addition of xanthine caused significant stabilisation of UapA-WT and UapA-G411V $\Delta_{1-11}$ <sup>93</sup>. This work used DDM, since this is the detergent

historically used for UapA structural characterisation<sup>1</sup>. Promisingly, these substrates do not appear to significantly destabilise UapA in the DDM-solubilised membrane environment, suggesting the structural characterisation of UapA with these substrates bound may be achievable.

### 3.3.5. Thermostability assays of purified UapA in detergent

As discussed in Section 3.3.4, cellular thermal shift assays and fluorescence size exclusion chromatography can utilise whole-cell, cell-lysate or solubilised membrane samples<sup>207,208</sup>. However the application of CETSA for UapA produced inconsistent results, and FSEC showed that addition of known substrates of UapA to detergent-solubilised membranes containing UapA had no observable effect on stability. It is postulated that this may be in part due to indirect effects of UapA being part of a heterogenous sample, since both used samples of solubilised membranes containing UapA-GFP, with fluorescence as the read-out. To explore this, differential scanning fluorimetry experiments were conducted on UapA purified in detergent.

Differential scanning fluorimetry can utilise both dye-based and dye-free approaches. Dye-based approaches require the addition of protein-reactive modifiers such as CPM (7-diethylamino-3-(4'-Maleimidylphenyl) or SYPRO™ Orange. CPM and SYPRO™ Orange are used due to their propensity to preferentially bind membrane and soluble proteins via their exposed cysteine residues and hydrophobic regions respectively as the proteins unfold upon heating<sup>211,212</sup>.

#### 3.3.5.1. Fluorescence-based thermostability assays using CPM

UapA-G411V $\Delta$ 1-11, UapA-Q408E $\Delta$ 1-11 and UapA-WT were incubated with the given substrate prior to the addition of the thiol reactive dye CPM (7-diethylamino-3-(4'-Maleimidylphenyl). The assay was incubated at 40 °C, and the normalised relative fluorescence units (excitation: 384 nm, emission: 470 nm) plotted against time.

UapA-G411V $\Delta_{1-11}$  appeared to be stabilised by xanthine, hypoxanthine and 3-benzylxanthine (5) relative to no substrate (Figure 34). This construct was most stabilised by 3-benzylxanthine (5). Xanthine is a known ligand of UapA-G411V $\Delta_{1-11}$  and was expected to stabilise the construct relative to no substrate, while hypoxanthine was not expected to stabilise UapA-G411V $\Delta_{1-11}$ , which may be due to non-specific binding interactions. UapA-Q408E $\Delta_{1-11}$  was similarly stabilised by xanthine, hypoxanthine and 3-benzylxanthine (5) relative to no substrate (Figure 35). It was most stabilised by hypoxanthine, which is consistent with prior studies that have shown UapA-Q408E $\Delta_{1-11}$  shows selectivity for hypoxanthine over xanthine<sup>93</sup>. As expected, UapA-WT showed the lowest overall stability (Figure 36). UapA-WT appeared to be slightly stabilised by 3-benzylxanthine (5), but generally, addition of xanthine and hypoxanthine did not appear to significantly improve protein stability.

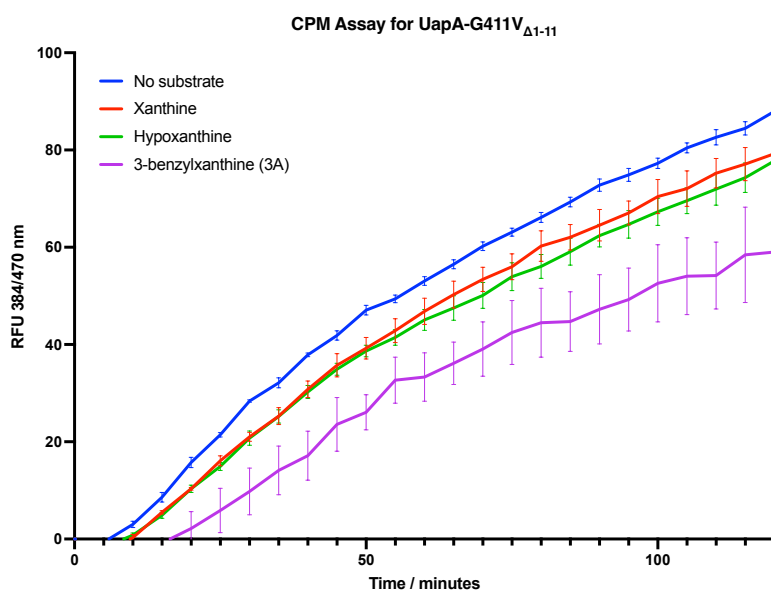


Figure 34: Thermal denaturation analysis of UapA-G411V $\Delta_{1-11}$  (0.067 mg/mL) with different substrates (0.6 mM). Experiments were completed in triplicate, mean values for each time point, with standard error bars shown.

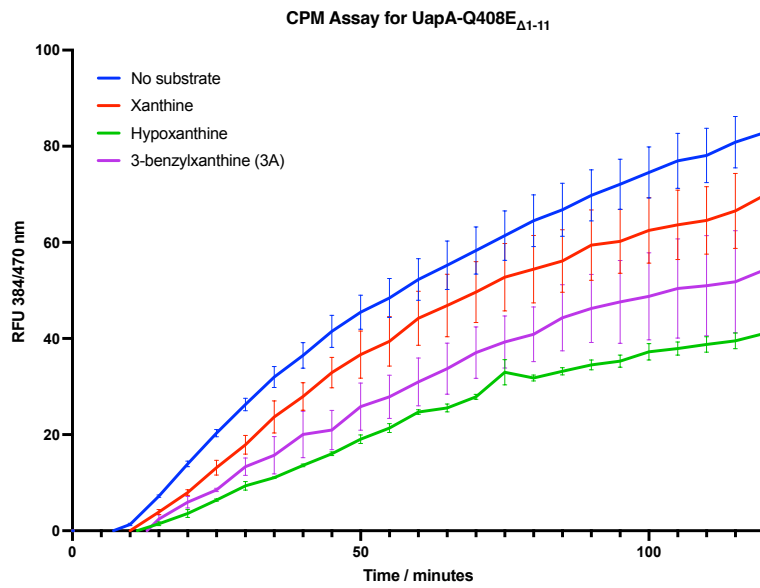


Figure 35: Thermal denaturation analysis of UapA-Q408E $\Delta$ 1-11 (0.067 mg/mL) with different substrates (0.6 mM). Experiments were completed in triplicate, mean values for each time point, with standard error bars shown.

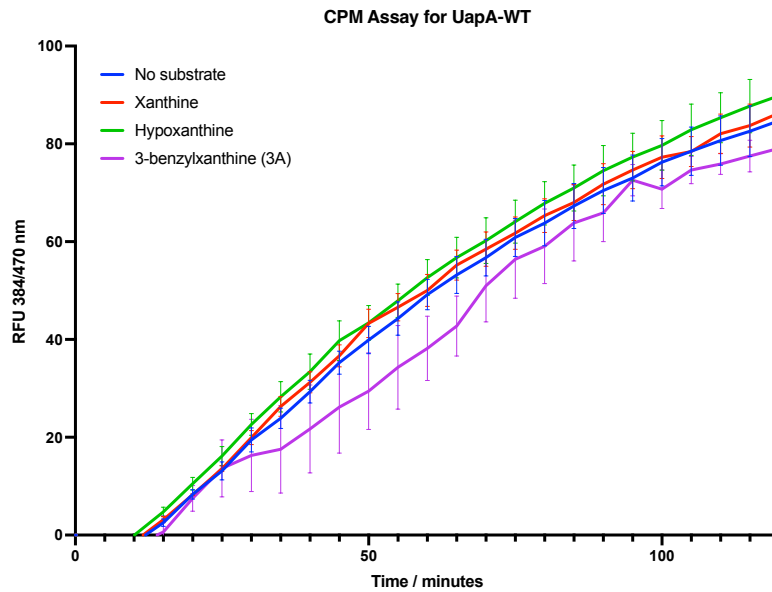


Figure 36: Thermal denaturation analysis of UapA-WT (0.067 mg/mL) with different substrates (0.6 mM). Experiments were completed in triplicate, mean values for each time point, with standard error bars shown.



### 3.3.5.2. Nano-differential scanning fluorimetry (Nano-DSF)

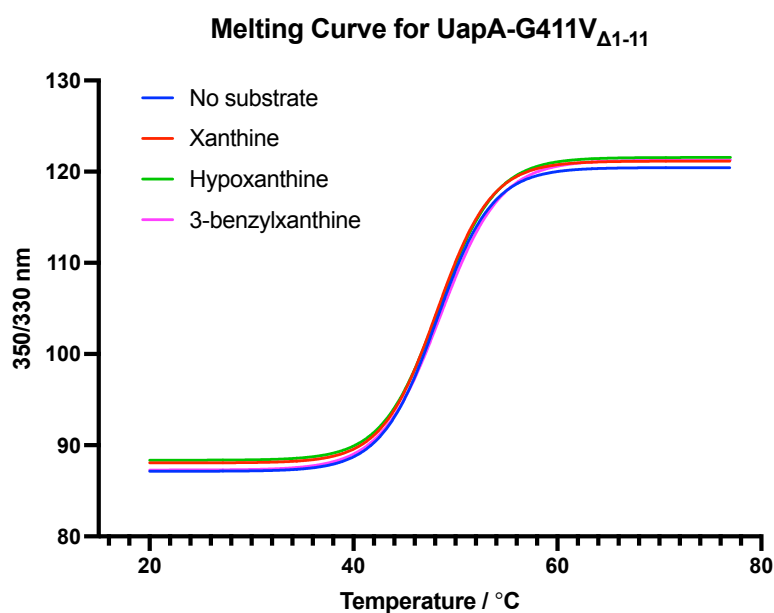
Nano-differential scanning fluorimetry offers a convenient dye or conjugate-fluorophore free alternative by taking advantage of the intrinsic fluorescence of tryptophan-containing proteins. On protein unfolding, there is a corresponding increase in tryptophan fluorescence, allowing for the precise calculation of melting temperatures from melting curves. This increase in tryptophan fluorescence upon unfolding results from decreased quenching of tryptophan residues by neighbouring residues, as a result of increased solvent exposure<sup>213</sup>. This technique was used to assess the thermostability of the three constructs of UapA (WT, Q408E $\Delta_{1-11}$  and G411V $\Delta_{1-11}$ ) with an array of substrates, at a concentration of 0.6 mM, the concentration of substrate historically used for successful crystallisation trials of UapA-G411V $\Delta_{1-11}$ <sup>93</sup>.

The melting temperature experiment was conducted as described in Section 3.2.9. Melting curves were plotted following the 350/330nm ratio against temperature. Samples were analysed in quadruplicate alongside a control of the same protein without any substrate. Above 77 °C, decreased values for 350/330nm were observed, due to the formation of large protein aggregates. This interfered with calculation of the inflection point of the melting curves, so the data was cropped to temperatures between 20-77 °C. The apparent melting temperature ( $T_m$ ) was calculated from the interpolation of the fitted sigmoidal distribution.

UapA-G411V $\Delta_{1-11}$  was unaffected by the addition of xanthine or hypoxanthine (Figure 37). In the absence of substrate, the melting temperature was calculated at 48.1 °C  $\pm$  0.1 (SE). This was within the standard error of melting temperatures for xanthine (48.1 °C  $\pm$  0.1 (SE)) and hypoxanthine (48.3 °C  $\pm$  0.2 (SE)). 3-benzylxanthine (**5**) did appear to slightly stabilise UapA-G411V $\Delta_{1-11}$  relative to no substrate, with a calculated melting temperature of 48.5 °C  $\pm$  0.2 (SE). The overall lack of effect of

substrate on UapA-G411V $\Delta$ 1-11 is likely to be a consequence of this mutant being conformationally locked in the inward-facing conformation<sup>93,214</sup>.

A



B

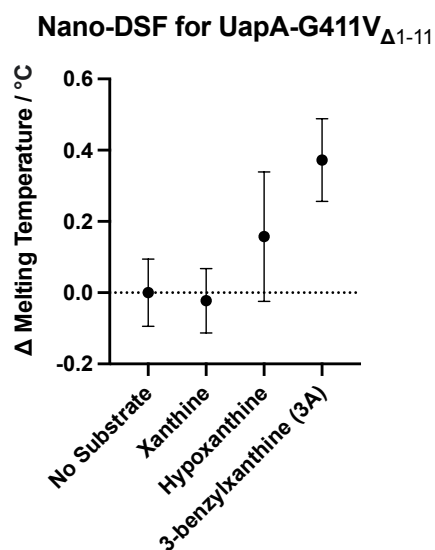
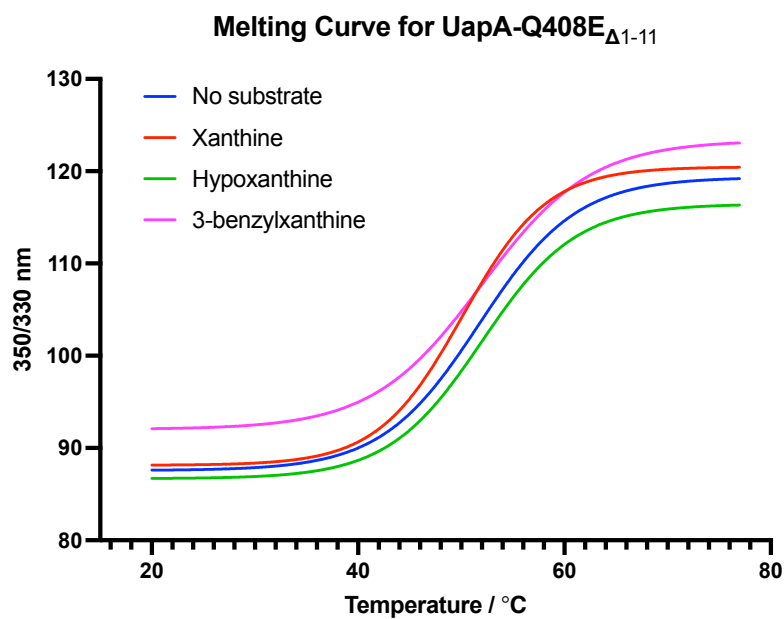


Figure 37: A) Nano-DSF melting curve representing mean of quadruplicate experiments. Nano-DSF experiments were run between 15–95 °C using the 350/330 nm fluorescence ratio. Curves were plotted in GraphPad Prism 9, using a sigmoidal standard curve. B) Change in melting temperatures of UapA-G411V $\Delta$ 1-11 (1 mg/mL) with given substrate (0.6 mM), relative to mean melting temperature in the presence of no substrate (dotted line). Melting temperatures calculated through interpolation of the standard curve. Standard error (SE) bars indicated.

Unlike UapA-G411V $_{\Delta 1-11}$ , UapA-Q408E $_{\Delta 1-11}$  is not conformationally locked, and still possesses weak, transport activity. UapA-Q408E $_{\Delta 1-11}$  stability was largely unaffected by the presence of hypoxanthine or 3-benzylxanthine (5) (Figure 38). However, the protein was significantly destabilised by the addition of xanthine (50.1 °C  $\pm$  0.3 (SE)). In the absence of substrate, the melting temperature was calculated at 52.1 °C  $\pm$  0.4 (SE). This was within the standard error of melting temperatures for hypoxanthine (48.3 °C  $\pm$  0.2 (SE)) and 3-benzylxanthine (5) (51.9 °C  $\pm$  0.1 (SE)). Xanthine destabilising UapA-Q408E $_{\Delta 1-11}$  is consistent with prior unpublished hydrogen-deuterium exchange mass spectrometry results by Dr Euan Pyle, which has suggested that UapA-Q408E $_{\Delta 1-11}$  when bound to xanthine is in a more outward-facing conformation, when compared with UapA-Q408E $_{\Delta 1-11}$  bound to hypoxanthine (see Section 4.3.6). Moreover, the greater standard errors observed in results from UapA-Q408E $_{\Delta 1-11}$  compared with UapA-G411V $_{\Delta 1-11}$  may reflect the fact that UapA-Q408E $_{\Delta 1-11}$  is able to undergo large conformational transitions.

Unfortunately, while the same experiment was completed for UapA-WT (Figure 39), significant aggregation was observed under the conditions of this experiment. The melting temperatures in the presence of no substrate (57.7 °C  $\pm$  0.5 (SE)) are not representative of the known instability of this construct. It is likely that reduced protein concentration and large aggregate formation led to a shallower sigmoidal standard curve, where there is greater error in calculation of the melting temperature.

A



B

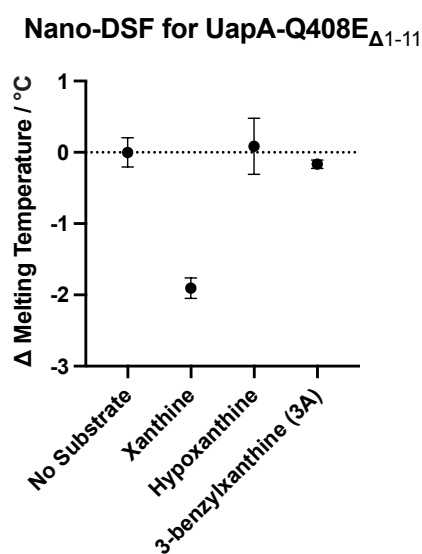
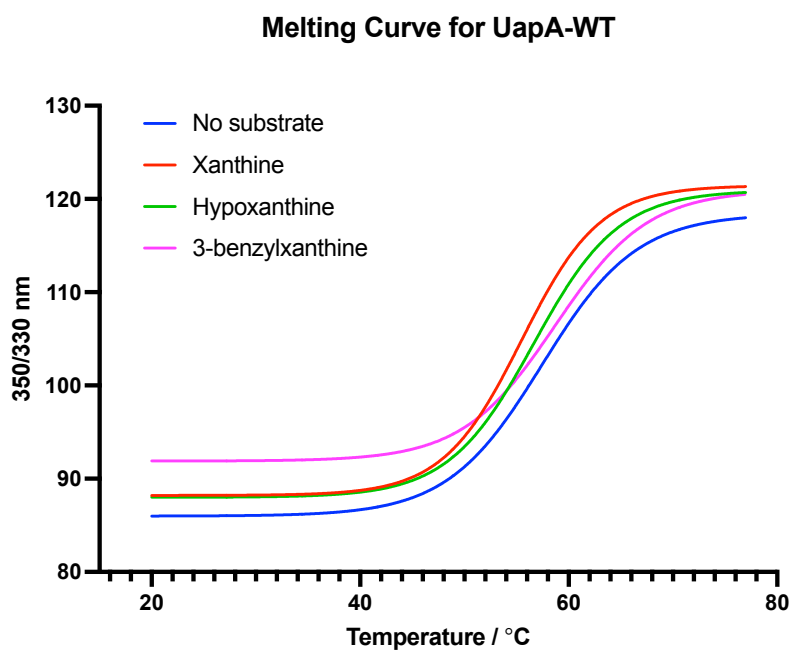


Figure 38: A) Nano-DSF melting curve of UapA-Q408E $\Delta$ 1-11 (1 mg/mL) with given substrate (0.6 mM), representing mean of quadruplicate experiments. Nano-DSF experiments were run between 15–95 °C using the 350/330 nm fluorescence ratio. Curves were plotted in GraphPad Prism 9, using a sigmoidal standard curve. B) Change in melting temperatures of UapA-Q408E $\Delta$ 1-11 (1 mg/mL) with given substrate (0.6 mM), relative to mean melting temperature in the presence of no substrate (dotted line). Melting temperatures calculated through interpolation of the standard curve. Standard error bars indicated.

A



B

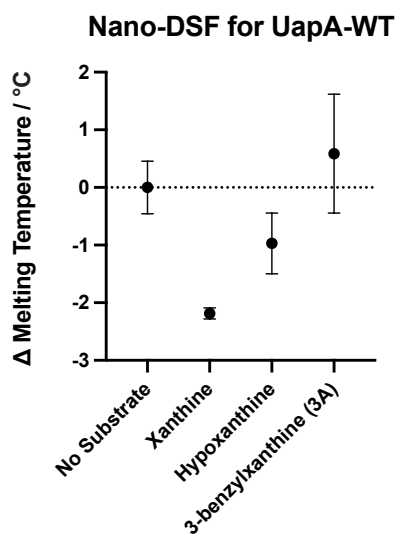


Figure 39: A) Nano-DSF melting curve representing mean of quadruplicate experiments. Nano-DSF experiments were run between 15–95 °C using the 350/330 nm fluorescence ratio. Curves were plotted in GraphPad Prism 9, using a sigmoidal standard curve. B) Change in melting temperatures of UapA-WT (1 mg/mL) with given substrate (0.6 mM), relative to mean melting temperature in the presence of no substrate (dotted line). Melting temperatures calculated through interpolation of the standard curve. Standard error bars indicated.

### 3.4. Discussion

Functional characterisation of the novel purine analogues required understanding their activity *in vitro* in strains of *Aspergillus nidulans*, and exploring their interaction at the level of the transporter, in crude solubilised membranes and with purified protein.

Competitive uptake assays using  $^3\text{H}$ -xanthine revealed that the novel substrates compounds **1**, **2**, **3**, **5** and **13** bind UapA, with affinities varying between 0.2–400  $\mu\text{M}$ . 3-benzylxanthine (**5**), appeared to bind UapA-WT with an affinity 35x greater than the native substrates xanthine and uric acid (0.2  $\mu\text{M}$ ). However, neither 3-benzylxanthine (**5**) nor the other newly synthesized analogues showed any toxicity towards strains of *A. nidulans*. They also could not act as nitrogen sources, at 1 mM, in fungal growth assays. Finally, they did not induce endocytosis of GFP-labelled UapA in *A. nidulans*, suggesting they may not be transported, instead acting as non-transportable competitive inhibitors.

The functional characterisation of these substrates and their effect on *A. nidulans* shows no evidence for substrate uptake by UapA. To show transport conclusively, it would be necessary to radiolabel the novel substrate. Alternatively, the UapA transporter could be reconstituted into artificial bilayers such as liposomes or expressed in oocytes. Uptake of a given substrate could then be assessed using liquid chromatography mass spectrometry<sup>215,216</sup>.

Finally, a variety of thermostability techniques were used to determine if these novel substrates were stabilising or destabilising UapA. Cellular thermal shift assays (CETSA) and fluorescence size exclusion chromatography (FSEC) were used to determine any effect of novel substrates on UapA-WT and mutants in solubilised membranes. Since this is a crude solubilised membrane sample, indirect effects,

such as the heterogeneous lipidic environment, were difficult to exclude. Subsequent thermostability assays with purified UapA in detergent utilised nano-differential scanning fluorimetry (nano-DSF) and CPM-based thermal stability assay.

3-benzylxanthine (**5**) binds UapA-WT with high affinity in *Aspergillus nidulans* (0.2  $\mu\text{M}$ ). CPM assays with purified protein suggest that 3-benzylxanthine (**5**) may stabilise UapA-WT relative to no substrate. Nano-DSF and CPM assay results both suggest that 3-benzylxanthine (**5**) may stabilise the conformationally locked UapA-G411V $\Delta_{1-11}$  mutant relative to no substrate. Finally, CPM results suggest that 3-benzylxanthine (**5**) appears to stabilise UapA-Q408E  $\Delta_{1-11}$  relative to no substrate or xanthine, but destabilise it relative to hypoxanthine. The relative inconsistencies in stabilisation or destabilisation between nano-DSF and CPM assays is possibly due to concentration of the substrate (0.6 mM) relative to concentration of the protein. For nano-DSF, the final concentration of UapA was 1 mg/mL or 16.4  $\mu\text{M}$  (monomer). For the CPM assays, the final concentration of UapA was 0.067 mg/mL or 1.1  $\mu\text{M}$  (monomer). Consequently, there was 37-fold and 550-fold more substrate than protein in nano-DSF and CPM assays respectively. Further experiments would need to be completed optimising the concentration of substrate, since indirect binding interactions may be influencing overall protein stability.

Ultimately, these thermostability assays have shown that 3-benzylxanthine (**5**) binding does not significantly destabilise UapA-WT, UapA-Q408E $\Delta_{1-11}$  or UapA-G411V $\Delta_{1-11}$ . If 3-benzylxanthine (**5**) is not being transported, and acting as a non-competitive inhibitor, it may be useful tool to trap UapA in a new conformation.

## 4. Structural characterisation of UapA with novel substrates

### 4.1. Introduction

In order to establish the precise nature of the interaction between 3-benzylxanthine (**5**) and UapA, UapA was purified in detergent or reconstituted into nanodiscs ready for structural studies. Techniques used in this work to structurally characterise UapA include X-ray crystallography, negative-stain electron microscopy, cryo-electron microscopy, and hydrogen-deuterium exchange mass spectrometry.

Three different UapA constructs were used in this work, UapA-WT, UapA-G411V $_{\Delta 1-11}$  and UapA-Q408E $_{\Delta 1-11}$ . Both UapA-G411V $_{\Delta 1-11}$  and UapA-Q408E $_{\Delta 1-11}$  lack the 11 N-terminal amino acids and have a single point mutation at G411 and Q408 respectively. Fluorescence microscopy of UapA-Q408E and UapA-G411V in *A. nidulans* have shown that these proteins traffic correctly to the membrane, with UapA-GFP fluorescence associated with the plasma membrane and the septa of growing hyphal cells.<sup>1</sup> In *A. nidulans*, UapA-G411V $_{\Delta 1-11}$  and UapA-Q408E $_{\Delta 1-11}$  exhibit no or minimal transport activity respectively in <sup>3</sup>H-xanthine uptake assays (described in Section 3.3.1).

As discussed in Section 3.2.4, UapA-WT, UapA-G411V $_{\Delta 1-11}$  and UapA-Q408E $_{\Delta 1-11}$  were heterologously expressed in *Saccharomyces cerevisiae* with C-terminal GFP. Both UapA-G411V $_{\Delta 1-11}$  and UapA-Q408E $_{\Delta 1-11}$  exhibit increased stability compared to UapA-WT in crude solubilised extracts<sup>93</sup>. This suggests that each mutant has reduced conformational flexibility relative to the WT<sup>93</sup>. UapA-G411V $_{\Delta 1-11}$  is known to bind xanthine with high affinity, and is conformationally locked in the inward



facing conformation<sup>1</sup>. UapA-Q408E<sub>Δ1-11</sub> in particular exhibits the ability to bind but not transport the non-physiological substrate, hypoxanthine<sup>1</sup> ( $K_i = 71 \mu\text{M}$ ).

The structure of UapA-G411V<sub>Δ1-11</sub> revealed that this construct is trapped in the inward facing conformation.<sup>1</sup> Currently no structure is currently available of the UapA-Q408E<sub>Δ1-11</sub>. A Q408E/G411V double mutant possesses reduced stability compared to the single mutants suggesting that each mutant may stabilise the protein in a different conformation<sup>93</sup>. In addition, previous unpublished work using hydrogen-deuterium mass spectrometry has suggested that UapA-Q408E<sub>Δ1-11</sub> may favour the outward-facing or occluded conformation<sup>113</sup> (Section 4.3.6).

Chapter 3 described the functional characterisation of novel xanthine analogues. 3-benzylxanthine (**5**) has been found to bind UapA-WT in *A. nidulans* with high affinity ( $K_i = 0.2 \mu\text{M}$ ). Fungal growth assays have shown that 3-benzylxanthine (**5**) has no effect on fungal growth, and there is no evidence for transport in either fungal growth assays or fluorescence microscopy. Consequently, it is unclear how 3-benzylxanthine (**5**) interacts with UapA-WT: whether it is a transportable substrate or if it acts as a non-transportable competitive inhibitor. It is also unclear how the thermostabilising mutations G411V and Q408E will affect the binding affinity of 3-benzylxanthine (**5**).

The aim of the research outlined in this chapter was to better understand the interaction between 3-benzylxanthine (**5**) and UapA. If 3-benzylxanthine (**5**) binds UapA-WT with high affinity ( $0.2 \mu\text{M}$ ) and is not transported, it may be possible that 3-benzylxanthine (**5**) is strongly binding the outward or occluded conformation of UapA. This novel substrate may provide a useful tool to stabilise UapA in the outward facing conformation.

Given the understanding that UapA-G411V $\Delta_{1-11}$  is conformationally locked in the inward facing conformation, and UapA-Q408E $\Delta_{1-11}$ , while conformationally flexible, may favour the outward-facing or occluded conformation, differential mutant stabilisation or destabilisation may provide information about which conformational state 3-benzylxanthine (**5**) may bind.

UapA-WT and its mutants were purified in detergent or reconstituted into nanodiscs ready for structural studies. Techniques used in this work to structurally characterise UapA include X-ray crystallography, negative-stain electron microscopy, cryo-electron microscopy, and hydrogen-deuterium exchange mass spectrometry.

## 4.2. Materials and methods

### 4.2.1. Expression and Purification of UapA in DDM

See Section 3.2.4 and 3.2.7.

### 4.2.2. Crystallisation trials

Following protein purification as described in Section 3.2.7, UapA was concentrated to 8–12-mg/mL with the concentration confirmed using a NanoDrop™ Lite Spectrophotometer. Initial crystallisation trials were set up using sitting drop vapour diffusion, utilizing sparse matrix screens from Molecular Dimensions, specially designed to include conditions known to aid crystallization of membrane proteins: MemStart/Sys, MemGold, MemMeso, MemTrans, MemChannel and MemGold2.<sup>119</sup>

Purified protein (100 nL) and crystallisation condition (100 nL) were combined utilising a Mosquito® crystallisation robot (TTP LabTech). The combined drop was left

to equilibrate with 85  $\mu\text{L}$  of precipitant in a plastic 96-well setup. All plates were covered and incubated for 24–96 hours at 4 °C or 20 °C. Plates were manually monitored and imaged using a Leica M125 microscope.

Optimisation screens were set up in Greiner 24-well Combo Plates (MD3-16) with sitting drop bridges (MD3-17). A reservoir of 500 or 800  $\mu\text{L}$  was used. Purified protein (11.5 mg/mL, 1  $\mu\text{L}$ ) was combined with reservoir (1  $\mu\text{L}$ ) in the inner well. Hanging-drop crystallisation trials were set up using pre-greased Greiner 24 well Combo Plates (MD3-21) with the protein (1  $\mu\text{L}$ ) and crystallisation condition (1  $\mu\text{L}$ ) combined on an inverted coverslip. A reservoir of 500/800  $\mu\text{L}$  was used. As before, all plates were covered and incubated for 24–96 hours at 20 °C. Plates were manually monitored and imaged using a Leica M125 microscope.

Crystals were fished and flash-frozen, ready for X-ray data collection using the I24 microfocus beamline at the Diamond Light Source in Oxfordshire<sup>127</sup>.

#### 4.2.3. Nanodisc reconstitution for UapA

This protocol was adapted from a previous PhD student<sup>113</sup>. Purification of UapA followed the same method outlined in Section 3.2.7. However, prior to the final size exclusion chromatography step, instead the protein concentration was estimated using a nano-drop. The protein was incubated with yeast polar extract lipids (see Section 4.2.5) and MSP1E3D1 (see Section 4.2.6 and 4.2.7) in a 1:5:500 UapA:MSP1E3D1:Lipid ratio. Samples were mixed for 1 hour with rocking at 4 °C. Biobeads SM-2 (Bio-Rad) (400 mg per 350  $\mu\text{g}$  UapA) were added to remove DDM. The mixture was incubated for a further 2 hours at 4 °C and then 1 hour at room temperature. Biobeads were removed by centrifugation (1000 g, 30 seconds). The mixture was then concentrated down to less than 500  $\mu\text{L}$  (100 kDa MWCO), before being injected into a *Superdex200* Increase 10/300 GL size exclusion

chromatography column pre-equilibrated in buffer I (20 mM Tris pH 7.5, 150 mM NaCl). Fractions containing nanodiscs with UapA reconstituted were identified by column retention time and confirmed by SDS-PAGE gel (see Section 3.2.8).

#### 4.2.4. Nanodisc reconstitution for UapA-GFP

Purification of UapA started by following the same method outlined in Section 3.2.7. However, TEV protease was not added to the overnight dialysis. After 16 hours, the dialysate was concentrated to 10 mL. Protein concentration was estimated by measuring GFP fluorescence. The protein was incubated with yeast polar extract lipids (see Section 4.2.5) and MSP1E3D1 (see Section 4.2.6 and 4.2.7) in a 1:5:500 UapA:MSP1E3D1:Lipid ratio. Samples were mixed for 1 hour with rocking at 4 °C. Biobeads SM-2 (Bio-Rad) (400 mg per 350 µg UapA) were added to remove DDM. The mixture was incubated for a further 2 hours at 4 °C and then 1 hour at room temperature. Biobeads were removed by centrifugation (1000 g, 30 seconds).

The sample was loaded onto a 5 mL HisTrap column (GE Healthcare) pre-equilibrated with buffer J (50 mL; 20 mM Tris pH 7.5, 150 mM NaCl, 15 mM imidazole). The column was washed with buffer K (50 mL; 20 mM Tris pH 7.5, 150 mM NaCl, 20 mM imidazole). The protein was eluted with 30 mL of buffer L (40 mM Tris pH 8, 0.3 M NaCl, 0.4M imidazole).

TEV protease was added (1:1 TEV:UapA) and the mixture dialysed (12 kDa MWCO) with buffer M (1500 mL; 20 mM TRIS pH 7.5, 150 mM NaCl, 5% glycerol) for 16 hours. Aggregated protein was pelleted (5 minutes, 2095 g, 4 °C), the supernatant filtered (0.2 µm), 10 mM imidazole added, and the sample loaded onto a pre-equilibrated His-Trap (5 mL). Flow through was concentrated (100 kDa MWCO) and then injected into a Superdex 200 Increase 10/300 GL SEC column pre-equilibrated in buffer I (20 mM TRIS pH 7.5, 150 mM NaCl). Fractions containing nanodiscs with

UapA reconstituted were identified by column retention time and confirmed by SDS-PAGE gel (see Section 3.2.8).

#### 4.2.5. Lipid reconstitution for nanodiscs

Polar extract lipids from *Saccharomyces cerevisiae* (Avanti Polar Lipids) were dissolved in chloroform at a concentration of 25 mg/mL. The chloroform was evaporated under a nitrogen stream to generate a lipid film. Lipids were resuspended in buffer H (20 mM Tris pH 7.5, 150 mM NaCl, 7.5 % DDM) to a final concentration of 40 mg/mL. The suspension was vortexed between cycles of freeze-thawing using liquid nitrogen. Lipids once dissolved, were aliquoted stored at -80 °C.

#### 4.2.6. MSP1E3D1 expression

The His-tagged membrane scaffold protein (MSP1D1E3) was incorporated into a pET-28a(+) plasmid and transformed into *Escherichia coli* (BL21 DE3 strain). Positive transformants were selected for on LB-agar plates containing 0.1 mg/mL kanamycin. A single colony was used to inoculate a 10 mL starter culture in terrific broth (TB) supplemented with 0.1 mg/mL kanamycin. The culture was incubated overnight (37 °C, 220 RPM), before being diluted in 6 x 1 L of TB media supplemented with 0.1 mg/mL kanamycin. The cultures were incubated until the OD600 reached 2.0-2.5 (37 °C, 220 RPM). Expression was induced by addition of 1 mM IPTG. The culture incubated for a further 4 hours (37 °C, 220 RPM) before the cells were harvested under centrifugation (10 minutes, 4000 g, 4 °C). The cell pellet was resuspended in lysis buffer (25 mL per L of culture; 20 mM sodium phosphate pH 7.4, 1% v/v Triton X-100). This mixture was supplemented with one Protease Inhibitor Cocktail tablet (Roche, cOmplete) and 1 mg deoxyribonuclease I.

#### 4.2.7. MSP1E3D1 purification

Cells were lysed using a Constant Systems cell disruptor (26 KPSI) and the lysate ultra-centrifuged at 4 °C, 41000 RPM, 2 hours. The soluble fraction was loaded onto a 5 mL HisTrap column (GE Healthcare) pre-equilibrated with 40 mM phosphate buffer, pH 7.4. The column was washed with Buffer N (40 mM Tris pH 8, 300 mM NaCl, 1 % v/v Triton X-100), Buffer O (40 mM Tris pH 8, 300 mM NaCl, 20 mM imidazole, 50 mM sodium cholate) and Buffer P (40 mM Tris pH 8, 0.3 M NaCl, 50 mM imidazole). The protein was eluted with 30 mL of buffer Q (40 mM Tris pH 8, 0.3 M NaCl, 0.4M imidazole). His-tagged TEV protease was added (80 µg TEV: 1 mg MSP1D1E3) to the elute, and the mixture dialysed (12 kDa MWCO) against Buffer R (20 mM Tris pH 7.5, 0.1 M NaCl, 0.5 mM EDTA) for 16 hours at 4 °C.

The dialysed sample was then loaded onto a 5 mL HisTrap column (GE Healthcare) pre-equilibrated with buffer S (40 mM phosphate buffer, pH 7.4). The flow-through was concentrated (30 kDa MWCO). Protein concentration was measured using a NanoDrop™ Lite Spectrophotometer and concentrated to 12–18 mg/mL ( $\epsilon = 29,910 \text{ (mg/ml)}^{-1}\text{cm}^{-1}$ ). The isolated protein was aliquoted, flash frozen in liquid nitrogen and stored at -80 °C until use.

#### 4.2.8. Hydrogen-deuterium exchange mass spectrometry

Samples of UapA-Q408E in nanodiscs were prepared as described in Section 4.2.4. Hydrogen-deuterium exchange mass spectrometry analysis was completed by Dr Waqas Javed in the research group of Professor Argyris Politis, associated with the University of Manchester. Both were formerly associated with Kings College London, where the initial data collection took place. These methods are not part of my experimental work. Protocols for sample labelling, sample digestion and data analysis were adapted from a prior PhD student's as yet unpublished work<sup>113</sup>.

#### 4.2.9. Negative-stain electron microscopy

UapA purified in DDM (see Section 3.2.7) or UapA reconstituted in nanodiscs (Section 4.2.4) was diluted to 0.01 mg/mL and used to prepare negative stain grids for electron microscopy screening. Carbon-coated copper grids (Carbon Film 300 Mesh Cu, Agar Scientific) were glow-discharged using an Agar Turbo Carbon Coater (Agar Scientific) for 60 seconds. A 3  $\mu$ L aliquot of protein was applied to each grid for 60 seconds. Grids were washed with 2% uranyl acetate (3 $\times$ 30  $\mu$ L). Following 60 seconds of incubation with 2% uranyl acetate, excess uranyl acetate was removed by blotting from the side with filter paper. The negative stain grids were then screened on a 120 keV Tecnai T12 electron microscope, with images collected using an FEI 2K eagle camera.

#### 4.2.10. Cryo-electron microscopy

UapA reconstituted in nanodiscs (Section 4.2.4) was diluted and concentrated to 0.7–1 mg/mL, and used to prepare cryo-electron microscopy grids, ready for screening. Quantifoil R 2/2 Cu 300 (Agar Scientific) were glow-discharged with Agar Turbo Carbon Coater (Agar Scientific) for 60 seconds. A 3  $\mu$ L aliquot of protein was applied to the grid, grids were blotted and then plunged into liquid ethane using a Vitrobot mark IV (Thermo Fisher Scientific). Sample application and blotting were performed at 4 °C and 100% humidity. Blotting times were optimised between 2 and 12 seconds. The blot force was varied between -2 and -4 (A.U.). Plunge frozen grids were stored under liquid nitrogen until screening.

Grids were screened by Dr Ben Phillips using the 200 keV Glacios 2 Cryo-TEM at the Institute of Cancer Research (ICR), London and the 200 keV Glacios XFEG at the Electron Microscopy facility within Imperial College London (ICL). Images were collected with magnification 1.1  $\text{\AA}/\text{pixel}$ , defocus 2–2.5  $\mu\text{m}$ , dose 40  $\text{e}/\text{\AA}^2$ . 5139

micrographs were collected, and 2D classes were generated from 187,887 particles.  
Data processing was conducted in CryoSparc by Dr Ben Phillips.



## 4.3. Results

### 4.3.1. Purification of UapA in DDM

UapA-G411V $\Delta_{1-11}$ , UapA-Q408E $\Delta_{1-11}$  and UapA-WT, were expressed and purified as described in Section 3.2.4 and 3.2.7. For UapA-WT, UapA-G411V $\Delta_{1-11}$  and UapA-Q408E $\Delta_{1-11}$ , the purified protein elutes between 10.5-12.5 mL, with slight variations in retention volume between the mutants (Figure 40). The elute was examined by SDS-PAGE analysis, which found that all proteins migrate as a single band at 40–50 kDa, with a second fainter band at 80–100 kDa corresponding to the dimer (Figure 41). UapA-WT is much less stable than the truncated mutants, with significant material lost by aggregation throughout the purification process. The elution peak in size exclusion chromatography (SEC) is not fully monodispersed, with a broad aggregate shoulder to the left hand side of the peak. However, SDS-PAGE analysis found that, as for the mutants, the protein migrates as a single band, with a second fainter band at 80–100 kDa corresponding to the dimer (Figure 41). This does not correlate with the known molecular weight of UapA (monomer: 61.1 kDa, dimer: 122.2 kDa). The anomalous SDS-PAGE migration of membrane proteins has previously been explained by detergent binding<sup>217</sup>.

UapA-G411V $\Delta_{1-11}$  and UapA-Q408E $\Delta_{1-11}$  are stabilised relative to the WT protein<sup>93</sup>. From a 6 L expression of UapA-G411V $\Delta_{1-11}$  and UapA-Q408E $\Delta_{1-11}$ , the average yield was between 0.7–0.8 mg in total. For UapA-WT, purification was from 12 L, and yielded between 0.5–0.6 mg of protein (57–69% less yield per L). Generally, purification of UapA was performed in the absence of substrate, to enable a variety of substrates to be added following successful isolation.

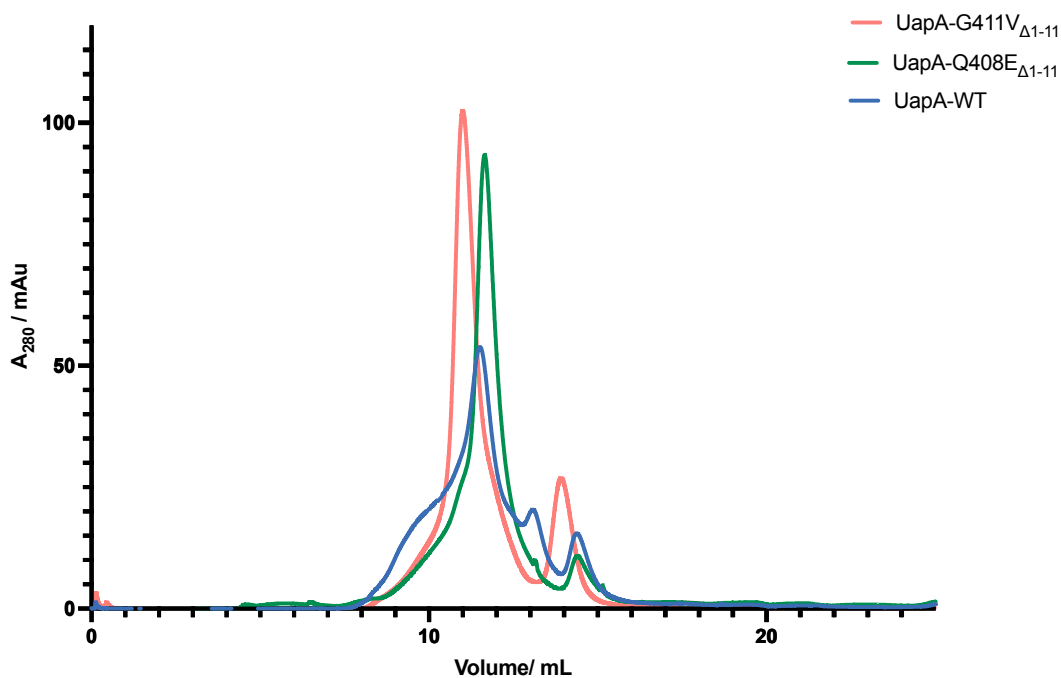


Figure 40: UV absorbance profile ( $A_{280\text{nm}}$ ) of UapA-G411V $_{\Delta 1-11}$  (red), UapA-Q408E $_{\Delta 1-11}$  (green) and UapA-WT (blue) following Size-Exclusion Chromatography (SEC).

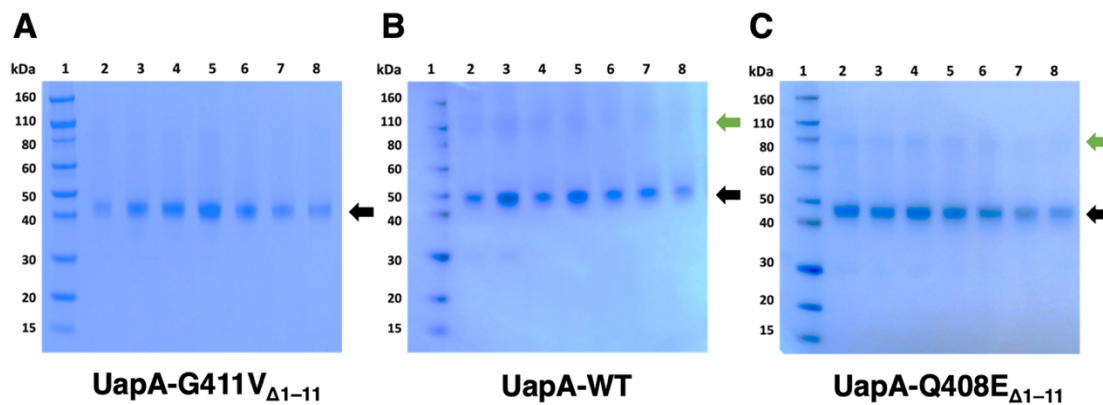


Figure 41: Fractions from size exclusion chromatography of UapA-G411V $_{\Delta 1-11}$  (A), UapA-WT (B) and UapA-Q408E $_{\Delta 1-11}$  (C) were examined using a NuPage™ 4-12% Bis-Tris SDS-PAGE Gel (35 minutes, 200 V, 120 mA), with a Novex pre-stained protein standard as reference. Gels were rinsed, Coomassie-stained and visualised in a BioRad Gel Imaging System. Generally, UapA migrates as a single band, between 40–50 kDa (black arrow). In some cases, a second band between 80–100 kDa is observed (green arrow), corresponding to the UapA dimer.

### 4.3.2. Crystallisation trials of UapA

Crystallisation trials of UapA-WT, UapA-G411V<sub>Δ1-11</sub> and UapA-Q408E<sub>Δ1-11</sub> were set up as described in Section 4.2.2. Crystals formed in several conditions, and across all constructs the hits were limited to two of the six sparse matrix screens: MemTrans and MemGold2.

#### 4.3.2.1. Crystallisation of UapA-G411V<sub>Δ1-11</sub> with 3-benzylxanthine (**5**)

The structure of UapA-G411V<sub>Δ1-11</sub> in complex with xanthine has successfully been determined using crystallography<sup>1</sup>. As such, initial co-crystallisation experiments of UapA-G411V<sub>Δ1-11</sub> with 3-benzylxanthine (**5**) were attempted using the same crystallisation conditions outlined in the literature (0.1 M MES pH 6.5, 30% PEG-300, 0.03% DDM, 1% n-hexyl-b-D-glucopyranoside vapour diffusion sitting drops at 20 °C). However, on replacement of xanthine with 3-benzylxanthine (**5**), no crystals formed. Consequently, co-crystallisation screening was attempted using sparse matrix screens MemStart/Sys, MemGold, MemMeso, MemTrans, MemChannel and MemGold2. However, once again, no crystallisation hits were identified.

Finally, soaking of 3-benzylxanthine (**5**) into pre-existing apo-crystals of UapA-G411V<sub>Δ1-11</sub> was attempted. In the absence of 3-benzylxanthine (**5**), UapA-G411V<sub>Δ1-11</sub> crystallised in MemTrans C5 (0.01M MnCl<sub>2</sub>·4H<sub>2</sub>O, 0.1M MES pH 6.5, 30% PEG 400) and MemTrans D3 (0.1 M MES 6.5, 15 % w/v PEG 2000 MME) (Table 9).

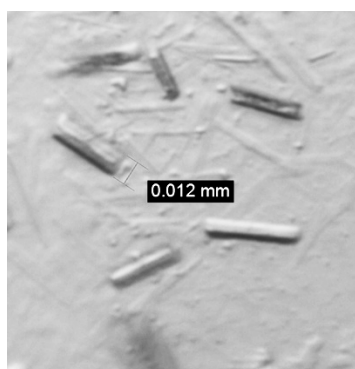
Table 9: Crystallisation hits for UapA-G411V $\Delta_{1-11}$  from initial screening using sparse matrix Molecular Dimensions screens MemStart/Sys, MemGold, MemMeso, MemTrans, MemChannel and MemGold2.

Screen	Condition	Substrate?	[Protein] mg/mL	T °C	Time hours
MemTrans	C5: 0.01M MnCl <sub>2</sub> .4H <sub>2</sub> O 0.1M MES pH 6.5, 30% PEG 400	Apo only	10.0	20.0	48
	D3: 0.1 M MES 6.5 15 % w/v PEG 2000 MME	Apo only	10.0	20.0	48

Optimisation screens were designed based on MemTrans C5 (Figure 42) and D3 (Figure 43), varying buffer pH and precipitant concentration. Optimisation screening around MemTrans D3 led to the identification of different crystal morphologies at different pH and precipitant concentration (Figure 43). Hanging and sitting drop optimisation screens were set up by hand with a protein concentration of 10 mg/mL, drop size of 1  $\mu$ L protein and 1  $\mu$ L precipitant, and 500–800  $\mu$ L of precipitant reservoir. The plates were incubated at 20 °C and monitored with a Leica M125 microscope.

		pH (0.1M MES)					
		5.5	6.0	6.5	7.0	7.5	8.0
% PEG-400	28						
	30		X	Y			
	32						
	34						

X



Y

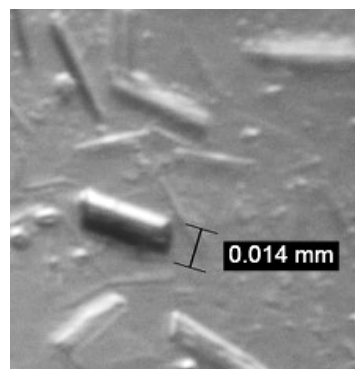


Figure 42: Top, Optimisation screen for apo UapA-G411V<sub>Δ1-11</sub> based upon MemTrans C5. Optimisation screens focused on varying buffer pH and PEG concentration. Hits are indicated by letters, corresponding to an image of the crystal in the panel below. Y indicated the original hit. Bottom, Visible light microscopy images of crystals obtained during MemTrans C5 optimisation screening, Leica M125 microscope. Crystals were generally rod-shaped, and varied between 12-14 μm in width. Scale bars are indicated.

		pH (0.1M MES)					
		5.5	6.0	6.5	7.0	7.5	8.0
% PEG-2000	13				Z		
	15		X	Y			
	17						
	19						

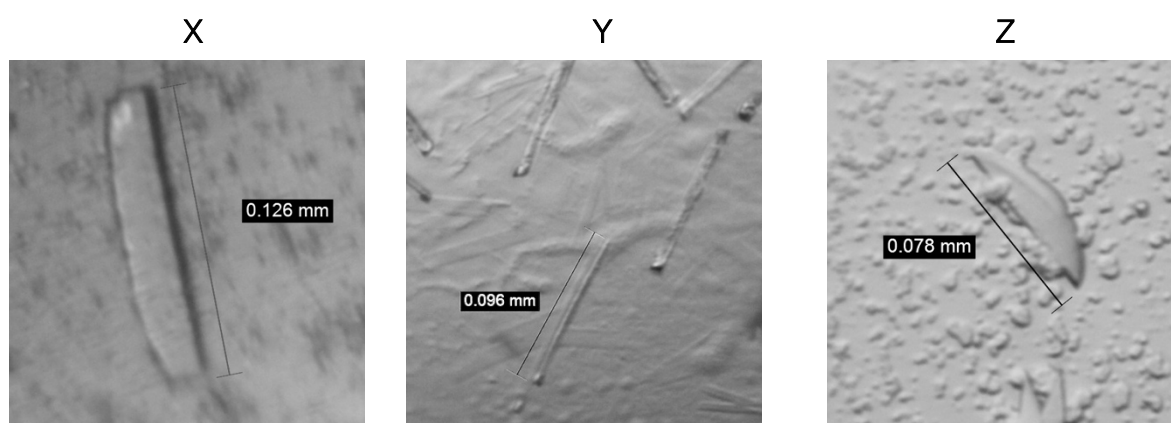


Figure 43: Top, Optimisation screen for apo UapA-G411V $_{\Delta 1-11}$  based upon MemTrans D3. Optimisation screens focused on varying buffer pH and PEG concentration. Hits are indicated by letters, corresponding to an image of the crystal in the panel below. Y indicated the original hit. Bottom, Visible light microscopy images of crystals obtained during MemTrans D3 optimisation screening, Leica M125 microscope. Crystal length (78–126  $\mu$ m) and shape (rod-shaped or curved) varies between conditions. Scale bars are indicated.

Apo crystals were fished, and then soaked in reservoir solution, with addition of 0.6 mM 3-benzylxanthine (5). However, crystals showed noticeable degradation within 1 hour. These crystals degraded further during attempted fishing, and as such were not suitable for data collection experiments.

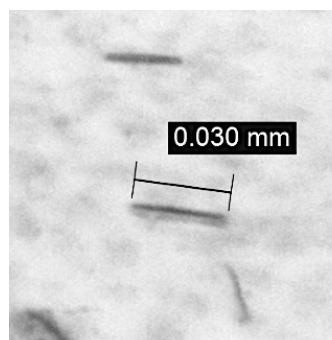
#### 4.3.2.2. Crystallisation of UapA-Q408E $_{\Delta 1-11}$ with 3-benzylxanthine (5)

As for the crystallisation screening of UapA-G411V $_{\Delta 1-11}$ , crystallisation trials for Q408E $_{\Delta 1-11}$  began with the use of sparse matrix screens MemStart/Sys, MemGold, MemMeso, MemTrans, MemChannel and MemGold2. For UapA-Q408E $_{\Delta 1-11}$ , two crystallisation hits were identified using MemGold2 (Table 10, Figure 44). In the presence or absence of 3-benzylxanthine (5), microcrystals formed in MemGold2 H9 and H12. Unfortunately, despite optimisation screening around these two conditions, no further increase in crystal size was observed. Nevertheless, these microcrystals were harvested and cryo-protected with 30% glycerol before flash freezing them in liquid nitrogen. The crystals were transported to Diamond Light Source in Oxfordshire, United Kingdom. X-ray diffraction data was collected using the I24 micro-focus beamline, a beamline that offers high flux densities. Unfortunately, none of the crystals obtained diffracted.

Table 10: Crystallisation hits for UapA-Q408E $\Delta$ 1-11 with 3-benzylxanthine (**5**) from initial screening using sparse matrix Molecular Dimensions screens MemStart/Sys, MemGold, MemMeso, MemTrans, MemChannel and MemGold2.

Screen	Condition	Substrate?	[Protein] mg/mL	T °C	Time, hours
MemGold2	H9: 2.75 M Ammonium chloride, 0.025 M Bis-Tris pH 7.0	3-benzylxanthine ( <b>5</b> ) or apo	10.0	20.0	48
MemGold2	H12: 0.01 M HEPES pH 7.5, 3.25 M 1,6-Hexanediol	3-benzylxanthine ( <b>5</b> ) or apo	10.0	20.0	48

**MemGold2 H9**



**MemGold2 H11**

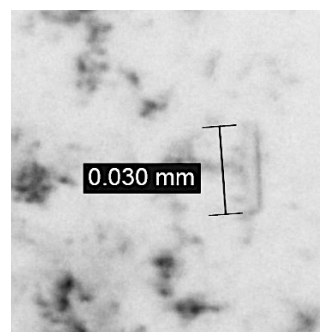


Figure 44: Visible light microscopy images of UapA-Q408E $\Delta$ 1-11 crystals obtained during MemGold2 screening, using a Leica M125 microscope. Crystals were generally rod-shaped, and were approximately 30  $\mu$ m in length. Scale bars are indicated.



#### 4.3.2.3. Crystallisation of UapA-WT with 3-benzylxanthine (5)

Initial crystallisation trials for UapA-WT began with the use of sparse matrix screens MemStart/Sys, MemGold, MemMeso, MemTrans, MemChannel and MemGold2. For UapA-WT, two crystallisation hits were identified using MemGold2 (Table 11, Figure 45). As for UapA-Q408E $_{\Delta 1-11}$ , in the presence or absence of 3-benzylxanthine (5), microcrystals formed in MemGold2 H9 and H12. Unfortunately, despite optimisation screening around these two conditions, no further increase in crystal size was observed. Nevertheless, these microcrystals were harvested and cryo-protected with 30% glycerol before flash freezing them in liquid nitrogen, prior to data collection using the I24 microfocus beamline. Unfortunately, as for UapA-Q408E $_{\Delta 1-11}$ , none of the UapA-WT crystals obtained diffracted.

Table 11: Crystallisation hits for UapA-WT with 3-benzylxanthine (**5**) from initial screening using sparse matrix Molecular Dimensions screens MemStart/Sys, MemGold, MemMeso, MemTrans, MemChannel and MemGold2.

Screen	Condition	Substrate?	[Protein] mg/mL	T °C	Time hours
MemGold2	H9: 2.75 M Ammonium chloride, 0.025 M Bis-Tris pH 7.0	3-benzylxanthine ( <b>5</b> ) or apo	10.0	20.0	48
MemGold2	H12: 0.01 M HEPES pH 7.5, 3.25 M 1,6-Hexanediol	3-benzylxanthine ( <b>5</b> ) or apo	10.0	20.0	48

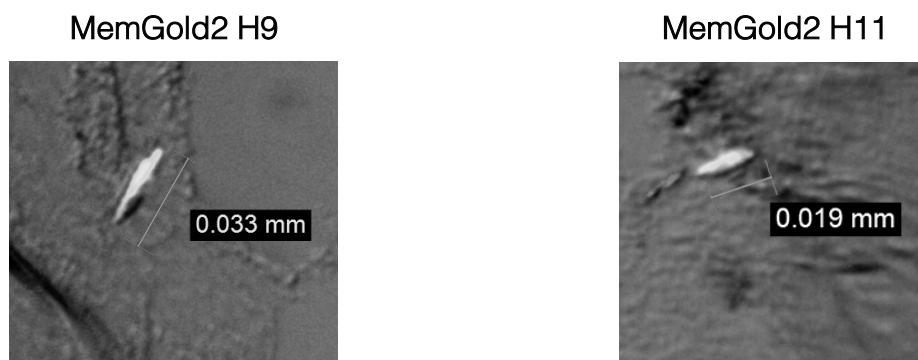


Figure 45: Visible light microscopy images of crystals obtained during MemGold2 screening. Conditions H9 and H12 produced shard-like crystals, with length varying from 19-33  $\mu$ m. Scale bars are indicated.

#### 4.3.3. Reconstitution of UapA into nanodiscs

UapA was reconstituted into nanodiscs to enable structural characterisation by cryo-EM and hydrogen-deuterium exchange mass spectrometry. Previous studies on UapA, have suggested shown that detergent solubilised UapA is less stable than UapA reconstituted into nanodiscs, and, as a consequence, is less suitable for hydrogen-deuterium exchange mass spectrometry<sup>113</sup>.

UapA-Q408E<sub>Δ1-11</sub> was purified in DDM, as described in Section 4.3.1, excluding the final size-exclusion chromatography step. UapA was combined with MSP1E3D1 and yeast polar extract lipids for reconstitution into nanodiscs. Samples were ultimately purified by size-exclusion chromatography (Figure 46) and examined by SDS-PAGE gel (Figure 47).

Unfortunately, using this purification method (Method A, Section 4.2.3) there was significant overlap between peaks of full nanodiscs (~10.5 mL) and empty nanodiscs (~12.5 mL). For hydrogen-deuterium mass spectrometry, 200 μL of sample at 4 mg/mL ( $A_{280}$ ) was required, which necessitated combining fractions from size-exclusion chromatography. Fractions indicated in orange (Figure 46, Figure 47) were combined and concentrated to an  $A_{280}$  of 4 mg/mL. Unfortunately, mass spectrometry analysis showed there was significant contamination of the sample by empty nanodiscs.

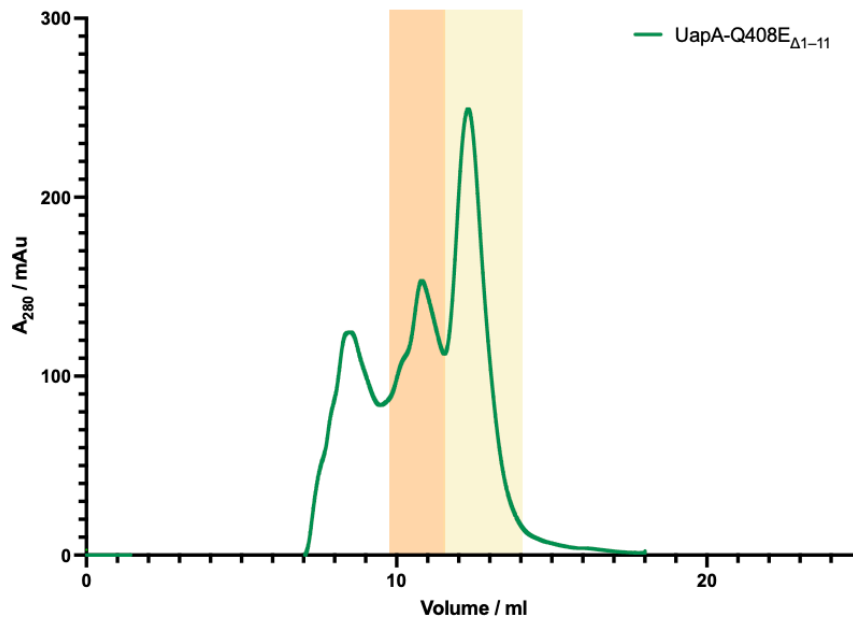


Figure 46: UV absorbance profile ( $A_{280\text{nm}}$ ) from Size-Exclusion Chromatography (SEC) of UapA-Q408E $\Delta_{1-11}$  (green) following reconstitution into MSP1E3D1 and yeast polar extract nanodiscs (1:5:500) using Method A. For UapA-Q408E $\Delta_{1-11}$ , three main peaks are observed, an aggregate peak (~8.5 mL), full nanodiscs (orange, ~10.5 mL) and empty nanodiscs (yellow, ~12.5 mL).

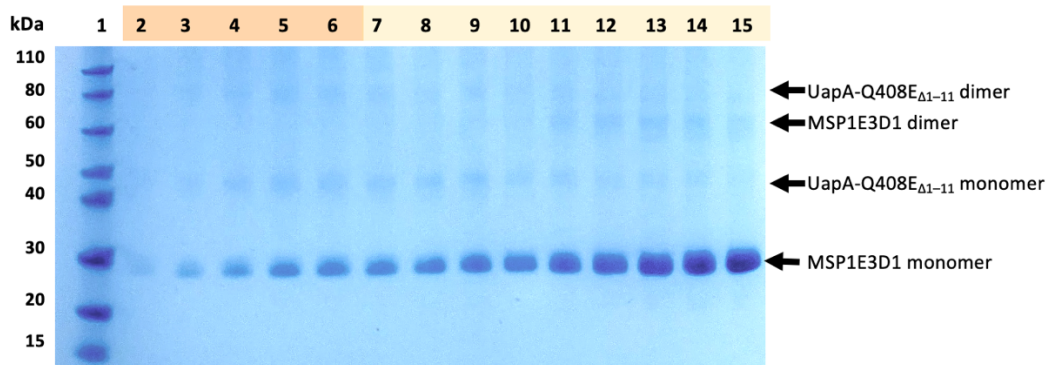


Figure 47: Fractions from size exclusion chromatography were examined using a NuPage<sup>TM</sup> 4-12% Bis-Tris SDS-PAGE Gel (35 minutes, 200 V, 120 mA), with a Novex pre-stained protein standard as reference. Gels were rinsed, Coomassie-stained and visualised in a BioRad Gel Imaging System. Lanes 2-6 (orange) contain predominantly UapA-Q408E reconstituted into nanodiscs (monomer: 40–50 kDa, dimer: 80–100 kDa). As you move from lane 7 to 15, the proportion of MSP1E3D1 (monomer: ~30 kDa, dimer: ~60 kDa) in the sample increases, and the concentration of UapA slowly decreases.

#### 4.3.4. Reconstitution of UapA-GFP-His into nanodiscs

In this alternative method (Method B, Section 4.2.4), the GFP-His tag was left on to enable separation of empty and full nanodiscs by a further Ni-NTA resin pass. As before, UapA-GFP-His was isolated using Ni-NTA affinity chromatography. However, rather than the His tag being cleaved by TEV protease, the tag was left on. UapA-GFP-His was combined with MSP1E3D1 and yeast polar extract lipids for reconstitution into nanodiscs. Following reconstitution, full nanodiscs were separated from empty nanodiscs by a second Ni-NTA chromatography step. The GFP-His tag was then cleaved by TEV protease, and removed from the sample mixture by a third Ni-NTA pass. Samples were ultimately purified by size-exclusion chromatography (Figure 48) and examined by SDS-PAGE gel (Figure 49).

While the adoption of Method B for the purification of UapA-Q408E $\Delta$ 1-11 successfully reduced the number of empty nanodiscs, leaving the GFP-His tag on reduced the stability of the protein in solution, and significant aggregation of protein was observed throughout the purification process. When this method was attempted for UapA-WT, the protein saw considerable aggregation, and negligible successfully reconstituted protein was recovered (Figure 48).

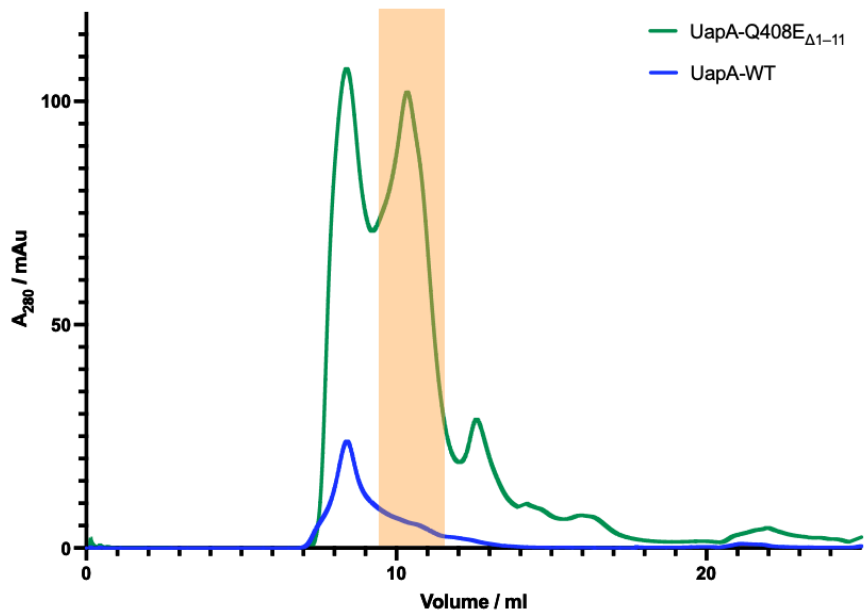


Figure 48: UV absorbance profile ( $A_{280\text{nm}}$ ) from Size-Exclusion Chromatography (SEC) of UapA-Q408E $\Delta_{1-11}$  (green) and UapA-WT (blue) following reconstitution into MSP1E3D1 nanodiscs, using Method B. For UapA-Q408E $\Delta_{1-11}$ , two main peaks are observed, an aggregate peak at approximately 8.5 mL, followed by successfully reconstituted protein at approximately 10.5 mL. The peak corresponding to empty nanodiscs (~12.5 mL) was significantly reduced using Method B. For UapA-WT the protein saw considerable aggregation, and little successfully reconstituted protein was recovered.

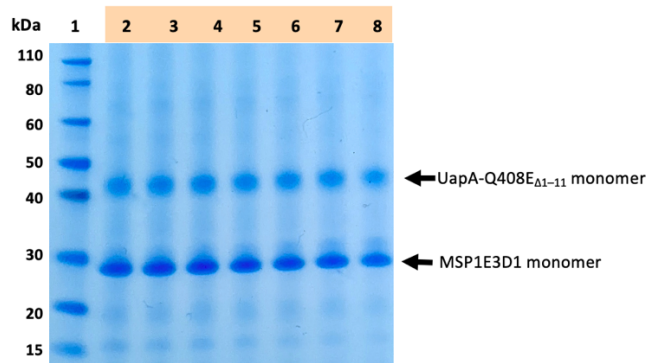


Figure 49: Fractions from SEC for UapA-Q408E $\Delta_{1-11}$  reconstituted into nanodiscs (orange, Figure 48) were examined using a NuPage<sup>TM</sup> 4-12% Bis-Tris SDS-PAGE Gel (35 minutes, 200 V, 120 mA), with a Novex pre-stained protein standard as reference. Gels were rinsed, Coomassie-stained and visualised in a BioRad Gel Imaging System. Lanes 2-8 (orange) contain UapA-Q408E $\Delta_{1-11}$  (monomer: 40-50 kDa) reconstituted into nanodiscs (MSP1E3D1 monomer: 30 kDa).

### 4.3.5. Electron Microscopy

#### 4.3.5.1. Negative-stain electron microscopy of UapA in DDM

The quality of detergent solubilised UapA-WT and UapA-Q408E $\Delta_{1-11}$ , prepared as in Section 4.3.1, was investigated using negative stain electron microscopy. From the micrographs (Figure 50), the sample appeared heterogeneous, with different sizes and shapes of particles. The concentration of protein, at 0.01 mg/mL was high, resulting in poor particle dispersity. There was evidence of aggregation of both proteins. Since, Section 4.3.2 has described the successful crystallisation of both of these protein constructs, this aggregation is unlikely to be caused by high concentration.

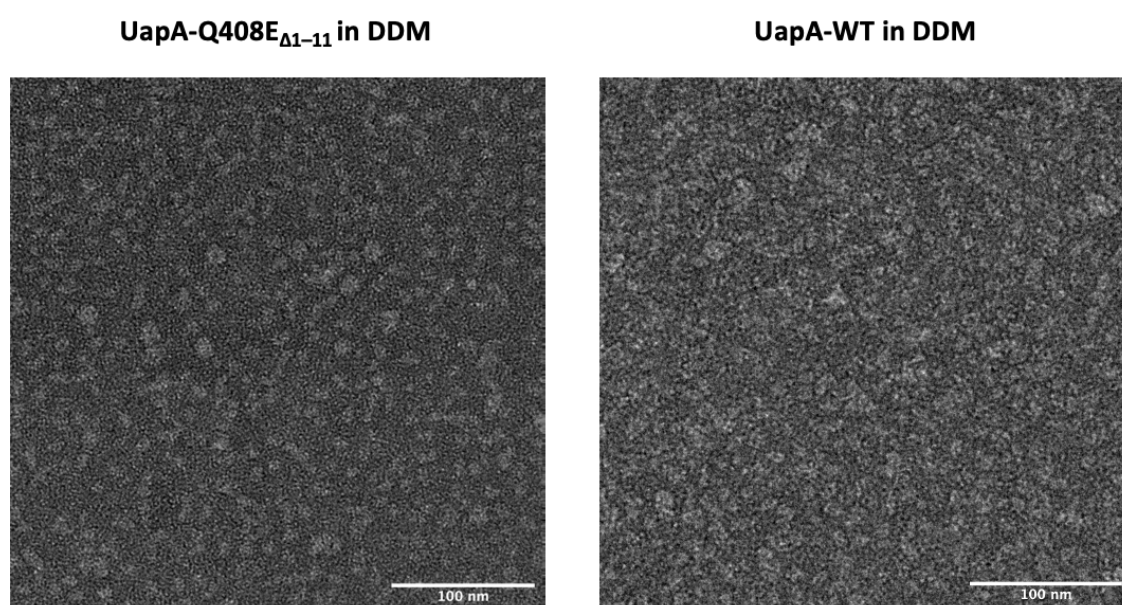


Figure 50: Micrographs of UapA-Q408E $\Delta_{1-11}$  and UapA-WT in DDM. Left, Negative stain micrograph of UapA-Q408E $\Delta_{1-11}$  in DDM purified in the absence of substrate. Right, Negative stain micrograph of UapA-WT in DDM purified in the absence of substrate. For both micrographs, the images are crowded and while the sample appeared heterogeneous, this may be due to different orientations of the protein being viewed, and the presence of some aggregation.

#### 4.3.5.2. Negative-stain electron microscopy of UapA in nanodiscs

The quality of UapA-Q408E $_{\Delta 1-11}$  reconstituted into MSP1E3D1 and yeast polar lipid nanodiscs, prepared using Method B (Section 4.2.4) was investigated using negative-stain electron microscopy. Grids were prepared as described in Section 4.2.9. The sample appeared homogeneous, with good dispersity at  $A_{280}$  of 0.01 mg/mL (Figure 51). The addition of xanthine or 3-benzylxanthine (**5**) appeared to slightly change the overall particle dispersity. However, this may have also resulted from small changes in sample application, uranyl acetate washing and blotting.

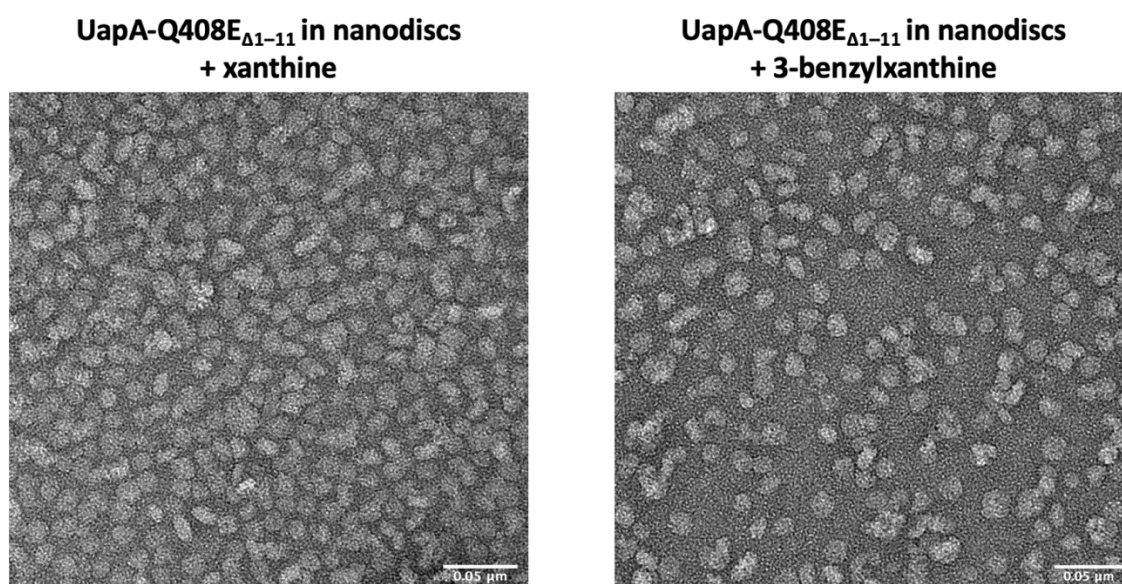


Figure 51: Representative negative-stain micrographs of UapA-Q408E $_{\Delta 1-11}$  reconstituted into nanodiscs in the presence of xanthine (0.6 mM) or 3-benzylxanthine (**5**, 0.6 mM). For both micrographs, the sample appeared homogeneous, with different sizes and shapes of particles. The addition of 3-benzylxanthine (**5**) over xanthine appeared to decrease overall particle dispersity. However, this may have also resulted from small changes in sample application, uranyl acetate washing and blotting.

Increased numbers of images would permit 2D classification, but given the expected detail available for this small sample in negative stain, the decision was made to proceed with cryo-EM instead.



#### 4.3.5.3. Cryo-electron microscopy of UapA-Q408E<sub>Δ1-11</sub> in nanodiscs

Since the negative stain micrographs of UapA reconstituted into nanodiscs looked better than negative stain micrographs of detergent-solubilised UapA, the decision was made to focus cryo-EM efforts on UapA reconstituted into nanodiscs. The sample of UapA-Q408E<sub>Δ1-11</sub> reconstituted into nanodiscs with 3-benzylxanthine (5) appeared homogenous and well-dispersed in negative stain micrographs (Figure 51). Consequentially, this sample was used to prepare cryo-electron microscopy grids (Quantifoil R 2/2 Cu 300), ready for screening. Grids were prepared as described in Section 4.2.10. Blotting times were optimised between 2 and 12 seconds. The blot force was varied between -2 and -4.

With the assistance of Dr Ben Phillips, grids were screened using the 200 keV Glacios 2 Cryo-TEM at the Institute of Cancer Research (ICR), London. The sample appeared more heterogenous on cryo-electron microscopy grids, than by negative stain. The better particles generally appeared in thicker ice, which limits the contrast and creates more background noise in the images (Figure 52). To reach an  $A_{280}$  of 1 mg/mL, it was necessary to combine fractions from size exclusion chromatography and concentrate. As a result, it is possible there is some contamination from empty nanodiscs.

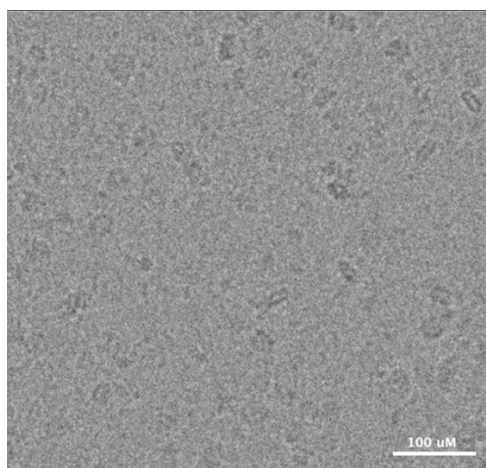


Figure 52: A representative cryo-electron micrograph of UapA-Q408E $_{\Delta 1-11}$  in nanodiscs with 3-benzylxanthine (**5**), collected using the 200 keV Glacios 2 Cryo-TEM at the Institute of Cancer Research (ICR), London. Magnification 1.1 Å/pixel, defocus 2.25 μm, dose 40 e $^{-}$ /Å $^2$ .

The initial 2D classes (Figure 53) are dominated by signal for the MSP1E3D1 component. Due to the small size of UapA, and that the majority of UapA is membrane embedded, the majority of UapA is expected to lie within the bounds of the nanodisc. As such, it is possible the UapA component is being obscured by noise in the classes and/or dominating signal from the nanodisc component. However, within these two 2D classes, there are putative side and top views (Figure 54)

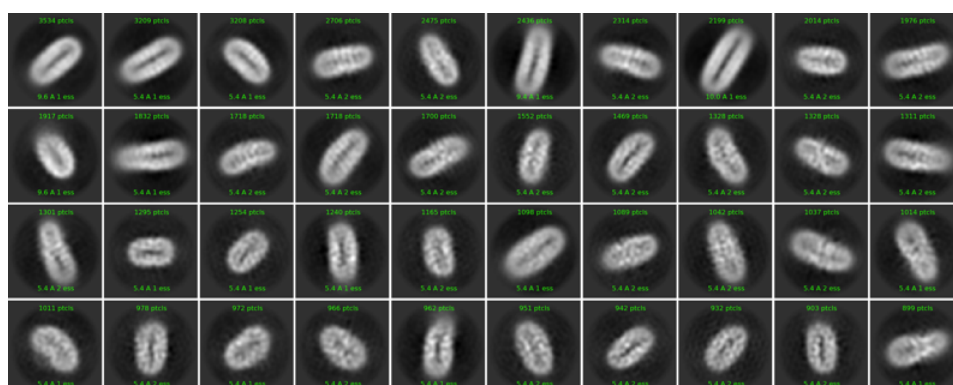


Figure 53: Early 2D classes generated from 187,887 particles (5139 micrographs). UapA-Q408E $_{\Delta 1-11}$  in nanodiscs with 3-benzylxanthine (**5**), collected using the 200 keV Glacios 2 Cryo-TEM at the Institute of Cancer Research (ICR), London. Micrographs were processed using CryoSparc.

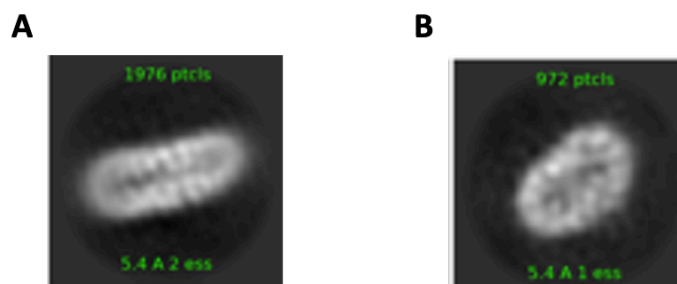


Figure 54: Putative side (A) and top (B) views of UapA-Q408E $\Delta$ 1-11 in nanodiscs with 3-benzylxanthine (**5**), collected using the 200 keV Glacios 2 Cryo-TEM at the Institute of Cancer Research (ICR), London. 2D class occupancy of 1976 (A) and 972 (B) particles, out of a total of 187,887 particles (5139 micrographs)

Due to the small size of UapA relative to the nanodisc, it is challenging to see the protein of interest within them. Due to the low yield from this purification, to reach an  $A_{280}$  of 1 mg/mL, it was necessary to combine fractions from size exclusion chromatography and concentrate. This may have resulted in contamination from empty nanodiscs. Further sample preparation optimisation is required to remove this, so as to improve sample homogeneity. Possible research avenues include exploring different lipid compositions for the nanodiscs, or alternative membrane mimetics like peptidiscs (see Section 1.2.4.2).

This work is being continued within the group and will hopefully lead to full structural characterisation of UapA-Q408E $\Delta$ 1-11 in nanodiscs with 3-benzylxanthine (**5**).

#### 4.3.6. Hydrogen-deuterium exchange mass spectrometry

Hydrogen-deuterium mass spectrometry (HDX-MS) measures the exchange of backbone amide hydrogen with deuterium from surrounding solvent. Rates of exchange can be affected by a variety of factors, including but not limited to solvent accessibility, protein flexibility, and H-bonding networks<sup>142</sup>. HDX-MS requires comparison of HDX rates between two conditions, which may be different mutants, or a single construct bound to different substrates. HDX-MS can be useful to understand protein conformation prior to structural analysis, or where full structural characterisation of the target protein is challenging.

Samples of UapA-Q408E $\Delta_{1-11}$  reconstituted into nanodiscs were prepared as described in Section 4.3.4. The purified protein sample was exchanged into buffer containing 0.6 mM xanthine, hypoxanthine or 3-benzylxanthine (**5**), ready for HDX-MS analysis. HDX-MS analysis was completed by Dr Waqas Javed. Protocols for sample labelling, sample digestion and data analysis were adapted from Dr Euan Pyle's as yet unpublished work<sup>113</sup>.

The sequence coverage for UapA-Q408E $\Delta_{1-11}$  in nanodiscs was 75%. Generally, it was found that the Q408E mutant showed an increase in deuterium uptake on the intracellular termini of transmembrane helices (Figure 55) in the presence of hypoxanthine relative to xanthine. This is consistent with previous HDX-MS studies performed by Dr Euan Pyle, which suggested that the Q408E mutant in complex with hypoxanthine is more inward facing than with xanthine.<sup>113</sup>

A comparison of UapA-Q408E $\Delta_{1-11}$  in nanodiscs bound to hypoxanthine vs novel substrate 3-benzylxanthine (**5**) found a greater number of peptides with a significant  $\Delta$ HDX across all timepoints. Preliminary data may suggest that UapA-Q408E $\Delta_{1-11}$  bound to 3-benzylxanthine (**5**) is in a different conformation to UapA-

Q408E<sub>Δ1-11</sub> bound to xanthine or hypoxanthine. It is possible that 3-benzylxanthine (5) is stabilising an alternative, and perhaps occluded, conformation.

Unfortunately, the UapA-Q408E<sub>Δ1-11</sub> with 3-benzylxanthine (5) sample was prepared on a different day than the hypoxanthine sample. As a result, any conclusions drawn must be taken with caution. This experiment was only conducted with n=1, since in June 2022, at the time of these experiments, the collaborators laboratory moved from Kings College London to the University of Manchester, resulting in instrument and experimental down-time. By the time the facility was back up and running in the new location, I had run out of time to repeat the experiment during my PhD. These experiments are planned for the future.

**UapA-Q408E<sub>Δ1-11</sub> in nanodiscs**  
*Hypoxanthine vs Xanthine*

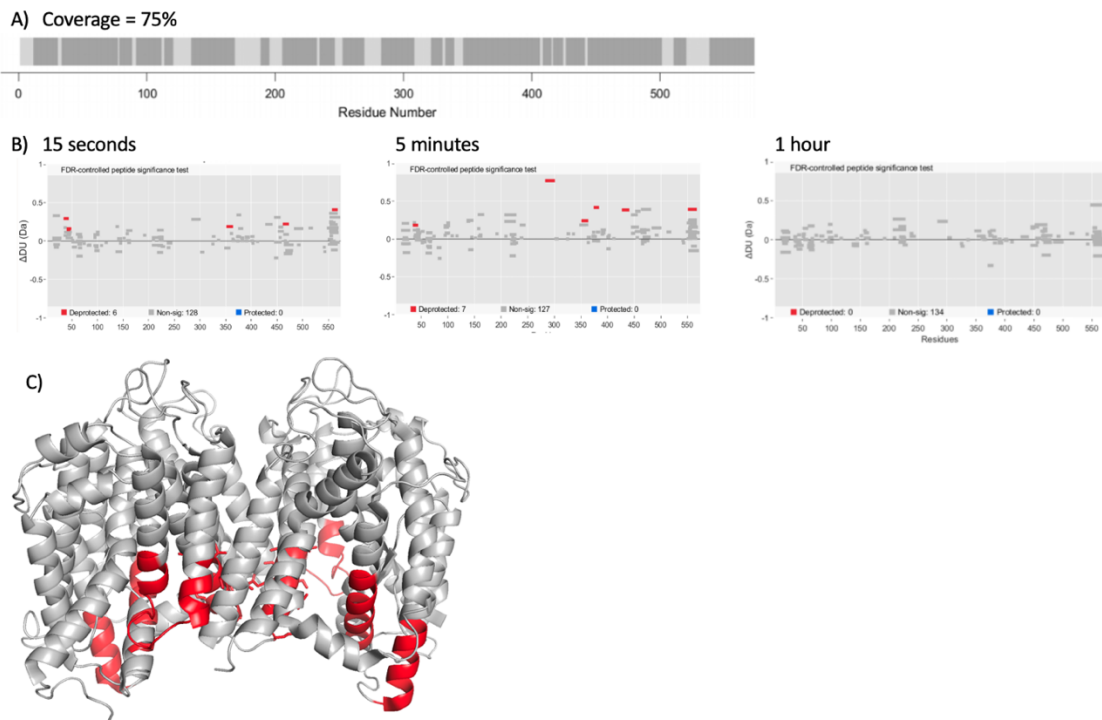


Figure 55:  $\Delta$ HDX between UapA Q408E<sub>Δ1-11</sub> with hypoxanthine vs xanthine in MSP1E3D1 and yeast polar lipid nanodiscs. A) The sequence coverage provided by the peptides detected during HDX-MS. B) Woods plot of  $\Delta$ HDX for 15 seconds, 5 minutes and 1 hour. Peptides with a significant  $\Delta$ HDX are coloured (99% confidence interval). C)  $\Delta$ HDX mapped onto a cartoon representation of the UapA-G411V<sub>Δ1-11</sub> crystal structure (PDB: 5I6C)<sup>1</sup>. Peptides with significantly greater D uptake in the presence of hypoxanthine are indicated in red. Peptides with insignificant  $\Delta$ HDX or where regions without sequence coverage are coloured grey.  $\Delta$ HDX was calculated from a sum of all recorded time points.

**UapA-Q408E $\Delta$ 1-11 in nanodiscs**  
*Hypoxanthine vs 3-benzylxanthine*

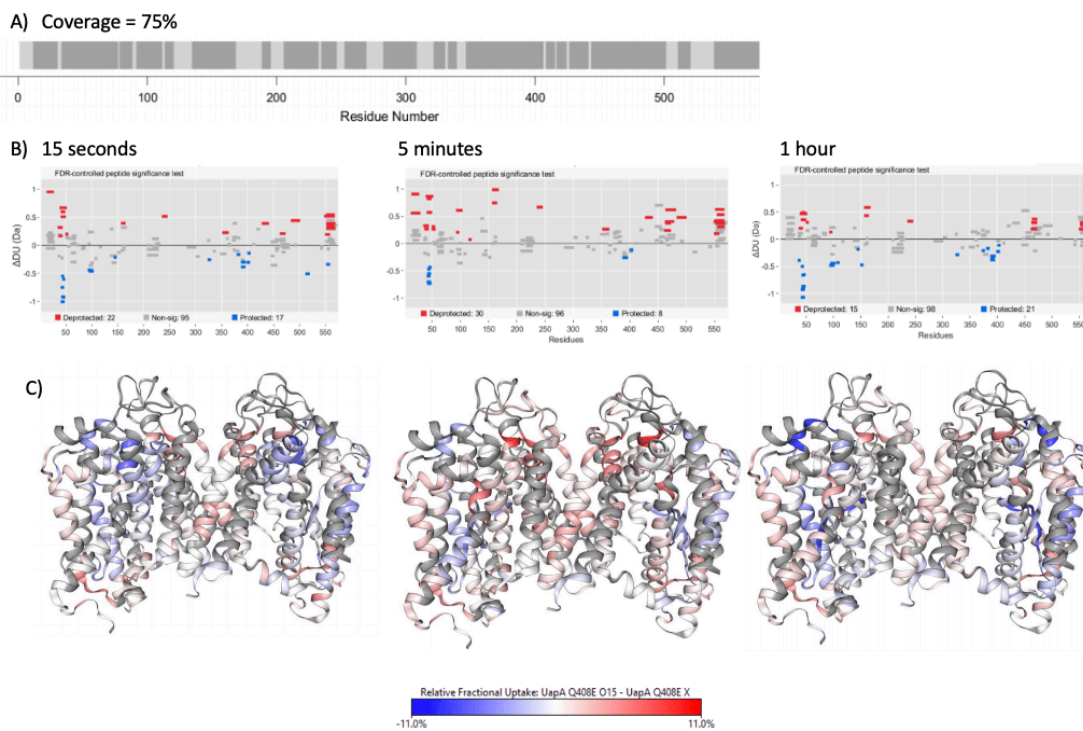


Figure 56:  $\Delta$ HDX between UapA Q408E $\Delta$ 1-11 with hypoxanthine vs 3-benzylxanthine (5) in MSP1 and yeast polar lipid nanodiscs. A) The sequence coverage provided by the peptides detected on HDX-MS. B) Woods plot of  $\Delta$ HDX for 15 seconds, 5 minutes and 1 hour. Peptides with a significant  $\Delta$ HDX are coloured (99% confidence interval). C)  $\Delta$ HDX mapped onto a cartoon representation of UapA-G411V $\Delta$ 1-11 crystal structure (PDB: 516C)<sup>1</sup>. Peptides with significantly greater D uptake in the Q408E mutant are indicated in red. Peptides with significantly lower D uptake in the Q408E mutant are indicated in blue. Peptides with insignificant  $\Delta$ HDX are indicated in white, and regions with no sequence coverage are left grey.

#### 4.4. Discussion

This chapter describes attempts to establish the interaction between 3-benzylxanthine (**5**) and UapA using a variety of structural characterisation techniques: X-ray crystallography, negative-stain electron microscopy, cryo-electron microscopy, and hydrogen-deuterium exchange mass spectrometry.

The addition of 3-benzylxanthine (**5**) to UapA-WT, UapA-G411V $_{\Delta 1-11}$  and UapA-Q408E $_{\Delta 1-11}$  purified in DDM changed the crystallisation pattern of the protein. UapA-G411V $_{\Delta 1-11}$  in DDM has previously been crystallised and structurally characterised to a final resolution of 3.7 Å.<sup>1</sup> Despite optimisation around the crystallisation conditions used in literature, and sparse matrix screening, UapA-G411V $_{\Delta 1-11}$  would not crystallise in the presence of 3-benzylxanthine (**5**). Soaking of 3-benzylxanthine (**5**) into apo crystals also disrupted the crystal packing, resulting in degradation of the crystals within 1 hour. Together, these results may suggest that the presence of 3-benzylxanthine (**5**) destabilises UapA-G411V $_{\Delta 1-11}$ , possibly as the result of attempting to force the protein into a different conformational state.<sup>1</sup> This is also supported by the more fruitful crystallisation trials of UapA-WT and UapA-Q408E $_{\Delta 1-11}$  with 3-benzylxanthine (**5**). New crystallisation conditions were identified for both of these proteins, apo and with 3-benzylxanthine (**5**). As discussed in Section 4.1, data from prior HDX-MS experiments and mutational analysis has suggested that UapA-Q408E $_{\Delta 1-11}$  may be preferentially in the outward facing or occluded conformation. New HDX-MS results suggest that 3-benzylxanthine (**5**) binds a conformation of UapA that is more outward facing.

Unfortunately, full structural characterisation of UapA-WT or UapA-Q408E $_{\Delta 1-11}$  with 3-benzylxanthine (**5**) was not achieved due to poor crystal diffraction, despite significant crystal optimisation. Since 3-benzylxanthine (**5**) binds UapA-WT with high affinity (200 nM) but is thought not to be transported, these crystallography results



support 3-benzylxanthine (**5**) strongly binding the outward or occluded conformation of UapA, and preventing transport.

Negative stain electron micrographs of UapA-WT and UapA-Q408E $\Delta_{1-11}$  in DDM showed poor particle dispersity with some protein aggregation. Previous work by Dr Euan Pyle<sup>113</sup> found that UapA-Q408E and UapA-WT reconstituted into nanodiscs were significantly more stable than the detergent-solubilised counterparts, and thus more suitable for structural characterisation by HDX-MS and cryo-EM. Adaption of the existing protocol for purification of UapA in detergent and subsequent reconstitution into MSP1E3D1 and yeast polar lipid based nanodiscs to enable separation of empty and full nanodiscs by Ni-NTA affinity chromatography was successful for UapA-Q408E $\Delta_{1-11}$ . However further optimisation around this protocol is required to enable purification of other UapA constructs, such as UapA-WT.

Hydrogen-deuterium mass spectrometry analysis suggested that UapA-Q408E $\Delta_{1-11}$  when bound to hypoxanthine is in a more inward facing conformation than when bound to xanthine. This is consistent with previous work conducted by Dr Euan Pyle<sup>113</sup>. Preliminary data also suggests that UapA-Q408E $\Delta_{1-11}$  bound to 3-benzylxanthine (**5**) is in a different conformation again, and may represent an intermediate or occluded state. Further repeats are required to confirm this hypothesis; these could not be completed within the timeframe of this work.

Negative-stain electron micrographs of UapA-Q408E $\Delta_{1-11}$  reconstituted into nanodiscs in the presence of 3-benzylxanthine (**5**) or xanthine showed homogeneity and good particle dispersion. This protein sample was advanced to cryo-electron microscopy, which yielded early 2D classes. While there is clear density for the MSP1E3D1, there is currently not clear density for the UapA dimer. It is possible that the density for UapA is being obscured by noise in the classes and/or dominating signal from the nanodisc component, since the majority of the UapA dimer is

expected to sit within the nanodisc. Further optimisation is required during sample preparation and data processing. In addition, it would be essential to collect a larger dataset. Unfortunately, this work was completed towards the end of PhD funding period, and could not be completed within the timeframe of this work.

Together, the summary of X-ray crystallography and hydrogen-deuterium exchange mass spectrometry data suggest that 3-benzylxanthine (**5**) may bind an occluded conformation of UapA-Q408E $\Delta$ 1-11. Initial negative-stain electron micrographs appear promising for nanodisc-stabilised UapA-Q408E $\Delta$ 1-11. Further work in this area may enable the structural determination of UapA-Q408E $\Delta$ 1-11 in an outward or occluded conformation, bound to xanthine or 3-benzylxanthine (**5**).

## 5. Final Discussion

Membrane proteins are of major biological and therapeutic interest, due to their broad and diverse roles across the proteome<sup>83</sup> (Section 1.2.3). Solute carriers have been shown to be targets for inhibition<sup>152</sup> for several approved drugs (Section 1.2.5), in addition to their role as biomarkers and crucially, drug carriers. There are many examples of solute carriers that mediate the uptake of drugs (Section 1.2.6). These examples form the rationale for harnessing the unique landscape of integral membrane transporters present in *Aspergilli*, lacking in humans, to specifically transport antifungals.

This work has focussed on Uric Acid Permease (Section 1.3.2), a nucleobase-ascorbate transporter from *Aspergillus nidulans*, which is of therapeutic interest in the treatment of Aspergillosis (Section 1.1). 5-fluorocytosine is an example of a toxic purine, known to be transported by an integral membrane transporter in *Aspergilli*, but shows poor activity *in vitro* due to development of resistance<sup>62</sup> (Section 1.1.5.4).

The existing X-ray crystal structure of UapA-G411V<sub>Δ1-11</sub> in complex with xanthine has provided invaluable information regarding the binding mode of xanthine (Section 1.3.3)<sup>1</sup> and enabled the structure guided design of xanthine analogues (Section 2.3.1). Positions N<sup>3</sup>, O<sup>6</sup> and N<sup>9</sup> on the xanthine ring were identified as potential vectors on the xanthine heterocycle for derivatisation<sup>183,185</sup>.

Chapter 2 described the successful synthesis and characterisation of the benzylated xanthine series (compound **1**, **3** and **5**), compound **2** and **13**, following the adaption of protocols existing in literature and their subsequent optimisation. Competitive uptake assays using <sup>3</sup>H-xanthine revealed that the novel substrates compounds **1**, **2**, **3**, **5** and **13** bind UapA, with affinities varying between 0.2–400 μM (Section 3.3.1). 3-benzylxanthine (**5**) inhibited <sup>3</sup>H-xanthine uptake 35x more than

unlabelled xanthine or hypoxanthine, suggesting that it is forming additional interactions with UapA ( $K_i = 0.2 \mu\text{M}$ ). Attempts to dock 3-benzylxanthine (**5**) and other synthesized derivatives into the existing crystal structure of UapA-G411V $\Delta_{1-11}$  in the inward facing conformation produced values that did not correlate with experimental uptake values. This is not unexpected; molecular docking experiments should always be taken with caution, but more so with transporters, given their high conformational flexibility<sup>218</sup>. These compounds may be binding a different (e.g. occluded or outward-facing) conformation of the protein than represented by the current crystal structure.

3-benzylxanthine (**5**) and the other newly synthesized analogues did not show any toxicity towards strains of *Aspergillus nidulans* (Section 3.3.2.1). There was no evidence of transport in fungal growth assays or fluorescence microscopy experiments (Section 3.3.3); they did not induce toxicity or act as nitrogen sources (Section 3.3.2.2), and they did induce endocytosis of GFP-labelled UapA in *Aspergillus nidulans*. However, this is not conclusive: compounds may be transported, but have no visible effect on these read-outs. On the other hand, they may not be transported, instead acting as non-competitive inhibitors. The latter seems likely, due to the high selectivity of these transporters for their substrates (Section 1.3.4). As discussed in Section 3.4, to show transport conclusively, it would be necessary to radiolabel the novel substrate or reconstitute the UapA transporter into artificial bilayers such as liposomes or expressed in oocytes, measuring uptake of the given substrate using liquid chromatography mass spectrometry<sup>215,216</sup>.

Instead of redirecting efforts towards setting up novel uptake assays, the decision was made to better understand how these novel analogues are interacting with and/or stabilising UapA-WT and its thermostabilised mutants (UapA-Q408E $\Delta_{1-11}$  and UapA-G411V $\Delta_{1-11}$ ). UapA-G411V $\Delta_{1-11}$  is known to be conformationally locked in the inward-facing conformation<sup>1</sup>. UapA-Q408E $\Delta_{1-11}$  is known to retain some transport activity and is more conformationally flexible than UapA-G411V $\Delta_{1-11}$ <sup>1</sup>. A variety of

thermostability techniques were used to determine if the novel substrates were stabilising or destabilising these three constructs. Cellular thermal shift assays (CETSA) and fluorescence size exclusion chromatography (FSEC) were used to determine any effect of novel substrates on UapA-WT and mutants in detergent-solubilised membranes. However, since this is a crude solubilised membrane sample, indirect effects, such as the heterogeneous lipidic environment, are difficult to control for. In addition, the protein was already stabilised by DDM, which means that small effects of a given compound on stability may not be significant.

Subsequent thermostability assays with purified UapA in detergent utilised nano-differential scanning fluorimetry (nano-DSF) and CPM-based thermal denaturation assays. CPM assays suggested that 3-benzylxanthine (**5**) may stabilise UapA-WT and UapA-G411V $_{\Delta 1-11}$  relative to no substrate. However, 3-benzylxanthine (**5**) also appeared to stabilise UapA-Q408E $_{\Delta 1-11}$  relative to no substrate or xanthine but destabilise it relative to hypoxanthine (Section 3.3.5.1). There were significant inconsistencies in stabilisation or destabilisation between nano-DSF and CPM assays, which may have been a consequence of varying the relative concentration of the substrate in reference to the protein between methods. Further experiments would need to be completed optimising the concentration of substrate, because indirect binding interactions may be influencing overall protein stability.

Despite inconsistencies, these thermostability assays have shown that 3-benzylxanthine (**5**) does not significantly destabilise UapA-WT, UapA-Q408E $_{\Delta 1-11}$  or UapA-G411V $_{\Delta 1-11}$ . Assuming 3-benzylxanthine (**5**) is a non-transportable competitive inhibitor of UapA activity, it was postulated that it may be a useful tool to stabilise UapA in a new conformation for structural studies.

3-benzylxanthine (**5**) appeared to change the crystallisation pattern of UapA-G411V $_{\Delta 1-11}$ , UapA-WT and UapA-Q408E $_{\Delta 1-11}$  (Section 4.3.2). In addition, soaking of 3-

benzylxanthine (**5**) into existing apo crystals of UapA-G411V $\Delta_{1-11}$  resulted in rapid degradation of the crystals, which may suggest that this compound is inducing conformational changes, which are in turn, disrupting crystal lattice packing. This is consistent with hydrogen-deuterium exchange mass spectrometry results, which suggest that UapA-Q408E $\Delta_{1-11}$  reconstituted into nanodiscs is in a more outward or occluded conformation when bound to 3-benzylxanthine (**5**) (Section 4.3.6). UapA-Q408E $\Delta_{1-11}$  was used in these HDX experiments, and for cryo-EM, due to its greater thermostability relative to the UapA-WT, but its retained conformational flexibility over UapA-G411V $\Delta_{1-11}$ . This is crucial, since it was unclear which conformation of UapA, 3-benzylxanthine (**5**) binds. However, Q408 is a key residue that constitutes the binding site of xanthine in the X-ray crystal structure of UapA-G411V $\Delta_{1-11}$ ; Q408 forms a key bidentate hydrogen bonding interactions with the NH at position 1 of xanthine and carbonyl at position 2. It is known that the Q408E mutation reduces affinity for xanthine, and increases the affinity for hypoxanthine, which lacks the carbonyl at position 2. Consequently, it is unknown how this conservative mutation will impact upon 3-benzylxanthine (**5**) binding affinity. This could be interrogated using competitive uptake assays in *A. nidulans*, expressing UapA-Q408E<sup>1</sup>. Despite these concerns, UapA-Q408E $\Delta_{1-11}$  was preferred for ongoing structural studies due to its retained conformational flexibility over UapA-G411V $\Delta_{1-11}$  but greater overall stability than UapA-WT.

Preliminary work in negative-stain electron microscopy showed that particles of UapA-Q408E $\Delta_{1-11}$  reconstituted into nanodiscs had improved particle dispersity and particle definition compared with particles of detergent solubilised UapA-Q408E $\Delta_{1-11}$  (Section 4.3.5.1 and 4.3.5.2). Due to the limited detail expected from this small sample in negative stain, the decision was made to proceed with cryo-EM. A small dataset was collected (5139 micrographs) which yielded early 2D classes from a total of 187,887 particles (Section 4.3.5.3). While there is clear density for the MSP1E3D1, there was not clear density for the UapA dimer. It is possible that the

density for UapA is being obscured by noise in the classes and/or dominating signal from the nanodisc component, since the majority of the UapA dimer is expected to sit within the nanodisc. While challenging, related solute carriers (e.g. OsBOR3) of a similar molecular weight have been structurally characterised by electron microscopy to low resolution (EMD-11996, 4.2 Å)<sup>219</sup>. Further optimisation is required during the preparation of UapA-Q408E<sub>Δ1-11</sub> in nanodiscs to improve stabilisation and nanodisc occupancy. Examples of avenues for exploration include using nanodiscs with different lipid compositions, changing the MSP size/length, or exploring the use of peptidiscs (see Section 1.2.4.2). The use of stabilising Fabs, may also assist with particle picking and particle alignment. Some of this work is ongoing within the group.

This work on UapA has provided further information regarding the substrate specificity of this transporter. Work is ongoing to structurally characterise this transporter with a novel compound, 3-benzylxanthine (**5**). If this is being transported by UapA, small changes could be made to the scaffold to introduce toxicity (a similar approach to 5-fluorocytosine). Alternatively, as discussed in Section 1.4, toxic moieties (e.g. temozolomide) could be conjugated at the N<sup>3</sup> position in the place of the benzyl group of 3-benzylxanthine (**5**). If the substrate is being transported, this could result in selective uptake of the toxic conjugate into fungal cells, to have an intracellular effect. If the resulting conjugate is not transported, but the xanthine portion shows selectivity for the outward-facing conformation of UapA, this may increase extracellular concentration of the tethered toxic moiety close to fungal cells. This approach is likened to that of ADCs (Section 1.2.5), except the antibody is replaced by a small molecule. Given the concerns regarding these novel substrates not being transported, and in the absence of alternative transport assays capable of showing direct uptake, this would be an option for the design of new, and potentially toxic, xanthine analogues.

## 6. Bibliography

H. Arst, personal communication, 3<sup>rd</sup> February 2021. Included with permission.

1. Alguel, Y. *et al.* Structure of eukaryotic purine/H<sup>+</sup>-symporter UapA suggests a role for homodimerization in transport activity. *Nat Commun* **7**, (2016).
2. Brown, G. D. *et al.* Hidden killers: Human fungal infections. *Sci Transl Med* **4**, 1–10 (2012).
3. World Health Organization. *WHO fungal priority pathogens list to guide research, development and public health action*. Licence: CC BY-NC-SA 3.0 IGO vol. 1 (2022).
4. Ben-Ami, R., Lewis, R. E. & Kontoyiannis, D. P. Enemy of the (immunosuppressed) state: An update on the pathogenesis of *Aspergillus fumigatus* infection. *Br J Haematol* **150**, 406–417 (2010).
5. Armstrong-James, D., Meintjes, G. & Brown, G. D. A neglected epidemic: Fungal infections in HIV/AIDS. *Trends Microbiol* **22**, 120–127 (2014).
6. Dupont, D. *et al.* Pulmonary aspergillosis in critically ill patients with Coronavirus Disease 2019 (Covid-19). *Med Mycol* **59**, 110–114 (2021).
7. Brown, G. D., Denning, D. W. & Levitz, S. M. Tackling human fungal infections. *Science (1979)* **336**, 647 (2012).
8. Leading International Fungal Education. <http://www.life-worldwide.org/> (2020).
9. Latgé, J. P. & Chamilos, G. *Aspergillus fumigatus* and aspergillosis in 2019. *Clin Microbiol Rev* **33**, 310–350 (2020).
10. Bennett, J. W. An overview of the genus *Aspergillus*. *Aspergillus: molecular biology and genomics* 1–17 (2010).
11. Dagenais, T. R. T. & Keller, N. P. Pathogenesis of *Aspergillus fumigatus* in invasive aspergillosis. *Clin Microbiol Rev* **22**, 447–465 (2009).
12. Yasui, M. *et al.* Invasive growth of *Aspergillus oryzae* in rice koji and increase of nuclear number. *Fungal Biol Biotechnol* **7**, 1–15 (2020).



13. Show, P. L. *et al.* Overview of citric acid production from *Aspergillus niger*. *Front Life Sci* **8**, 271–283 (2015).
14. Cairns, T. C., Nai, C. & Meyer, V. How a fungus shapes biotechnology: 100 years of *aspergillus niger* research. *Fungal Biol Biotechnol* **5**, 1–14 (2018).
15. Galagan, J. E. *et al.* Sequencing of *Aspergillus nidulans* and comparative analysis with *A. fumigatus* and *A. oryzae*. *Nature* **438**, 1105–1115 (2005).
16. Garcia-Rubio, R., de Oliveira, H. C., Rivera, J. & Trevijano-Contador, N. The Fungal Cell Wall: *Candida*, *Cryptococcus*, and *Aspergillus* Species. *Front Microbiol* **10**, 1–13 (2020).
17. Gregory, D. & Marshall, D. *Aspergillus fumigatus*, conidia, close-up SEM. *Wellcome Collection, United Kingdom - CC BY*  
<https://wellcomecollection.org/works/hbcfz3zu>.
18. Hohl, T. M. & Feldmesser, M. *Aspergillus fumigatus*: Principles of pathogenesis and host defense. *Eukaryot Cell* **6**, 1953–1963 (2007).
19. Perez-Cuesta, U. *et al.* Nitrogen, iron and zinc acquisition: Key nutrients to *aspergillus fumigatus* virulence. *Journal of Fungi* **7**, 1–19 (2021).
20. Schrettl, M. *et al.* Siderophore biosynthesis but not reductive iron assimilation is essential for *Aspergillus fumigatus* virulence. *Journal of Experimental Medicine* **200**, 1213–1219 (2004).
21. Haas, H. Molecular genetics of fungal siderophore biosynthesis and uptake: The role of siderophores in iron uptake and storage. *Appl Microbiol Biotechnol* **62**, 316–330 (2003).
22. Pantazopoulou, A. & Diallinas, G. Fungal nucleobase transporters. *FEMS Microbiol Rev* **31**, 657–675 (2007).
23. Mousavi, B., Hedayati, M. T., Hedayati, N., Ilkit, M. & Syedmousavi, S. *Aspergillus* species in indoor environments and their possible occupational and public health hazards. *Curr Med Mycol* **2**, 36–42 (2016).
24. Grahl, N., Shepardson, K. M., Chung, D. & Cramer, R. A. Hypoxia and fungal pathogenesis: To air or not to air? *Eukaryot Cell* **11**, 560–570 (2012).

25. Willger, S. D. *et al.* A sterol-regulatory element binding protein is required for cell polarity, hypoxia adaptation, azole drug resistance, and virulence in *Aspergillus fumigatus*. *PLoS Pathog* **4**, 1–18 (2008).
26. Fang, W. & Latgé, J. P. Microbe profile: *Aspergillus fumigatus*: A saprotrophic and opportunistic fungal pathogen. *Microbiology (United Kingdom)* **164**, 1009–1011 (2018).
27. Margalit, A. & Kavanagh, K. The innate immune response to *Aspergillus fumigatus* at the alveolar surface. *FEMS Microbiol Rev* **39**, 670–687 (2015).
28. Croft, C. A., Culibrk, L., Moore, M. M. & Tebbutt, S. J. Interactions of *Aspergillus fumigatus* conidia with airway epithelial cells: A critical review. *Front Microbiol* **7**, 1–15 (2016).
29. Hasenberg, M., Behnsen, J., Krappmann, S., Brakhage, A. & Gunzer, M. Phagocyte responses towards *Aspergillus fumigatus*. *International Journal of Medical Microbiology* **301**, 436–444 (2011).
30. Schaffner, A., Douglas, H. & Braude, A. Selective protection against conidia by mononuclear and against mycelia by polymorphonuclear phagocytes in resistance to aspergillus. Observations on these two lines of defense in vivo and in vitro with human and mouse phagocytes. *Journal of Clinical Investigation* **69**, 617–631 (1982).
31. Gazendam, R. P. *et al.* Human Neutrophils Use Different Mechanisms To Kill *Aspergillus fumigatus* Conidia and Hyphae: Evidence from Phagocyte Defects . *The Journal of Immunology* **196**, 1272–1283 (2016).
32. NHS. NHS - Aspergillosis. <https://www.nhs.uk/conditions/aspergillosis/> (2018).
33. Shah, A. & Panjabi, C. Allergic bronchopulmonary aspergillosis: A perplexing clinical entity. *Allergy Asthma Immunol Res* **8**, 282–297 (2016).
34. Kousha, M., Tadi, R. & Soubani, A. O. Pulmonary aspergillosis: A clinical review. *European Respiratory Review* **20**, 156–174 (2011).
35. Filler, S. G. & Sheppard, D. C. Fungal invasion of normally non-phagocytic host cells. *PLoS Pathog* **2**, 1099–1105 (2006).

36. Abad, A. *et al.* What makes *Aspergillus fumigatus* a successful pathogen? Genes and molecules involved in invasive aspergillosis. *Rev Iberoam Micol* **27**, 155–182 (2010).
37. Taccone, F. S. *et al.* Epidemiology of invasive aspergillosis in critically ill patients: Clinical presentation, underlying conditions, and outcomes. *Crit Care* **19**, 1–15 (2015).
38. Allen, D., Wilson, D., Drew, R. & Perfect, J. Azole antifungals: 35 years of invasive fungal infection management. *Expert Rev Anti Infect Ther* **13**, 787–798 (2015).
39. Mesa-Arango, A. C., Scorzoni, L. & Zaragoza, O. It only takes one to do many jobs: Amphotericin B as antifungal and immunomodulatory drug. *Front Microbiol* **3**, 1–10 (2012).
40. Agarwal, R. & Singh, N. Amphotericin B is still the drug of choice for invasive aspergillosis [1]. *Am J Respir Crit Care Med* **174**, 1 (2006).
41. Segal, B. H. & Walsh, T. J. Current approaches to diagnosis and treatment of invasive aspergillosis. *Am J Respir Crit Care Med* **173**, 707–717 (2006).
42. Faustino, C. & Pinheiro, L. Lipid systems for the delivery of amphotericin B in antifungal therapy. *Pharmaceutics* **12**, 1–47 (2020).
43. Sucher, A. J., Chahine, E. B. & Balcer, H. E. Echinocandins: The newest class of antifungals. *Annals of Pharmacotherapy* **43**, 1647–1657 (2009).
44. Ghannoum, M. A. & Rice, L. B. Antifungal agents: Mode of action, mechanisms of resistance, and correlation of these mechanisms with bacterial resistance. *Clin Microbiol Rev* **12**, 501–517 (1999).
45. Albengres, E., le Louët, H. & Tillement, J. P. Systemic antifungal agents. Drug interactions of clinical significance. *Drug Saf* **18**, 83–97 (1998).
46. Weber, K., Wehland, J. & Herzog, W. Griseofulvin interacts with microtubules both in vivo and in vitro. *J Mol Biol* **102**, 817–829 (1976).
47. Heidelberger, C. *et al.* Fluorinated pyrimidines, a new class of tumour-inhibitory compounds. *Nature* **179**, 663–6 (1957).

48. Danby, C. S., Boikov, D., Rautemaa-Richardson, R. & Sobel, J. D. Effect of pH on in vitro susceptibility of *Candida glabrata* and *Candida albicans* to 11 antifungal agents and implications for clinical use. *Antimicrob Agents Chemother* **56**, 1403–1406 (2012).
49. Lockhart, S. R., Beer, K. & Toda, M. Azole-Resistant *Aspergillus fumigatus*: What You Need To Know. *Clin Microbiol Newsl* **42**, 1–6 (2020).
50. Wiederhold, N. P. Antifungal resistance: current trends and future strategies to combat. *Infect Drug Resist* **10**, 249–259 (2017).
51. Rajendran, R. *et al.* Azole resistance of *Aspergillus fumigatus* biofilms is partly associated with efflux pump activity. *Antimicrob Agents Chemother* **55**, 2092–2097 (2011).
52. Xiang, M. J. *et al.* Erg11 mutations associated with azole resistance in clinical isolates of *Candida albicans*. *FEMS Yeast Res* **13**, 386–393 (2013).
53. e Silva, A. P. *et al.* FKS1 mutation associated with decreased echinocandin susceptibility of *Aspergillus fumigatus* following anidulafungin exposure. *Sci Rep* **10**, 1–6 (2020).
54. Perfect, J. R. The antifungal pipeline: A reality check. *Nat Rev Drug Discov* **16**, 603–616 (2017).
55. Oliver, J. D. *et al.* F901318 represents a novel class of antifungal drug that inhibits dihydroorotate dehydrogenase. *Proc Natl Acad Sci U S A* **113**, 12809–12814 (2016).
56. Miyazaki, M. *et al.* In vitro activity of E1210, a novel antifungal, against clinically important yeasts and molds. *Antimicrob Agents Chemother* **55**, 4652–4658 (2011).
57. Wiederhold, N. P. *et al.* The novel arylamidine T-2307 demonstrates in vitro and in vivo activity against echinocandin-resistant *Candida glabrata*. *Journal of Antimicrobial Chemotherapy* **71**, 692–695 (2016).

58. Nakamura, I. *et al.* ASp2397 is a novel natural compound that exhibits rapid and potent fungicidal activity against *Aspergillus* species through a specific transporter. *Antimicrob Agents Chemother* **63**, 1–13 (2019).
59. National Institute for Health and Care Excellence. Drugs A to Z. <https://bnf.nice.org.uk/drugs/>.
60. Lyu, X., Zhao, C., Yan, Z. & Hua, H. Efficacy of nystatin for the treatment of oral candidiasis: a systematic review and meta-analysis. *Drug Des Devel Ther* **10**, 1161–1171 (2016).
61. Hamill, R. J. Amphotericin B formulations: A comparative review of efficacy and toxicity. *Drugs* **73**, 919–934 (2013).
62. Vermes, A., Guchelaar, H. J. & Dankert, J. Flucytosine: A review of its pharmacology, clinical indications, pharmacokinetics, toxicity and drug interactions. *Journal of Antimicrobial Chemotherapy* **46**, 171–179 (2000).
63. Sawyer, P. R., Brogden, R. N., Pinder, K. M., Speight, T. M. & Avery, G. Clotrimazole: A Review of its Antifungal Activity and Therapeutic Efficacy. *Drugs* **9**, 424–447 (1975).
64. Sawyer, P. R., Brogden, R. N., Pinder, R. M., Speight, T. M. & Avery, G. S. Miconazole: A Review of its Antifungal Activity and Therapeutic Efficacy. *Drugs* **9**, 406–423 (1975).
65. Choi, F. D., Juhasz, M. L. W. & Atanaskova Mesinkovska, N. Topical ketoconazole: a systematic review of current dermatological applications and future developments. *Journal of Dermatological Treatment* **30**, 760–771 (2019).
66. Pasko, M. T., Piscitelli, S. C. & van Slooten, A. D. Fluconazole: A New Triazole Antifungal Agent. *Annals of Pharmacotherapy* **24**, 860–867 (1990).
67. Vermes, A., Guchelaar, H. J. & Dankert, J. Itraconazole: A Review of its Pharmacodynamic and Pharmacokinetic Properties, and Therapeutic Use in Superficial and Systemic Mycoses. *Drugs* **37**, 310–344 (1989).

68. Groll, A. H. *et al.* Clinical Pharmacokinetics, Pharmacodynamics, Safety and Efficacy of Liposomal Amphotericin B. *Clinical Infectious Diseases* **68**, S260–S274 (2019).
69. Letscher-Bru, V. & Herbrecht, R. Caspofungin: The first representative of a new antifungal class. *Journal of Antimicrobial Chemotherapy* **51**, 513–521 (2003).
70. Greer, N. D. Voriconazole: The Newest Triazole Antifungal Agent. *Baylor University Medical Center Proceedings* **16**, 241–248 (2003).
71. de La Torre, P. & Reboli, A. C. Micafungin: An evidence-based review of its place in therapy. *Core Evid* **9**, 27–39 (2014).
72. Davis, S. L. & Vazquez, J. A. Anidulafungin: An evidence-based review of its use in invasive fungal infections. *Core Evid* **2**, 241–249 (2008).
73. Samson, M. *et al.* Pharmacologic and clinical evaluation of posaconazole. **155**, 3–12 (2017).
74. Aditya K Gupta, Ryder, J. E., Lynch, L. E. & Tavakkol, A. The use of terbinafine in the treatment of onychomycosis in adults and special populations: A review of the evidence. *Journal of Drugs in Dermatology* **4**, 302–308 (2005).
75. Gamal, A. *et al.* Ibrexafungerp, a Novel Oral Triterpenoid Antifungal in Development: Overview of Antifungal Activity Against *Candida glabrata*. *Front Cell Infect Microbiol* **11**, 1–9 (2021).
76. Alberts, Bruce; Johnson, Alexander; Lewis, Julian; Raff, Martin; Roberts, Keith; Walter, P. The Lipid Bilayer. in *Molecular Biology of the Cell* (New York: Garland Science, 2002).
77. Alberts, Bruce; Johnson, Alexander; Lewis, Julian; Raff, Martin; Roberts, Keith; Walter, P. Principles of Membrane Transport. in *Molecular Biology of the Cell* (New York: Garland Science, 2002).
78. Futerman, A. H. Chapter 9 - Sphingolipids. in *Biochemistry of Lipids, Lipoproteins and Membranes (Seventh Edition)* 281–316 (2021).

79. Watson, H. Biological membranes. *Essays Biochem* **59**, 43–70 (2015).
80. Renard, K. & Byrne, B. Insights into the role of membrane lipids in the structure, function and regulation of integral membrane proteins. *Int J Mol Sci* **22**, 1–20 (2021).
81. Bechara, C. & Robinson, C. v. Different modes of lipid binding to membrane proteins probed by mass spectrometry. *J Am Chem Soc* **137**, 5240–5247 (2015).
82. Landreh, M., Marty, M. T., Gault, J. & Robinson, C. v. A sliding selectivity scale for lipid binding to membrane proteins. *Curr Opin Struct Biol* **39**, 54–60 (2016).
83. GM., C. Cell Membranes. in *The Cell: A Molecular Approach. 2nd edition.* (2000).
84. Almén, M. S., Nordström, K. J. V., Fredriksson, R. & Schiöth, H. B. Mapping the human membrane proteome: A majority of the human membrane proteins can be classified according to function and evolutionary origin. *BMC Biol* **7**, 50 (2009).
85. Tamm, L. K., Hong, H. & Liang, B. Folding and assembly of  $\beta$ -barrel membrane proteins. *Biochim Biophys Acta Biomembr* **1666**, 250–263 (2004).
86. Forst, D., Welte, W., Wacker, T. & Diederichs, K. Structure of the sucrose-specific porin ScrY from *Salmonella typhimurium* and its complex with sucrose. *Nat Struct Biol* **5**, 37–46 (1998).
87. Cecchetti, C., Pyle, E. & Byrne, B. Transporter oligomerisation: Roles in structure and function. *Biochem Soc Trans* **47**, 433–440 (2018).
88. Sprovieri, P. & Martino, G. The role of the carbohydrates in plasmatic membrane. *Physiol Res* **67**, 1–11 (2018).
89. Goldschen-Ohm, M. P. & Chanda, B. SnapShot: Channel Gating Mechanisms. *Cell* **170**, 594-594.e1 (2017).

90. DUBYAK, G. R. Ion homeostasis, channels, and transporters: An update on cellular mechanisms. *American Journal of Physiology - Advances in Physiology Education* **28**, 143–154 (2004).
91. DOYLE, D. A. *et al.* The structure of the potassium channel: Molecular basis of K<sup>+</sup> conduction and selectivity. *Science (1979)* **280**, 69–77 (1998).
92. OLEG, J. Simple allosteric model for membrane pumps. *Nature* **211**, 969–970 (1966).
93. LEUNG, J., CAMERON, A. D., DIALLINAS, G. & BYRNE, B. Stabilizing the heterologously expressed uric acid-xanthine transporter UapA from the lower eukaryote *Aspergillus nidulans*. *Mol Membr Biol* (2013) doi:10.3109/09687688.2012.690572.
94. DREW, D., NORTH, R. A., NAGARATHINAM, K. & TANABE, M. Structures and General Transport Mechanisms by the Major Facilitator Superfamily (MFS). *Chem Rev* **121**, 5289–5335 (2021).
95. PAUFF, S. M. & MILLER, S. C. Kinetic Evidence Is Consistent with the Rocker-Switch Mechanism of Membrane Transport by GlpT†. *Bone* **78**, 711–716 (2012).
96. FORREST, L. R. & RUDNICK, G. The Rocking Bundle: A Mechanism for Ion-Coupled Solute Flux by Symmetrical Transporters. *Gerontology* **61**, 515–525 (2015).
97. REYES, N., GINTER, C. & BOUDKER, O. Transport mechanism of a bacterial homologue of glutamate transporters. *Nature* **462**, 880–885 (2009).
98. RUAN, Y. *et al.* Direct visualization of glutamate transporter elevator mechanism by high-speed AFM. *Proc Natl Acad Sci U S A* **114**, 1584–1588 (2017).
99. SANTOS, R. *et al.* A comprehensive map of molecular drug targets. *Nat Rev Drug Discov* **16**, 19–34 (2016).
100. OVERINGTON, J. P., AL-LAZIKANI, B. & HOPKINS, A. L. How many drug targets are there? *Nat Rev Drug Discov* **5**, 10 (2006).



101. Carpenter, E. P., Beis, K., Cameron, A. D. & Iwata, S. Overcoming the challenges of membrane protein crystallography. *Current Opinion in Structural Biology* vol. 18 581–586 Preprint at <https://doi.org/10.1016/j.sbi.2008.07.001> (2008).
102. He, Y., Wang, K. & Yan, N. The recombinant expression systems for structure determination of eukaryotic membrane proteins. *Protein Cell* **5**, 658–672 (2014).
103. Lee, H. J., Lee, H. S., Youn, T., Byrne, B. & Chae, P. S. Impact of novel detergents on membrane protein studies. *Chem* **8**, 980–1013 (2022).
104. Lee, H. J., Lee, H. S., Youn, T., Byrne, B. & Chae, P. S. Impact of novel detergents on membrane protein studies. *Chem* **8**, 980–1013 (2022).
105. Newstead, S., Hobbs, J., Jordan, D., Carpenter, E. P. & Iwata, S. Insights into outer membrane protein crystallization. *Mol Membr Biol* **25**, 631–638 (2008).
106. Newstead, S., Ferrandon, S. & Iwata, S. Rationalizing  $\alpha$ -helical membrane protein crystallization. *Protein Science* **17**, 466–472 (2008).
107. Moraes, I. *Advances in experimental medicine and biology: The next generation in membrane protein structure determination. Advances in Experimental Medicine and Biology* vol. 922 (2016).
108. Kotov, V. *et al.* High-throughput stability screening for detergent-solubilized membrane proteins. *Sci Rep* **9**, 1–19 (2019).
109. Arachea, B. T. *et al.* Detergent selection for enhanced extraction of membrane proteins. *Protein Expr Purif* **86**, 12–20 (2012).
110. Chorev, D. S. & Robinson, C. v. The importance of the membrane for biophysical measurements. *Nat Chem Biol* **16**, 1285–1292 (2020).
111. H. Bayburt, T., v. Grinkova, Y. & G. Sligar, S. Self-Assembly of Discoidal Phospholipid Bilayer Nanoparticles with Membrane Scaffold Proteins. *Nano Lett* **2**, 853–856 (2002).

112. G. Denisov, I., v. Grinkova, Y., A. Lazarides, A. & G. Sligar, S. Directed Self-Assembly of Monodisperse Phospholipid Bilayer Nanodiscs with Controlled Size. *J Am Chem Soc* **126**, 3477–3487 (2004).
113. Pyle, E. Insights into Protein-Lipid Interactions by Structural Mass Spectrometry. (2019).
114. Pyle, E. *et al.* Structural Lipids Enable the Formation of Functional Oligomers of the Eukaryotic Purine Symporter UapA. *Cell Chem Biol* (2018) doi:10.1016/j.chembiol.2018.03.011.
115. Carlson, M. L. *et al.* The peptidisc, a simple method for stabilizing membrane proteins in detergent-free solution. *Elife* **7**, 1–23 (2018).
116. Hesketh, S. J. *et al.* Styrene maleic-acid lipid particles (SMALPs) into detergent or amphipols: An exchange protocol for membrane protein characterisation. *Biochim Biophys Acta Biomembr* **1862**, 183192 (2020).
117. Deisenhofer, J., Epp, O., Miki, K., Huber, R. & Michel, H. Structure of the protein subunits in the photosynthetic reaction center of. *Nature* **318**, 618–624 (1985).
118. Automated protein crystal optimisation with TTP Labtech's Dragonfly. *Acta Crystallogr A* **69**, 655 (2013).
119. Dimensions, M. Membrane Proteins. <https://moleculardimensions.com/products/membrane-proteins> (2022).
120. Cherezov, V. Lipidic Cubic Phase Technologies for Membrane Protein Structural Studies. *Curr Opin Struct Biol* **21**, 559–566 (2011).
121. Cox, M. J. & Weber, P. C. An investigation of protein crystallization parameters using successive automated grid searches (SAGS). *J Cryst Growth* **90**, 318–324 (1988).
122. McPherson, A., Nguyen, C., Cudney, R. & B. Larson, S. The Role of Small Molecule Additives and Chemical Modification in Protein Crystallization. *Crystal Growth & Design* **11**, 1469–1474 (2011).

123. D'Arcy, A., Bergfors, T., Cowan-Jacob, S. W. & Marsh, M. Microseed matrix screening for optimization in protein crystallization: What have we learned? *Acta Crystallographica Section:F Structural Biology Communications* **70**, 1117–1126 (2014).
124. Wiene-Schmidt, B., Oebbeke, M., Ngo, K., Heine, A. & Klebe, G. Two Methods, One Goal: Structural Differences between CocrySTALLization and Crystal Soaking to Discover Ligand Binding Poses. *ChemMedChem* **16**, 292–300 (2021).
125. Douangamath, A. *et al.* Achieving Efficient Fragment Screening at XChem Facility at Diamond Light Source. *J Vis Exp* 1–22 (2021) doi:10.3791/62414.
126. Cheng, R., Huang, C., Hennig, M., Nar, H. & Schnapp, G. In situ crystallography as an emerging method for structure solution of membrane proteins: the case of. **287**, 866–873 (2020).
127. Diamond. I24: Microfocus MX.  
<https://www.diamond.ac.uk/Instruments/Mx/I24.html>.
128. Callaway, E. Revolutionary cryo-EM is taking over structural biology. *Nature* **578**, 201 (2020).
129. Lepault, J., Booy, F. P. & Dubochet, J. Electron microscopy of frozen biological suspensions. *J Microsc* **129**, 89–102 (1983).
130. Nygaard, R., Kim, J. & Mancina, F. Cryo-electron microscopy analysis of small membrane proteins. *Curr Opin Struct Biol* **64**, 26–33 (2020).
131. Assaiya, A., Burada, A. P., Dhingra, S. & Kumar, J. An overview of the recent advances in cryoelectron microscopy for life sciences. *Emerg Top Life Sci* **5**, 151–168 (2021).
132. Hauer, F. *et al.* GraDeR: Membrane Protein Complex Preparation for Single-Particle Cryo-EM. *Structure* **23**, 1769–1775 (2015).

133. Autzen, H. E., Julius, D. & Cheng, Y. Membrane mimetic systems in CryoEM: keeping membrane proteins in their native environment. *Curr Opin Struct Biol* **58**, 259–268 (2019).
134. Mukherjee, S. *et al.* Synthetic antibodies against BRIL as universal fiducial marks for single-particle cryoEM structure determination of membrane proteins. *Nat Commun* **11**, 1–14 (2020).
135. Wu, S. *et al.* Fabs enable single particle cryoEM studies of small proteins. *Structure* **20**, 582–592 (2012).
136. Uchański, T. *et al.* Megabodies expand the nanobody toolkit for protein structure determination by single-particle cryo-EM. *Nat Methods* **18**, 60–68 (2021).
137. Arora, A. Chapter 24: Solution NMR Spectroscopy for the Determination of Structures of Membrane Proteins in a Lipid Environment. in *Lipid-Protein Interactions Methods and Protocols* 599–644 (2003).
138. Liang, B., Tamm, L. K. & Struct Mol Biol Author manuscript, N. NMR as a Tool to Investigate Membrane Protein Structure, Dynamics and Function. *Nat Struct Mol Biol* **23**, 468–474 (2016).
139. Aisenbrey, C., Salnikow, E. S., Raya, J., Michalek, M. & Bechinger, B. Chapter 23: Solid-State NMR Approaches to Study Protein Structure and Protein-Lipid Interactions. in *Lipid-Protein Interactions Methods and Protocols* 563–598 (2003).
140. Applications of solid-state NMR to membrane proteins. *Biochim Biophys Acta Proteins Proteom* **1865**, 1577–1586 (2017).
141. Murray, D. T., Griffin, J. & Cross, T. A. Detergent optimized membrane protein reconstitution in liposomes for solid state NMR. *Biochemistry* **53**, 2454–2463 (2014).
142. Konermann, L., Pan, J. & Liu, Y. H. Hydrogen exchange mass spectrometry for studying protein structure and dynamics. *Chem Soc Rev* **40**, 1224–1234 (2011).

143. Molodenskiy, D. S., Mertens, H. D. T. & Svergun, D. I. An automated data processing and analysis pipeline for transmembrane proteins in detergent solutions. *Sci Rep* **10**, 1–11 (2020).
144. Berthaud, A., Manzi, J., Pérez, J. & Mangenot, S. Modeling Detergent Organization around Aquaporin-0 Using Small-Angle X-ray Scattering. *J Am Chem Soc* **134**, 10080–10088 (2012).
145. Jeffries, C. M. *et al.* Small-angle X-ray and neutron scattering. *Nature Reviews Methods Primers* **1**, 1–39 (2021).
146. King, S. M. Small Angle Neutron Scattering. *Large-Scale Structures Group, ISIS Facility, STFC Rutherford Appleton Laboratory* <https://www.isis.stfc.ac.uk/Pages/introduction-to-sans14599.pdf> (1995).
147. Tatulian, S. A. FTIR Analysis of Proteins and Protein–Membrane Interactions. in *Lipid-Protein Interactions Methods and Protocols* 281–326 (2003).
148. Giacomini, K. M. *et al.* Membrane transporters in drug development. *Nat Rev Drug Discov* **9**, 215–236 (2010).
149. Aguayo-Ortiz, R. *et al.* A multiscale approach for bridging the gap between potency, efficacy, and safety of small molecules directed at membrane proteins. *Sci Rep* **11**, 1–14 (2021).
150. Várady, G., Cserepes, J., Németh, A., Szabó, E. & Sarkadi, B. Cell surface membrane proteins as personalized biomarkers: Where we stand and where we are headed. *Biomark Med* **7**, 803–819 (2013).
151. Sriram, K. & Insel, P. A. G protein-coupled receptors as targets for approved drugs: How many targets and how many drugs? *Mol Pharmacol* **93**, 251–258 (2018).
152. Lin, L., Yee, S. W., Kim, R. B. & Giacomini, K. M. SLC transporters as therapeutic targets: Emerging opportunities. *Nat Rev Drug Discov* **14**, 543–560 (2015).

153. Lee, H. T., Lee, S. H. & Heo, Y. S. Molecular interactions of antibody drugs targeting PD-1, PD-L1, and CTLA-4 in immuno-oncology. *Molecules* **24**, 1–16 (2019).
154. Dodd, R. B., Wilkinson, T. & Schofield, D. J. Therapeutic Monoclonal Antibodies to Complex Membrane Protein Targets: Antigen Generation and Antibody Discovery Strategies. *BioDrugs* **32**, 339–355 (2018).
155. Tucker, D. F. *et al.* Isolation of state-dependent monoclonal antibodies against the 12-transmembrane domain glucose transporter 4 using virus-like particles. *Proc Natl Acad Sci U S A* **115**, E4990–E4999 (2018).
156. Ross, S. L. *et al.* Identification of antibody and small molecule antagonists of ferroportin-hepcidin interaction. *Front Pharmacol* **8**, 1–21 (2017).
157. Hazen, M. *et al.* An improved and robust DNA immunization method to develop antibodies against extracellular loops of multi-transmembrane proteins. *MAbs* **6**, 95–107 (2014).
158. Khongorzul, P., Ling, C. J., Khan, F. U., Ihsan, A. U. & Zhang, J. Antibody-drug conjugates: A comprehensive review. *Molecular Cancer Research* **18**, 3–19 (2020).
159. Lin, J. *et al.* Emerging protein degradation strategies: Expanding the scope to extracellular and membrane proteins. *Theranostics* **11**, 8337–8349 (2021).
160. Ahn, G. *et al.* LYTACs that engage the asialoglycoprotein receptor for targeted protein degradation. *Nat Chem Biol* **17**, 937–946 (2021).
161. Cotton, A. D., Nguyen, D. P., Gramespacher, J. A., Seiple, I. B. & Wells, J. A. Development of Antibody-Based PROTACs for the Degradation of the Cell-Surface Immune Checkpoint Protein PD-L1. *J Am Chem Soc* **143**, 593–598 (2021).
162. Rannard, S. Two heads are better than one. *Trends Polym Sci* **3**, 280–281 (1995).

163. Ecker, G. & Chiba, P. Biological Membranes and Drug Transport. in *Transporters as Drug Carriers: Structure, Function, Substrates* 231–262 (2009).
164. Delma, F. Z. *et al.* Molecular mechanisms of 5-fluorocytosine resistance in yeasts and filamentous fungi. *Journal of Fungi* **7**, 1–14 (2021).
165. Kramer, W. *et al.* Substrate specificity of the ileal and the hepatic Na<sup>+</sup>/bile acid cotransporters of the rabbit. I. Transport studies with membrane vesicles and cell lines expressing the cloned transporters. *J Lipid Res* **40**, 1604–1617 (1999).
166. Petzinger, E., Wickboldt, A., Pagels, P., Starke, D. & Kramer, W. Hepatobiliary transport of bile acid amino acid, bile acid peptide, and bile acid oligonucleotide conjugates in rats. *Hepatology* **30**, 1257–1268 (1999).
167. Lin, L., Yee, S. W., Kim, R. B. & Giacomini, K. M. SLC Transporters as Therapeutic Targets: Emerging Opportunities. *Physiol Behav* **14**, 543–560 (2015).
168. Gournas, C., Papageorgiou, I. & Diallinas, G. The nucleobase-ascorbate transporter (NAT) family: Genomics, evolution, structure-function relationships and physiological role. *Mol Biosyst* **4**, 404–416 (2008).
169. Lu, F. *et al.* Structure and mechanism of the uracil transporter UraA. *Nature* **472**, 243–247 (2011).
170. Yamamoto, S. *et al.* Identification and functional characterisation of the first nucleobase transporter in mammals: Implication in the species difference in the intestinal absorption mechanism of nucleobases and their analogs between higher primates and other mammals. *Journal of Biological Chemistry* **285**, 6522–6531 (2010).
171. Koukaki, M. *et al.* The Nucleobase-ascorbate transporter (NAT) signature motif in UapA defines the function of the purine translocation pathway. *J Mol Biol* **350**, 499–513 (2005).

172. Savini, I., Rossi, A., Pierro, C., Avigliano, L. & Catani, M. v. SVCT1 and SVCT2: Key proteins for vitamin C uptake. *Amino Acids* **34**, 347–355 (2008).
173. Harrison, F. E. *et al.* Low vitamin C and increased oxidative stress and cell death in mice that lack the sodium-dependent vitamin C transporter SVCT2. *Free Radic Biol Med* **49**, 821–9 (2010).
174. Kourkoulou, A., Pittis, A. A. & Diallinas, G. Evolution of substrate specificity in the Nucleobase-Ascorbate Transporter (NAT) protein family. *Microbial Cell* **5**, 280–292 (2018).
175. Frillingos, S. Insights to the evolution of nucleobase-ascorbate transporters (NAT/NCS2 family) from the Cys-scanning analysis of xanthine permease XanQ. *Int J Biochem Mol Biol* **3**, 250–272 (2012).
176. Leung, J., Karachaliou, M., Alves, C., Diallinas, G. & Byrne, B. Expression and purification of a functional uric acid-xanthine transporter (UapA). *Protein Expr Purif* **72**, 139–46 (2010).
177. Goudela, S., Karatza, P., Koukaki, M., Frillingos, S. & Diallinas, G. Comparative substrate recognition by bacterial and fungal purine transporters of the NAT/NCS2 family. *Mol Membr Biol* **22**, 263–275 (2005).
178. Kryptou, E. & Diallinas, G. Transport assays in filamentous fungi: Kinetic characterisation of the UapC purine transporter of *Aspergillus nidulans*. *Fungal Genetics and Biology* **63**, 1–8 (2014).
179. Boswell-Casteel, R. C. & Hays, F. A. Equilibrative nucleoside transporters—A review. *Nucleosides Nucleotides Nucleic Acids* **36**, 7–30 (2017).
180. Sun, H. L. *et al.* Function of Uric Acid Transporters and Their Inhibitors in Hyperuricaemia. *Front Pharmacol* **12**, 1–15 (2021).
181. Papageorgiou, I. *et al.* Specific Interdomain Synergy in the UapA Transporter Determines Its Unique Specificity for Uric Acid among NAT Carriers. *J Mol Biol* **382**, 1121–35 (2008).



182. Vlanti, A., Amillis, S., Koukaki, M. & Diallinas, G. A novel-type substrate-selectivity filter and ER-exit determinants in the UapA purine transporter. *J Mol Biol* **357**, 808–19 (2006).
183. Pantazopoulou, A. & Diallinas, G. The first transmembrane segment (TMS1) of UapA contains determinants necessary for expression in the plasma membrane and purine transport. *Mol Membr Biol* **23**, 337–348 (2006).
184. Diallinas, G. Allopurinol and xanthine use different translocation mechanisms and trajectories in the fungal UapA transporter. *Biochimie* **95**, 1755–64 (2013).
185. Gournas, C., Amillis, S., Vlanti, A. & Diallinas, G. Transport-dependent endocytosis and turnover of a uric acid-xanthine permease. *Mol Microbiol* **75**, 246–260 (2010).
186. Elion, G. B. The purine path to chemotherapy. *Biosci Rep* **244**, 41–7 (1989).
187. Bérubé, G. An overview of molecular hybrids in drug discovery. *Expert Opin Drug Discov* **11**, 281–305 (2016).
188. Ueno, T. & Nagano, T. Fluorescent probes for sensing and imaging. *Nat Methods* **8**, 642–645 (2011).
189. Wang, P., Zhou, D. & Chen, B. A fluorescent dansyl-based peptide probe for highly selective and sensitive detect Cd<sup>2+</sup> ions and its application in living cell imaging. *Spectrochim Acta A Mol Biomol Spectrosc* **207**, 276–283 (2019).
190. Yuan, W., Zhao, X. Y., Chen, X. & Zhan, C. G. Purin-6-One Derivatives as Phosphodiesterase-2 Inhibitors. *J Chem* **2016**, 1–10 (2016).
191. Barbosa, M. L. D. C. *et al.* Novel 2-chloro-4-anilino-quinazoline derivatives as EGFR and VEGFR-2 dual inhibitors. *Eur J Med Chem* **71**, 1–14 (2014).
192. Holmes, J. L. *et al.* Synthesis of Novel Hydroxymethyl-Substituted Fused Heterocycles. *Synthesis (Germany)* **48**, 1226–1234 (2016).
193. Li, F. *et al.* An efficient construction of quinazolin-4(3H)-ones under microwave irradiation. *Arkivoc* **2007**, 40–50 (2007).

194. Wang, S. L., Yang, K., Yao, C. S. & Wang, X. S. Green synthesis of quinazolinone derivatives catalyzed by iodine in ionic liquid. *Synth Commun* **42**, 341–349 (2012).
195. Ganiu, M. O., Nepal, B., van Houten, J. P. & Kartika, R. A decade review of triphosgene and its applications in organic reactions. *Tetrahedron* **76**, 139–148 (2020).
196. Coxon, C. R. *et al.* Cyclin-Dependent Kinase (CDK) Inhibitors: Structure-Activity Relationships and Insights into the CDK-2 Selectivity of 6-Substituted 2-Arylamino-purines. *J Med Chem* **60**, 1746–1767 (2017).
197. Chae, M. Y. *et al.* 8-Substituted O6-Benzylguanine, Substituted 6(4)-(Benzyloxy)pyrimidine, and Related Derivatives as Inactivators of Human O6-Alkylguanine-DNA Alkyltransferase. *J Med Chem* **38**, 359–365 (1995).
198. Lembicz, N. K. *et al.* Facilitation of displacements at the 6-position of purines by the use of 1,4-diazabicyclo[2.2.2]octane as leaving group. *J Chem Soc Perkin 1* **1997**, 185–186 (1997).
199. Lafleur, K., Huang, D., Zhou, T., Caflisch, A. & Nevado, C. Structure-based optimization of potent and selective inhibitors of the tyrosine kinase erythropoietin-producing human hepatocellular carcinoma receptor B4 (EphB4). *J Med Chem* **52**, 6433–46 (2009).
200. Batey, R. A., Santhakumar, V., Yoshina-Ishii, C. & Taylor, S. D. An efficient new protocol for the formation of unsymmetrical tri- and tetrasubstituted ureas. *Tetrahedron Lett* **39**, 6267–6270 (1998).
201. Kryptou, E. & Diallinas, G. Transport Assays in *Aspergillus nidulans*. *Bio Protoc* **3**, (2013).
202. Amillis, S., Koukaki, M. & Diallinas, G. Substitution F569S converts UapA, a specific uric acid-xanthine transporter, into a broad specificity transporter for purine-related solutes. *J Mol Biol* **313**, 765–774 (2001).
203. Diallinas, G. Unpublished Work. (2021).

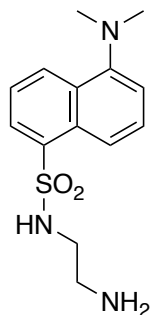
204. Gorfinkiel, L., Djalinas, G. & Scazzocchio, C. Sequence and regulation of the *uapA* gene encoding a uric acid-xanthine permease in the fungus *Aspergillus nidulans*. *Journal of Biological Chemistry* **268**, 23376–23381 (1993).
205. Thomas, D. M. & Zalcborg, J. R. 5-Fluorouracil: a Pharmacological Paradigm in the Use of Cytotoxics. *Clin Exp Pharmacol Physiol* **25**, 887–95 (1998).
206. Senisterra, G., Chau, I. & Vedadi, M. Thermal denaturation assays in chemical biology. *Assay Drug Dev Technol* **10**, 128–136 (2012).
207. Hattori, M., Hibbs, R. & Gouaux, E. A Fluorescence-Detection Size-Exclusion Chromatography-Based Thermostability Assay for Membrane Protein Precrystallization Screening. *Structure* **20**, 1293–1299 (2012).
208. Hashimoto, M., Girardi, E., Eichner, R. & Superti-Furga, G. Detection of Chemical Engagement of Solute Carrier Proteins by a Cellular Thermal Shift Assay. *ACS Chem Biol* **13**, 1480–1486 (2018).
209. Hashimoto, M., Girardi, E., Eichner, R. & Superti-Furga, G. Detection of Chemical Engagement of Solute Carrier Proteins by a Cellular Thermal Shift Assay. *ACS Chem Biol* **13**, 1480–1486 (2018).
210. Celej, M. S., Montich, G. G. & Fidelio, G. D. Protein stability induced by ligand binding correlates with changes in protein flexibility. *Protein Science* **12**, 1496–1506 (2003).
211. Lavinder, J. J., Hari, S. B., Sullivan, B. J. & Magliery, T. J. High-throughput thermal scanning: A general, rapid dye-binding thermal shift screen for protein engineering. *J Am Chem Soc* **131**, 3794–3795 (2009).
212. Hawe, A., Sutter, M. & Jiskoot, W. Extrinsic fluorescent dyes as tools for protein characterisation. *Pharm Res* **25**, 1487–1499 (2008).
213. Eftink, M. R. The use of fluorescence methods to monitor unfolding transitions in proteins. *Biophys J* **66**, 482–501 (1994).
214. Qiu, Y., Alguel, Y. & Byrne, B. Alternative substrate binding to stabilize purine transporter UapA from *Aspergillus nidulans*. (Imperial College London, 2015).

215. Jørgensen, M., Crocoll, C., Halkier, B. & Nour-Eldin, H. Uptake Assays in *Xenopus laevis* Oocytes Using Liquid Chromatography-mass Spectrometry to Detect Transport Activity. *Bio Protoc* **7**, 1–13 (2017).
216. Scalise, M., Pochini, L., Giangregorio, N., Tonazzi, A. & Indiveri, C. Proteoliposomes as tool for assaying membrane transporter functions and interactions with xenobiotics. *Pharmaceutics* **5**, 472–497 (2013).
217. Rath, A., Glibowicka, M., Nadeau, V. G., Chen, G. & Deber, C. M. Detergent binding explains anomalous SDS-PAGE migration of membrane proteins. *Proc Natl Acad Sci U S A* **106**, 1760–1765 (2009).
218. Huang, S. Y. & Zou, X. Advances and challenges in Protein-ligand docking. *Int J Mol Sci* **11**, 3016–3034 (2010).
219. Saouros, S. *et al.* Structural and functional insights into the mechanism of action of plant borate transporters. *Sci Rep* **11**, 1–12 (2021).

## 7. Supplemental Information

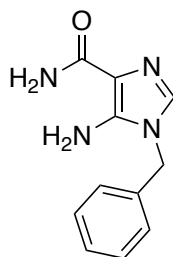
### 7.1. Protocols and characterisation data for key intermediates

#### 8: *N*-(2-aminoethyl)-5-(dimethylamino)naphthalene-1-sulfonamide



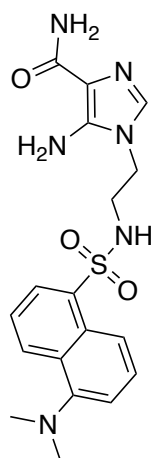
Dansyl chloride (300 mg, 1.1 mmol, 1.0 eq) in dichloromethane (5 mL) was added slowly to ethylenediamine (232.5  $\mu$ L, 1.1 mmol, 1.0 eq) and triethylamine (74.1  $\mu$ L, 1.7 mmol, 1.5 eq) in dichloromethane (5 mL). The mixture was stirred at RT until the reaction appeared completed by TLC, the precipitate (241 mg, 0.82 mmol, 75%) was filtered, washed with cold ether, and dried under vacuum.  $^1\text{H}$  NMR (400 MHz,  $\text{CDCl}_3$ )  $\delta$  8.57 (dt,  $J$  = 8.5, 1.1 Hz, 1H), 8.33 (dt,  $J$  = 8.7, 1.0 Hz, 1H), 8.29 (dd,  $J$  = 7.3, 1.3 Hz, 1H), 7.60 (dd,  $J$  = 8.7, 7.6 Hz, 1H), 7.55 (dd,  $J$  = 8.6, 7.3 Hz, 1H), 7.22 (dd,  $J$  = 7.6, 0.9 Hz, 1H), 2.97 – 2.89 (m, 3H), 2.92 (s, 6H), 2.75 – 2.69 (m, 2H).  $^{13}\text{C}$  NMR (101 MHz,  $\text{CDCl}_3$ )  $\delta$  152.0, 134.6, 133.3, 130.5, 129.9, 129.7, 128.4, 123.2, 118.7, 115.2, 45.5, 45.4, 40.8. HRMS (ESI $^+$ ): calculated for  $\text{C}_{14}\text{H}_{19}\text{N}_3\text{O}_2\text{S}^+$  294.1276, found 294.1268.

9: 5-amino-1-benzyl-1*H*-imidazole-4-carboxamide



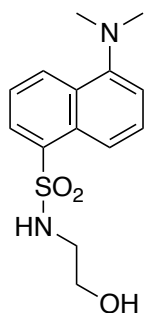
2-amino-2-cyanoacetamide (0.496 g, 5.00 mmol, 1.0 eq) was suspended in absolute acetonitrile (7.5 mL). Triethylorthoformate (0.69 mL, 5.75 mmol, 1.15 eq) and pyridine (7.5  $\mu$ L, 0.02 eq) were added, and the mixture refluxed (100  $^{\circ}$ C, 1 hour). Benzyl amine (**7**, 546  $\mu$ L, 5.00 mmol, 1.0 eq) was added dropwise over 3 – 5 minute period, and the resulting mixture refluxed (100  $^{\circ}$ C, 15 minutes). The reaction was cooled to room temperature, the white crystalline product precipitated and was collected by filtration (0.498 g, 2.30 mmol, 46%).  $^1\text{H}$  NMR (400 MHz, DMSO)  $\delta$  7.41 – 7.31 (m, 2H), 7.34 – 7.25 (m, 1H), 7.23 – 7.20 (m, 2H), 7.20 (s, 1H), 6.79 (s, 1H), 6.65 (s, 1H), 5.84 (s, 2H), 5.08 (s, 2H).  $^{13}\text{C}$  NMR (101 MHz, DMSO)  $\delta$  167.2, 143.5, 137.4, 130.3, 129.1, 128.0, 127.7, 112.9, 46.1. HRMS (ESI $^+$ ): calculated for  $\text{C}_{11}\text{H}_{13}\text{N}_4\text{O}^+$  217.1089, found 217.1087.

**10:** 5-amino-1-(2-((5-(dimethylamino)naphthalene)-1-sulfonamido)ethyl)-1*H*-imidazole-4-carboxamide



The formation of the intermediate **10** followed the synthetic route reported for compound **9**, with **8** (50 mg, 0.17 mmol, 1 eq) replacing benzylamine as the starting amine. Compound **10** was obtained as a grey powder (30.8 mg, 0.08 mmol, 46%).  $^1\text{H}$  NMR (400 MHz,  $\text{CDCl}_3$ )  $\delta$  8.55 (d,  $J = 8.6$  Hz, 1H), 8.30 (d,  $J = 8.6$  Hz, 1H), 8.23 (d,  $J = 7.4$  Hz, 1H), 7.54 – 7.49 (m, 3H), 7.16 (d,  $J = 7.6$  Hz, 1H), 6.96 (s, 1H), 5.31 (s, 2H), 3.95 (t, 2H), 3.21 (t, 3H), 2.94 – 2.81 (m, 6H).  $^{13}\text{C}$  NMR (101 MHz,  $\text{CDCl}_3$ )  $\delta$  149.9, 130.6, 129.9, 129.5, 129.4, 123.0, 43.1, 29.7, 14.8. (some  $^{13}\text{C}$  environments are not resolved). HRMS (ESI<sup>+</sup>): calculated for  $\text{C}_{18}\text{H}_{22}\text{N}_6\text{O}_2\text{S}^+$  403.1552, found 403.1548.

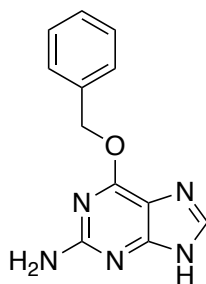
12: *N*-(2-(λ3-oxidaneyl)ethyl)-5-(dimethylamino)naphthalene-1-sulfonamide



A solution of pyridine (3 mL) and ethanolamine (281 mg, 4.6 mmol) under nitrogen was treated with dansyl chloride (500 mg, 1.9 mmol, 1 eq) and stirred for 17 hours. Water (15 mL) was added, stirred for 1 hour, extracted with ethyl acetate (3 × 25 mL). The combined organic phase was washed with brine (2 × 75 mL), dried with sodium sulfate and concentrated in vacuo to give the title compound as a pale yellow oil (0.271g, 0.9 mmol, 47%) <sup>1</sup>H NMR (400 MHz, DMSO) δ 8.47 (dt, *J* = 8.6, 1.1 Hz, 1H), 8.30 (dt, *J* = 8.7, 1.0 Hz, 1H), 8.12 (dd, *J* = 7.3, 1.3 Hz, 1H), 7.93 (br, 1H), 7.61 (ddd, *J* = 14.5, 8.6, 7.4 Hz, 2H), 7.27 (dd, *J* = 7.6, 0.9 Hz, 1H), 4.67 (s, 1H), 3.37 – 3.28 (m, 5H), 2.84 (s, 6H). HRMS (ESI<sup>+</sup>): calculated for C<sub>14</sub>H<sub>19</sub>N<sub>2</sub>O<sub>3</sub>S<sup>+</sup> 295.1116, found 295.1109.

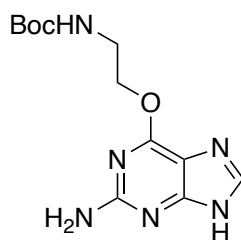


13: 6-(benzyloxy)-9H-purin-2-amine



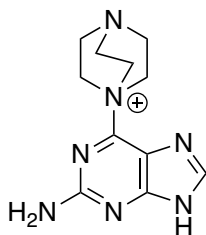
Sodium hydroxide (0.241 g, 6 mmol, 2 eq) was dissolved in benzyl alcohol (3.14 mL, 30 mmol, 10 eq). The mixture was cooled and 6-chloro-9H-purin-2-amine (0.5 g, 3 mmol, 1 eq) added in portions. The resulting mixture was heated (90 °C, 5 hours), the mixture allowed to cool, ether (20 mL) added and extracted with sodium hydroxide (1M, 3 × 20 mL). Then aqueous layers were combined and washed with toluene (3 × 20 mL), before being neutralised (pH 6-8). On neutralisation, a white precipitate formed. The title compound was collected by filtration, washed with water and dried *in vacuo* (0.480 g, 2.0 mmol, 67%). <sup>1</sup>H NMR (400 MHz, DMSO) δ 12.47 (s, 1H), 7.84 (s, 1H), 7.55 – 7.47 (m, 2H), 7.45 – 7.36 (m, 2H), 7.40 – 7.31 (m, 1H), 6.30 (s, 2H), 5.49 (s, 2H). <sup>13</sup>C NMR (101 MHz, DMSO) δ 160.1, 137.3, 129.4, 128.9, 128.5, 67.2 (some <sup>13</sup>C environments are not resolved). HRMS (ESI<sup>+</sup>): calculated for C<sub>12</sub>H<sub>12</sub>N<sub>5</sub>O<sub>2</sub><sup>+</sup> 242.1036, found 242.1033.

14: *tert*-butyl (2-((2-amino-9*H*-purin-6-yl)oxy)ethyl)carbamate



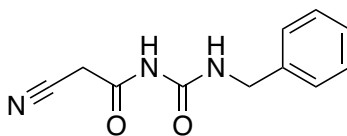
Compound **17** 1-(2-amino-9*H*-purin-6-yl)-1,4-diazabicyclo[2.2.2]octan-1-ium (200 mg, 0.68 mmol, 1 eq) was added to a mixture of *N*-Boc ethanolamine (), DMSO and sodium hydride, at room temperature. The temperature was slowly raised to 100 °C, and left stirring for 4 hours. The title compound was extracted with dichloromethane, washed with water and dried *in vacuo* (24.0 mg, 0.08 mmol, 12%). <sup>1</sup>H NMR (400 MHz, DMSO) δ 12.41 (s, 1H), 7.81 (s, 1H), 7.05 (t, J = 5.8 Hz, 1H), 6.24 (s, 2H), 5.77 (s, 1H), 4.37 (t, J = 5.8 Hz, 2H), 3.32 (s, 3H), 1.38 (s, 9H). HRMS (ESI<sup>+</sup>): calculated for C<sub>12</sub>H<sub>19</sub>N<sub>6</sub>O<sub>3</sub><sup>+</sup> 295.1519, found 295.1522

17: 1-(2-amino-9*H*-purin-6-yl)-1,4-diazabicyclo[2.2.2]octan-1-ium



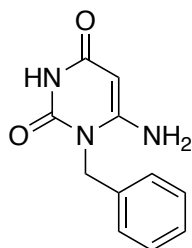
6-chloroguanine (1 g, 4.1 mmol, 1 eq) and DABCO (3.3 g, 22.3 mmol, 5.5 eq) was suspended in DMSO, and stirred at room temperature for 12 hours. The title compound precipitated and was isolated by filtration, diethylether (Et<sub>2</sub>O) washes, and drying *in vacuo* (0.98 g, 4.0 mmol, 98%). <sup>1</sup>H NMR (400 MHz, DMSO) δ 8.36 (s, 1H), 7.11 (s, 2H), 4.05 (t, *J* = 7.5 Hz, 6H), 3.26 (t, *J* = 7.5 Hz, 6H), 2.55 (s, 1H), 1.25 (s, 1H). NMR consistent with data found in literature. HRMS (ESI<sup>+</sup>): calculated for C<sub>11</sub>H<sub>16</sub>N<sub>7</sub><sup>+</sup> 246.1467, found 246.1472

20: *N*-(benzylcarbamoyl)-2-cyanoacetamide



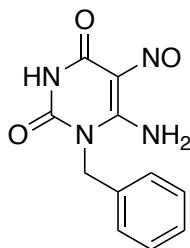
Cyanoacetic acid (0.438 mL, 6.6 mmol, 1 eq), acetic anhydride (0.629 mL, 6.6 mmol, 1 eq) and benzylurea (**18**, 1 g, 6.6 mmol, 1 eq) were refluxed (2 hours), solvent removed in vacuo, and ice added to the residue. The title compound precipitated as a white crystalline powder, which was collected by filtration (0.88 g, 4.1 mmol, 62%). <sup>1</sup>H NMR (400 MHz, DMSO) δ 10.64 (s, 1H), 8.45 (s, 1H), 7.39 – 7.20 (m, 5H), 4.37 (d, J = 6.0 Hz, 2H), 3.94 (s, 2H). <sup>13</sup>C NMR (101 MHz, DMSO) δ 165.5, 152.9, 139.6, 128.8, 127.7, 127.4, 115.6, 43.1, 27.2. HRMS (ESI<sup>+</sup>): calculated for C<sub>11</sub>H<sub>12</sub>N<sub>3</sub>O<sub>2</sub><sup>+</sup> 218.0929, found 218.0935.

22: 6-amino-1-benzylpyrimidine-2,4(1*H*,3*H*)-dione



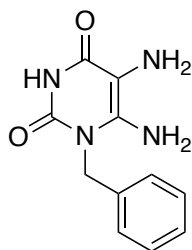
*N*-(benzylcarbamoyl)-2-cyanoacetamide (**20**, 1 g, 4.6 mmol, 1 eq) was suspended in sodium hydroxide solution (20%, 150 mL) and heated (90°C, 1 hour). The mixture was allowed to cool to room temperature, acidified with hydrochloric acid (7 mL, 3M) and the title compound precipitated as a white crystalline powder, which was collected by filtration (0.67 g, 3.1 mmol, 67%). <sup>1</sup>H NMR (400 MHz, DMSO) δ 10.51 – 10.46 (m, 1H), 7.39 – 7.31 (m, 2H), 7.31 – 7.23 (m, 1H), 7.23 – 7.16 (m, 2H), 6.79 (s, 2H), 5.02 (s, 2H), 4.59 (d, J = 2.1 Hz, 1H). <sup>13</sup>C NMR (101 MHz, DMSO) δ 162.8, 156.2, 151.9, 137.1, 128.9, 127.6, 126.8, 76.0, 44.0.

**24:** 6-amino-1-benzyl-5-nitrosopyrimidine-2,4(1*H*,3*H*)-dione



To a mixture of 6-amino-1-benzylpyrimidine-2,4(1*H*,3*H*)-dione (**22**, 0.15 g, 0.69 mmol, 1 eq) in water (0.6 mL) and acetic acid (0.288 mL) at -5 °C, sodium nitrite (52.4 mg, 0.76 mmol, 1.1 eq) was added in small portions. The mixture was stirred at room temperature (19 hours), and the title compound was collected as a purple solid via filtration, washed with cold water and dried in vacuo (0.16 g, 0.65 mmol, 93%). <sup>1</sup>H NMR (400 MHz, DMSO) δ 13.33 (s, 1H), 11.68 (s, 1H), 9.15 (s, 1H), 7.38 – 7.32 (dd, *J* = 8.1, 6.4 Hz, 2H), 7.32 – 7.23 (m, 3H), 5.09 (s, 2H). <sup>13</sup>C NMR (101 MHz, DMSO) not resolved. HRMS (ESI<sup>+</sup>): calculated for C<sub>11</sub>H<sub>11</sub>N<sub>4</sub>O<sub>3</sub><sup>+</sup> 247.0831, found 247.0832.

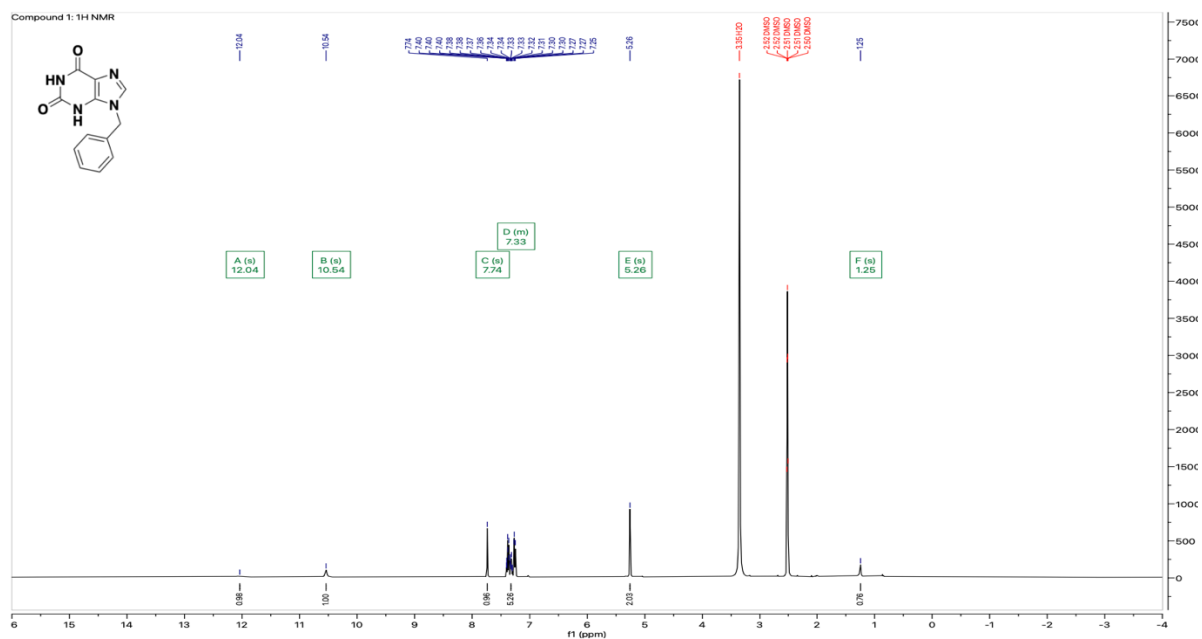
**26**, 5,6-diamino-1-benzylpyrimidine-2,4(1*H*,3*H*)-dione



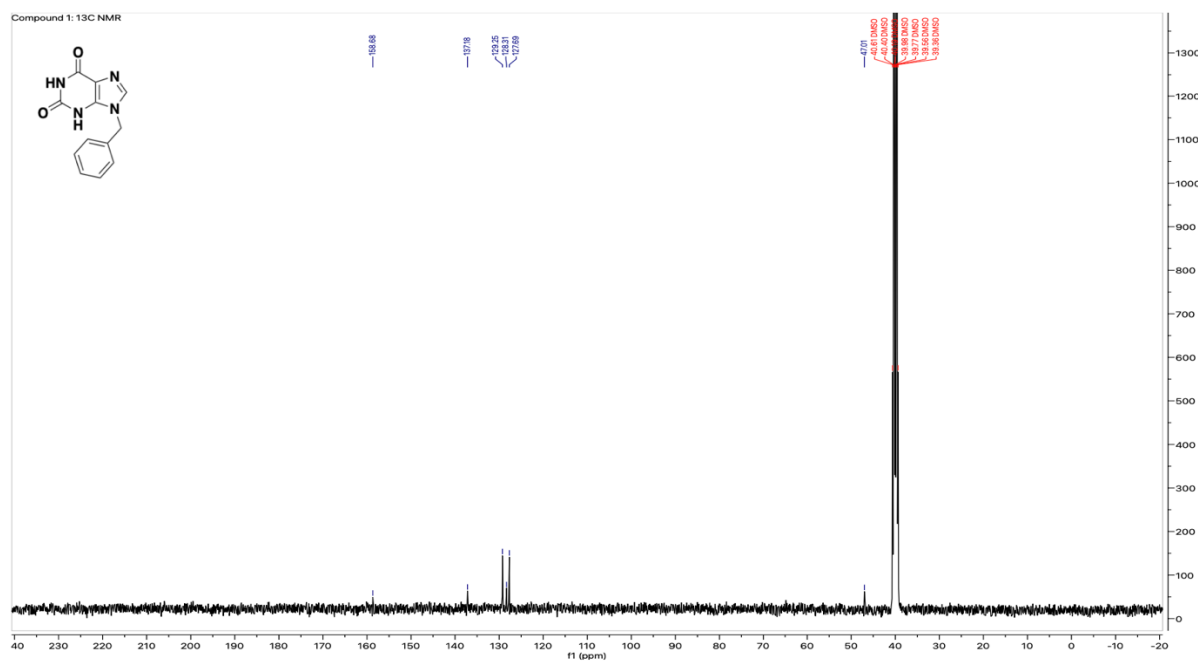
To a mixture of 6-amino-1-benzyl-5-nitrosopyrimidine-2,4(1*H*,3*H*)-dione (**24**, 0.12 g, 0.49 mmol, 1 eq) in aqueous ammonia (25%, 0.6 M), sodium dithionate (0.297g, 1.71 mmol, 3.5 eq) was added in small portions. The mixture was stirred (1 hour, 35C) until the purple pigment of nitroso was lost. Then the reaction mixture was stirred (1 hour at 60 °C, 17 hours at room temperature). The title compound was collected as a white solid via filtration, washed with cold water and dried in vacuo (61.6 mg, 0.27 mmol, 55%). <sup>1</sup>H NMR (400 MHz, DMSO) δ 10.73 (s, 1H), 7.34 (m, 2H), 7.31 – 7.22 (m, 1H), 7.25 – 7.18 (m, 2H), 6.13 (s, 2H), 5.08 (s, 2H), 2.89 (s, 2H). <sup>13</sup>C NMR (101 MHz, DMSO) δ 160.1, 150.1, 145.7, 137.4, 128.9, 127.5, 126.9, 96.9, 44.5. HRMS (ESI<sup>+</sup>): calculated for C<sub>11</sub>H<sub>11</sub>N<sub>4</sub>O<sub>2</sub><sup>+</sup> 231.0882, found 231.0885.

Intermediates **14**, **15**, **19**, **21**, **23**, **25** and **27** were not synthesized in this work.

## 7.2. Nuclear magnetic resonance (NMR) spectra

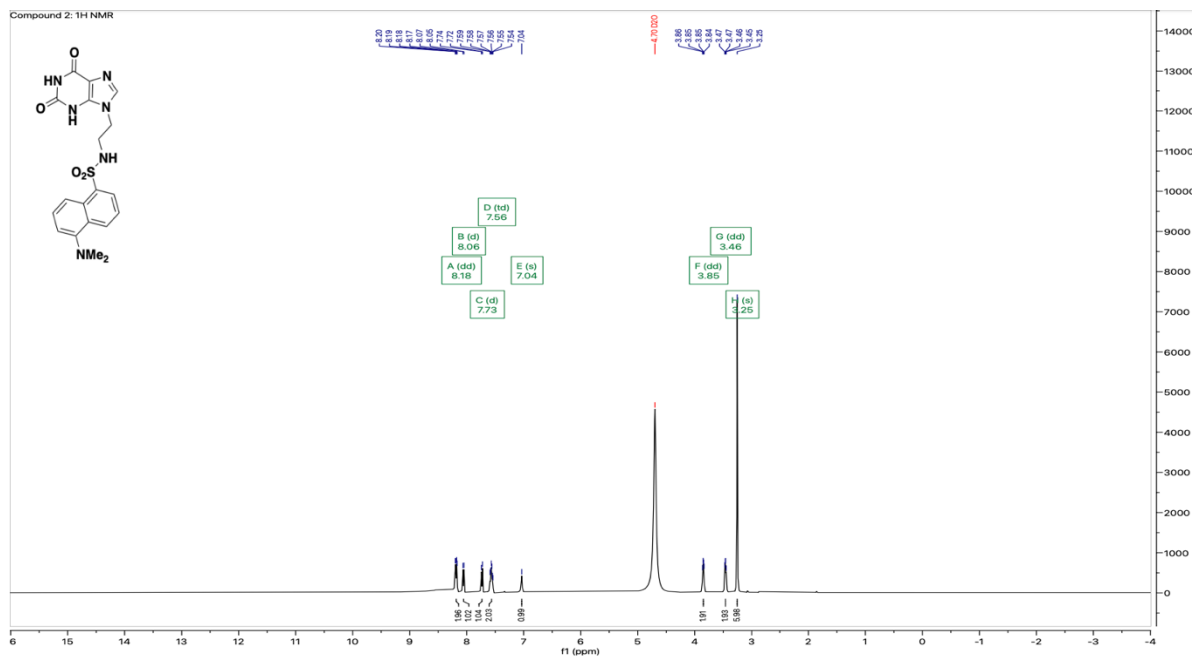


Supplementary Figure 1: <sup>1</sup>H NMR (400 MHz, DMSO) for Compound 1

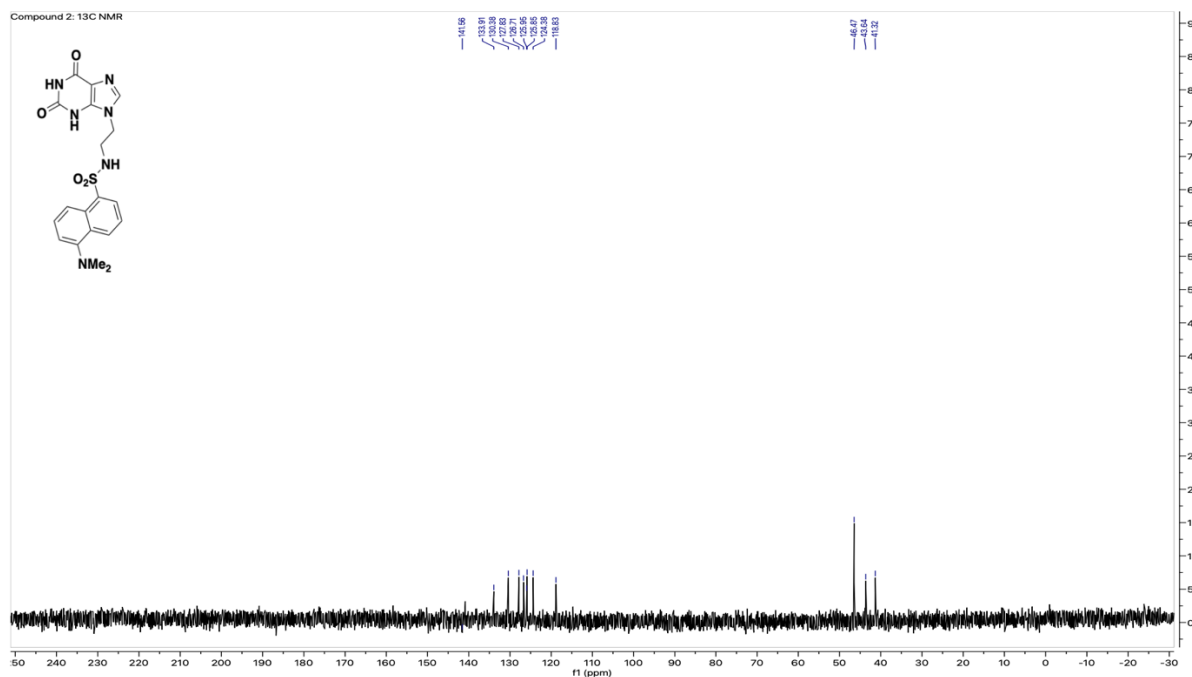


Supplementary Figure 2: <sup>13</sup>C NMR (400 MHz, DMSO) for Compound 1





Supplementary Figure 3: <sup>1</sup>H NMR (400 MHz, D<sub>2</sub>O) for Compound 2



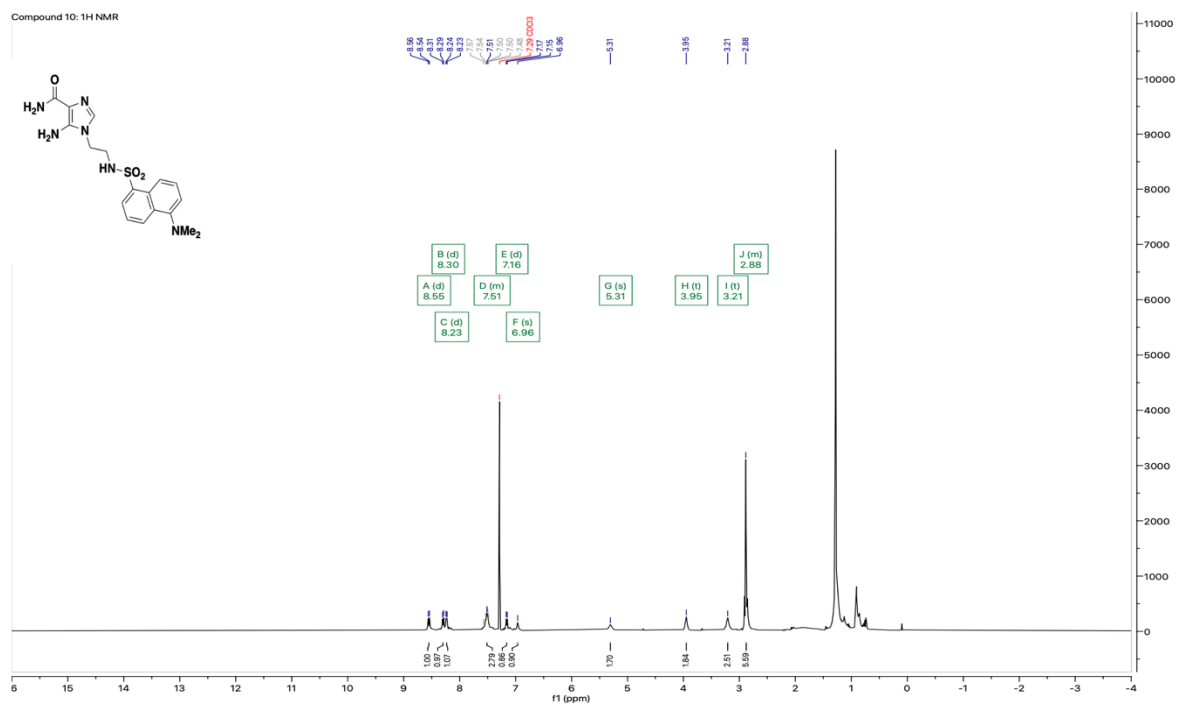
Supplementary Figure 4: <sup>13</sup>C NMR (400 MHz, D<sub>2</sub>O) for Compound 2



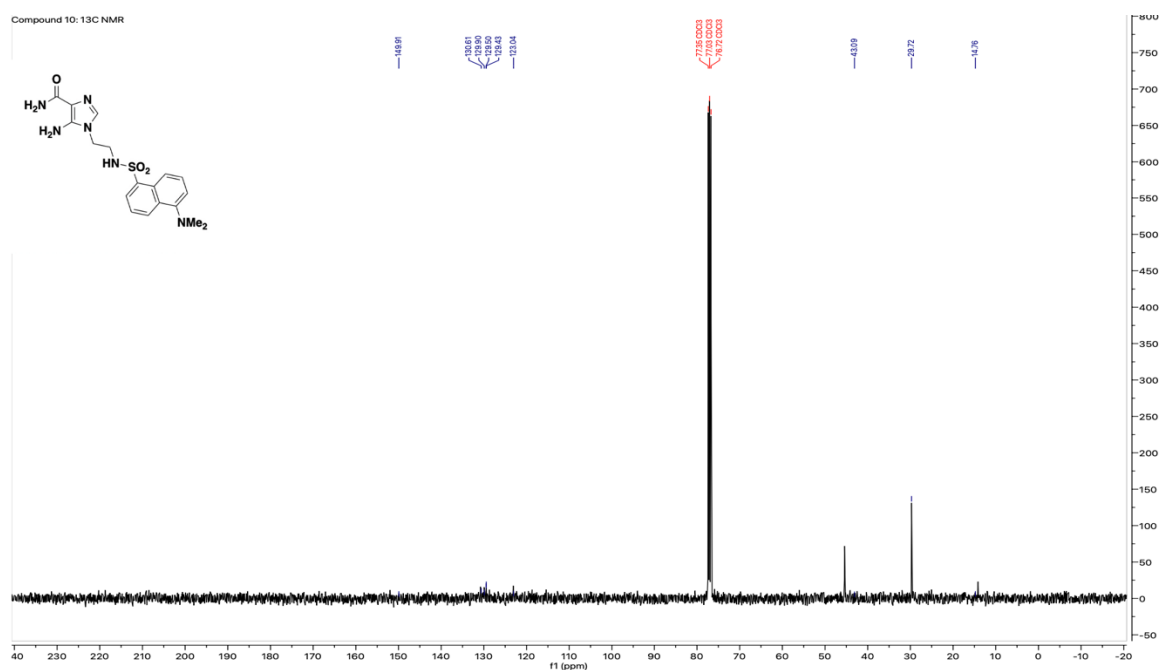




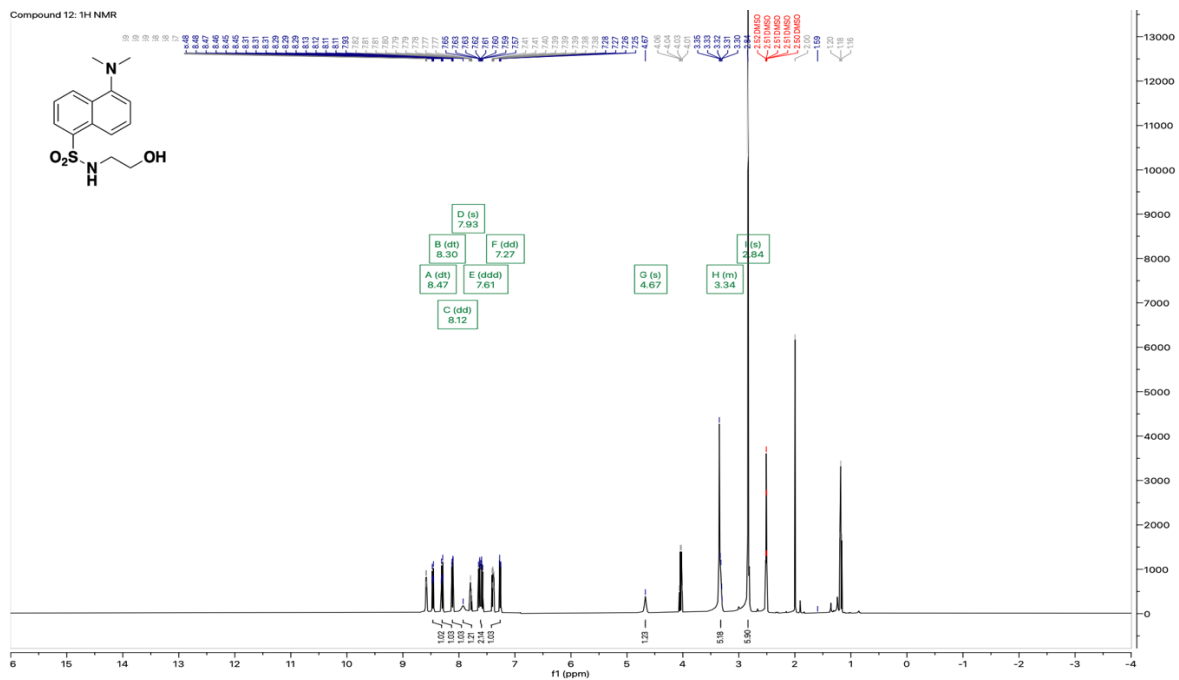




Supplementary Figure 13: <sup>1</sup>H NMR (400 MHz, CDCl<sub>3</sub>) for Compound 10



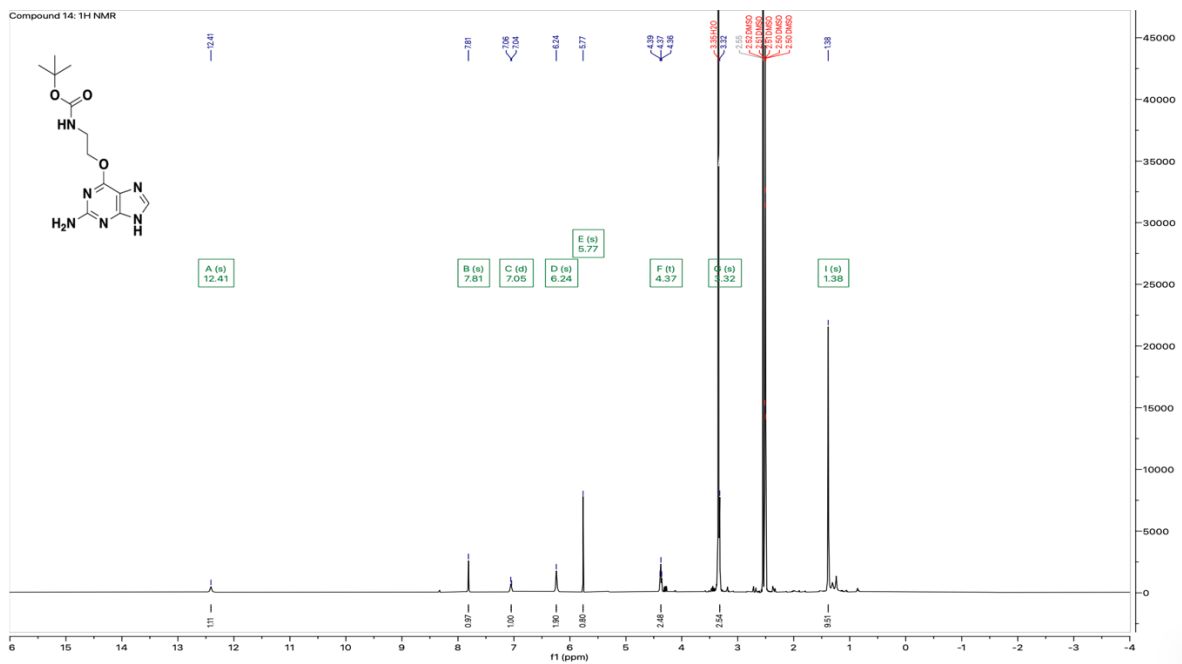
Supplementary Figure 14: <sup>13</sup>C NMR (400 MHz, CDCl<sub>3</sub>) for Compound 10



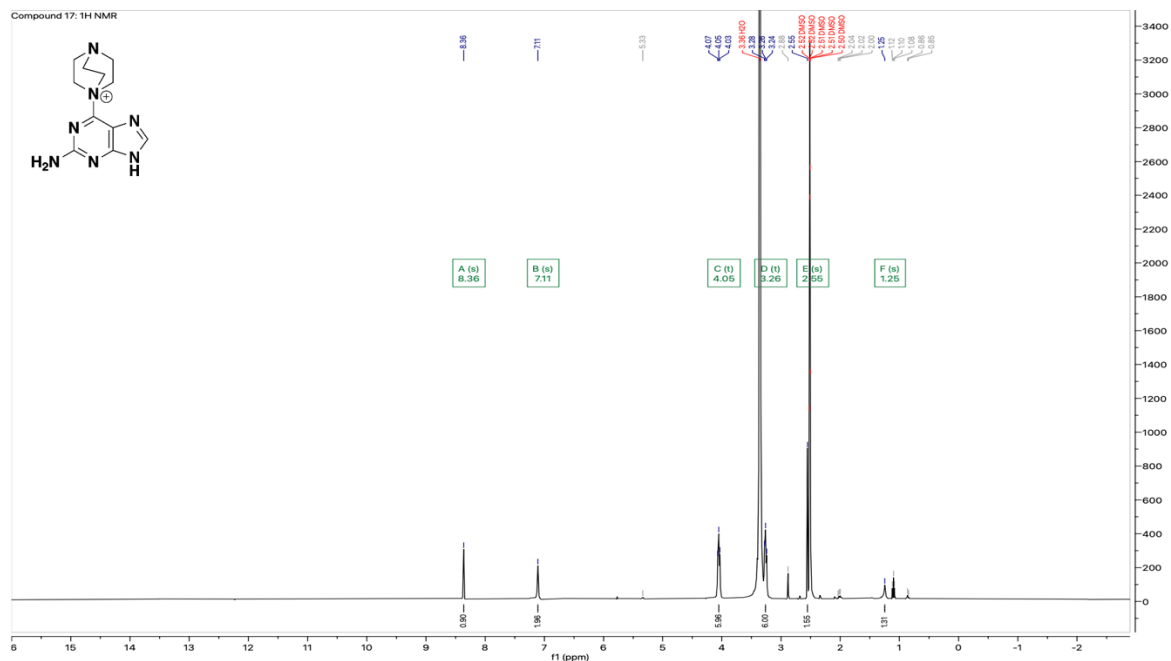
Supplementary Figure 15: <sup>1</sup>H NMR (400 MHz, DMSO) for Compound 12



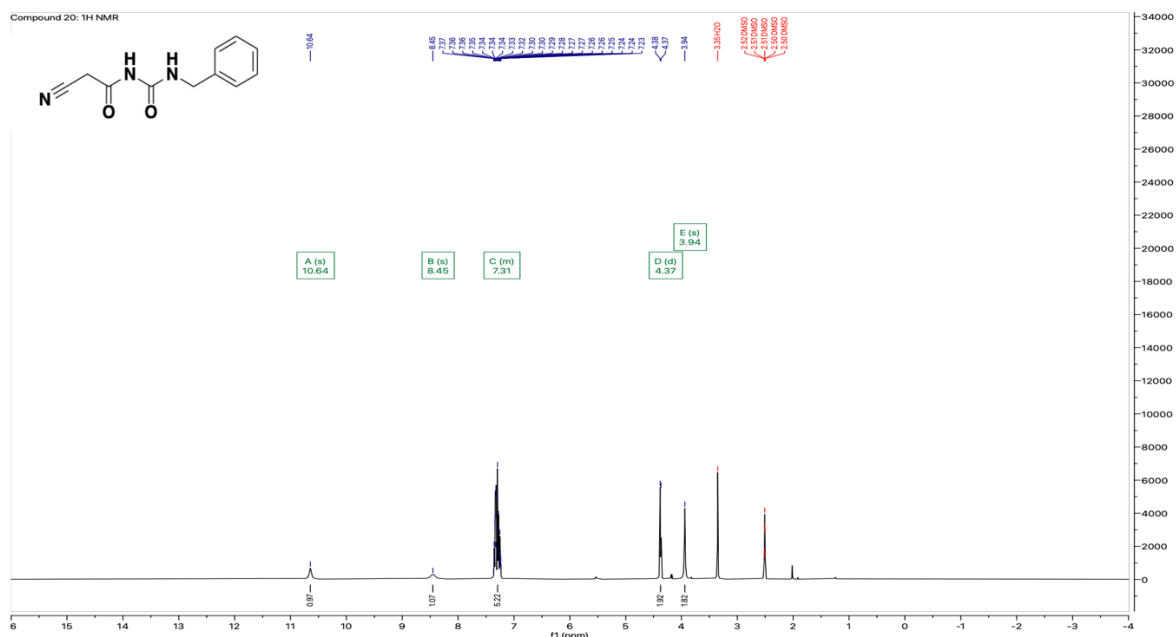




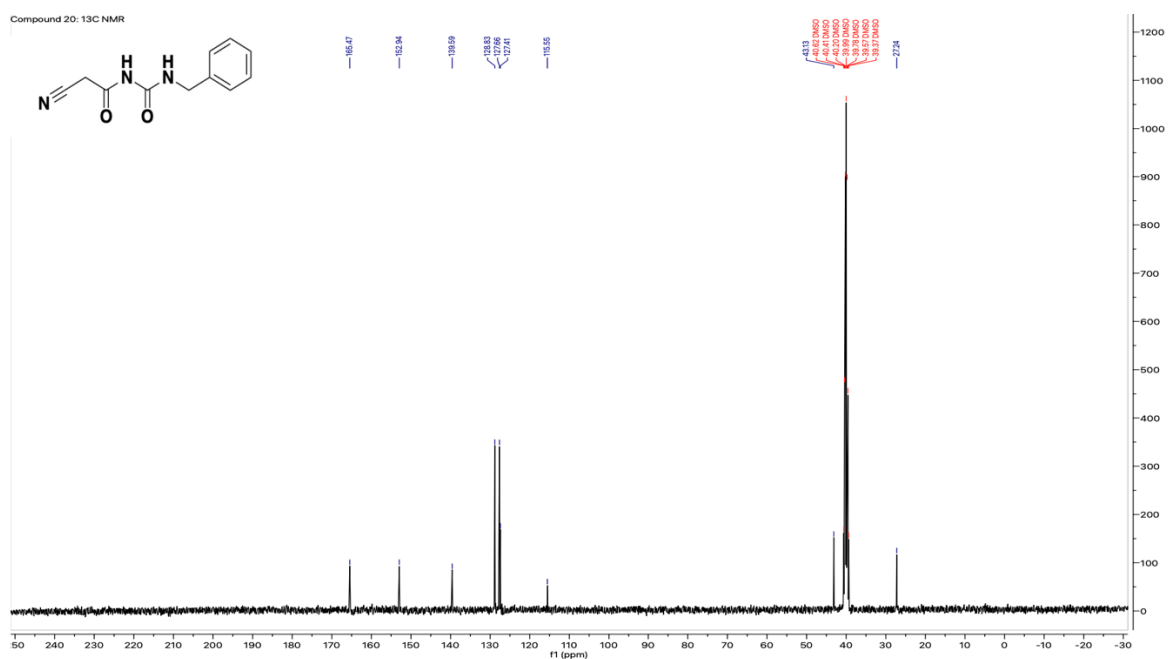
Supplementary Figure 18: <sup>1</sup>H NMR (400 MHz, DMSO) for Compound 14



Supplementary Figure 19: <sup>1</sup>H NMR (400 MHz, DMSO) for Compound 17

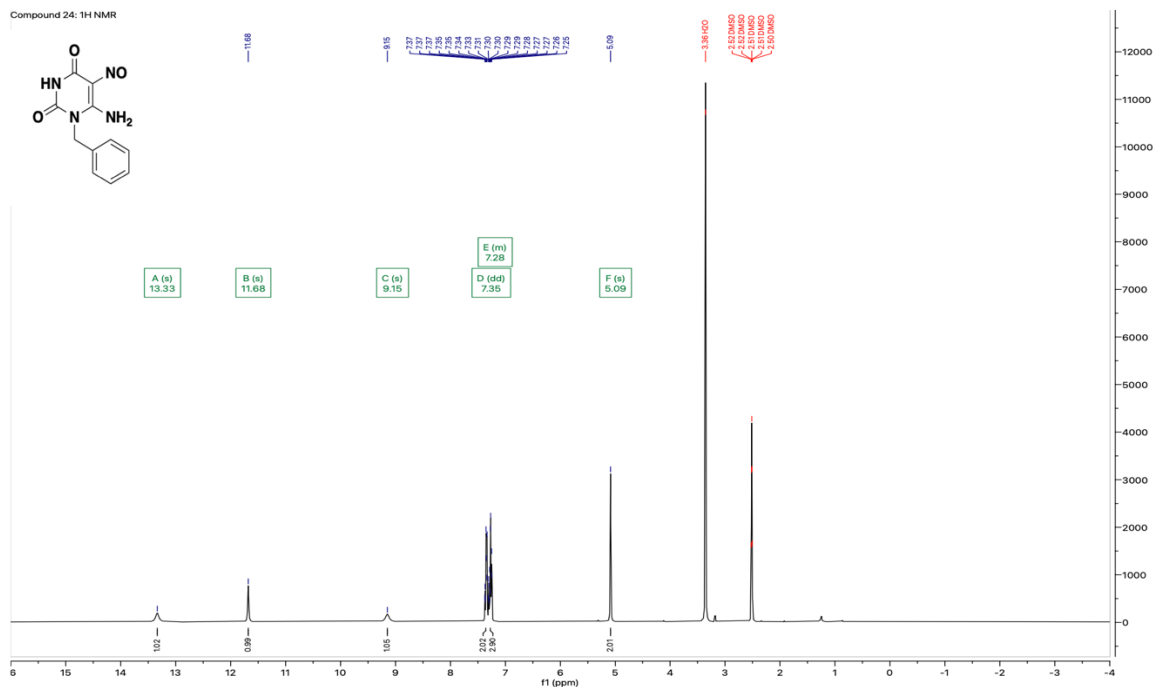


Supplementary Figure 20: <sup>1</sup>H NMR (400 MHz, DMSO) for Compound 20

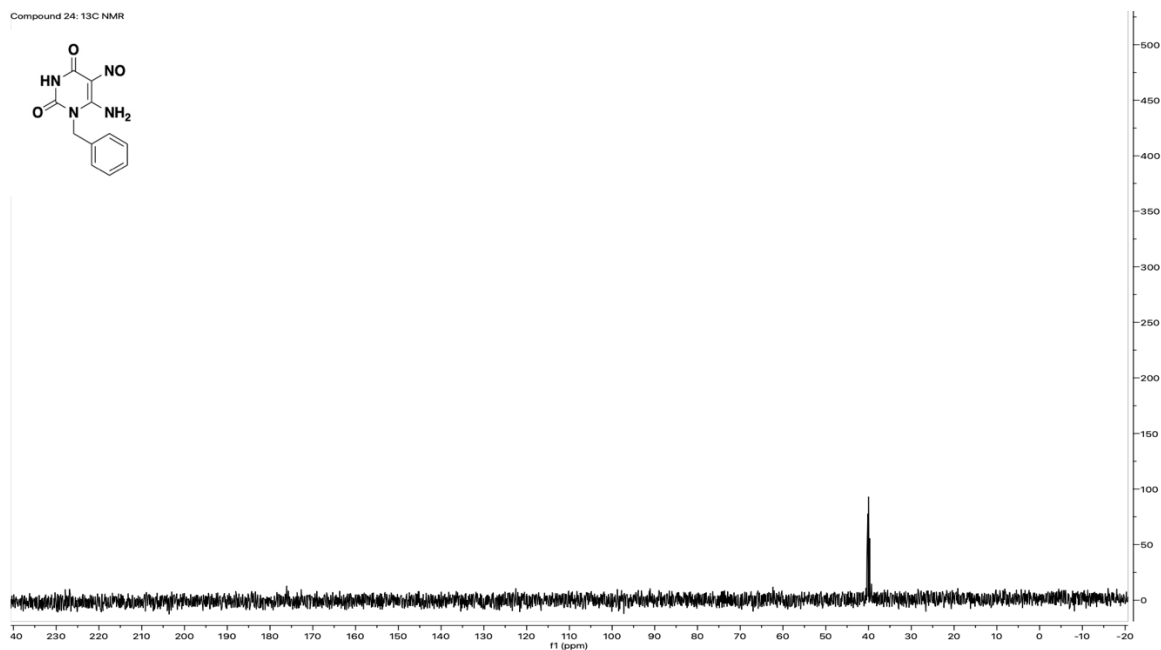


Supplementary Figure 21: <sup>13</sup>C NMR (400 MHz, DMSO) for Compound 20





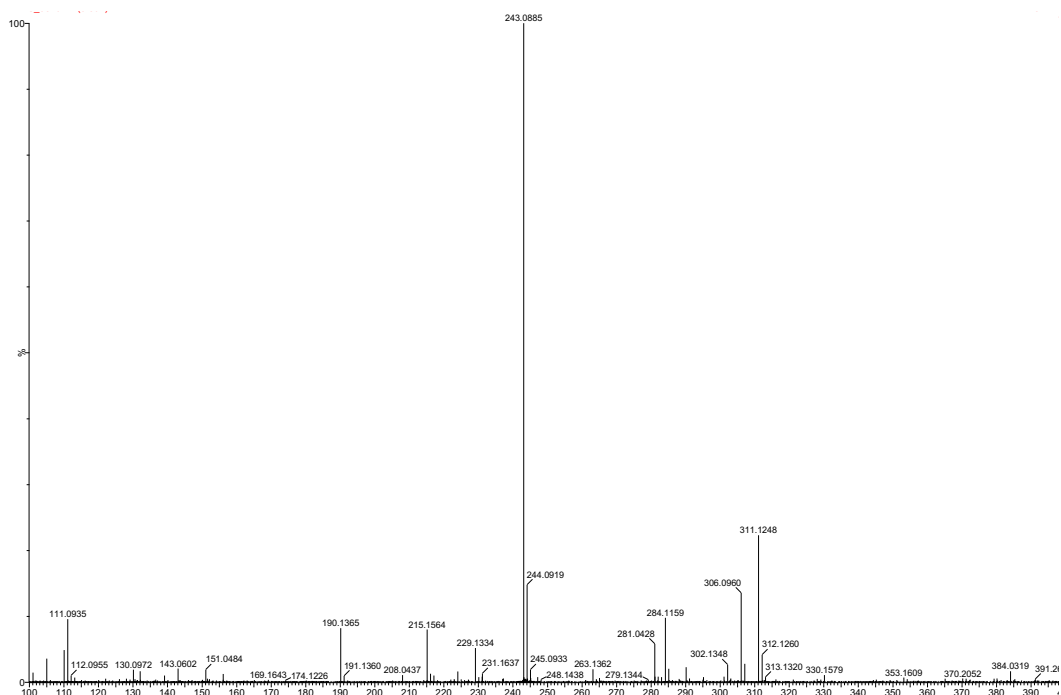
Supplementary Figure 24: <sup>1</sup>H NMR (400 MHz, DMSO) for Compound **24**



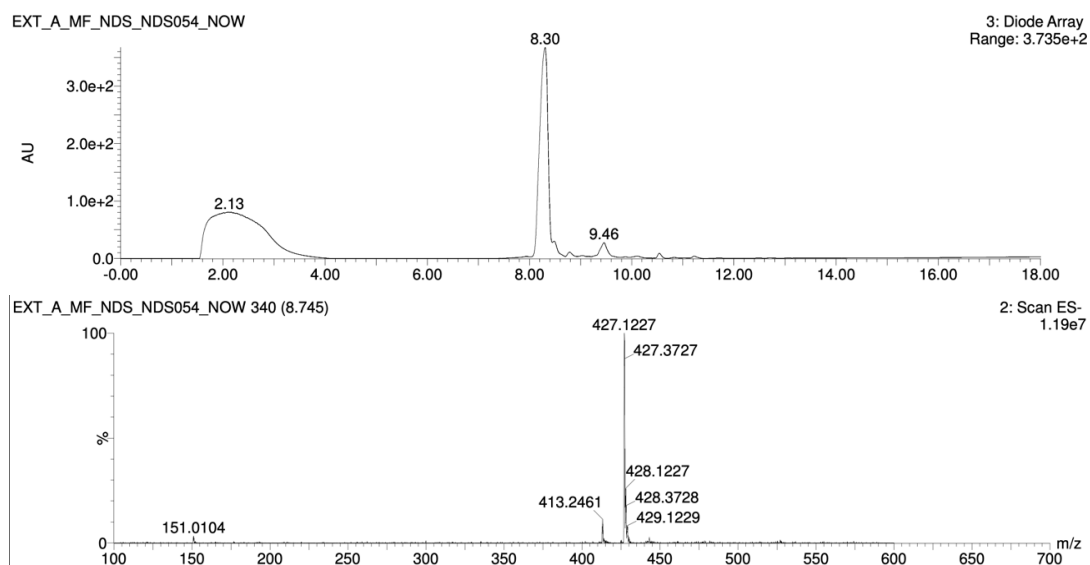
Supplementary Figure 25: <sup>13</sup>C NMR (400 MHz, DMSO) for Compound **24**



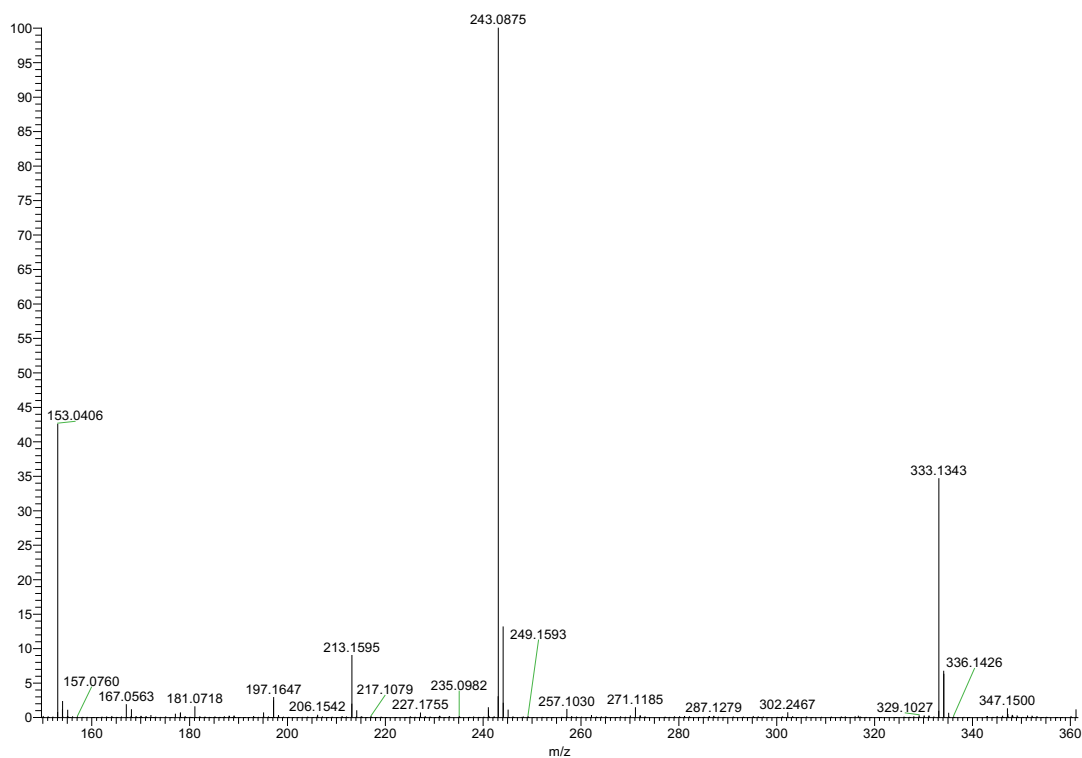
### 7.3. Mass Spectrometry



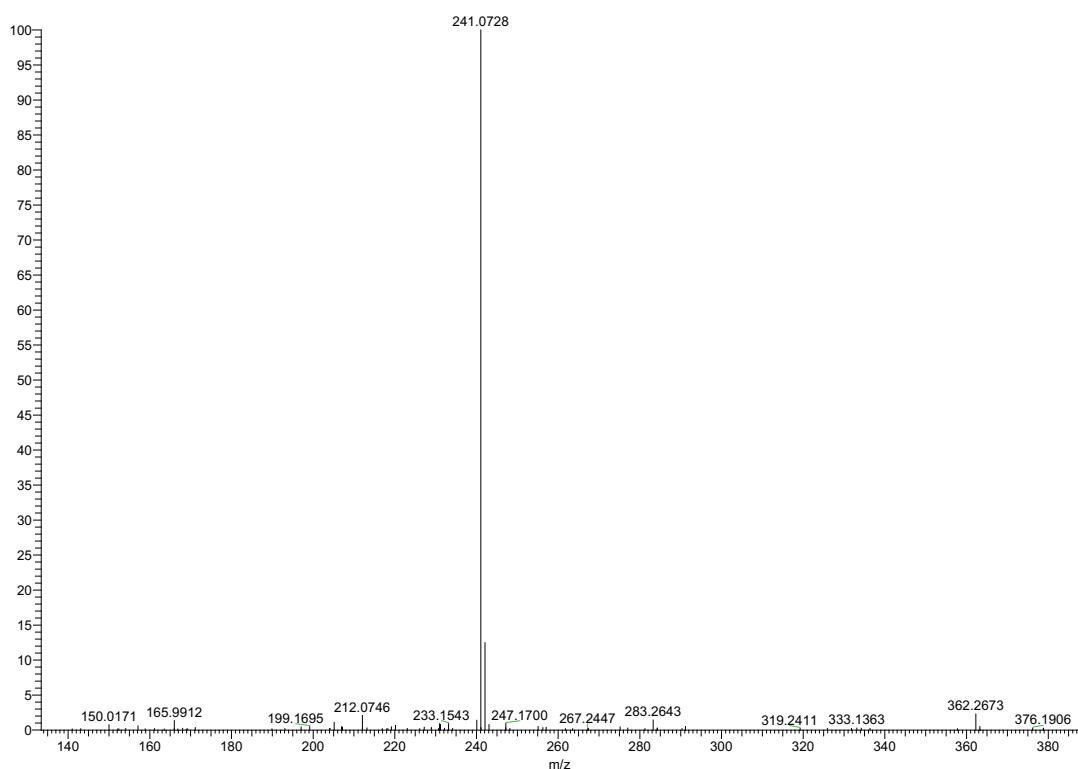
Supplementary Figure 28: Mass Spectra of Compound 1. HRMS (ESI+): calculated for  $C_{12}H_{11}N_4O_2^+$  243.0882, found 243.0885.



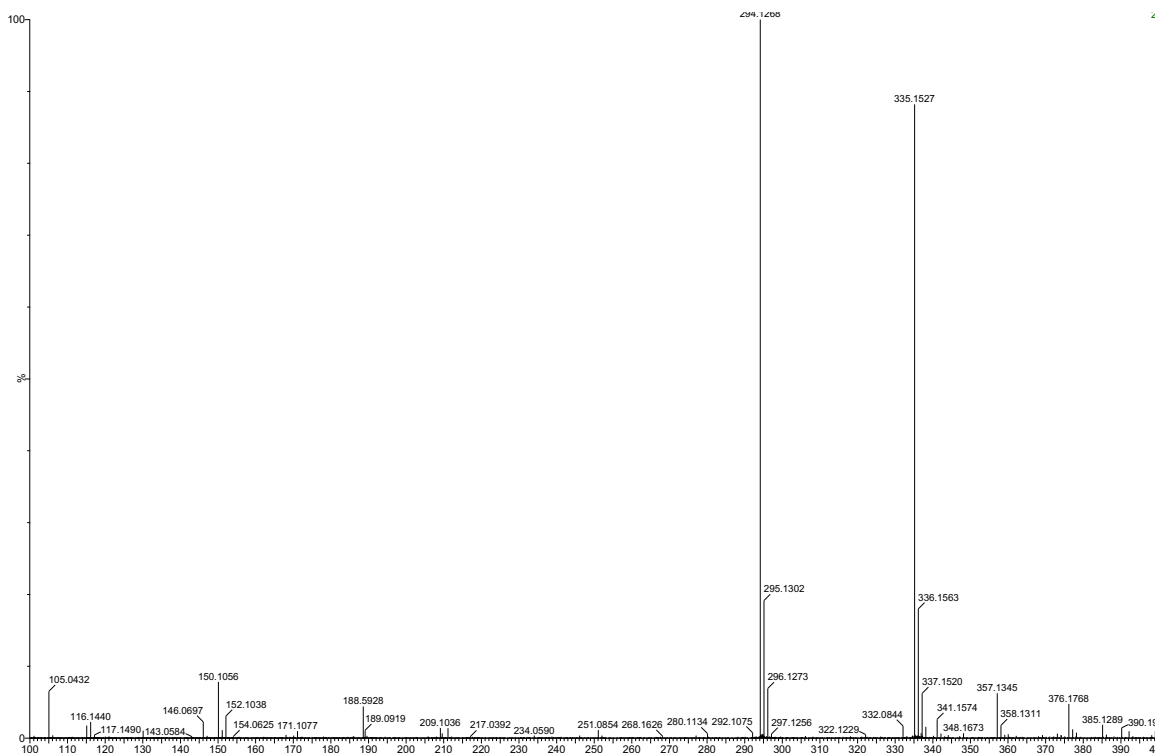
Supplementary Figure 29: LCMS for Compound 2. LCMS (ESI-): 5-98% gradient AcCN/H<sub>2</sub>O, RT 8.30, mass calculated for  $C_{19}H_{19}N_6O_4S^-$  427.1189, found 427.1227.



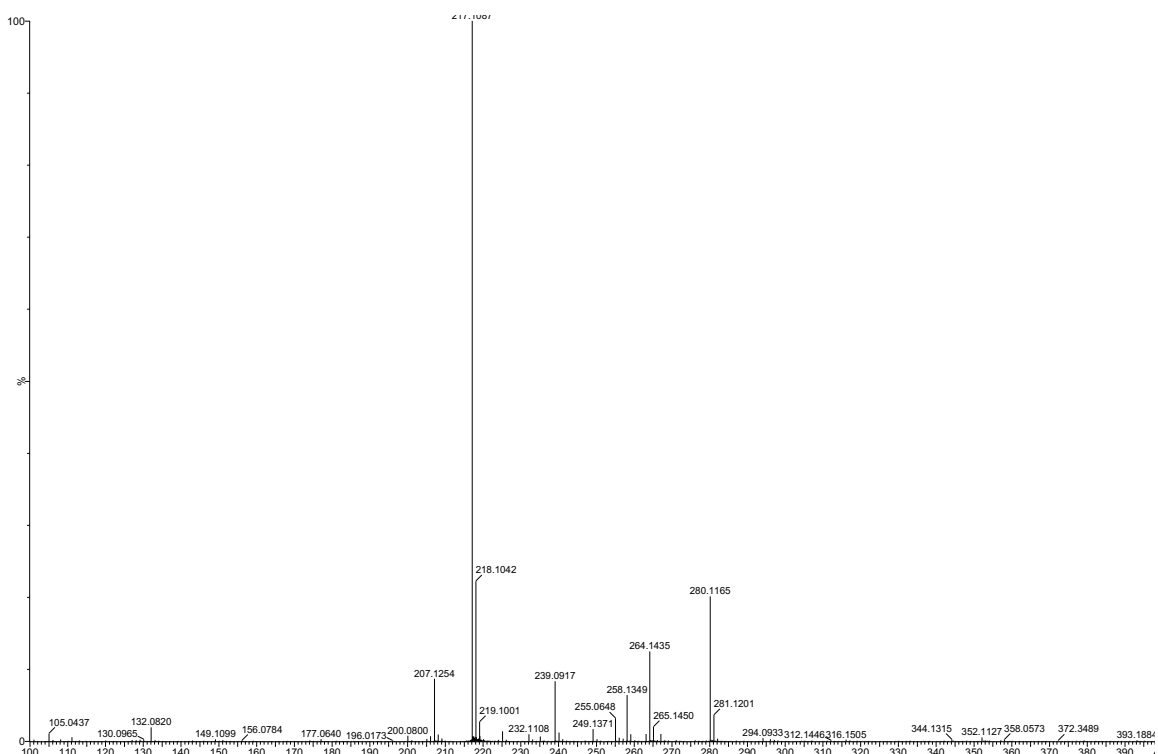
Supplementary Figure 30: Mass Spectra of Compound **3**. HRMS (ESI+): calculated for  $C_{12}H_{11}N_4O_2^+$  243.0882, found 243.0875.



Supplementary Figure 31: MS Spectra of Compound **5**. HRMS (ESI-): calculated for  $C_{12}H_9N_4O_2^-$ , 241.0720 found 241.0728.

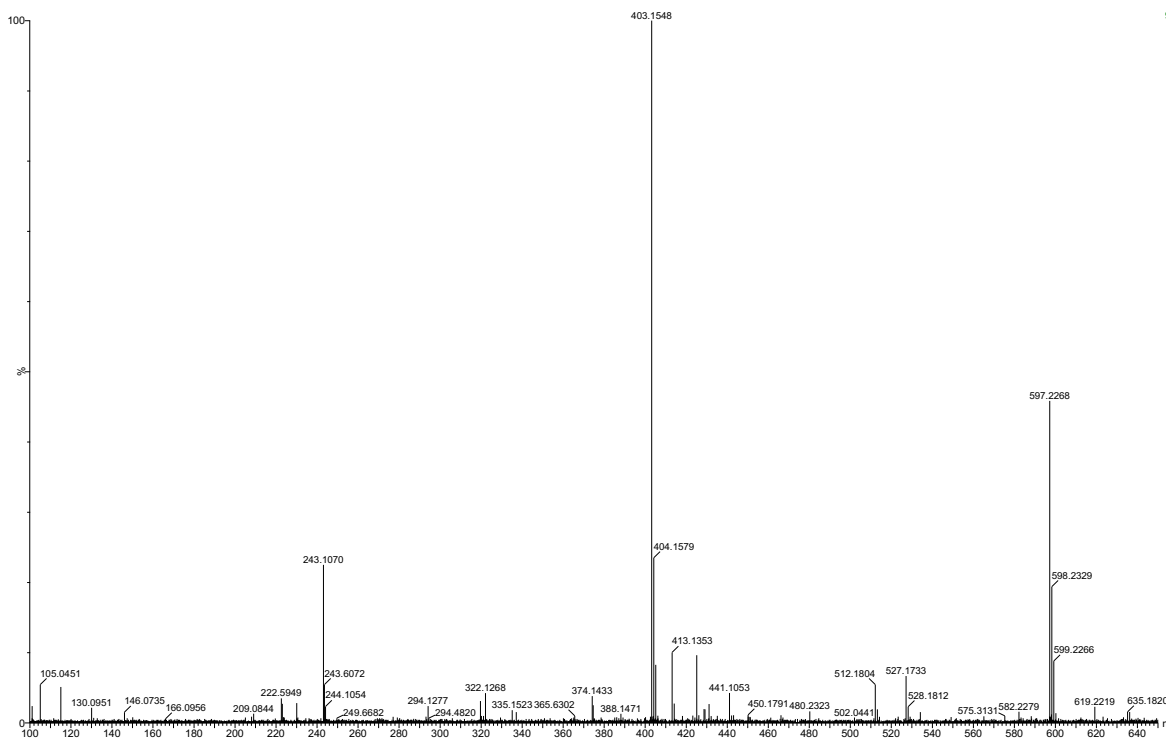


Supplementary Figure 32: Mass Spectra of Compound **8**. HRMS (ESI+): calculated for  $C_{14}H_{19}N_3O_2S^+$  294.1276, found 294.1268.

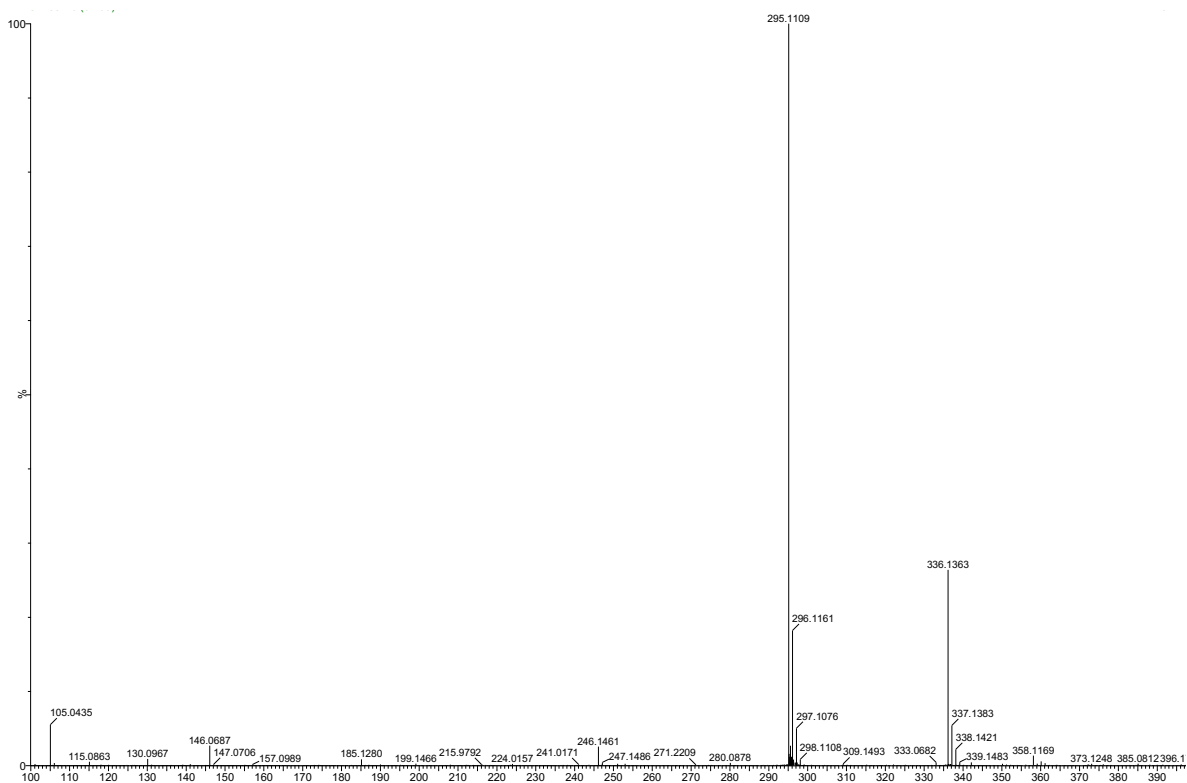


Supplementary Figure 33: Mass Spectra of Compound **9**. HRMS (ESI+): calculated for  $C_{11}H_{13}N_4O^+$  217.1089, found 217.1087.

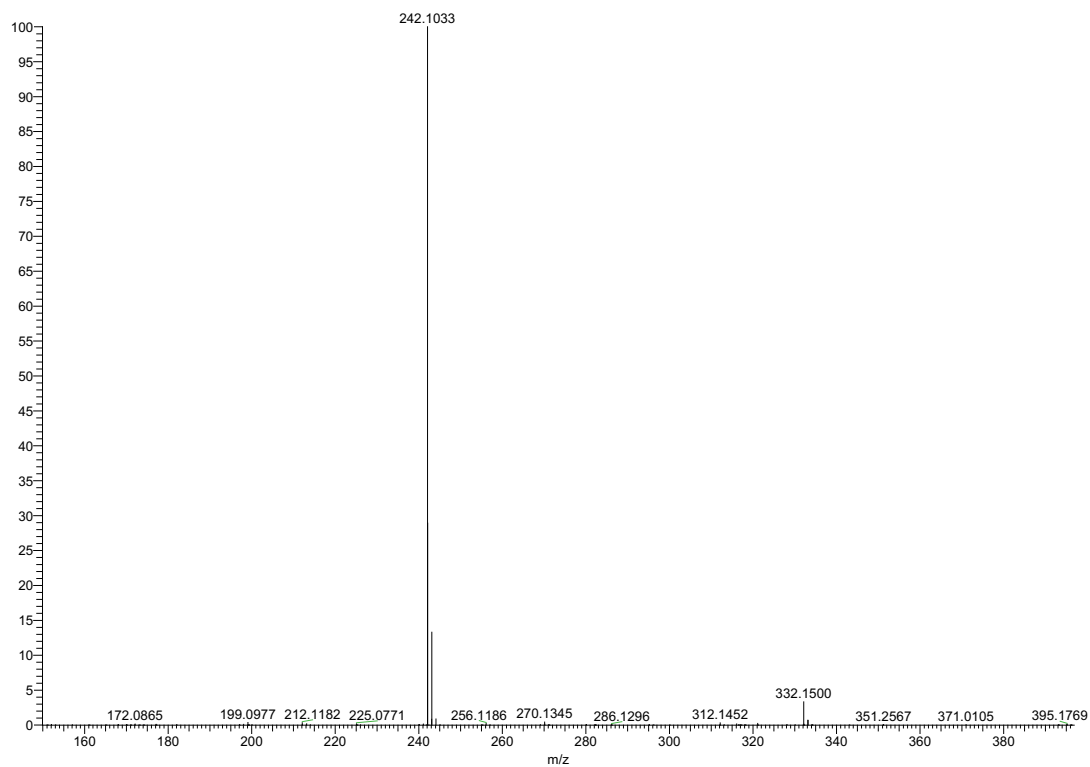




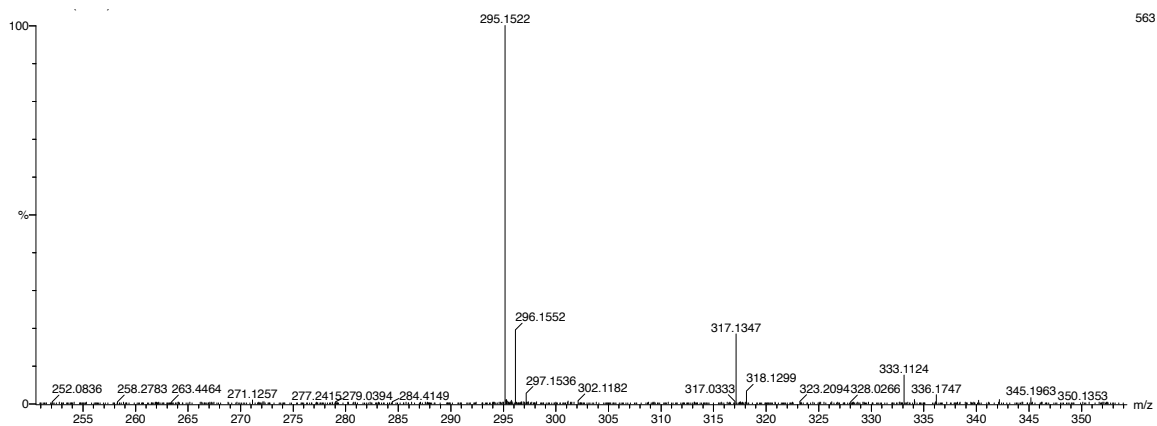
Supplementary Figure 34: Mass Spectra of Compound 10. HRMS (ESI+): calculated for  $C_{18}H_{22}N_6O_3S^+$  403.1552, found 403.1548.



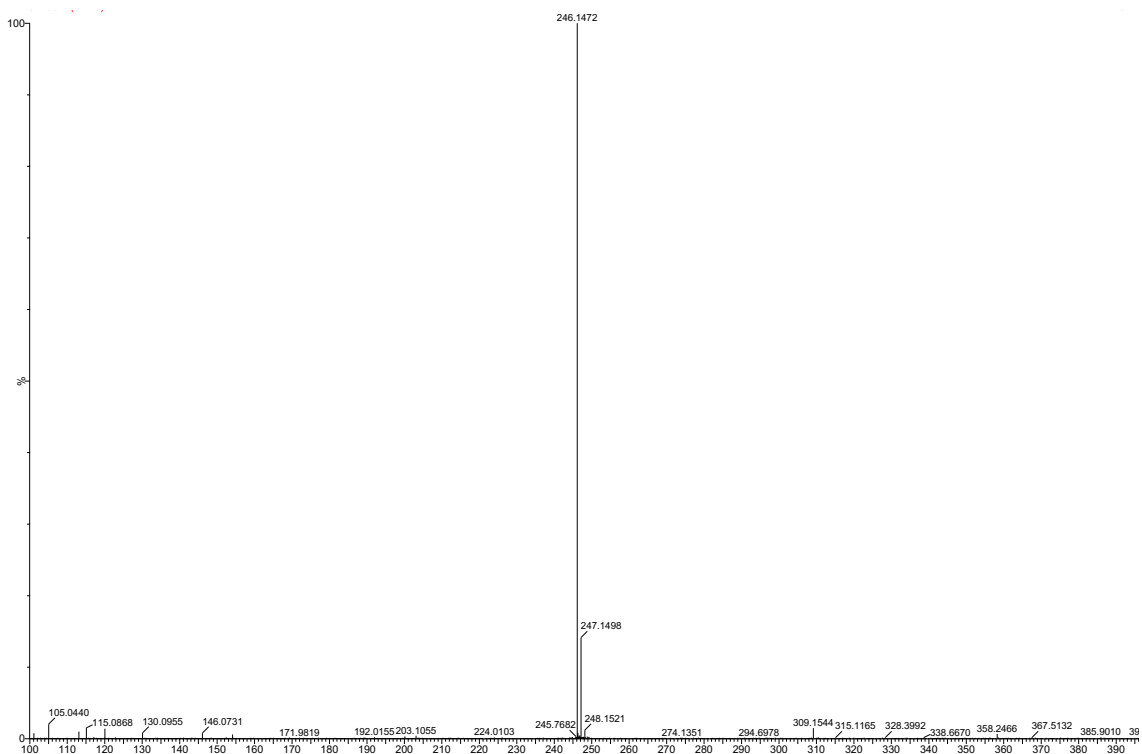
Supplementary Figure 35: Mass Spectra of Compound 12. HRMS (ESI+): calculated for  $C_{14}H_{19}N_2O_3S^+$  295.1116, found 295.1109.



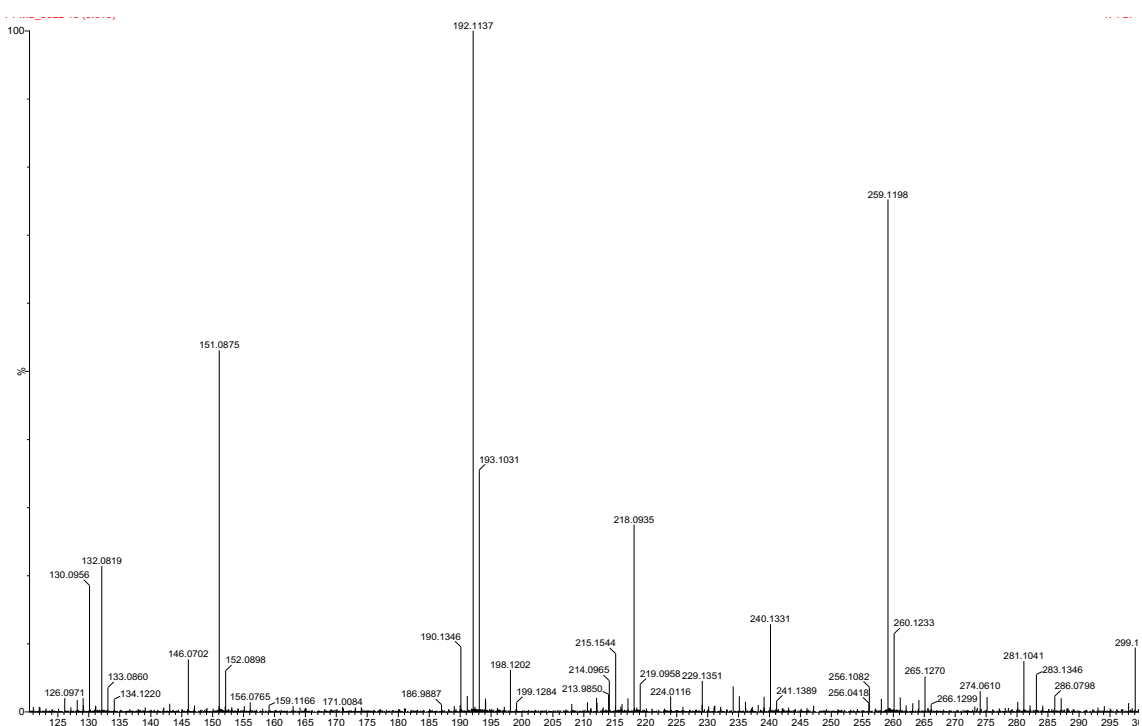
Supplementary Figure 36: Mass Spectra of Compound **13**. HRMS (ESI+): calculated for  $C_{12}H_{12}N_5O_2^+$  242.1036, found 242.1033.



Supplementary Figure 37: Mass Spectra of Compound **14**. HRMS (ESI+): calculated for  $C_{12}H_{19}N_6O_3^+$  295.1519, found 295.1522.

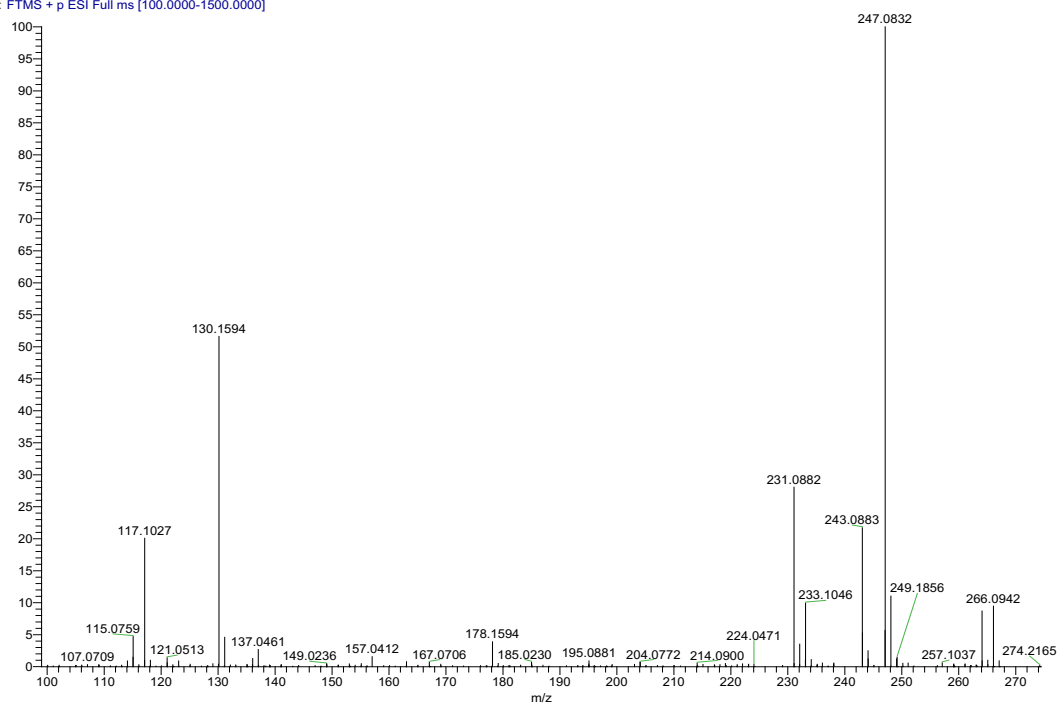


Supplementary Figure 38: Mass Spectra of Compound **17**. HRMS (ESI+): calculated for  $C_{12}H_{19}N_6O_3^+$  295.1519, found 295.1522.



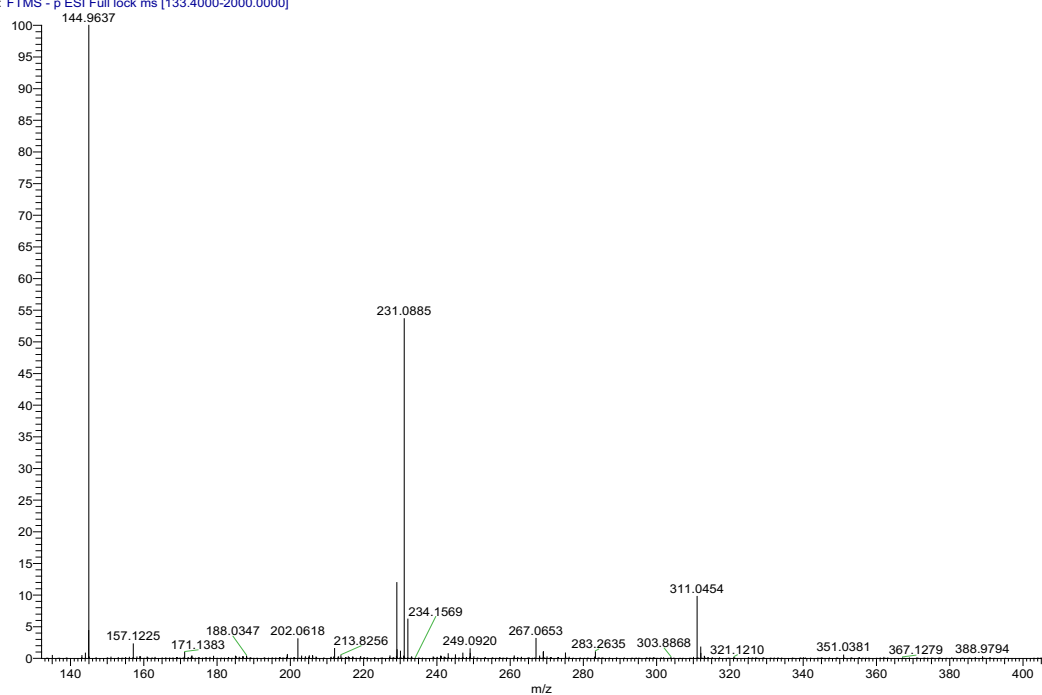
Supplementary Figure 39: Mass Spectra of Compound **20**. HRMS (ESI+): calculated for  $C_{11}H_{12}N_3O_2^+$  218.0929, found 218.0935.

200720\_PPMS3683 #327 RT: 0.77 AV: 1 SB: 390 0.05-0.85 , 0.93-1.C 7.30E8  
T: FTMS + p ESI Full ms [100.0000-1500.0000]



Supplementary Figure 40: Mass Spectra of Compound **24**. HRMS (ESI+): calculated for  $C_{11}H_{10}N_4O_3^+$  247.0831, found 247.0832.

200720\_PPMS3681 #122-124 RT: 0.54-0.55 AV: 3 SB: 27 0.33-0.45 3E7  
T: FTMS - p ESI Full lock ms [133.4000-2000.0000]



Supplementary Figure 41: MS Spectra of Compound **26**. HRMS (ESI-): calculated for  $C_{11}H_{11}N_4O_2^-$  231.0882, found 231.0885.